STUDIES OF BIOMACROMOLECULE ADSORPTION AND ACTIVITY AT SOLID SURFACES BY SURFACE PLASMON RESONANCE AND QUARTZ CRYSTAL MICROBALANCE WITH DISSIPATION MONITORING

Zelin Liu

A dissertation submitted to the faculty of the

Virginia Polytechnic Institute and State University

in partial fulfillment of the requirements for the degree of

Doctor of Philosophy

in

Chemistry

Alan R. Esker, Chairman
T. Daniel Crawford
Kevin J. Edgar
Hervé Marand
John R. Morris
Maren Roman

September 7, 2010

Blacksburg, Virginia

Keywords: Polysaccharides, Pullulan, Cellulose, Cellulase, Adsorption, Surface Plasmon Resonance, QCM-D

STUDIES OF BIOMACROMOLECULE ADSORPTION AND ACTIVITY AT SOLID SURFACES BY SURFACE PLASMON RESONANCE AND QUARTZ CRYSTAL MICROBALANCE WITH DISSIPATION MONITORING

Zelin Liu

ABSTRACT

Self-assembly of polysaccharide derivatives at liquid/solid interfaces was studied by surface plasmon resonance spectroscopy (SPR) and quartz crystal microbalance with dissipation monitoring (QCM-D). Carboxymethyl cellulose (CMC) adsorption onto cellulose surfaces from aqueous solutions was enhanced by electrolytes, especially by divalent cations. A combination of SPR and QCM-D results showed that CMC formed highly hydrated layers on cellulose surfaces (90 to 95% water by mass). Voigt-based viscoelastic modeling of the QCM-D data was consistent with the existence of highly hydrated CMC layers with relatively low shear viscosities of ~ 10^{-3} N•s•m^{-2} and elastic shear moduli of ~ 10^{5} N•m^{-2}.

Adsorption of pullulan 3-methoxycinnamates (P3MC) and pullulan 4-chlorocinnamates (P4CC) with different degrees of cinnamate substitution (DS_{Cinn}) onto cellulose, cellulose acetate propionate (CAP), poly(L-lactic acid) (PLLA), and methyl-terminated self-assembled monolayer (SAM-CH_3) surfaces was also studied by SPR and QCM-D. Hydrophobic cinnamate groups promoted the adsorption of pullulan onto all surfaces and the adsorption onto hydrophobic surfaces was significantly greater than onto hydrophilic surfaces. SPR and QCM-D results showed that P3MC and P4CC also formed highly hydrated layers (70 to 90% water by mass) with low shear viscosities and elastic shear moduli.

Finally, cellulose adsorption and activity on pullulan cinnamate (PC) and cellulose blend films were studied via QCM-D and in situ atomic force microscopy (AFM). The hydrophobicity of PC surfaces was controlled by adjusting the degree of cinnamate substitution per anhydroglucose unit (DS_{Cinn}). It was found that cellulase showed weak adsorption onto low DS_{Cinn} PC surfaces, whereas cellulase adsorbed strongly onto high DS_{Cinn} PC surfaces, a clear indication of the role surface hydrophobicity played on enzyme adsorption. Moreover, cellulase catalyzed hydrolysis of cellulose/PC and cellulose/polystyrene (PS) blend surfaces was studied. The QCM-D results showed that the cellulase hydrolysis rate on cellulose in cellulose/PC blend surfaces decreased with increasing DS_{Cinn}. AFM images revealed smooth surfaces for cellulose/PC ($DS_{Cinn} = 0.3$) blend surfaces and laterally phase separated morphologies for cellulose/PC ($DS_{Cinn} \geq 0.7$) blend surfaces. The combination of QCM-D and AFM measurements indicated that cellulase catalyzed hydrolysis was strongly affected by surface morphology. The cellulase hydrolysis activity on cellulose in cellulose/PS blend surfaces was similar with cellulose/PC blend surfaces ($DS_{Cinn} \geq 0.7$).

These studies showed self-assembly of macromolecules could be a promising strategy to modify material surfaces and provided further fundamental understanding of adsorption phenomena and bioactivity of macromolecules at liquid/solid interfaces.

Acknowledgements

There are many people who helped me during my Ph. D. study at Virginia Tech. First I need to thank my advisor, Dr. Alan R. Esker, for offering the opportunity to work in his group. I want to thank Dr. Esker for encouraging me and being patient for the last five years. Even beyond supervising me on laboratory scientific research, Dr. Esker did a great job of keeping a coherent group and teaching us the language and culture which is a tremendous benefit for an international student. I would like to thank my committee members: Prof. T. Daniel Crawford, Prof. Kevin J. Edgar, Prof. Hervé Marand, Prof. John R. Morris, and Prof. Maren Roman for their valuable discussion and comments on my Ph. D. work. I am also grateful to Prof. Thomas Heinze (Friedrich Schiller University of Jena, Germany) and Prof. Paul Gatenholm (Chalmers University of Technology, Sweden) for their help in my study.

In particular, I am thankful to Feng Jiang and Shuping Dong in Prof. Roman's group for the help in cellulase work. I would also like to thank Steven Burrows in Prof. Morris's group for the help in AFM measurements. I thank Dr. Bin Li, Sidd Pawar, and Daiqiang Xu in Prof. Edgar's group for the help in organic synthesis.

I would like to thank my many colleagues, Suolong Ni, Bingbing Li, Ritu Paul, Woojin Lee, Abdulaziz Kaya, Ufuk Karabiyik, Wen Yin, Joshua Kittle, Qiongdan Xie, Jae Hyun Sim, Yang Liu, Xiaosong Du, Chuanzi OuYang, Chao Wang, Xiao Zhang, and Chen Qian. I would also like to thank my friends in Blacksburg: Jielu Zhao, Jianfei Zhang, Sha Yang, Ende Pan, Ting Cai, Fan Yang, Zhiyuan Lin for the help in my life. Thanks to all of you for your help during all these years.

As always, I would like to thank my family for their unconditional love and support all over the years. They are the important reason I continued and finished my Ph. D. study.

Table of Contents

List of Figures

Chapter 2

Chapter 3

Chapter 6

Chapter 7

Chapter 8

List of Tables

Chapter 7

CHAPTER 1

Overview

Adsorption of biomacromolecules such as polysaccharides and proteins at liquid/solid interfaces is relevant to many biological processes, and understanding the process of adsorption may provide a promising approach to control surface properties of bulk materials.[1-3] One aim of this study was to modify polymer surfaces via self-assembly of water soluble polysaccharide derivatives in an effort to improve the biocompatibility of materials and enhance the strength of composite materials. Another aim was to create model systems for studying enzymatic activity which could prove useful in improving the efficiency of bioconversion of lignocellulosic biomass. Surface techniques such as surface plasmon resonance (SPR), quartz crystal microbalance with dissipation monitoring (QCM-D), and in situ atomic force microscopy (AFM) were employed to monitor adsorption, investigate viscoelastic properties of thin adsorbed layers and understand the fundamental interactions between bioactivity and surface morphology.

This dissertation consists of eight chapters. Chapter 2 provides an overall introduction and review related to this study and begins with a general introduction of cell wall structures and wood-plastic composites, polysaccharides and pullulan derivatives, and bioconversion of lignocellulosic biomass. Subsequent discussion includes thermodynamic treatments of an interface, the Gibbs adsorption isotherm and theoretical predictions for neutral polymer and polyelectrolyte adsorption at liquid/solid interfaces. Next, polymer blend thin films and thin film phase separation are introduced. Finally, several techniques including spincoating, contact angle measurements, surface tension measurements, AFM, SPR and QCM-D are presented.

Material synthesis, substrate preparation, and experimental procedures for this study are provided in Chapter 3. The description of experimental methods will not be repeated in subsequent chapters.

Chapter 4 describes the self-assembly of carboxymethyl celluloses (CMC) onto cellulose surfaces from different electrolyte solutions. Salt effects on CMC adsorption are discussed. SPR and QCM-D were combined to study the hydration of the CMC adsorbed layers. Viscoelastic modeling of QCM-D data is discussed and the viscosities and shear moduli of adsorbed CMC layers are presented. Adsorption isotherms of CMC from calcium chloride solutions were also studied by QCM-D and the data fit by Langmuir and Freundlich adsorption isotherms are presented.

Chapter 5 describes the adsorption of pullulan cinnamates (PC) onto cellulose, thermoplastic, and methyl-terminated self-assembly monolayer (SAM) surfaces. Surface tension experiments used to probe aqueous solution properties of pullulan cinnamates and characterization of substrate surfaces are discussed. The dominant role of hydrophobic interactions between pullulan cinnamates and substrates on the adsorption processes is the primary focus of this chapter. Next, water content and viscoelastic properties of PC adsorbed layers determined by SPR and QCM-D are provided. Finally, comparisons between CMC and PC adsorption based on SPR and QCM-D results are discussed.

In Chapter 6, studies of the adsorption of enzymes onto model lignocellulosic surfaces are presented. Model pullulan derivative surfaces characterized by AFM and static contact angle measurements are the focus of this chapter. Investigations of cellulase adsorption, an enzyme mixture, onto the model surfaces by QCM-D and in situ AFM measurements are also provided. This study yields direct information about the

adsorption process and further understanding of the interactions behind the adsorption of cellulases onto lignocellulosic biomass.

Chapter 7 is a continuation of work presented in Chapter 6. The pullulan derivatives used in Chapter 6 were mixed with trimethylsilyl cellulose (TMSC) to prepare thin blend films as model lignocellulosic surfaces. Cellulase adsorption onto and activity on blend surfaces was studied by QCM-D and in situ AFM. The relationship between cellulase hydrolysis rates and surface chemical composition and morphology is discussed. Comparisons are also made to studies of cellulase activity on cellulose/polystyrene blend surfaces.

Finally, Chapter 8 summarizes the overall conclusions of this study and provides suggestions for future work. In particular some novel polysaccharide derivatives were synthesized and further adsorption studies are proposed.

References:

(1) Combes, C.; Rey, C. *Biomaterials* **2002**, *23*, 2817-2823.

(2) Roach, P.; Eglin, D.; Rohde, K.; Perry, C. C. *J. Mater. Sci.: Mater. Med.* **2007**, *18*, 1263-1277.

(3) Goddard, J. M.; Hotchkiss, J. H. *Progress in Polymer Science* **2007**, *32*, 698-725.

CHAPTER 2

Introduction and Review

2.1 Introduction to Wood and Composite Materials

2.1.1 Structure of Cell Walls in Wood

Wood is a porous substance consisting of a vast number of cells.[1] Wood has the functions of structural support, nutrient conduction, and energy storage. Those cells that function as conductors and those that provide structural support make up 60 to 90% of wood by volume. These cells are actually "dead," for only a hollow shell with rigid walls is left behind. The only living cells within the wood portion of the tree are the food-storage cells.[2] All of the cells making up the wood are derived from the layer directly outside of the wood known as the vascular cambium. There are two kinds of cells in the vascular cambium: spindle-shaped, axialy elongated cells, termed as fusiform initials, and ray initials, which are as broad as they are high.[1] A mature wood cell consists of a primary wall and a secondary wall that deposits onto the internal side of the primary wall to increase the rigidity and thickness of the cell wall. **Figure 2.1** shows structures of mature cells in the wood. Adjacent cells are united by a thin layer of intercellular substance, referred to as the middle lamella. Primary walls for the cells are adjacent to both sides of the middle lamella. Adjacent to the primary cell wall is the first layer of the secondary cell wall, the S1 layer. The central layer, the S2 layer, is the thickest of the three layers of the secondary cell wall. Finally, the innermost layer adjacent to the lumen is called the S3 layer.[2]

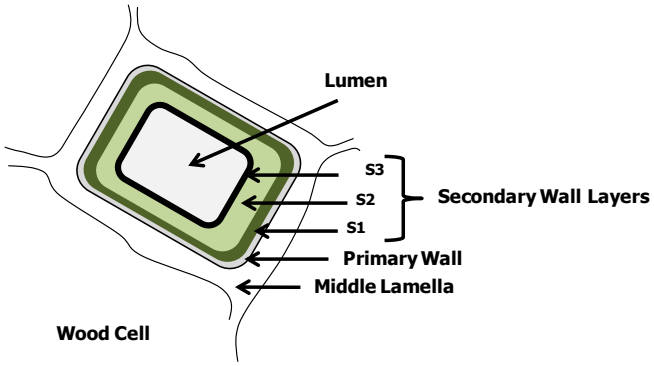

Figure 2.1. Hierarchical structure of wood cells.

Wood cell walls are multi-component materials composed of cellulose, hemicelluloses, lignin, pectin and proteins. For the primary cell wall, the cellulose microfibrils are crosslinked by hemicelluloses to form a composite structure that is embedded in the pectin matrix.[3] For the secondary cell walls, the cellulose microfibrils are also crosslinked by hemicelluloses, whereas lignin, a complex phenolic polymer, fills the spaces between cellulose microfibrils and hemicelluloses. The cellulose content is 43 ± 2% by weight for both softwoods and hardwoods.[3] The lignin content of hardwoods varies between 18 and 25% by weight, whereas softwood varies between 25% and 35% by weight.[3] The hemicellulose content of the cell wall varies between 20 and 35% by weight in hardwoods, versus as much as 30% by weight in softwoods.[4]

2.1.2 Cellulose

Cellulose is the largest component of the cell wall. This polymer is a linear chain composed of anhydroglucose units (AGUs) linked by β-(1-4) glucosidic bonds as shown in **Figure 2.2**.[5] The two chain ends are chemically different. One end has a D-glucopyranose unit in which the anomeric carbon atom is involved in a glucosidic linkage, whereas the other end has a D-glucopyranose unit in which the anomeric carbon atom is free. These

D-glucopyranose rings are found to have the $^4C_1$ chair conformation, in which hydroxyl groups are in equatorial positions.[6] Therefore, cellulose is an extended, linear polymer chain containing a large number of hydroxyl groups (3 per AGU) in the thermodynamically preferred conformation of $^4C_1$. To preserve the bond angles for acetal-oxygen bridges, every other AGU is rotated 180 °in the plane of the molecule.[7] The dimer (cellobiose) is actually the repeating unit of cellulose, but AGUs are used for determining the degree of polymerization (DP).[8]

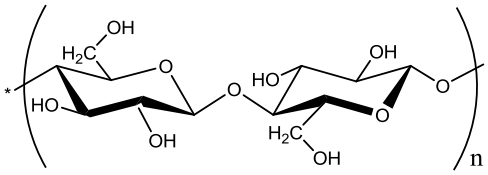

Figure 2.2. Repeating unit of cellulose.

Cellulose chains can associate by hydrogen bonds and van der Waals interactions.[9] The large number of hydrogen bonds makes the linear cellulose molecules strongly associate with each other and makes cellulose insoluble in most solvents. In the cell wall, cellulose exists in the form of threadlike structures which are called microfibrils.[10] These microfibrils are about 10 to 29 nm in diameter, which is much greater than the diameter of single cellulose chain. Some microfibrils consist of about 2000 cellulose molecules arranged in a parallel orientation which form a crystalline array.[11] These cellulose microfibrils represent a dry weight of 20 to 30% of the wall material and constitute the basic framework of the cell conveying a great resistance to tensile forces.[12]

The free hydroxyl groups present in the cellulose macromolecules are likely to be involved in a number of intramolecular and intermolecular hydrogen bonds, which may give rise to various ordered crystalline arrangements.[13] Four principal polymorphs of

cellulose (I, II, III, and IV) have been identified. Cellulose I is the form found in nature and it occurs in two different allomorphs (I_α and I_β).[8] Cellulose I can be made to undergo an irreversible transition to a stable crystalline form, cellulose II, by two distinct processes: regeneration and mercerization.[6] Treatment with liquid ammonia or certain amines such as ethylene diamine (EDA) allow for the preparation of cellulose III from either cellulose I or cellulose II. Cellulose III treated at high temperatures in glycerol can be converted into cellulose IV.[14]

2.1.3 Hemicelluloses

Hemicelluloses are also polymeric materials composed of anhydrosugar units. The difference between hemicelluloses and cellulose is that the hemicelluloses are composed of several different sugar units and typically contain a much smaller number of sugar units per polymer chain. In plant cell walls, hemicelluloses are situated between the cellulose microfibrils and the lignin. They form hydrogen bonds with cellulose and covalent bonds with lignin. Some examples of sugars in hemicelluloses of wood are D-glucose, D-mannose, D-galactose, D-xylose, L-arabinose, and D-glucuronic acid (**Figure 2.3**).[5]

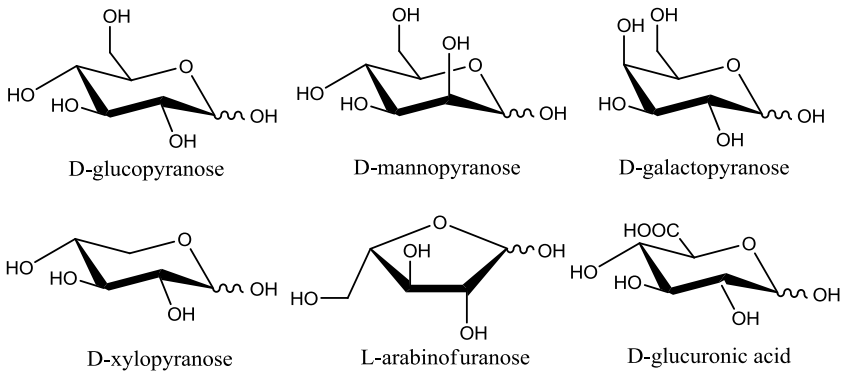

Figure 2.3. Main sugars that occur in hemicelluloses.

In contrast to cellulose, hemicelluloses are non-crystalline heteropolysaccharides and

are classically defined as the alkaline soluble material in plants. They form hydrogen bonds with cellulose, covalent bonds with lignin and ester linkages with acetyl units and hydroxycinnamic acids.[15] Hemicelluloses are typically branched polymers with a DP ranging between 80 and 200. The general formulae of hemicelluloses are $(C_5H_8O_4)_n$ and $(C_6H_{10}O_5)_n$, and these units are termed as pentosans and hexosans, respectively. Softwood hemicelluloses consist of galactoglucomannan, arabinoglucuronoxylan, and a small amount of arabino-(4-O-methylglucurono)-xylan. Hardwood hemicelluloses consist of glucuronoxylan and a small amount of glucomannans.[16]

2.1.4 Lignin

Lignins are unlike the other two components of wood in that they are not carbohydrates. Instead, they are very complex, crosslinked, and three-dimensional polymers formed from phenolic units (**Figure 2.4**)[2] and are distributed with hemicelluloses in the spaces between cellulose microfibrils in primary and secondary walls, and in middle lamellae.[17] Configurations of lignin vary in different morphological regions, different types of cells, and different types of wood. Lignins can be divided into three broad groups: softwood lignin, hardwood lignin, and grass lignin. Softwood lignin, also called guaiacyl lignin, originates from the precursor, coniferyl alcohol. Hardwood lignin is made up of coniferyl and sinapyl alcohol units. Grass lignin is derived from coniferyl, sinapyl, and p-coumaryl alcohol units.[18]

It is believed that lignin is a polymer formed by the enzymatic dehydrogenation of phenylpropanes followed by radical coupling. Lignin is an amorphous polymer and there are no reports of crystalline lignin.[2] It is also optically inactive, which is unusual for a biopolymer. The optical inactivity may be expected from a three-dimensional network. In

addition, because lignin is insoluble in virtually all simple solvents, it is not possible to isolate lignin quantitatively from plant materials without chemical or mechanical degradation. In the isolation process, lignin usually degrades into fragments of varying size. In their natural unprocessed form, molar masses of lignins could be 15,000 g•mol^{-1} or more.[19]

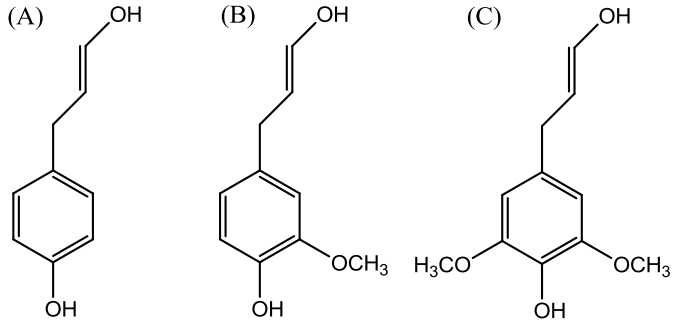

Figure 2.4. Lignin precursors (A) p-coumaryl alcohol, (B) coniferyl alcohol, and (C) sinapyl alcohol.

2.1.5 Wood-Plastic Composites

Many materials found in nature such as wood, tendon, and bone, exhibit a combination of properties that are better than those of any synthetic material.[20] It is well known that wood is a biological composite material possessing an excellent combination of mechanical properties. On a unit mass basis, the stiffness and strength of wood is comparable to materials such as aluminum, steel, and glass-fiber composites. Another attractive mechanical property of wood is the high resistance to the propagation of cracks upon the introduction of a stress.[9] The excellent properties of natural materials arises from precise hierarchical organization over a range of length scales.

Over the past decade, wood and natural fiber-filled thermoplastic composite materials have increased to a production level of 2 billion pounds per year.[21] Wood has long been

used by the plastics industry as an inexpensive filler to increase strength and stiffness of thermoplastics or to reduce raw material costs.[22,23] Wood-plastic composites consist primarily of wood and thermoplastic polymers, where wood fiber serves as a reinforcing filler in a continuous thermoplastic matrix. In the plastics industry, fillers can be classified into two major groups: particle and fiber. Particles have dimensions that are approximately equal in all directions and can be any shape, whereas fibers have greater lengths than their cross-sectional dimension. For wood-plastic composites, the wood is generally in the form of a short fiber, particle or flour. These fillers integrate well into the processing techniques utilized by the plastics industry. Many species including pine, maple, and oak are used in commercial production.

Thermoplastics used in wood-plastic composites can be classified into amorphous and semi-crystalline polymers. The primary selection criterion for a thermoplastic used in wood-plastic composite is a melting or softening temperature less than the thermal degradation temperature of wood (~ 210 ℃). Commonly used thermoplastic polymers that are suitable for wood-plastic composite include polystyrene (PS), polyvinyl chloride (PVC), low- and high-density polyethylene (LDPE and HDPE), and polypropylene (PP). PS and PVS are amorphous polymers with randomly configured polymer chains, while PE and PP are semi-crystalline polymers with varying degrees of crystallinity.

Wood-plastic composites exhibit hybrid properties of wood and thermoplastic. In general, adding wood to a thermoplastic matrix increases the mechanical properties and thermal stability compared to the solid thermoplastics. Conversely, the thermoplastic component can offer moisture barriers to the wood elements, thereby decreasing water absorption compared to wood. Wood-thermoplastic composites have many processing

advantages compared to synthetic and mineral-filled thermoplastics. Wood fibers provide a sufficient reinforcement at a much lower cost than synthetic fibers, while the composite product density is much lower than synthetic and mineral filled thermoplastics.

Significant research efforts focus on the preparation of wood-plastic composite materials. Interfacial interactions within wood-plastic composites govern the adhesion, water adsorption, durability, and processing of the materials.[21] Cellulose surfaces can be partially modified chemically to alter the surface energies and adhesion, which yields improved mechanical properties. Another strategy involves a biomimetic approach through self-assembly of amphiphilic or ionic biopolymers.

2.2 Pullulan Derivatives

2.2.1 Polysaccharides

Polysaccharides are polymeric carbohydrate materials that offer a very wide range of glycosidically linked structures based on about 40 different monosaccharides.[24] Most polysaccharides are formed from a relatively limited range of hexoses and pentoses, but especially among prokaryotes, a number of rare and unusual sugars are found. This provides an extensive group of different architectures resulting in sheets, spirals and single, double, and triple helices. Polysaccharides are recognized to have a variety of biological functions such as storage of chemical energy, structural materials for the cell walls of plants and microorganisms, protection of organisms, etc.

Polysaccharides are also renewable resources that offer a wide variety of potentially useful products to man. A number of plant polysaccharides such as starch have long been used in food and other applications. Cellulose and its derivatives have been used as bulk chemicals in place of expensive products due to their easy availability and low cost. Some

marine algae have yielded water-soluble polysaccharides that are capable of altering rheology of aqueous solutions. Within the past 40 years, microorganisms have been seen as a renewable source of utilizable polysaccharides, and the fermentation industry has provided a small number of novel products with distinctive properties for the food and pharmaceutical industry.[25]

Polysaccharides can be divided into two classes: homopolysaccharides derived from single sugar and heteropolysaccharides consisting of two or more monosaccharide units.[5,24] In the heteropolysaccharides, the sequence of the glucose units is usually in a definite, repeating pattern rather than random. Furthermore, the linkages can be homolinkages with either an α- or β-configuration to a single position, whereas a mixture of α- and β-configurations and/or a mixture of positions are present in the heterolinkages. Thus, polysaccharides can have different sequences of glucose units, different sequences of glycosidic linkages and different kinds of branching. In general, branched polysaccharides are easily soluble in water and have thickening powers, while linear polysaccharides are excellent structural materials because they pack closely and have many intermolecular interactions.

Polysaccharides can be obtained from plants, algae, fungi, and microorganisms. Cellulose and hemicelluloses introduced in Chapter 2.1, as major components of cell walls, are the most common plant polysaccharides. Starch is another plant polysaccharide consisting of glucose units linked by α-(1-4) glucosidic bonds as an energy storage polymer. Starch comprises two types of structures: the linear and helical amylose and branched amylopectin. Typically, starch contains about 20-25 % amylose and up to 75% amylopectin. Polysaccharides from the marine algae have been used in traditional foods,

and now are more widely employed in various technological applications. Alginate, a polysaccharide extracted from marine brown algae, is a linear anionic polysaccharide consisting of sequences of D-mannuronic acid and L-guluronic acid residues.[26] Alginate absorbs water quickly and forms hydrogels with divalent cations such as calcium cations, so it is used as an additive in dehydrated products and as a gelling agent. Bacteria produce a more diverse range of polysaccharides such as curdlan, dextran, and others. Curdlan is a linear polysaccharide consisting of glucose units linked by β-(1-3) glucosidic bonds.[27] Dextran is a branched polysaccharide consisting of glucose units linked by α-(1-6) glucosidic bonds in the straight chain and α-(1-4) glucosidic bonds between branches and backbones at the 2, 3, and 4 positions.

2.2.2 Pullulan

Pullulan is a water-soluble polysaccharide extracellularly produced by a fungus, *Aureobasidium pullulans* or *Pullularia pullulans*. This fungus is commonly called "black yeast" and grows on starch syrups. The structure of pullulan (**Figure 2.5**) is proposed to consist predominantly of maltotriose units composed of three anhydroglucose units which are connected in a linear fashion via two α-(1-4)-linkages and one α-(1-6)-linkage.[5,28] Pullulan is a promising environmentally benign material because it is biodegradable and is produced from plant-based starch or sugars obtained through natural photosynthesis of carbon dioxide and water. Since pullulan is a linear polymer (no branching) and is water soluble, it has been used as a model compound in many investigations.[29]

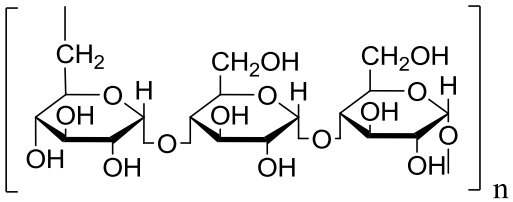

Figure 2.5. Repeating unit of pullulan.

2.2.3 Chemical Modification of Pullulan

Many studies on the chemical modification of pullulan have been reported for a variety of applications. Schacht and co-workers explored the possibilities of pullulan derivatives as macromolecular prodrug carriers.[30-32] They modified pullulan using oxidation, carbonation, and succinoylation reactions. Periodate oxidation led to polyaldehyde structures which were substantially more sensitive to acid hydrolysis;[30] chloroformate activation was used to prepare amine-containing pullulan derivatives;[31] and succinoylation of pullulan was performed by reaction with succinic anhydride in dimethyl sulfoxide as a solvent and N,N'-dimethylaminopyridine as a catalyst.[32] After these modifications, the pullulan had suitable functional groups to covalently couple drugs.

Pullulan can not be used in thermoplastic materials because pullulan begins to degrade at approximately 250 ℃ without exhibiting a clear glass transition temperature (T_g) or melting temperature (T_m). In addition, pullulan has poor water-resistance and toughness.[33] Donabedian *et al.* reported that the pullulan acetates synthesized by the reaction of pullulan with acetic anhydride and pyridine showed a T_g around 160 ℃,[34] and Teramoto *et al.* reported that pullulan acetates synthesized by the reaction of pullulan with acetyl chloride showed a higher decomposition temperature (306-363 ℃).[35] Shibata *et al.* reported the synthesis of pullulan derivatives with urethane groups in the side chain by the reaction of

pullulan with isocyanate compounds.[33] The tensile strength of all the modified pullulans was improved.

Graft copolymerization of varying monomers onto pullulan was one of the most effective methods for the incorporation of desirable properties. Donabedian *et al.* grafted ε-caprolactone and L-lactide onto pullulan by ring-opening polymerization using a tin octanoate [$Sn(Oct)_2$] catalyst system in DMSO and observed different melting behavior for these pullulan derivatives.[36] Methyl acrylate was also grafted onto pullulan using ceric ammonium nitrate as an initiator to decrease water absorption capacity.[37]

Pullulan also can be modified for potential biomedical applications. Cholesterol-bearing pullulan formed stable nanoparticles by self-aggregation (diameter 20-30 nm) and absorbed various proteins to serve as a carrier for proteins.[38] Moreover, photoreactive pullulan was synthesized by incorporating 4-azidobenzonic acid and was used as a surface modification agent for hepatocyte culture.[39]

2.2.4 Self-Assembly Behavior of Pullulan Derivatives

Pullulan is a water-soluble polymer, although pullulan derivatives can be surface-active amphiphilic polymers with hydrophilic backbones and hydrophobic side groups. There have been numerous investigations into the self-assembly behavior of pullulan in solution and at interfaces because of their unique associative behavior and their potential applications in pharmaceuticals, cosmetics, coatings, etc.[40]

Sunamoto *et al.* reported that hydrophobized pullulan containing 1.6 cholesterol groups per 100 AGUs could form nanoparticles with relatively uniform size distributions (mean diameter ~25 nm) in dilute solution.[38] Cholesterol-bearing pullulans (CHP) self-aggregated and provided colloidally stable and monodisperse nanoparticles above a

critical concentration. CHP self-aggregation was a potent vessel for making stable complexes with various hydrophobic and less hydrophilic substances. The main driving force is hydrophobic interactions. With increasing CHP solution concentration, self-assembly of CHP changes. In semi-dilute solutions above approximately 2% (w/w), the viscosity of CHP solutions drastically increased. At higher concentrations, they formed macroscopic gels with a structure in which the nanoparticles were linked. Such nanostructure gels showed unique properties that included quick responses to an external stimulus and the formation of co-nanoparticle networks.[41] Recently, it was found that CHP nanoparticles could bind bioactive oligomers to reduce their cytotoxicity.[42]

Baszkin *et al.* investigated the surface properties of cholesterol-pullulan derivatives by surface tension measurements at the air/water interface.[43] Their results revealed that these properties were related to the nature of the hydrophobic cholesterol group substituted in pullulan, and that unsubstituted pullulan did not display any surface activity. The adsorption kinetics of such an amphiphilic polymer have been shown to be diffusion controlled, obeying the Ward and Tordai diffusional model[44] at low solution concentrations. Furthermore, the authors found that the surface potentials of adsorbed monolayers of cholesterol-pullulan derivatives are highly dependent on the degree of cholesterol grafted onto pullulan.[45] Moreover, some other hydrophobic molecules including dodecanoic acid,[46] and perfluoroalkyl carboxylic acid[47] have been used to modify the pullulan to create hydrophobic pullulan derivatives. The critical micelle concentrations decrease with increasing degree of substitution. The dodecanoic acid modified pullulans also formed micelles, alone or in mixtures with other surfactants.[46]

Ionic pullulan derivatives also were prepared and their physicochemical properties

were studied.[48-53] The results showed that the aggregation of these pullulan derivatives depended on both degree of substitution and ionic strength of the solution. Picton *et al.* investigated the adsorption properties of esterified carboxymethyl pullulans (CMP) with different degrees of modification of alkyl chains (C_8) at solid/liquid interfaces.[51] The adsorption of CMP on polystyrene latex particles could occur through hydrophobic interactions and was described by Langmuir isotherms. The difference between the level of adsorption and the layer thickness resulted from different degrees of modification by octyl groups. The adsorption behavior of hydrophobically modified 6-carboxypullulan onto smooth, hydrophobic polystyrene films was investigated.[52] At low pH, the modified polymers adsorbed much more strongly to a hydrophobic polystyrene surface than pullulan and carboxypullulan. At high pH, adsorption occurred only for the highest degree of alkylation. The partially esterified carboxymethyl pullulan was able to form Langmuir films. The Langmuir films were highly stable and LB-films obtained on CaF_2 substrates were very resistant to mechanical and chemical treatments.[53]

Pullulan derivatives were also used to make polymer blends with other copolymers. Thermo-responsive hydrogel nanoparticles were prepared by self-assembly of cholesterol-bearing pullulan derivatives and a copolymer of *N*-isopropylacrylamide.[49,54] The mixing of these polymers via hydrophobic[54] and covalent interactions formed stable functional hydrogel nanoparticles.[49]

In this thesis, water soluble pullulan derivatives with varied amounts of hydrophobic side chains were synthesized by the incorporation of cinnamate groups and used as models for lignin-carbohydrate complex. Studies of pullulan cinnamate adsorption onto cellulose and thermoplastics at liquid/solid interfaces provided further understanding of molecular

level interactions between polymers, which aims to generate biomimetic approaches for improving adhesion between components in composite materials.

2.3 Bioconversion of Lignocellulosic Materials

2.3.1 Processes for Bioconversion

High worldwide demand for energy, unstable and uncertain petroleum sources, and concern over global climate change have led to a resurgence in the development of alternative energy sources such as solar, nuclear, wind, and tidal. Starch from corn grain and sugars from sugarcane and beets are currently being used directly for ethanol fermentation.[55] However, ethanol from grain starch has many limitations. Most debates focus on the soaring price of food, which has a great impact on the whole chain of agricultural products and could lead to a food crisis. As a result, people have paid greater attention to the bioconversion of lignocellulosic biomass into ethanol.[56,57] Normally, lignocellulosic biomass includes agricultural residues (corn stover, rice straw, and bagasse), forestry wastes (wood chips and sawdust), and industrial wastes (paper sludge and recycled newspaper).

Lignocellulose, a natural complex composite, consists primarily of cellulose, hemicelluloses, and lignin. Many natural factors contribute to the recalcitrance of lignocellulosic feedstock, including the epidermal tissue of the plant body, the arrangement and density of the vascular bundles, the degree of lignification,[58] the structural heterogeneity and complexity of cell-wall constituents,[59] the challenges for enzymes acting on an insoluble substrate,[60] and the inhibitors to subsequent fermentations that exist naturally in cell walls or are generated during conversion processes.[61] These chemical and structural features of biomass affect liquid penetration and/or enzyme accessibility and

activity.

The bioconversion of lignocellulosic biomass basically involves three steps: biomass pretreatment, enzymatic hydrolysis, and fermentation (**Figure 2.6**).[62] The purpose of pretreatment is to produce reactive cellulosic materials from the lignin matrix and open or partially break up recalcitrant structure while minimizing chemical degradation of fermentable sugars. Then after a pretreatment, biomass can be more readily hydrolyzed by mixed cellulases into monosaccharides. Microbes utilize these sugars, through a process called fermentation, for producing cellulosic ethanol or other biofuels. The final product is separated by distillation followed by dehydration.

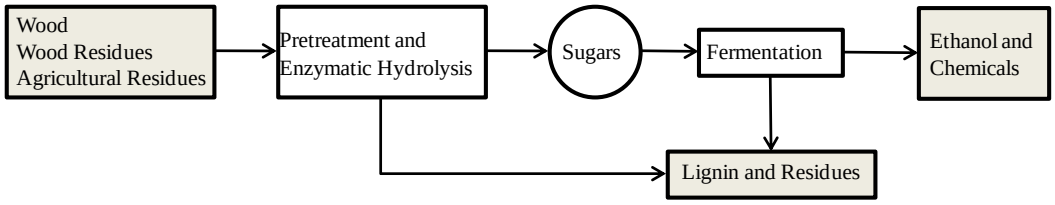

Figure 2.6. General flowchart for the conversion of lignocellulosic biomass into ethanol.

Pretreatment is among the most costly steps in bioconversion of lignocellulosic biomass, accounting for up to 40% of the total processing cost.[63] Moreover, it strongly affects the downstream costs of operation including enzymatic hydrolysis and fermentation. Generally, pretreatment methods for lignocellulosic biomass can be divided into three categories: physical, chemical, and biological methods. The combination of these approaches also has been used for a long time. For example, physical-chemical pretreatment methods, such as ammonia fiber expansion[64] and supercritical fluid extraction[65] were developed. Recently, more pretreatment technologies have been created, such as ozone pretreatment,[66] alkali plus peracetic acid pretreatment,[67] and microwave

irradiation.[68] However, many problems remain, such as the use of toxic chemical reagents, high reaction temperatures, low digestibility, high cost of chemicals, and poor chemical recovery efficiency.

2.3.2 Cellulases

The enzymes used in the second step for bioconversion of lignocellulosic biomass play important roles in the process. Intense efforts are currently being undertaken to develop cheaper and more active enzyme systems that can enable the utilization of lignocellulosic feedstocks.[69] The pretreatment methods partially remove and degrade the hemicelluloses in lignocellulosic materials. Therefore, researchers have focused on improving cellulase activites and decreasing the costs associated with the enzymatic hydrolysis of cellulose.[70]

The biochemical analysis of cellulase systems from aerobic and anaerobic bacteria and fungi has been comprehensively reviewed during the past two decades.[71] Components of cellulase systems were classified based on their mode of catalytic action and more recently have been classified based on structural properties.[72] Three major types of cellulases are found: (1) endoglucanases (EG) or 1,4-β-D-glucan-4-glucanohydrolases, (2) exoglucanases, including 1,4-β-D-glucan glucanohydrolases and 1,4-β-D-glucan cellobiohydrolases (CBH), and (3) β-glucosidases (BGL) or β-glucoside glucohydrolases. Endoglucanases randomly cut at internal amorphous sites in the cellulose chains, generating oligosaccharides of various lengths and new chain ends. Exoglucanases act on the reducing or non-reducing ends of cellulose chains in both amorphous and crystalline regions, liberating either glucose or cellobiose as major products.[73] β-Glucosidases hydrolyze soluble cellobiose to glucose (**Figure 2.7**). Cellulases are distinguished from other glycoside hydrolases by their ability to hydrolyze β-(1-4)-glucosidic bonds between

glucosyl residues. The enzymatic breakage of the β-(1-4)-glucosidic bonds in cellulose proceeds through an acid hydrolysis mechanism, using a proton donor and nucleophile or base.[74]

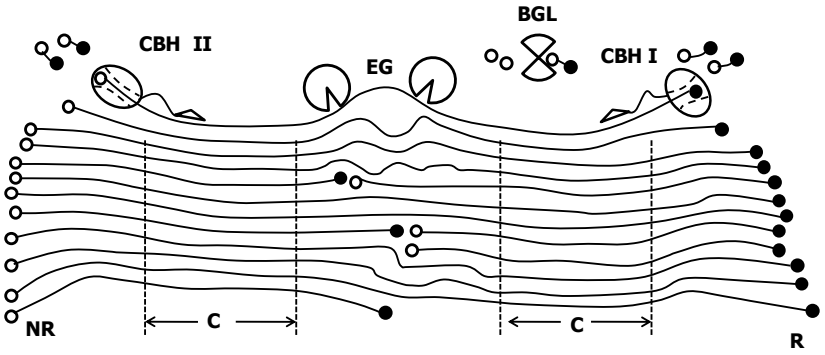

Figure 2.7. Mechanistic scheme of enzymatic cellulose hydrolysis by the *Trichoderma* noncomplexed cellulase system. Cellulose consists both of crystalline (C) and amorphous domains. The open circles, denoted NR, represent non-reducing ends and filled circles, denoted R, represent reducing ends. Cellobiohydrolases (CBH) attack the crystalline areas from reducing ends (CBH I) and non-reducing ends (CBH II), respectively, while endoglucanases (EG) attack the amorphous areas in the middle of the cellulose chains. β-Glucosidases (BGL) hydrolyze soluble cellobiose to glucose. "Reprinted from Trends in Biotechnology, 15, Tuula, T. Teeri, Crystalline cellulose degradation: new insight into the function of cellobiohydrolases, 160-167, Copyright (1997), with permission from Elsevier."

A general feature of most cellulases is a modular structure including both catalytic modules (CMs) and carbohydrate-binding modules (CBMs). The function of the CBM is to bring the CM in close contact with the insoluble cellulose substrate and ensure the correct orientation.[75] Therefore, the presence of CBMs is essential for fast and correct docking of

the cellulases on the cellulose. Removal of CBMs significantly lowers the rate of cellulose hydrolysis.

Microorganisms have adapted different approaches to effectively hydrolyze cellulose that is naturally occurring in insoluble particles or imbedded within hemicellulose and lignin domains.[76] The enzymes from aerobic fungi do not form stable high-molecular weight complexes and therefore are called "noncomplexed" systems. By contrast, anaerobic bacteria lack the ability to effectively penetrate cellulosic material and had to find alternative mechanisms for degrading cellulose and gaining access to products of cellulose hydrolysis in the presence of competition from other microorganisms and with limited ATP available for cellulase synthesis. This could have led to the development of "complexed" cellulase systems, which position cellulase-producing cells at the site of hydrolysis.

In particular, the cellulase system of *T. reesei* (also called *Trichoderma viride*) has been the focus of research for 50 years.[77] *T. reesei* produces at least two exoglucanases (CBH I and CBH II), five endoglucanases (EG I, EG II, EG III, EG IV, and EG V), and two β-glucosidases (BGL I and BGL II).[78] The necessity for the two exoglucanases has been attributed to their particular preferences for the reducing (CBH I) and nonreducing (CBH II) ends of cellulose chains of microcrystalline cellulose. Crystallography has elucidated the three-dimensional structures of the two CBHs.[79] CBH I contains four surface loops that give rise to a tunnel with a length of 50 Å; CBH II contains two surface loops that give rise to a tunnel of 20 Å. These tunnels proved to be essential to the CBHs for the processive cleavage of cellulose chains from the reducing or non-reducing ends. The three-dimensional structure of CBH I confirmed that cellobiose is the major hydrolytic

product as the cellulose chain passes through the tunnel. The structures of some EGs (EG I and EG III) have also been resolved to reveal the presence of a groove that allows entry of the cellulose chain for subsequent cleavage.[80,81]

2.3.3 Cellulase Adsorption and Desorption

Cellulase adsorption onto substrates is important in the development of cellulose hydrolysis processes with optimal use of enzymes. Adsorption of cellulase onto cellulose is a prerequisite step in cellulase catalyzed hydrolysis and usually reached equilibrium within a short time.[82] This adsorption is commonly described using a Langmuir isotherm.[83] While the Langmuir equation usually provides a good fit, more complicated situations exist. Partially irreversible adsorption or entrapment by a substrate matrix,[84] interaction among several cellulase components,[85] multi-layer adsorption,[86] and multi-cellulase competitive adsorption with various affinities,[87] all can occur. Even though a large number of values exist for parameters of the Langmuir equation, these data have a wide variation, due to different measurements and experimental conditions. Considering the complexity of cellulase systems and various properties of different substrates, numerous studies have been conducted and several different conclusions and hypotheses have been developed.[83] For example, some cellulases can bind in a completely reversible fashion to some cellulosic materials while other binding is partially irreversible.[88] Different cellulase components may competitively adsorb to the same site on the substrate,[85] and have different binding preferences.[89] From a structural point of view, the adsorption of cellulase onto the substrate appears to be through the carbohydrate-binding modules (CBMs).[90]

Desorption of cellulase also affects the potential of cellulase recycling and re-utilization. In the hydrolysis of pure cellulose, theoretically all the cellulase molecules

should adsorb onto the substrates reversibly so that they can move onto new substrates after they finish their job at the previous site. However, irreversible adsorption of cellulase sometimes occurs.[91] Cellulase hydrolysis of lignocellulosic substrates is more complicated due to the presence of lignin, hemicellulose and other components such as protein or hydrolysis inhibitors. Cellulase can unproductively adsorb onto these fractions, thereby hindering the hydrolysis process[92] and making it difficult to remove or recycle the cellulase.[93]

2.3.4 Substrate Properties

Cellulase hydrolysis of lignocellulosic materials is a heterogeneous process, including both soluble enzymes and insoluble substrates. Therefore, characteristics of substrates also strongly affect the hydrolysis process. Raw lignocellulosic biomasses are indeed composite materials composed of cellulose, hemicelluloses, and lignin. Cellulose, as the major component of the biomass, shows a highly crystalline structure, producing a straight, stable supramolecular structure with low enzyme accessibility. The three most investigated structural characteristics of cellulose are considered the most important factors influencing the rate of cellulose hydrolysis. They are crystallinity, degree of polymerization, and accessibility (including particle size, pore volume and accessibility to certain molecules).

Crystallinity of cellulose has been proposed as an indicator of substrate reactivity since 1975.[94] Generally, wide-range X-ray diffraction is used to quantitatively determine the crystallinity of dried cellulose samples. Based on crystallinity, cellulose can generally be classified into crystalline cellulose and amorphous cellulose. Cellulose hydrolysis rates mediated by fungal cellulases are typically 3 to 30 times faster for the amorphous fraction than crystalline one.[83] Due to preferential hydrolysis of amorphous cellulose,[95] the

percentage of crystallinity of cellulose was supposed to increase during hydrolysis. However, contradictory observations were reported.[96] Numerous conflicting results on how crystallinity changes during hydrolysis suggest that crystallinity may not be a key substrate characteristic.[83,93]

The degree of polymerization (DP) of cellulose substrates determines the relative abundance of terminal β-glucosidic bonds[83] and changes over the hydrolysis period. The DP change is affected by the relative proportion of exo- and endo-glucanases as well as substrate properties.[97] Exo-glucanases attach to the end of the cellulose chain and lead to a slow decrease in DP,[98] while endo-glucanases act on the middle of accessible cellulose chains causing a dramatic decrease in DP.[99] Various cellulose materials have different DPs.[83] Different DPs also result in different cellulase preferences because of catalytic domain variation between different cellulases.[73,80]

Substrate accessibility is of great importance to heterogeneous hydrolysis, in which most of the β-glucosidic bonds are not accessible to cellulase. The geometric sizes and configurations of cellulosic substrates vary, causing different accessibilities to enzymes. Cellulose particles contain both external and internal surfaces. The internal surface area of cellulose is generally 1-2 orders of magnitude greater than the external surface area,[100] except for bacterial cellulose. There are many techniques available for measuring the internal surface area of cellulose, such as size exclusion, small angle X-ray scattering (SAXS), and water vapor adsorption.[101] The external surface area of cellulose is closely related to the shape and particle size of cellulosic samples, and can be estimated by microscopy.[102,103] Gross cellulose accessibility is generally measured by the molecular adsorption method, using nitrogen, argon, water, alkali, or organic liquids.[83] The most

widely used procedure for the determination of the gross surface area is the Brunauer-Emmett-Teller (BET) method based on nitrogen adsorption.[104] However, molecules such as nitrogen or water are much smaller than the cellulase molecules, hence they can access many pores and cavities on the fiber surface that cellulases cannot enter. Therefore, these methods are sometimes misleading.

In this thesis, thin film substrates as models of lignocellulosic biomass were created using organic soluble pullulan derivatives and pullulan-based blends. Morphology and hydrophobicity of the model films could be controlled, so studies of cellulase adsorption and activity on the model films provided a new perspective on the optimization of the bioconversion process.

2.4 Adsorption Phenomena

2.4.1 Thermodynamic Treatment of Interfaces

The term adsorption was first introduced by Kayser in 1881 to describe his observations for the condensation of gas molecules on free surfaces, a phenomenon discovered independently by both Scheele[105] and Fontana[106] some years earlier. An increase of the solute concentration in the interfacial region is called adsorption. When adsorption occurs through a chemical bond, the process is called chemisorption, whereas adsorption processes through physical interactions are called physisorption. Adsorption may occur at any interface, gas/liquid, liquid/liquid, gas/solid, or liquid/solid. Adsorption of gas molecules onto solid surfaces can only occur if the Gibbs free energy change, (ΔG_{ads}) is negative:

$$\Delta G_{ads} = \Delta H_{ads} - T\Delta S_{ads} < 0 \qquad (2\text{-}1)$$

where ΔH_{ads} and ΔS_{ads} are the changes in enthalpy and entropy, respectively.

Gibbs developed a thermodynamic model for analyzing a two phase system (α and β phases) by assigning a dividing surface, σ, providing a powerful basis for studying interfacial phenomena (**Figure 2.8**).[107] This dividing surface is a mathematical plane with no thickness in the third (z) direction. Because the molecular composition changes across the interface, the number of moles of component i in each phase, n_i^{α} and n_i^{β}, in a two-phase multi-component system can be defined as

$$n_i^{\alpha} = c_i^{\alpha} V^{\alpha} \text{ and } n_i^{\beta} = c_i^{\beta} V^{\beta} \quad (2\text{-}2)$$

where c_i^{α} and c_i^{β} represent the concentrations of the solute in bulk phases of α and β with volumes of V^{α} and V^{β}, respectively. The number of moles of component i in the interfacial region is

$$n_i^{\sigma} = n_i - n_i^{\alpha} - n_i^{\beta} \quad (2\text{-}3)$$

where n_i is the total number of moles of species i in the entire system. Here, we can define surface concentration or surface excess (Γ_i) for component i as

$$\Gamma_i = \frac{n_i^{\sigma}}{A^{\sigma}} \quad (2\text{-}4)$$

where A^{σ} is the cross-sectional area of the dividing surface.

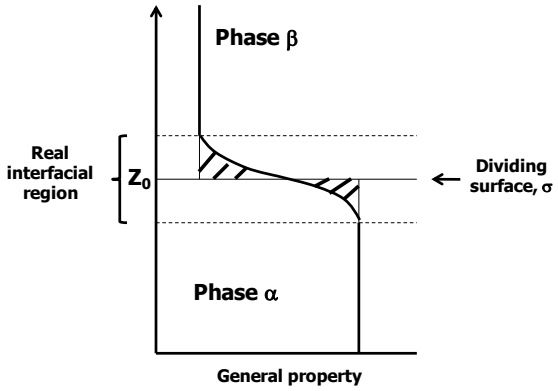

Figure 2.8. Variation of a general property (Gibbs free energy, internal energy, entropy, etc.) in the vicinity of an interface between bulk phases α and β with respect to position (z) measured along a line normal to the interface.

By varying the location of the dividing surface, z_0, n_i^σ and thus Γ_i can be either positive or negative. Furthermore, the thermodynamic relationships for the interfacial variables can be developed in a way that is analogous to those used for bulk phases. The total differential of the surface internal energy is

$$dU^\sigma = TdS^\sigma + \gamma dA^\sigma + \sum_i \mu_i(T) dn_i^\sigma \qquad (2\text{-}5)$$

where U^σ is the interfacial internal energy, S^σ is the interfacial entropy, and γ is the interfacial tension. In Equation 2-5, γdA^σ replaces the bulk work term PdV, where P is the pressure of the system, because the interface has no volume but does have an area. At equilibrium, the bulk and surface have the same temperature (T) and components at the surface and in bulk have the same temperature dependent chemical potential, $\mu_i(T)$. If Equation 2-5 is integrated over a finite area of constant T, γ, and $\mu_i(T)$, the interfacial internal energy is obtained as:

$$U^\sigma = TS^\sigma + \gamma A^\sigma + \sum_i \mu_i(T) n_i^\sigma \qquad (2\text{-}6)$$

Combining the total differential of Equation 2-6 with Equation 2-5 yields

$$0 = S^{\sigma} dT + A^{\sigma} d\gamma + \sum_i n_i^{\sigma} d\mu_i \qquad (2\text{-}7)$$

At a constant temperature, Equation 2-8 gives the Gibbs adsorption isotherm:

$$-d\gamma = \sum_i \frac{n_i^{\sigma}}{A^{\sigma}} d\mu_i = \sum_i \Gamma_i d\mu_i \qquad (2\text{-}8)$$

which relates the surface tension change ($d\gamma$) to the chemical potential changes of species i ($d\mu_i$) through the surface excesses (Γ_i). For a two component system of solvent (1) and solute (2), Equation 2-8 becomes

$$-d\gamma = \Gamma_1 d\mu_1 + \Gamma_2 d\mu_2 \qquad (2\text{-}9)$$

Concentrations of solute and solvent are dependent on the position of the dividing plane (**Figure 2.9**). The dividing plane is drawn so that the two shaded areas in **Figure 2.9a** are equal. Thus, the surface excess of the solvent is zero, $\Gamma_1 = 0$. In contrast, the shaded area which lies above of the dividing plane minus the smaller area which lies under the dividing plane gives positive surface excess values for the solute (**Figure 2.9b**).

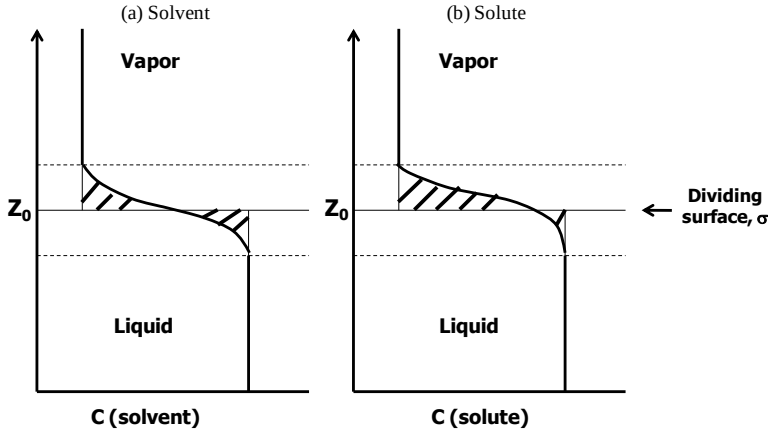

Figure 2.9. Schematic illustration of surface excess at a vapor/liquid interface. c is the concentration of (a) the solvent or (b) solute, and z_0 is the position of the interface along the surface normal.

Choosing the position of the dividing plane, z_0, in a place that $\Gamma_1 = 0$, converts Equation 2-9 into

$$\Gamma_2 = -\frac{d\gamma}{d\mu_2} \tag{2-10}$$

where Γ_2 is the surface excess or surface concentration of the solute. We can substitute the activity for chemical potential of the solute through

$$d\mu_2 = RTd \ln a_2 = RTd \ln x_2\gamma_2 \tag{2-11}$$

where a_2 is the activity of the solute in the solvent, x_2 is the mole fraction of the solute in the solvent, and γ_2 is the activity coefficient of the solute in the solvent. This substitution yields

$$\Gamma_2 = -\frac{1}{RT}\frac{d\gamma}{d\ln a_2} = -\frac{1}{RT}\frac{d\gamma}{d\ln x_2\gamma_2} \tag{2-12}$$

Finally, for ideal (dilute) solutions, the activity coefficient (γ_2) approaches unity, such that the mole fraction of the solute (x_2) can be replaced by the molar concentration of the solute (c_2) to obtain

$$\Gamma_2 = -\frac{1}{RT}\frac{d\gamma}{d\ln c_2} \tag{2-13}$$

Equation 2-13 is the relationship between the experimentally measurable quantities (e.g γ, c_2, and T) to the surface concentration of the solute (Γ_2).[107-110]

2.4.2 Adsorption Isotherms

A fundamental concept in surface science is the adsorption isotherm. It is the equilibrium relationship between the amount of adsorbate and the pressure or concentration of the bulk fluid phase at a constant temperature.[111] For example, adsorption at gas/liquid interfaces can be described by the Gibbs adsorption isotherm. However, the adsorption of molecules at liquid/solid interfaces is different from that at gas/liquid

interfaces and can be reversible or irreversible. For reversible adsorption to occur, the adsorption and desorption isotherms must coincide. Therefore, when the chemical potential is reduced by dilution of the molecules in bulk, there should be spontaneous desorption to reach a new equilibrium state. In an irreversible adsorption process, although there is a driving force for desorption upon dilution, the system reaches a metastable state and there is no or little desorption.[112] For adsorption at liquid/solid interfaces, a wide variety of adsorption isotherms are observed depending on the physicochemical conditions.

The Langmuir isotherm was introduced by Langmuir to describe the adsorption of gas molecules onto planar surfaces.[113] The key assumptions of the Langmuir adsorption isotherm are non-interacting, equivalent adsorption sites on a homogeneous surface that lack dislocations or any other structural nonidealities that might induce preferential adsorption, and the maximal adsorption of a single monolayer, whereby an equilibrium constant (K_L) is the ratio of the adsorption rate constant (k_{ads}) to the desorption rate constant (k_{des}).[107] These assumptions are most often valid for gas adsorption onto solid surfaces. The mathematical expression of the Langmuir isotherm can be written as:

$$\Gamma = \frac{\Gamma_m K_L C}{1 + K_L C} \Rightarrow \frac{1}{\Gamma} = \frac{1}{\Gamma_m} + \left(\frac{1}{\Gamma_m K_L} \right) \frac{1}{C} \qquad (2\text{-}14)$$

where K_L is the Langmuir constant, C is the bulk concentration of the adsorbate in solution, and Γ_m is the monolayer capacity at infinite bulk concentration.[114] The linearized form of the Langmuir adsorption isotherm is also shown in Equation 2-14. Therefore, plots of $1/\Gamma$ versus 1/C should be linear for Langmuir adsorption and values of the Langmuir constant (K_L) and monolayer capacity (Γ_m) can be deduced from the slope and intercept, respectively. If the plot is not linear, the model is inappropriate for describing the

adsorption process.[108]

The Langmuir isotherm has some limitations, because it assumes the surface is homogeneous. Attempts to explain surface heterogeneity through adsorption isotherms have been more successful for the adsorption of gas molecules onto solid surfaces than the adsorption of solutes onto solids from dilute solutions. One probable reason for this difference is that fewer interactions need to be considered for a gas than a solution.[109] The Freundlich adsorption isotherm represents an empirical attempt to describe adsorption for heterogeneous systems.[115] It is possible to derive the Freundlich isotherm by using a model which assumes exponentially increasing heats of adsorption as surface coverage increases.[108] The Freundlich isotherm is written as:

$$\Gamma = K_F C^{(1/n_F)} \Rightarrow \ln \Gamma = \ln K_F + (1/n_F) \ln C \qquad (2\text{-}15)$$

where K_F is the adsorbent capacity, C is the bulk concentration, and $1/n_F$ is the adsorption affinity constant.[116] A Freundlich adsorption isotherm can describe adsorption behavior in excess of monolayer coverage. A linear form of the Freundlich adsorption isotherm is also shown in Equation 2-15. Adsorbent capacity, K_F, and the adsorption affinity constant, $1/n_F$, can be obtained from the intercept and slope, respectively. In reality, the Freundlich isotherm also has some limitations and can fail to describe an adsorption process. The reason for the failings of the Freundlich isotherm is that its derivation assumes highly specific adsorption site energies which may not properly account for surface heterogeneity.[109] In fact, the Langmuir and Freundlich isotherms are the same in the limit where $K_L C \rightarrow 0$ and $n_F \rightarrow 1$.

2.4.3 Polymer Adsorption onto Solid Surfaces

Polymers can adsorb onto solid surfaces from polymer solutions and this phenomenon

is important in many applications such as steric stabilization of colloids, adhesion in composites, and surface modification. Polymer adsorption onto solid surfaces is rarely an equilibrium process and most of the time it is irreversible. The polymer cannot easily desorb from the surface once it adsorbs onto the surface for two reasons. The first reason is the very low probability of all segments desorbing simultaneously. If each segment is treated independently of each another, then the probability of a polymer chain desorbing is $(P_{des})^N$, where P_{des} is the probability of desorption of a segment and N is the number of segments in one polymer chain in contact with the surface. The second reason is the conformational flexibility of polymers. In a desorption experiment, when a few polymer segments are detached from the surface, the conformational entropy of the adsorbed polymer chain increases, which decreases the driving force for the desorption of additional segments.[117]

Figure 2.10 shows the volume fraction profile $\Phi(z)$ of monomers as a function of distance from the surface. In the bulk, far away from the surface, the volume fraction of the monomer is Φ_b, whereas near the surface it is Φ_s. Normally, Φ_s is greater than Φ_b, if polymers adsorb onto the surface. However, the opposite case (depletion) sometimes occurs when surface-segment interactions are less favorable than solvent-surface interactions. The concentration near the surface is smaller than the bulk concentration ($\Phi_s < \Phi_b$).[118] Theoretical models try to address these cases through the conformations of polymer chains near the surface, the local concentration of polymer chains, and the total amount of adsorbed polymer chains.

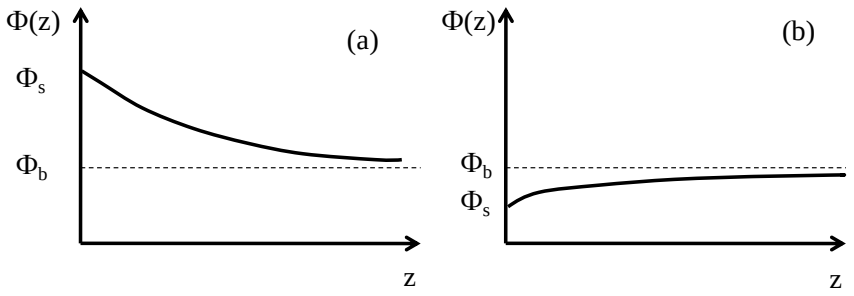

Figure 2.10. Schematic depictions of volume fractions of a solute as a function of distance from a flat substrate for (a) adsorption and (b) depletion.

In the last few years, several theoretical models have been proposed to describe polymer adsorption at liquid/solid interfaces. The theoretical treatments were divided into two groups. The first group consists of methods based on conformational statistics that track various polymer chain conformations and calculate the contributions of trains, loops, and tails. These methods include exact enumeration, Monte Carlo simulations,[119-123] and mean (self-consistent) field approaches.[124,125] The second group consists of methods that start from segment density profiles and try to express all the properties as a function of the local concentration only. These methods include the lattice model of Roe and Helfand[126] and a scaling theory proposed by de Gennes.[127,128]

2.4.3.1 Conformational Statistical Methods

Exact enumeration is one of the conformational statistical methods used to describe the adsorption of polymer chains onto solid surfaces.[129] In this method, a computer algorithm is used to generate the complete set of translationally invariant self-avoiding conformations of a single chain in a lattice. Usually, solvent effects are not considered. The exact enumeration method is limited to chains that have at least one segment in the surface plane. A chain of r segments on a cubic lattice will have conformations on the order of

5^{r}.[130] Given the complete set of conformations, it is straightforward to estimate various properties of the adsorbed chain such as the bound fraction, the adsorption energy, and the volume fraction. As a model of polymer adsorption, this method is only of limited interest as it is mainly concerned with a single random walk, although recently some attempts have been made to consider the influence of neighboring walks.[131] The Monte Carlo method is an alternative approach for obtaining the conformational statistics of an adsorbed polymer chain by using a sampling scheme, where a representative subset of the total number of possible conformations is generated.[132,133] This approach is a useful exercise, given that a polymer chain of 100 segments on a cubic lattice will have ~10^{50} conformations.

2.4.3.2 Mean (Self-Consistent) Field Approaches

The Flory-Huggins lattice theory of homogeneous solutions[134] has been extended by Scheutjens and Fleer[124,125] to describe the adsorption of flexible polymers at surfaces.[135] In the Scheutjens and Fleer (SF) theory, space is divided into layers of lattice sites parallel to the planar surface. Each lattice site is occupied by a polymer segment or solvent molecule which is assumed to have equal sizes. Attractions between polymer segments and solvent molecules characterized by a Flory-Huggins interaction parameter (χ) mediate site exclusion (repulsion). The use of a random mixing approximation within each layer represents a mean-field attempt to account for interactions of segments separated by great distances along the contour of the chain, that still lies in close spatial proximity. Segments in the first layer have contact with the surface and receive an additional energy increment of $\chi_s \bullet kT$ (χ_s is adsorption energy parameter[126,136]) which characterizes the adsorption strength of segments relative to solvent molecules.[137] In most cases, the grand canonical partition function is calculated for large numbers of conformations of each adsorbed

polymer chain.

The conformation of an adsorbed flexible polymer molecule on flat solid surface can best be described in terms of three contributors depicted in **Figure 2.11**:[138]

1) the trains, segments of consecutive monomers adsorbed at the interface,

2) the loops, segments of the chain that extend into the adjacent bulk phase between two trains, and

3) the tails, two segments at the ends of the polymer chain; these generally have lower free energies of adsorption than other segments and thus tend to extend into the bulk phase.

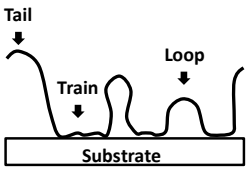

Figure 2.11. Schematic representation of an adsorbed polymer layer where loops, trains, and tails are depicted.

Scheutjens and Fleer (SF) theory has been employed to predict homopolymer adsorption. The distribution of trains, loops, and tails depends on the free energy of adsorption of segments of the polymers, the flexibility of the chain and the concentration of the polymer solution. The importance of the tail segments decreases with increasing molar mass.[139] However, at high polymer concentrations, the importance of tails increases, because the chains compete for surface sites and form much thicker layers (2/3 of chain length), with tails dominating in the periphery of the adsorbed layer.[124]

However, SF theory has some limitations. The model equations are cast in a finite difference form that facilitates a numerical solution but fail to explain some of the

underlying physics. The division of space into discrete lattice layers, which necessitate the selection of a particular lattice geometry, is an artificial approximation that may not accurately reflect continuous space. To overcome these limitations, Ploehn and co-workers[137,140] introduced an analytical formulation based on a self-consistent field (SCF) approach originally developed by Edwards[141] for polymer solutions. Self-consistent means the potential field depends on the local concentration and these local concentrations depend on the potential field. In the SCF approach, polymer walks in a potential field that depends on local concentrations are considered. Self-consistent equations can be solved if a suitable relationship between the field and local concentration is formulated.[129]

2.4.3.3 Scaling Theory Approaches

The scaling model is a method that treats the interfacial layers in term of a local concentration and concentration gradients. Individual conformations of polymer chains are not considered, but only their overall effect on the concentration profile is taken into account. The basic idea of the scaling approach is to set up a framework for a theory describing the adsorption of polymers from a good solvent. The aim is to derive power laws for certain regimes, so numerical coefficients are ignored. By using scaling theory, de Gennes[142] predicted that long, linear, flexible polymer chains strongly adsorb onto a solid surface in a good solvent in the semi-dilute concentration regime to form a self-similar diffuse adsorbed layer. The concentration profile in the adsorbed layer could be divided into three distinct regions. In the proximal region, the short-range forces between the segments and the surface are important and the segment density profile ($\Phi(z)$) changes slowly with distance z from the surface. In the central region, $\Phi(z)$ was universal and did not depend on the bulk polymer concentration (Φ_b). In this region, $\Phi(z)$ decayed as a power

law $\Phi(z) \sim z^{-m}$:

$$\phi(z) = (a/z)^{-4/3} \qquad (2\text{-}16)$$

where the critical exponent was m ≈ 4/3 and a is the size of the monomer. Experimentally this relationship was confirmed by neutron scattering experiments for the adsorption of monodisperse poly(dimethylsiloxane) (PDMS) onto mesoporous silica.[143] In the distal region, the excess polymer concentration decayed exponentially to the bulk value (Φ_b):

$$\phi(z) - \phi_b \approx 4\phi(z)\exp(-2z/\zeta^b) \qquad (2\text{-}17)$$

where ζ^b is the bulk correlation length.

2.4.4 Polyelectrolyte Adsorption onto Solid Surfaces

2.4.4.1 Polyelectrolyte Solutions

Polyelectrolytes are polymers with ionic groups.[144-146] Well known examples of such systems include proteins, nucleic acids, and synthetic systems such as poly(acrylic acid) and sulfonated polystyrene. Electrostatic interactions between charges lead to rich behavior for polyelectrolyte solutions that is qualitatively different from those of uncharged polymers.[147,148] For example:

1) The crossover from the dilute to semi-dilute solution regime occurs at much lower polymer concentrations than for solutions of neutral chains;

2) The osmotic pressure of polyelectrolytes in salt-free solutions exceeds the osmotic pressure of neutral polymers at similar polymer concentrations by several orders of magnitude. It increases almost linearly with polymer concentration and is independent of the chain molecular weight in over a wide range of polymer concentrations; and

3) The viscosity of polyelectrolyte solutions is proportional to the square root of polymer concentration $\eta \sim \sqrt{c}$ (Fuoss' law),[149] while the viscosity of solutions of

uncharged polymers at similar concentrations is directly proportional to polymer concentration.

The origin of these phenomena comes from the interplay of high molecular weight chains and electrostatic interactions.[150] Both long-range (Coulombic) interactions and short-ranged (excluded volume) interactions are present in polyelectrolyte solutions. The presence of these long-range interactions makes it difficult to apply theoretical models such as scaling concepts and renormalization group theories to polyelectrolytes in contrast to neutral polymers.[146] The success of these theories on neutral polymer solutions is based on the fact that the range of the interactions between molecules is much smaller than the size of the polymer chain. For polyelectrolyte solutions, the screening of the electrostatic interactions introduce an intermediate length scale that is comparable to the size of the polymer chain.

2.4.4.2 Polyelectrolyte Adsorption

Compared with the adsorption of uncharged polymers onto solid surfaces, the electrostatic interaction is an additional feature for polyelectrolyte adsorption. The main factors that govern polyelectrolyte adsorption are salt concentration (c_s), surface charge density (σ_0), linear charge density of the polyelectrolyte (τ), and nonelectrostatic interactions between surfaces and polyelectrolytes.[151]

One of the early theories for polyelectrolyte adsorption on a charged surface was provided by Wiegel.[152] Assuming Gaussian statistics of a polyelectrolyte chain, he calculated the adsorption threshold and the thickness of the adsorbed layer as a function of salt concentration. The interaction between the charged monomers along the polymer chain was taken into account by Muthukumar,[153] who considered a general case of the adsorption

of a polyelectrolyte chain that can take any conformation between a self-avoiding walk and a rod, depending on the ionic strength of the solution. This theory was later extended to polyelectrolyte adsorption onto patterned charged surfaces[154] and was validated by Monte Carlo simulations.[154,155]

Another early theory for polyelectrolyte adsorption was proposed by Hesselink et al. who used uncharged nonionic polymer adsorption theories as a foundation and then added electrostatic interactions.[156] The predicted adsorption isotherm had a high-affinity character where the adsorbed amount rose very steeply and saturated at very low polyelectrolyte concentrations. Hesselink's theory predicted that increasing salt concentration generally increased the adsorption; however, increased salt concentration actually decreased the adsorption if electrostatic interactions were the main driving force for adsorption.

Lyklema and Van der Schee applied self-consistent field (SCF) theories for polymer adsorption to polyelectrolyte adsorption.[157] They have shown that strong repulsion between charged monomers leads to very thin adsorbed layers on oppositely charged surfaces at low ionic strength. The adsorbed amount increases and the adsorbed layer becomes thicker, if this repulsion is screened by adding salt. The extension of the Van der Schee and Lyklema theory was employed to describe the adsorption of weak polyelectrolytes. Evers et al. calculated the adsorbed amount as a function of solution pH for the adsorption of a weak polyacid onto a surface that had different amounts of constant surface charge.[158] If the polyelectrolyte and the surface were oppositely charged, a maximum in the adsorbed amount occurred around the pK_a where the degree of dissociation (α) of the acidic protons varied strongly. This maximum was situated slightly

below the pK_a of the polyacid and occurred only if χ_s was not too large.[158] At the maximum, the surface charge density was about the same as the charge density of the polyelectrolyte. The overall charge of the polyelectrolyte and the lateral repulsion between segments was small.[159]

Van der Schee et al. also created a model for the polyelectrolyte adsorption based on SCF theory.[160] They defined two regimes for polyelectrolyte adsorption onto oppositely charged surfaces: screening-enhanced adsorption and screening-reduced adsorption. In this theoretical model, Γ_0 represented the adsorbed amount at very low salt concentrations where electrostatic screening was negligible, and Γ_∞ represented the adsorbed amount at very high salt concentrations where electrostatic interactions were virtually eliminated. For the screening-reduced adsorption regime ($\Gamma_0 > \Gamma_\infty$), electrostatic attractions between the segment and surface were dominant. Γ decreased with increasing salt concentration because the salt screened the electrostatic attraction and reduced the adsorption. In the screening-enhanced adsorption regime ($\Gamma_0 < \Gamma_\infty$), non-electrostatic interactions between the segment and the surface were dominant. Γ increased with increasing salt concentration because the salt screened the repulsion between segments and enhanced adsorption.

Recently, Dobrynin et al. developed a scaling theory for polyelectrolyte adsorption onto oppositely charged surfaces.[161,162] They predicted two dimensional (2D) adsorbed layers at low surface charge densities and three dimensional (3D) adsorbed layers at high surface charge densities. 2D adsorbed layers were caused by the balance between the energy gained through electrostatic attractions between charged monomers and the surface and a loss of confinement entropy that arose from chain localization at low surface charge densities. In contrast, 3D adsorbed layers were caused by a balance of electrostatic

attractions between charged monomers and the surface and short-range monomer-monomer repulsion at high surface charge densities. The crossover between 2D adsorbed layers and 3D adsorbed layers occurred at $\sigma_e \approx fa^{-2}$ where f was the fraction of charged monomers and a was the bond length.[162]

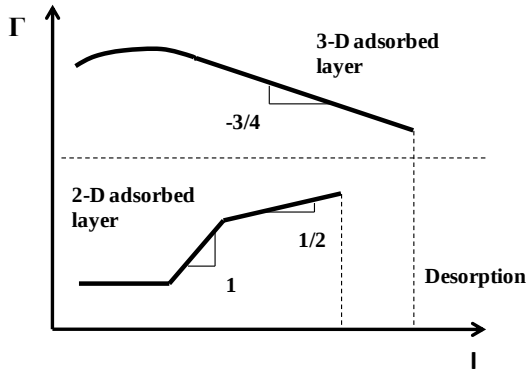

Figure 2.12. Dependence of Γ on ionic strength for a semilogarithmic scale. Predicted scaling exponents are illustrated for 2D and 3D adsorbed layers.[161] "Reprinted from Progress in Polymer Science, 30, Andrey V. Dobrynin and Michael Rubinstein, Theory of polyelectrolytes in solutions and at surfaces, 1049-1118, Copyright (2005), with permission from Elsevier."

The model proposed by van de Steeg et al. about screening reduced adsorption regime and screening enhanced adsorption regime was consistent with polyelecrolyte adsorption theory proposed by Dobrynin et al. For a 2D adsorbed layer, added salt screened the repulsion between segments and largely overcompensated the surface charge that led to screening enhanced adsorption. At higher salt concentrations, the adsorbed amount was independent of surface charge, depended on the linear charge density of polyelectrolyte chains (τ), and increased with the square root of the ionic strength (**Figure 2.12**). For a 3D adsorbed layer, polyelectrolyte adsorption increased at low salt concentrations

(screening-enhanced adsorption), decreased at higher salt concentrations (screening-reduced adsorption), and exhibited a maximum in the adsorbed amount at intermediate salt concentrations.[161]

Screening-enhanced adsorption was observed by Kawaguchi et al. for the adsorption of poly(4-vinyl-N-n-propylpyridinium bromide) onto silica.[163] There was a linear relationship between the polymer surface excess and the square root of salt concentration Screening-reduced adsorption was also observed for adsorption of two high-molecular-weight polyacrylamides onto an unbleached and a bleached hardwood cellulose.[164]

2.5 Polymer Blend Thin Films

Polymer blend thin films are employed for modern technological applications in photoresist lithography, electrooptical devices, gas separation membranes, and nanometer-scale surface patterning.[165,166] The nature of the interface specifies important properties such as adhesion, interfacial fracture toughness, friction and wear, adsorption, wettability, and compatibility with adjacent phases.

Here, the simplest case where both the bottom surface of the polymer blend thin film (against the substrate) and the top surface (against the air) are perfectly flat and structureless will be considered. The demixing phase transition of a polymer blend in this geometry may lead to inhomogeneous structures. **Figure 2.13** is a schematic description of equilibrium structures of phase separated binary polymer mixtures (A and B) in a thin film geometry.[167] **Figure 2.13a-c** refer to cases where adsorption of the B-rich phase at both the solid substrate and the air is energetically favorable, while **Figure 2.13d-e** refers to situations where the B-rich phase only preferentially wets the air surface, while the A-rich

phase prefers the solid substrate. Note that case **Figure 2.13c** occurs as a metastable state. In the non-wetting case, the interface between A and B meets the air surface or the substrate surface, respectively, with nonzero contact angles θ_{air} and θ_{wall} (**Figure 2.13a**). For the wetting case this interface envelops the A-rich phase, whereby a B-rich enrichment layer at the surface encapsulates the A-rich phase (**Figure 2.13b**). In the case where the two surfaces prefer different phases (**Figure 2.13d** and **e**), the example with a single interface in the center of the film (**Figure 2.13d**) is still in the one phase region of the film, $T > T_c(D)$, with D being the thickness of the film and $T_c(D) \approx T_w$, the wetting transition temperature in a semi-infinite geometry. For simplicity it is assumed that both air and solid substrate have the same wetting transition temperature. For $T \leq T_c(D)$, the A-B interface sticks to the walls, and only a microscopically thin enrichment layer remains at both walls, and the perpendicular part of the A-B interface ultimately develops nonzero contact angles with both surfaces, as in **Figure 2.13a** for $T << T_w$.

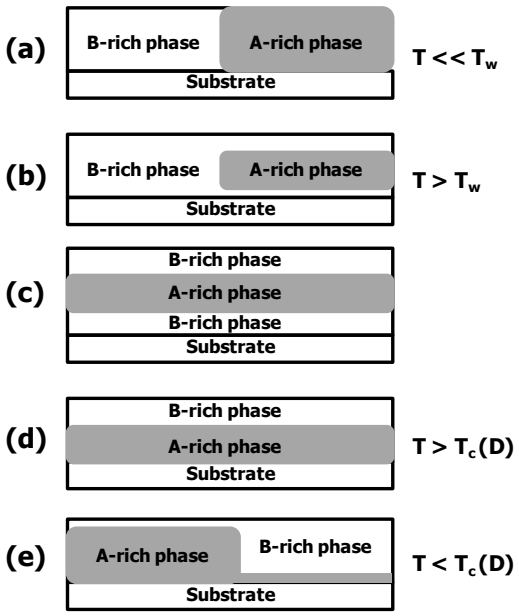

Figure 2.13. Schematic description of phase structures of phase separated binary polymer blend (A and B) thin films for different preferential wetting scenarios: (**a**-**c**) wetting by the B-rich phase is energetically preferred at both the solid and air surfaces and (**d**-**e**) wetting by the B-rich phase is preferred at the air surface while wetting by the A-rich phase is preferred at the solid surface. T_w is the wetting temperature and $T_c(D)$ is the critical temperature for the blend thin film where $T_w \approx T_c(D)$.[166] "Reprinted from Advances in Polymer Science, 138, K. Binder, Phase transitions of polymer blends and block copolymer melts in thin films, 1-89, Copyright (1999), with permission from Springer."

For the study of phase behavior in polymer blends in thin films, some insights have been gained from both computer simulations[168] and from phenomenological, mean field type theories.[169] Starting from the Flory-Huggins theory for a binary polymer blend and a phenomenological term describing the wall effects, one obtains a useful qualitative description of the behavior.[170] **Figure 2.14** shows a qualitative phase diagram of a binary (A plus B) mixture that is symmetrical with respect to molar mass in both a thin film of

thickness D and a semi-infinite geometry (D→∞). In this representation the axes are the inverse Flory-Huggins parameter χ^{-1} (proportional to temperature) and average volume fraction of component A (ϕ_A) in the system. Assuming a symmetrical mixture in the bulk (D→∞), the critical volume fraction is ϕ_{crit}=1/2, and for $\chi^{-1} < \chi^{-1}_{crit}$ the volume fractions of the two coexisting phases, ϕ_{coex1} and ϕ_{coex2}, are related by the symmetry relation ϕ_{coex1} = 1-ϕ_{coex2}. Assuming preferential attraction of one species (B) by the substrate, this symmetry is broken, and both the critical volume fraction ϕ_{crit}(D) and the volume fraction of the A-rich branch of the coexistence curve ϕ_{coex2}(D) are shifted towards smaller volume fractions relative to the bulk blend.

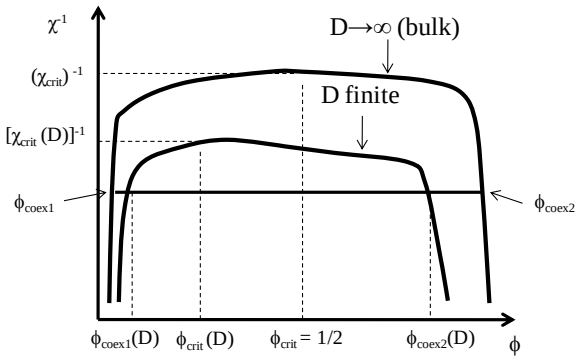

Figure 2.14. Phase diagram of a binary (A plus B) polymer blend (symmetrical with respect to molar mass) in bulk and as a thin film. Component B is preferentially attracted by the substrate.[166] "Reprinted from Advances in Polymer Science, 138, K. Binder, Phase transitions of polymer blends and block copolymer melts in thin films, 1-89, Copyright (1999), with permission from Springer."

Spincoating is a widely used method to prepare polymer blend thin films on solid surfaces and offers many possible morphologies for systems that undergo phase separation. It is a complex non-equilibrium process and the surface morphology is very sensitive to the

details of the solvent used and the precise spinning conditions. The phase separation can take place perpendicular to the plane of the film.[171,172]

For the thin films in which a pair of immiscible polymers are cast from a common solvent, **Figure 2.15** shows a multistage process to form a phase separated morphology. First, the thinning film splits into two layers during solvent evaporation. Second, the interface between these two layers develops an instability with a well defined wavevector. When the instabilities grow to such an extent that the highest interfacial protrusions touch the top surface of the film, the film breaks up rapidly into lateral domains. This feature has been observed in a number of spin-cast polymer blend systems, for example, blends of polybutadiene and PS cast from toluene,[171] PS and polyaniline cast from chloroform,[173] and polyfluorenes for some spinning conditions.[174]

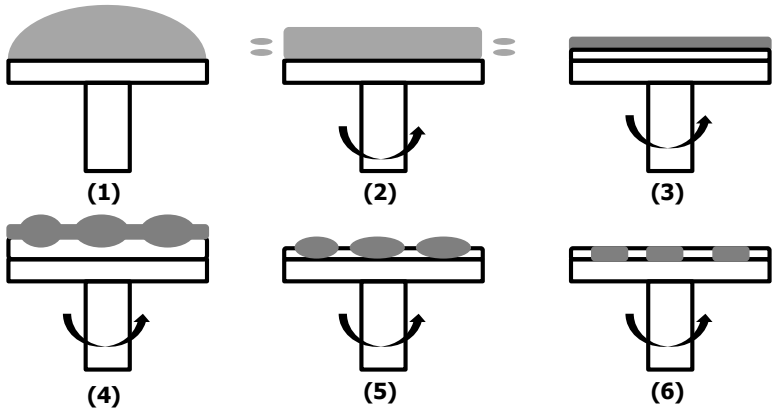

Figure 2.15. A schematic model showing film formation during spincoating and the final film morphology for binary blends.

2.6 Surface Analysis Techniques

2.6.1 Model Surfaces

2.6.1.1 Spincoated Polymer Films

Spincoating is a method for the preparation of thin, uniform polymer films on flat solid substrates.[175] An excess amount of polymer solution is placed on the substrate. Then, the substrate is rotated at high speed in order to spread the fluid by centrifugal force. Rotation is continued for some time, with fluid being spun off the edges of the substrate. The solvent is usually volatile, providing for its simultaneous evaporation.

The simplest analysis of the key elements of spincoating concerns the spincoating of a nonvolatile Newtonian fluid. An excellent treatment is given in detail by Middleman.[176] Further development yields the film thickness as a function of material and process parameters:

$$\frac{H}{H_0} = \frac{1}{\sqrt{1 + \frac{4\rho\omega^2}{3\eta} H_0^2 t}} \qquad (2\text{-}18)$$

where H is the thickness of the film, H_0 is the initial thickness of solution on the substrate, and t is the spinning time. η is fluid viscosity, ρ is fluid density, and ω is rotation speed. Note that at long times, the film thickness is independent of its initial "wet" thickness.

Both the volatility of the solvent and non-Newtonian fluid flow are important in actual spincoating operations. Indeed, these effects are coupled because the solvent diffusivity and solution viscosity are functions of the polymer concentration. Flack *et al.* have provided a more detailed analysis of these effects.[177] The effects of convection are dominant early in the process while evaporation of the solvent becomes more important at later time.

Recently, spincoating has been introduced as a simplified method to prepare model surfaces of cellulose for fundamental studies.[178] Cellulose has been dissolved in solvents such as dimethylacetamide with lithium chloride (DMAc-LiCl) or N-methylmorpholine-N-oxide (NMMO) and spincoated onto substrates, resulting in regenerated cellulose films when exposed to water. Cellulose nanocrystal suspensions have been spincoated onto substrates, resulting in crystalline cellulose I films.[179] Aqueous suspensions of native cellulose microfibrils (MFC) have also been used to form cellulose I films by spincoating, including both crystalline and amorphous regions.[180] Trimethylsilyl cellulose (TMSC), a non-polar derivative of cellulose, has been spincoated onto substrates from toluene to form amorphous cellulose films. The spincoated TMSC thin films were regenerated to cellulose films through vapor phase acid catalyzed hydrolysis.[178] Moreover, the morphology of cellulose films have also been controlled by spincoating polymer blends. Kontturi *et al.* prepared model cellulose films by spincoating TMSC blended with polystyrene (PS) onto a silicon substrate.[181] TMSC was regenerated to cellulose through vapor phase acid hydrolysis, leaving domains of cellulose and PS embedded on a layer of cellulose. Dissolution of PS left a rough surface like natural cellulose with domains whose size depended on the original TMSC/PS ratio.

2.6.1.2 Self-Assembled Monolayers (SAMs)

Self-assembled monolayers (SAMs)[182,183] are also employed to tailor the surface properties of substrates for this work, because they can make substrate surfaces hydrophobic or hydrophilic, thereby allowing us to evaluate the relative importance of different functional groups to polysaccharide adsorption onto regenerated cellulose surfaces. SAMs are organic assemblies formed by the adsorption of molecular constituents

from solutions or the gas phase onto the solid surfaces. The molecules or ligands that form SAMs have a chemical functionality, or "headgroup", with a specific affinity for a substrate.[184] **Figure 2.16** shows a schematic depiction of a SAM, including a breakdown of the key parts of a SAM molecule (head group (S), alkyl chain spacer, and tail group (R)). Examples of SAM molecules include fatty acids adsorbed onto metal oxides,[185-188] organosilicons adsorbed onto hydroxylated surfaces,[189] and organosulfurs adsorbed onto metals.[190]

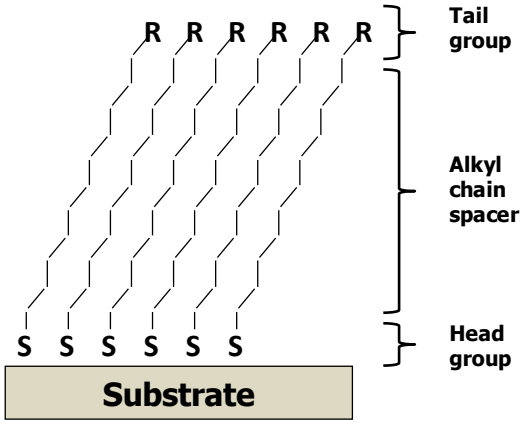

Figure 2.16. Schematic representation of the three components of a SAM. S corresponds to the chemisorbing head group and R indicates the tail group which can be of widely varying chemical functionality.

The most extensively studied class of SAMs is derived from the adsorption of alkanethiols onto gold[191] and silver.[192] The high affinity of thiols onto the metal surfaces makes it possible to generate well-defined organic surfaces with useful and highly alterable chemical functionalities.[193] It is believed that the reaction occurs by oxidative addition of the S-H bond to the gold surface, followed by a reductive elimination of hydrogen (**Figure 2.17**). The hydrogen atoms released combine to form H_2 molecules.[182] This mechanism is

consistent with the fact that monolayers can be prepared from the gas phase in the absence of oxygen.[194,195]

$$R-SH+Au_n^0 \rightarrow R-S^-Au^+Au_{n-1}^0+1/2H_2(g)$$

Figure 2.17. Oxidative addition of an alkyl thiol to gold with subsequent reductive elimination of H_2.

n-Alkyl thiols with different alkyl chain spacers ($CH_3(CH_2)_nSH$, where n = 1 to 21) self-assembled onto gold surfaces from dilute solutions were studied by ellipsometry, infrared spectroscopy, and electrochemistry.[196] All three techniques showed that there were structural differences between the short-chain and long-chain thiol monolayers. It was found that long-chain thiols formed a densely packed crystalline structure and the long alkyl chains were tilted from the surface normal by 20 to 30 °. As the chain length of the thiol decreased, the structure became disordered with lower packing densities. As a result of strong interactions between the head group and the substrate, the molecules bound at every available binding site. After all binding sites were occupied, the alkyl chains assembled into a more energetically favorable conformation. The alkyl chains had a tilted structure that minimized the steric repulsions and maximized van der Waal's interactions between neighboring chains.[197]

Alkyl thiols in ethanol solutions are a simple method for the preparation of SAMs from solution.[184] SAM formation on the substrate in a laboratory atmosphere is basically an exchange process between the desired adsorbate and adventitious materials adsorbed onto the substrate prior to immersion of the substrate in an alkyl thiol solution. Displacement with thiols requires desorption of contaminants and impurities on the surface, thus

desorption processes affect the kinetics of SAM formation. Normally, the substrates are cleaned with strong oxidizing chemicals such as piranha solution (a mixture of sulfuric acid and hydrogen peroxide) for SAM preparation.[183]

2.6.2 Contact Angle Measurements

The contact angle of a liquid on a solid surface is one of the primary characteristics of any immiscible, two- or three-phase system containing two condensed phases. By measuring the contact angle between a free-standing liquid drop and a solid surface under specified conditions of time, temperature, and humidity, the hydrophobicity of the solid surface and relative energetics between the liquid and solid can be evaluated. If a drop of a liquid is placed on an impermeable solid surface, there are two possibilities: the liquid spreads on the surface completely (contact angle $\theta = 0°$) or a finite contact angle is established. In the second case, a three-phase contact line (also called the wetting line) is formed. At this line, the solid, the liquid, and the gas phases are in contact (**Figure 2.18**). Young's equation relates the contact angle (θ) to the solid/gas, liquid/gas, and solid/liquid interfacial tensions, γ_{SG}, γ_{LG}, and γ_{SL}, respectively:[198]

$$\gamma_{LG} \bullet \cos\theta = \gamma_{SG} - \gamma_{SL} \qquad (2\text{-}19)$$

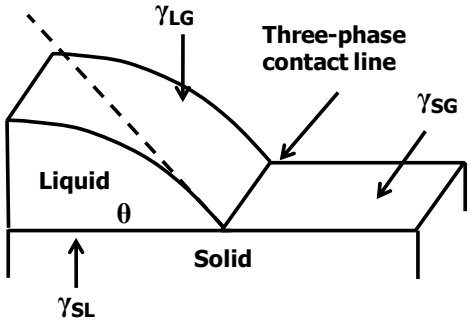

Figure 2.18. A liquid drop with a contact angle θ on a solid surface.

If $\gamma_{SG} > \gamma_{LG}$, the right hand side of Young's equation is positive. Then cos θ values are positive and the contact angle is less than 90°; the liquid partially wets the solid. Conversely, if the $\gamma_{SG} < \gamma_{LG}$, cos θ values are negative and the contact angle will exceed 90°.

In addition to this simple characterization, by measuring the contact angle using two different liquids, the solid surface energy (surface tension of the solid) can be calculated.[199] This surface energy (γ or γ_{SG}) is often decomposed into additive dispersive (γ_d) and polar (γ_p) components where $\gamma = \gamma_d + \gamma_p$. Normally, measured contact angles are used with published surface energy values for water (1 in Equation 2-20) and methylene iodide (2 in Equation 2-21) to obtain surface energy values.[200]

$$(1+\cos\theta_1)\gamma_1 = 4((\gamma_1^d\gamma_s^d/(\gamma_1^d+\gamma_s^d)+\gamma_1^p\gamma_s^p/(\gamma_1^p+\gamma_s^p)) \qquad (2\text{-}20)$$

$$(1+\cos\theta_2)\gamma_2 = 4((\gamma_2^d\gamma_s^d/(\gamma_2^d+\gamma_s^d)+\gamma_2^p\gamma_s^p/(\gamma_2^p+\gamma_s^p)) \qquad (2\text{-}21)$$

Equations 2-20 and 2-21 are forms of Young's Equation (Equation 2-19) and can be solved simultaneously.

2.6.3 Surface Tension Measurements

Surface tension (γ) results from an attraction between molecules through different interactions such as van der Waals forces or hydrogen bonds in condensed phases. Without this attraction there would not be a condensed phase. At the surface, molecules are only partially surrounded by other molecules and the number of adjacent molecules is lower than in the bulk. A net inward force pulls the interfacial molecules into the bulk to minimize the surface area. With this view, surface tension is defined as the change in the Gibbs free energy per unit area change at constant temperature and pressure:

$$\gamma = \left(\frac{\partial G}{\partial A} \right)_{T,P,n} \qquad (2\text{-}22)$$

where G is Gibbs free energy and A is the surface area. For example, water has a high surface tension of about 73 $mN \cdot m^{-1}$ at 20 ℃ and 1 atm relative to normal organic solvents.

When amphiphiles are spread onto water, the interactions between water molecules and the hydrophilic head will lower the surface energy resulting in a decrease in the surface tension. These amphiphilic molecules consist of two dissimilar parts, one part is hydrophilic (usually polar) and is commonly referred to as the "head", and the rest of the molecule is generally hydrophobic, e.g. one or more saturated alkane chains ("tail"). The resulting surface films from amphiphiles are nominally a monolayer thick and are called monolayers.[201] Monolayers formed by amphiphiles that are insoluble in the liquid subphase are called Langmuir monolayers, whereas amphiphiles that are soluble in liquid subphase may preferentially adsorb to the interface to form Gibbs monolayers. The Gibbs isotherm introduced previously in Chapter 2.4.1 provides the relationship between the amphiphile concentration and the surface tension at gas/liquid interfaces.

Various techniques have been developed for the measurement of the surface tension of liquids. Langmuir used a strip of waxed paper as a float to measure the surface tension in 1917.[202] This technique became known as the Langmuir film balance. Other more common techniques such as the pendant drop method, the maximum-bubble-pressure method, the drop weight method, the Du-Noüy ring tensiometer, and the Wilhelmy plate technique were also developed.[203] Here, the Wilhelmy plate method for surface tension measurements of liquids will be discussed.

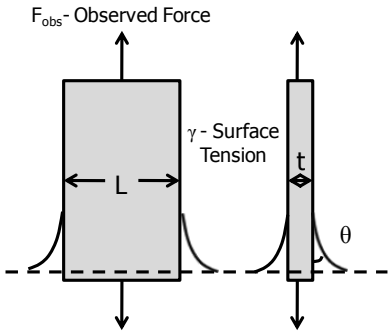

Figure 2.19. Wilhelmy plate technique for measuring surface tension (γ) at the air/water interface.

For the Wilhemy plate technique, absolute forces acting on the plate, usually made of platinum or filter paper and partially immersed in the subphase, are measured (**Figure 2.19**). Downward forces working on the plate such as gravity and surface tension are balanced by upward forces, buoyancy which results from the displacement of the water by the plate and the pressure sensor itself. These forces are usually measured with a sensitive electrobalance.[204] The surface tension and surface pressure can be calculated from:

$$\gamma = \frac{F_{obs,0} - W}{2(L+t)\cos\theta} \qquad (2\text{-}23)$$

where $F_{obs,0}$ is the force measured by the wet Wilhelmy plate in contact with the surface, W is the gravitational force acting on the wet plate when it is not in contact with the surface, L is the width of plate and t is thickness of the plate. T is often so small compared to L and can sometimes be ignored. θ is the contact angle between the liquid subphase and the plate at the interface. The measured surface tension depends on the contact angle of the liquid with the plate, and the plate is frequently designed to ensure it is complete wetted by the subphase leading (θ = 0°). One important drawback of Wilhelmy plate method is under

increasing surface pressure, monolayers may be deposited onto the plate, thereby changing the contact angle. The wetting problem may be avoided by using freshly cleaned paper plate for each experiment or by increasing the width of the paper plate.[204]

2.6.4 Atomic Force Microscopy

The atomic force microscope (AFM), a high-resolution type of scanning probe microscope, is one of the foremost tools for imaging, measuring and manipulating matter at the nanoscale.[205] The AFM consists of a microscale cantilever with a sharp tip (probe) at its end that is used to scan the sample surface. The cantilever is typically silicon or silicon nitride with a tip radius of curvature on the order of nanometers. When the tip is brought near a sample surface, forces between the tip and the surface lead to a deflection of the cantilever. Forces measured in AFM include mechanical contact forces, van der Waals forces, capillary forces, chemical bonding, and electrostatic forces. Typically, the deflection is measured using a laser spot reflected from the top of the cantilever into an array of photodiodes.[206]

The AFM can be operated in a number of modes, depending on the application. In general, imaging modes include static modes (contact modes) and dynamic modes. In contact mode operation, static tip deflection is used as a feedback signal. Because the measurement of a static signal is prone to noise and drift, low stiffness cantilevers are used to boost the deflection signal. The disadvantage of this mode is that because the tip is close to the surface of the sample, attractive forces can be quite strong, causing the tip to penetrate into the surface. Thus contact mode AFM is almost always done for surfaces where the overall force is repulsive. In this mode, the force between the tip and the surface is kept constant during scanning by maintaining a constant deflection.

In the dynamic mode, the cantilever is externally oscillated at or close to its resonance frequency. The oscillation amplitude, phase, and resonance frequency are modified by tip-sample interactions. These changes in oscillation with respect to the external reference oscillation provide information about characteristics of the sample. Schemes for dynamic mode operation include frequency modulation and the more common amplitude modulation. In frequency modulation, changes in the oscillation frequency provide information about tip-sample interactions. Frequency can be measured with very high sensitivity, thus the frequency modulation mode allows for the use of very stiff cantilevers. In amplitude modulation, changes in the oscillation amplitude or phase provide a feedback signal for imaging. In this modulation, changes in the phase of oscillation can be used to discriminate between different types of materials on the surface.

Recently, AFM with commercially available fluid cells (**Figure 2.20**) are used to investigate the surface morphology of samples at liquid/solid interfaces.[29] The in situ AFM measurement can monitor the structural changes and kinetic process in real time and in physiological environments for important biochemical problems such as the adsorption of proteins,[207] formation of phospholipid layers,[208] and self-assembly of nucleic acids.[209] In my research, in situ AFM was used to investigate the adsorption of enzymes onto polymer thin films at liquid/solid interfaces.

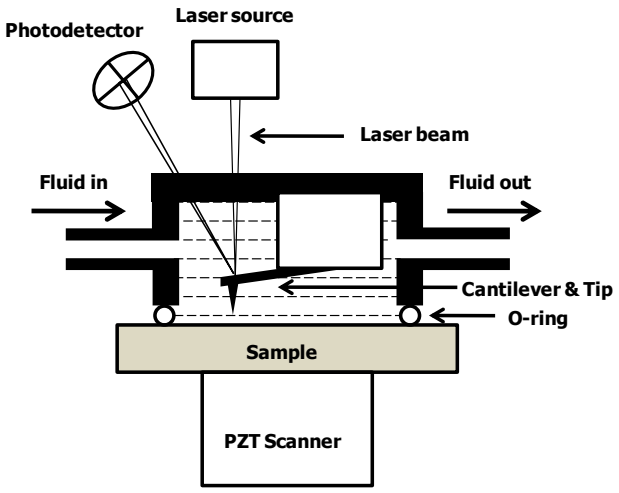

Figure 2.20. A schematic depiction of an AFM instrument with a flow cell.

2.6.5 Surface Plasmon Resonance (SPR)

Surface plasmon resonance (SPR) is an optical technique that is widely used in biochemistry and chemistry. SPR can be used to probe refractive index changes that occur within the vicinity of a sensor surface. Thus, any physical phenomena, such as adsorption or chemical transformations, at the surface that alter the refractive index will elicit a response.[210]

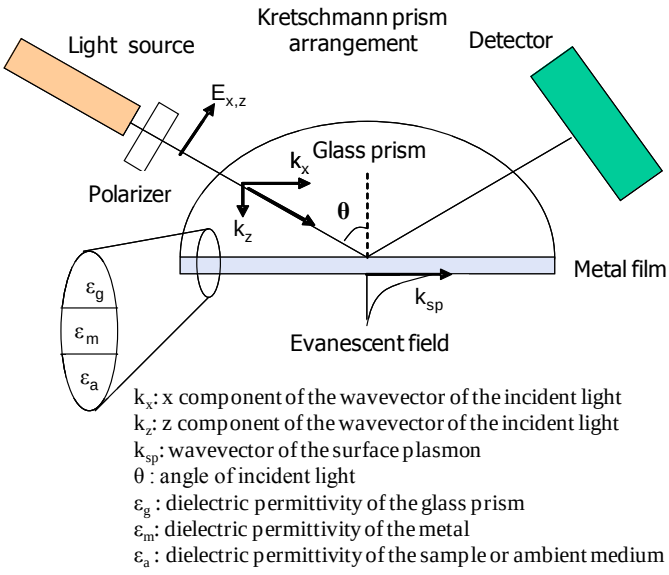

Figure 2.21. Schematic of the Kretschmann prism configuration.

The Kretschmann prism arrangement is the most frequently used geometry employed for a SPR sensor (**Figure 2.21**). The Kretschmann prism arrangement uses an evanescent wave created by total internal reflection at a wave guide interface to excite the surface plasmon (SP) on the metal film. A waveguide is a physical medium which guides the light in much the same way as a conductor guides an electrical current. When total internal reflection occurs, the light is confined inside the waveguide without significant leakage into the surroundings. For any waveguide, the refractive index of the waveguide medium must be greater than the surroundings.[211] Snell's law (**Figure 2.22**) can be used to determine the critical angle of reflection for light traveling through two media. According to Snell's law:[212]

$$n_1 \sin\theta_1 = n_2 \sin\theta_2 \qquad (2\text{-}24)$$

where n_1 is the refractive index of medium 1, and n_2 is the refractive index of medium 2.

Figure 2.22 shows the propagation of the light through the two media, and shows the angles defined in Equation 2-24. Total internal reflection occurs when the incident angle (θ_1) is equal to or greater than the critical angle (θ_c).[211] The critical angle is the incident angle where the refracted angle (θ_2) equals 90 °. Therefore, the critical angle can be expressed by as:[212]

$$\sin\theta_c = \frac{n_2}{n_1} \quad \text{for} \quad n_1 > n_2 \qquad (2\text{-}25)$$

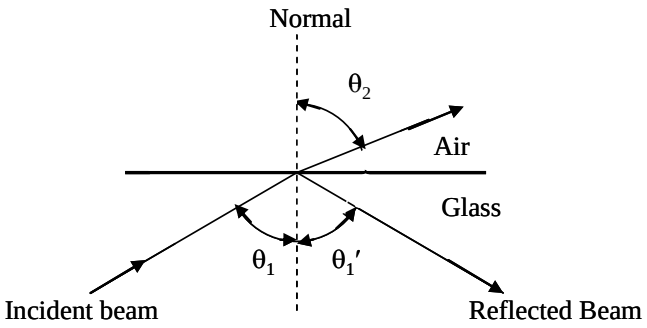

Figure 2.22. Schematic of Snell's law.

Thin gold or silver films are generally used as SPR support materials because of the optical qualities and relative ease of deposition onto a substrate with good thickness control. The metal film is deposited onto a glass substrate that will be optically coupled to a waveguide. The main criterion for a material to support surface plasmons is that the real part of the dielectric permittivity of the material must be negative. Dielectric permittivity is a measurable physical parameter that determines the optical properties of the material.[211]

As shown in **Figure 2.21**, a monochromatic, p-polarized light source is used to generate the incident light beam. The light travels through the optically dense waveguide (glass) toward the less dense medium (air). When the incident angle is larger than the

critical angle, total internal reflection occurs and the light is reflected back into the glass. However, some of the energy of a guided wave makes its way outside of the waveguide boundary and creates what is referred to as an evanescent field. If the metal film is thin enough, the evanescent field can penetrate through and couple with oscillating electrons on the metal surface to form a surface plasmon.[213]

The surface plasmon is a wave that propagates along the metal/air or metal/solution interface with a wave vector described by:

$$k_{sp} = \frac{2\pi}{\lambda}\sqrt{\frac{\varepsilon_m \varepsilon_a}{\varepsilon_m + \varepsilon_a}} \qquad (2\text{-}26)$$

where λ is the wavelength of incident light, ε_m is the dielectric permittivity of the metal, and ε_a is the dielectric permittivity of the ambient medium.[214] The propagation vector of the incident light that travels through the prism can be expressed as:

$$k = \frac{2\pi}{\lambda}\sqrt{\varepsilon_g} \qquad (2\text{-}27)$$

where ε_g is the dielectric permittivity of the glass prism. Moreover, the surface-parallel component of the incident light, k_x, is tuned for a given wavelength of light until k_x can coincide with k_{sp}. The surface parallel component, k_x, is described by

$$k_x = k\sin\theta \qquad (2\text{-}28)$$

where θ is the angle of the incident beam. From Equations 2-27 and 2-28, we obtain

$$k_x = \frac{2\pi}{\lambda}\sqrt{\varepsilon_g}\sin\theta \qquad (2\text{-}29)$$

Recalling that $\sqrt{\varepsilon}$ = n (refractive index) for a non-polar insulator allows Equation 2-28 to be expressed in terms of refractive indices.[214] By varying the angle of the incident light beam, the condition $k_x = k_{sp}$ can be obtained such that,

$$n_g \sin\theta_{sp} = \sqrt{\frac{n_m^2 n_a^2}{n_m^2 + n_a^2}} \qquad (2\text{-}30)$$

where n_m and n_a are the refractive indices of the metal and ambient medium, respectively. At the value of θ_{sp} that satisfies Equation 2-30, most of the incident light is transferred to the surface plasmon, and hence there is a minimum in the reflected intensity. Since the glass prism, light source, and metal are not varied during the course of an experiment, the only way to alter the resonance angle, θ_{sp}, is by altering the refractive index of the ambient medium, n_s. Thus, if a substance adsorbs onto the surface of the metal during an experiment, or if a change occurs in the refractive index of the ambient medium, a change in the resonance angle is observed.

The change in refractive index between the adsorbed layer and the ambient medium, Δn_a, can be used to determine the surface concentration, Γ, of adsorbed materials on the metal surface through an equation developed by de Feijter et al.:[215]

$$\Gamma = \frac{L\Delta n_a}{(dn/dc)} \qquad (2\text{-}31)$$

where L is the thickness of the adsorbed layer and (dn/dc) is the refractive index increment of the adsorbed material. The refractive index increment of the adsorbed material can be expressed as:

$$\left(\frac{dn}{dc}\right) = \left(\frac{dn}{d\theta_{sp}}\right)\left(\frac{d\theta_{sp}}{dc}\right) \qquad (2\text{-}32)$$

where ($dn/d\theta_{sp}$) is obtained by calibration of the SPR instrument with refractive index standards, and ($d\theta_{sp}/dc$) is the change in the resonant angle with bulk analyte concentration. The thickness of the adsorbed layer, L, is obtained by using a simulation of the SPR response due to the adsorbed layer:

$$L = \Delta\theta_a\left(\frac{dL}{d\theta}\right) \qquad (2\text{-}33)$$

where $\Delta\theta_a$ is the change in angle due to surfactant adsorption. The value of $\Delta\theta_a$ in Equation 2-33 must be corrected for bulk contributions to refractive index changes:

$$\Delta\theta_a = \Delta\theta_{sp} - c\left(\frac{d\theta_{sp}}{dc}\right) \qquad (2\text{-}34)$$

The correction of $\Delta\theta_{sp}$ in Equation 2-34 to obtain $\Delta\theta_a$ is necessary when increasing adsorbate concentrations change the refractive index of the ambient medium.[216] Since the SPR instrument yields $\Delta\theta_{sp}$ as a function of time, these equations can be used to determine the time-dependent thickness of the material adsorbed to the gold surface.

The success of SPR comes from three factors: (1) real time measurements are employed to study biomolecular interactions, (2) adsorption of unlabeled analyte molecules can be monitored, and (3) SPR has a high degree of surface sensitivity which allows one to monitor weak binding systems.[217] SPR has grown into a versatile technique used in a variety of applications. These include adsorption,[218] biokinetic and biosensing techniques,[219] immunosensing,[220] and thin-film characterization.[221]

2.6.6 Quartz Crystal Microbalance with Dissipation Monitoring (QCM-D)

2.6.6.1 Principle of QCM-D

The quartz crystal microbalance with dissipation monitoring (QCM-D) technique is a valuable tool for a wide range of measurements, from biological processes occurring at surfaces to characterization of properties of thin polymer films. The signal transduction mechanism of the quartz crystal microbalance (QCM) technique due to the piezoelectric effect in quartz crystals was first discovered in 1880 by the Curie brothers.[222] In 1959, the QCM was first used in a sensing mode when Sauerbray reported a linear relationship

between the frequency decrease of a quartz crystal and the bound mass.[223] In the 1980s, solution based QCM developed as a new technology to measure changes in frequency that could be related to changes in viscosity and density in liquid media.[224,225] Recently, conventional QCM are complemented with dissipation (D) measurements to measure mass changes associated with liquid/solid interfacial phenomena, as well as to characterize energy dissipative or viscoelastic behavior of the bound mass.

The advantages of the QCM-D technique are the following:

1) It provides a sensitive detection capability for surface bound mass with a surface viscoelastic characterization capability for the bound mass;

2) Samples for QCM-D measurements do not need any specific labeling treatment;

3) Signal transduction via the piezoelectric mechanism operates well in complex, often optically opaque solution media;

4) The electrochemical quartz crystal microbalance (EQCM) variant allows the investigator to apply a potential on the upper metal electrode, thereby creating an electrochemical cell, enabling electrochemical measurements.

Typically for QCM-D measurements, thin diskshaped AT-cut quartz crystals are used as the sensors. This geometry provides a stable oscillation with almost no temperature-induced fluctuation in the frequency (f) at room temperature. Au and Pt can be deposited upon the upper and lower quartz surfaces to make QCM-D sensors. The sensors, as electrodes are then connected to an oscillator circuit. The QCM-D technique relies upon quartz crystals operating in the thickness shear mode of oscillation, where motion is lateral to the surface as shown in **Figure 2.23**. Under these conditions, the lateral amplitude of a vibrating crystal is 1 to 2 nm. Any mass bound to the surface will tend to oscillate with the

same lateral displacement and frequency as the underlying crystal. If the bound mass is purely elastic, then there is no energy loss for this process. If energy loss accompanies this mass oscillation, then the process is said to be viscoelastic. The solution penetration depth of the lateral shear wave resulting from the oscillating crystal is ~ 0.25 μm perpedicular to the upper surface at 20 ℃.

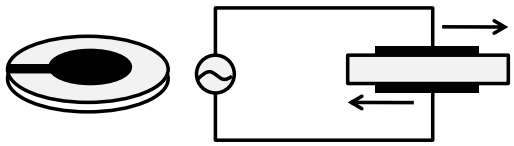

Figure 2.23. A metal coated QCM quartz crystals with a thickness shear mode (TSM) of oscillation.

An increase in bound mass to the QCM-D sensor surface causes the frequency of the crystal to decrease. For the situation of purely elastic added mass, the well-known linear Sauerbray equation was first observed and used to precisely calculate the quantity of the elastic mass[223]

$$\Delta m = -\frac{A\sqrt{\mu\rho_q}}{2nf^2}\Delta f = -\frac{C}{n}\Delta f \qquad (2\text{-}35)$$

where Δf is the measured resonant frequency decrease, f is the actual crystal frequency, Δm is the change in bound mass, A is the electrode area, ρ_q is the density of quartz (2650 kg•m^{-3}) and μ is the shear modulus of quartz (2.95×10^9 N•m^{-2}).

The Sauerbrey equation is valid for a bound mass that is evenly distributed, rigidly attached, and small compared to the mass of the crystal. For measurements associated with a liquid phase and viscoelastic soft materials, it is difficult to extract corresponding nound masses binding quantities from observed frequency decreases. QCM-D also provides

information about energy dissipation along with the frequency change. During QCM-D measurements, the decay of the oscillations in the crystal after the driving alternating current voltage is removed is monitored. The decay rate depends on the viscoelastic properties of the crystal, the bound mass, and the surrounding solution. The dissipation factor is defined as a ratio between the energy dissipated and the energy stored during a single oscillation:[226]

$$D = \frac{E_{dissipated}}{2\pi E_{stored}} \tag{2-36}$$

When a quartz crystal is immersed a Newtonian fluid, the frequency and the dissipation factor values are affected by the liquid density and viscosity. The Δf and ΔD induced by the coupling of the crystal motion to a Newtonian fluid were worked out by Stockbridge in 1966:[227]

$$\Delta f = -\sqrt{f^3}\frac{\sqrt{n\rho_l\eta_l}}{\sqrt{\pi\rho_q\mu_q}} \tag{2-37}$$

$$\Delta D = 2\sqrt{f}\frac{\sqrt{\rho_l\eta_l}}{\sqrt{n\pi\rho_q\mu_q}} \tag{2-38}$$

where f is the actual crystal frequency, ρ_q is the density of quartz (2650 kg•m^{-3}), μ_q is the shear modulus of quartz (2.95×10^9 N•m^{-2}), ρ_l is the density of fluid, and η_l is the viscosity of fluid.

2.6.6.2 Viscoelastic Modeling

A Voigt-based viscoelastic model[228] was used to analyze the QCM-D data for viscoelastic biomacromolecule layers at liquid/solid interfaces. The Voigt element is a parallel combination of a spring and a dashpot used to represent the elastic (storage) and viscous (damping) behavior of a material, respectively (**Figure 2.24a**). In this model, the

adsorbed layer is represented by a single Voigt element with a (frequency-dependent) complex shear modulus according to

$$G = G' + iG'' = \mu_f + i2\pi f\eta_f \tag{2-39}$$

where μ_f is the elastic shear (storage) modulus, η_f is the shear viscosity (loss modulus), and f is the oscillation frequency. Furthermore, the adsorbed layer is treated as a viscoelastic layer between the quartz crystal and a semi-infinite Newtonian liquid layer (**Figure 2.24b**) under no-slip boundary conditions. The quartz crystals are assumed to be purely elastic, and the surrounding solution is assumed to be purely viscous. The adsorbed polymer layer is represented by four unknown parameters (thickness h_f, density ρ_f, viscosity η_f, and elastic shear modulus μ_f). Then Δf and ΔD are deduced from Equations 2-40 through 2-45:

$$\Delta f = \mathrm{Im}(\beta)/2\pi\rho_q h_q \tag{2-40}$$

$$\Delta D = -\mathrm{Re}(\beta)/\pi\rho_q h_q \tag{2-41}$$

where

$$\beta = \xi_1 \frac{2\pi f\eta_f - i\mu_f}{2\pi f} \frac{1-\alpha\exp(2\xi_1 h_f)}{1+\alpha\exp(2\xi_1 h_f)} \tag{2-42}$$

$$\alpha = \frac{\frac{\xi_1}{\xi_2}\frac{2\pi f\eta_f - i\mu_f}{2\pi f\eta_l} + 1}{\frac{\xi_1}{\xi_2}\frac{2\pi f\eta_f - i\mu_f}{2\pi f\eta_l} - 1} \tag{2-43}$$

$$\xi_1 = \sqrt{-\frac{(2\pi f)^2\rho_f}{\mu_f + i2\pi f\eta_f}} \tag{2-44}$$

$$\xi_2 = \sqrt{i\frac{2\pi f\rho_l}{\eta_l}} \tag{2-45}$$

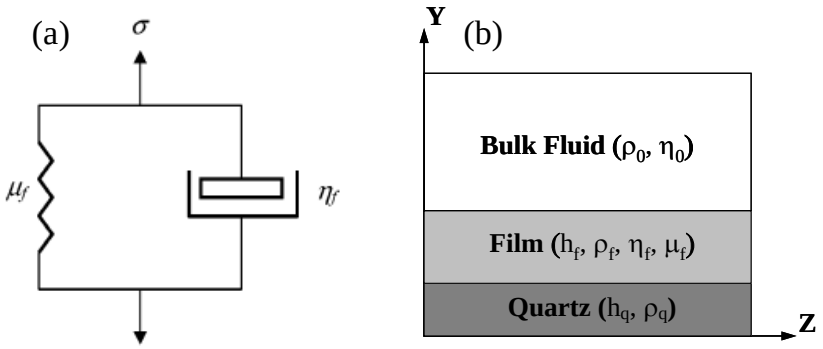

Figure 2.24. (a) Voigt element with shear viscosity η_f and shear modulus μ_f. (b) Diagram of the system modeled by the Kelvin-Voigt viscoelastic model. The quartz crystal is covered by a thin film that can be described by h_f, ρ_f, η_f, and μ_f under no slip boundary conditions. The film is covered by a semi-infinite Newtonian fluid with ρ_0 and η_0.

Viscoelastic modeling for QCM-D results has been employed to study the rheological properties of proteins[229-231] and synthetic polymers[232] at liquid/solid interfaces. Hook et al. used this model to study the viscoelasticity of an adsorbed protein film both before and after cross-linking.[230] Adsorption and viscoelastic properties of type I collagen, in native and heat-denatured forms, on polystyrene were studied by Gurdak et al.[231] Moreover, a combination of QCM-D and SPR techniques offers further understanding of thin layer properties at liquid/solid interfaces such as thin film density, water content, and degree of hydration.[230]

2.7 References:

(1) Jane, F. W. *The Structure of Wood*; 2nd ed.; Adam & Charles Black: London, 1970.

(2) Thomas, R. J. In *Wood Technology: Chemical Aspects*; Goldstein, I. S., Gould, R. F., Eds.; American Chemical Society: Washington, D. C.: Washington, D. C., 1977; Vol. ACS Symposium Series, p 2-34.

(3) Reiter, W.-D. *Current Opinion in Plant Biology* **2002**, *5*, 536-542.

(4) Saka, S. In *Wood and Cellulosic Chemistry*; 2nd ed.; Hon, D. N.-S., Shiraishi, N., Eds.; Marcel Dekker, Inc.: New York, N. Y: 2001, p 51-81.

(5) Singh, S. K.; Gross, R. A. In *Biopolymers from Polysaccharides and Agroproteins*; Gross, R. A., Scholz, C., Eds.; American Chemical Society: Washington, D. C.: Washington, D. C., 2001; Vol. 786, p 2-40.

(6) OSullivan, A. C. *Cellulose* **1997**, *4*, 173-207.

(7) Klemm, D.; Heublein, B.; Fink, H.-P.; Bohn, A. *Angew. Chem., Int. Ed.* **2005**, *44*, 3358-3393.

(8) Kontturi, E.; Tammelin, T.; Osterberg, M. *Chem. Soc. Rev.* **2006**, *35*, 1287-1304.

(9) Jeronimidis, G. *Proc. R. Soc. Lond. B.* **1980**, *208*, 447-460.

(10) Fujita, M.; Harada, H. In *Wood and Cellulosic Chemistry* Hon, D. N.-S., Shirashi, N., Eds.; Marcel Dekker, Inc.: New York, NY, 2001.

(11) Currey, J. D. *Journal of Materials Education* **1987**, *9*, 118-296.

(12) Dadswell, H. E.; Hillis, W. E. In *Wood Extractives*; Hillis, W. E., Ed.; Academic Press Inc,: 1962; Vol. New York, NY.

(13) Williamson, R. E.; Burn, J. E.; Hocart, C. H. *Cellular and Molecular Life Sciences* **2001**, *58*, 1475-1490.

(14) Sarko, A. In *Wood and cellulosics: Industrial utilization, biotechnology, structure and properties*; Kennedy, J. F., Phillips, G. O., Williams, P. A., Eds.; Ellis Horwood Limited: Chichester: 1987, p 55-69.

(15) Sun, R.; Sun, X. F.; Tomkinson, J. In *Hemicelluloses: Science and Technology*; Gatenholm, P., Tenkanen, M., Eds.; American Chemical Society: Washington, D. C.: Washington, D. C., 2004; Vol. 864, p 2-34.

(16) Mitikka, M.; Teeaar, R.; Tenkanene, M.; Laine, J.; Vuorinene, T. In *8th International Symposium on Wood and Pulping Chemistry* Helsinki, Finland, 1995, 231-236.

(17) Higuchi, T. *J. Wood Sci.* **2006**, *52*, 2-8.

(18) Suhas; Carrott, P. J. M.; Carrott, M. M. L. R. *Bioresour. Technol.* **2007**, *98*, 2301-2312.

(19) Lin, S. Y.; Dence, C. W. In *Methods in Lignin Chemistry*; Lin, S. Y., Dence, C. W., Eds.; Springer-Verlag: Berlin: Berlin, 1992.

(20) Bond, G. M.; Richman, R. H.; Mcnaughton, W. P. *Journal of Materials Engineering and Performance* **1995**, *4*, 334-345.

(21) Renneckar, S.; Zink-Sharp, A.; Esker, A. R.; Johnson, R. K.; Glasser, W. G. In *Cellulose Nanocomposites Processing, Characterization, and Properties*; Oksman, K., Sain, M., Eds.; American Chemical Society: Washington, D. C.: Washington, D. C., 1996; Vol. 938, p 78-99.

(22) Wolcott, M. P.; K., E. In *33rd International Particleboard/Composite Materials Symposium Proceedings* 1999.

(23) Coats, E. R.; Loge, F. J.; Wolcott, M. P.; Englund, K.; McDonald, A. G. *Bioresource Technology* **2008**, *99*, 2680-2686.

(24) Tsai, C. S. *Biomacromolecules: introduction to structure, function, and informatics*; John Wiley & Sons, Inc.: Hoboken, NJ, 2007.

(25) Baldwin, A. D.; Kiick, K. L. *Biopolymers* **2010**, *94*, 128-140.

(26) Gacesa, P. *Carbohydr. Polym.* **1988**, *8*, 161-82.

(27) Lee, I.-Y. *Biopolymers* **2002**, *5*, 135-158.

(28) Shingel, K. I. *Carbohydr. Res.* **2004**, *339*, 447-460.

(29) Kaya, A.; Du, X.; Liu, Z.; Lu, J. W.; Morris, J. R.; Glasser, W. G.; Heinze, T.; Esker, A. R. *Biomacromolecules* **2009**, *10*, 2451-2459.

(30) Bruneel, D.; Schacht, E. *Polymer* **1993**, *34*, 2628-2632.

(31) Bruneel, D.; Schacht, E. *Polymer* **1993**, *34*, 2633-2637.

(32) Bruneel, D.; Schacht, E. *Polymer* **1994**, *35*, 2656-2658.

(33) Shibata, M.; Asahina, M.; Teramoto, N.; Yosomiya, R. *Polymer* **2001**, *42*, 59-64.

(34) Donabedian, D.; Gross, R.; McCarthy, S. *Polym Prepr (Am Chem Soc, Mater Sci Eng)* **1992**, *67*, 301-305.

(35) Teramoto, N.; Shibata, M. *Carbohydr. Polym.* **2006**, *63*, 476-481.

(36) Donabedian, D. H.; McCarthy, S. P. *Macromolecules* **1998**, *31*, 1032-1039.

(37) Wu, S.; Jin, Z.; Kim, J. M.; Tong, Q.; Chen, H. *Carbohydr. Polym.* **2009**, *76*, 129-132.

(38) Akiyoshi, K.; Deguchi, S.; Moriguchi, N.; Yamaguchi, S.; Sunamoto, J. *Macromolecules* **1993**, *26*, 3062-3068.

(39) Hasuda, H.; Kwon, O. H.; Kang, I.-K.; Ito, Y. *Biomaterials* **2005**, *26*, 2401-2406.

(40) Singh, R. S.; Saini, G. K.; Kennedy, J. F. *Carbohydr. Polym.* **2008**, *73*, 515-531.

(41) Kuroda, K.; Fujimoto, K.; Sunamoto, J.; Akiyoshi, K. *Langmuir* **2002**, *18*, 3780-3786.

(42) Boridy, S.; Takahashi, H.; Akiyoshi, K.; Maysinger, D. *Biomaterials* **2009**, *30*, 5583-5591.

(43) Deme, B.; Rosilio, V.; Baszkin, A. *Colloids Surf., B* **1995**, *4*, 357-365.

(44) Ward, A. F. H.; Tordai, L. *J. Chem. Phys.* **1946**, *14*, 453-461.

(45) Deme, B.; Rosilio, V.; Baszkin, A. *Colloids Surf., B* **1995**, *4*, 367-373.

(46) Sallustio, S.; Galantini, L.; Gente, G.; Masci, G.; La Mesa, C. *J. Phys. Chem. B* **2004**, *108*, 18876-18883.

(47) Glinel, K.; Huguet, J.; Muller, G. *Polymer* **1999**, *40*, 7071-7081.

(48) Duval-Terrie, C.; Huguet, J.; Muller, G. *Colloids Surf., A* **2003**, *220*, 105-115.

(49) Morimoto, N.; Winnik, F. M.; Akiyoshi, K. *Langmuir* **2007**, *23*, 217-223.

(50) Souguir, Z.; Roudesli, S.; About-Jaudet, E.; Picton, L.; Le Cerf, D. *Carbohydr. Polym.* **2010**, *80*, 123-129.

(51) Simon, S.; Picton, L.; Le Cerf, D.; Muller, G. *Polymer* **2005**, *46*, 3700-3707.

(52) Paris, E.; Stuart, M. A. C. *Macromolecules* **1999**, *32*, 462-470.

(53) Alexandre, S.; Derue, V.; Gomes-Ferreira, S.; Huguet, J.; Valleton, J. M. *Langmuir* **1999**, *15*, 7708-7713.

(54) Akiyoshi, K.; Kang, E. C.; Kurumada, S.; Sunamoto, J.; Principi, T.; Winnik, F. M. *Macromolecules* **2000**, *33*, 3244-3249.

(55) Himmel, M. E.; Ding, S. Y.; Johnson, D. K.; Adney, W. S.; Nimlos, M. R.; Brady, J. W.; Foust, T. D. *Science* **2007**, *315*, 804-807.

(56) Nonhebel, S. *Renew. Sustain. Energy Rev.* **2005**, *9*, 191-201.

(57) Tilman, D.; Hill, J.; Lehman, C. *Science* **2006**, *314*, 1598-600.

(58) Cosgrove, D. J. *Nat. Rev. Mol. Cell Biol.* **2005**, *6*, 850-861.

(59) Iiyama, K.; Lam Thi Bach, T.; Stone, B. A. *Plant Physiol.* **1994**, *104*, 315-20.

(60) Himmel, M. E.; Ruth, M. F.; Wyman, C. E. *Curr. Opin. Biotechnol.* **1999**, *10*, 358-364.

(61) Wyman, C. E.; Dale, B. E.; Elander, R. T.; Holtzapple, M.; Ladisch, M. R.; Lee, Y. Y. *Bioresour. Technol.* **2005**, *96*, 1959-1966.

(62) Berlin, A.; Balakshin, M.; Gilkes, N.; Kadla, J.; Maximenko, V.; Kubo, S.; Saddler, J. *J. Biotechnol.* **2006**, *125*, 198-209.

(63) Lynd, L. R. *Annual Review of Energy and the Environment* **1996**, *21*, 403-465.

(64) Dale, B. E.; Leong, C. K.; Pham, T. K.; Esquivel, V. M.; Rios, I.; Latimer, V. M. *Bioresource Technology* **1996**, *56*, 111-116.

(65) Kim, K. H.; Hong, J. *Bioresource Technology* **2001**, *77*, 139-144.

(66) Garcia-Cubero, M. T.; Gonzalez-Benito, G.; Indacoechea, I.; Coca, M.; Bolado, S. *Bioresource Technology* **2009**, *100*, 1608-1613.

(67) Zhao, X. B.; Peng, F.; Cheng, K.; Liu, D. H. *Enzyme and Microbial Technology* **2009**, *44*, 17-23.

(68) Zheng, G. J.; Zhou, Y. J.; Zhang, J.; Cheng, K. K.; Zhao, X. B.; Zhang, T.; Liu, D. H. *Journal of Wood Chemistry and Technology* **2007**, *27*, 65-71.

(69) Joergensen, H.; Kristensen, J. B.; Felby, C. *Biofuels, Bioprod. Biorefin.* **2007**, *1*, 119-134.

(70) Schubert, C. *Nat. Biotechnol.* **2006**, *24*, 777-784.

(71) Lynd, L. R.; Weimer, P. J.; van Zyl, W. H.; Pretorius, I. S. *Microbiol. Mol. Biol. Rev.* **2002**, *66*, 506-577.

(72) Henrissat, B.; Teeri, T. T.; Warren, R. A. J. *FEBS Lett.* **1998**, *425*, 352-354.

(73) Terri, T. T. *Trends Biotechnol.* **1997**, *15*, 160-167.

(74) Birsan, C.; Johnson, P.; Joshi, M.; MacLeod, A.; McIntosh, L.; Monem, V.; Nitz, M.; Rose, D. R.; Tull, D.; Wakarchuck, W. W.; Wang, Q.; Warren, R. A. J.; White, A.; Withers, S. G. *Biochem. Soc. Trans.* **1998**, *26*, 156-160.

(75) Teeri, T. T.; Koivula, A.; Linder, M.; Wohlfahrt, G.; Divne, C.; Jones, T. A. *Biochem. Soc. Trans.* **1998**, *26*, 173-178.

(76) Tomme, P.; Warren, R. A.; Gilkes, N. R. *Adv Microb Physiol* **1995**, *37*, 1-81.

(77) Mandels, M.; Reese, E. T. *J. Bacteriol.* **1957**, *73*, 269-78.

(78) Nogawa, M.; Goto, M.; Okada, H.; Morikawa, Y. *Curr. Genet.* **2001**, *38*, 329-334.

(79) Divne, C.; Staahlberg, J.; Reinikainen, T.; Ruohonen, L.; Pettersson, G.; Knowles, J. K. C.; Teeri, T. T.; Jones, T. A. *Science* **1994**, *265*, 524-8.

(80) Kleywegt, G. J.; Zou, J.-Y.; Divne, C.; Davies, G. J.; Sinning, I.; Stahlberg, J.; Reinikainen, T.; Srisodsuk, M.; Teeri, T. T.; Jones, T. A. *J. Mol. Biol.* **1997**, *272*, 383-397.

(81) Sandgren, M.; Shaw, A.; Ropp, T. H.; Wu, S.; Bott, R.; Cameron, A. D.; Stahlberg, J.; Mitchinson, C.; Jones, T. A. *J. Mol. Biol.* **2001**, *308*, 295-310.

(82) Turon, X.; Rojas, O. J.; Deinhammer, R. S. *Langmuir* **2008**, *24*, 3880-3887.

(83) Zhang, Y.-H. P.; Lynd, L. R. *Biotechnol. Bioeng.* **2004**, *88*, 797-824.

(84) Lee, S. B.; Kim, I. H.; Ryu, D. D. Y.; Taguchi, H. *Biotechnol. Bioeng.* **1983**, *25*, 33-51.

(85) Jeoh, T.; Wilson, D. B.; Walker, L. P. *Biotechnol. Prog.* **2002**, *18*, 760-769.

(86) Carrard, G.; Linder, M. *Eur. J. Biochem.* **1999**, *262*, 637-643.

(87) Beldman, G.; Voragen, A. G. J.; Rombouts, F. M.; Searle-van-Leeuwen, M. F.; Pilnik, W. *Biotechnol. Bioeng.* **1987**, *30*, 251-7.

(88) Palonen, H.; Tjerneld, F.; Zacchi, G.; Tenkanen, M. *J. Biotechnol.* **2004**, *107*, 65-72.

(89) Boraston, A. B. *Biochem. J.* **2005**, *385*, 479-484.

(90) Carrard, G.; Koivula, A.; Soderlund, H.; Beguin, P. *Proc. Natl. Acad. Sci.* **2000**, *97*, 10342-10347.

(91) Jung, H.; Wilson, D. B.; Walker, L. P. *Biotechnol. Bioeng.* **2003**, *84*, 151-159.

(92) Tu, M.; Chandra, R. P.; Saddler, J. N. *Biotechnol. Prog.* **2007**, *23*, 398-406.

(93) Mansfield, S. D.; Mooney, C.; Saddler, J. N. *Biotechnol. Prog.* **1999**, *15*, 804-816.

(94) Wood, T. M. *Biotechnol. Bioeng. Symp.* **1975**, *5*, 111-37.

(95) Ooshima, H.; Sakata, M.; Harano, Y. *Biotechnol. Bioeng.* **1983**, *25*, 3103-14.

(96) Puls, J.; Wood, T. M. *Bioresource Technology* **1991**, *36*, 15-19.

(97) Zhang, Y. H. P.; Lynd, L. R. *Biotechnol. Bioeng.* **2006**, *94*, 888-898.

(98) Kleman-Leyer, K. M.; Siika-Aho, M.; Teeri, T. T.; Kirk, T. K. *Appl. Environ. Microbiol.* **1996**, *62*, 2883-2887.

(99) Srisodsuk, M.; Kleman-Leyer, K.; Keranen, S.; Kirk, T. K.; Teeri, T. T. *European Journal of Biochemistry* **1998**, *251*, 885-892.

(100) Chang, M. M.; Chou, T. Y. C.; Tsao, G. T. *Adv. Biochem. Eng.* **1981**, *20*, 15-42.

(101) Neuman, R. P.; Walker, L. P. *Biotechnol. Bioeng.* **1992**, *40*, 226-34.

(102) Henrissat, B.; Vigny, B.; Buleon, A.; Perez, S. *FEBS Lett.* **1988**, *231*, 177-82.

(103) Lehtio, J.; Sugiyama, J.; Gustavsson, M.; Fransson, L.; Linder, M.; Teeri, T. T. *Proc. Natl. Acad. Sci.* **2003**, *100*, 484-489.

(104) Brunauer, S.; Emmett, P. H.; Teller, E. *J. Am. Chem. Soc.* **1938**, *60*, 309-19.

(105) Fontana, F. *Memorie Mat. Fis. Soc. Ital. Sci.* **1777**, *1*, 679.

(106) Tien, C. *Adsorption Calculations and Modeling*; Butterworth-Heinemann: Newton, 1994.

(107) Evans, D. F.; Wennerström, H. *The Colloidal Domain: Where Physics, Chemistry, Biology, and Technology Meet*; 2nd ed.; Wiley-VCH: New York, 1999.

(108) Myers, D. *Surfaces, Interfaces, and Colloids: Principles and Applications*; VCH Publishers, Inc.: New York, 1991.

(109) Hiemenz, P. C.; Rajagopalan, R. *Principles of Colloid and Surface Chemistry*; Marcel Dekker, Inc.: New York, 1997.

(110) Adamson, A. W. *Physical Chemistry of Surfaces*; 5th ed.; John Wiley & Sons, Inc.: New York, 1990.

(111) Dabrowski, A. *Advances in Colloid and Interface Science* **2001**, *93*, 135-224.

(112) Haynes, C. A.; Norde, W. *Colloids Surf., B* **1994**, *2*, 517-66.

(113) Langmuir, I. *J. Am. Chem. Soc.* **1918**, *40*, 1361-1402.

(114) Romero-Cano, M. S.; Martin-Rodriguez, A.; de las Nieves, F. J. *J. Colloid Interface Sci.* **2000**, *227*, 322-328.

(115) Blackburn, R. S.; Harvey, A.; Kettle, L. L.; Payne, J. D.; Russell, S. J. *Langmuir* **2006**, *22*, 5636-5644.

(116) Kaggwa, G. B.; Froebe, S.; Huynh, L.; Ralston, J.; Bremmell, K. *Langmuir* **2005**, *21*, 4695-4704.

(117) Cheng, Y.-L.; Lok, B. K.; Robertson, C. R. In *Surface and Interfacial Aspects of Biomedical Polymers: Protein Adsorption*; Andrade, J., Ed.; Plenum Press: New York: 1985, p 121-150.

(118) Netz, R. R.; Andelman, D. *Phys. Rep.* **2003**, *380*, 1-95.

(119) Simha, R.; Frisch, H. L.; Eirich, F. R. *J. Phys. Chem.* **1953**, *57*, 584-9.

(120) Silberberg, A. *J. Phys. Chem.* **1962**, *66*, 1872-83.

(121) Silberberg, A. *J. Phys. Chem.* **1962**, *66*, 1884-907.

(122) DiMarzio, E. A. *J. Chem. Phys.* **1965**, *42*, 2101-6.

(123) Roe, R. J. *J. Chem. Phys.* **1965**, *43*, 1591-8.

(124) Scheutjens, J. M. H. M.; Fleer, G. J. *J. Phys. Chem.* **1980**, *84*, 178-90.

(125) Scheutjens, J. M. H. M.; Fleer, G. J. *J. Phys. Chem.* **1979**, *83*, 1619-35.

(126) Roe, R.-J. *J. Chem. Phys.* **1974**, *60*, 4192-207.

(127) de Gennes, P. G. *Scaling Concepts in Polymer Physics*; Cornell Univ. Press: Ithaca, N. Y., 1979.

(128) de Gennes, P. G. *Macromolecules* **1980**, *13*, 1069-75.

(129) Fleer, G. J.; Stuart, M. A. C.; Scheutjens, J. M. H. M.; Cosgrove, T.; Vincent, B. *Polymers at Interfaces*; Chapman & Hall: London, 1993.

(130) Sykes, M. F.; Guttmann, A. J.; Watts, M. G.; Roberts, P. D. *J. Phys. A* **1972**, *5*, 653-60.

(131) Torrie, G. M.; Barrett, J.; Whittington, S. G. *J. Chem. Soc., Faraday Trans. II* **1979**, *75*, 369-78.

(132) Binder, K. *Colloid Polym. Sci.* **1988**, *266*, 871-85.

(133) Carmesin, I.; Kremer, K. *Macromolecules* **1988**, *21*, 2819-23.

(134) Flory, P. J. *Principles of Polymer Chemistry*; Cornell University Press: Ithaca, New York, 1953.

(135) Schillen, K.; Claesson, P. M.; Malmsten, M.; Linse, P.; Booth, C. *J. Phys. Chem. B* **1997**, *101*, 4238-4252.

(136) Silberberg, A. *J. Chem. Phys.* **1968**, *48*, 2835-51.

(137) Ploehn, H. J.; Russel, W. B. *Macromolecules* **1989**, *22*, 266-76.

(138) Fleer, G. J.; Scheutjens, J. M. H. M. *Adv. Colloid Interface Sci.* **1982**, *16*, 341-59.

(139) Macritchie, F. In *Advances in Protein Chemistry*; Anfinsen, C. B., Edsall, J. T., Eds.; Academic Press: New York: 1978, p 283-326.

(140) Ploehn, H. J.; Russel, W. B.; Hall, C. K. *Macromolecules* **1988**, *21*, 1075-85.

(141) Edwards, S. F. *Proc. Phys. Soc., London* **1965**, *85*, 613-24.

(142) de Gennes, P. G. *Macromolecules* **1981**, *14*, 1637-44.

(143) Auvray, L.; Cotton, J. P. *Macromolecules* **1987**, *20*, 202-7.

(144) Foerster, S.; Schmidt, M. *Adv. Polym. Sci.* **1995**, *120*, 51-133.

(145) Oosawa, F. *Polyelectrolytes*; Marcel Dekker, New York, 1971.

(146) Barrat, J.-L.; Joanny, J.-F. *Adv. Chem. Phys.* **1996**, *94*, 1-66.

(147) Doi, M.; Edwards, S. F. *The theory of polymer dynamics*; Oxford: Clarendon Press, 1989.

(148) Rubinstein, M.; Colby, R. H. *Polymer physics*; Oxford University Press, New York, 2003.

(149) Fuoss, R. M. *J. Polym. Sci.* **1948**, *3*, 603-4.

(150) Mandel, M. In *Polyelectrolytes: Science and Technology*; Hara, M., Ed.; Marcel Dekker, Inc.: New York, N. Y.: 1993.

(151) Shubin, V. *J. Colloid Interface Sci.* **1997**, *191*, 372-377.

(152) Wiegel, F. W. *J Phys Condens Matter* **1977**, *10*, 299-306.

(153) Muthukumar, M. *J. Chem. Phys.* **1987**, *86*, 7230-5.

(154) Muthukumar, M. *J. Chem. Phys.* **1995**, *103*, 4723-31.

(155) Kong, C. Y.; Muthukumar, M. *J. Chem. Phys.* **1998**, *109*, 1522-1527.

(156) Hesselink, F. T. *J. Colloid Interface Sci.* **1977**, *60*, 448-66.

(157) Van der Schee, H. A.; Lyklema, J. *J. Phys. Chem.* **1984**, *88*, 6661-7.

(158) Evers, O. A.; Fleer, G. J.; Scheutjens, J. M. H. M.; Lyklema, J. *J. Colloid Interface Sci.* **1986**, *111*, 446-54.

(159) Bohmer, M. R.; Evers, O. A.; Scheutjens, J. M. H. M. *Macromolecules* **1990**, *23*, 2288-301.

(160) Van de Steeg, H. G. M.; Cohen Stuart, M. A.; De Keizer, A.; Bijsterbosch, B. H. *Langmuir* **1992**, *8*, 2538-46.

(161) Dobrynin, A. V.; Rubinstein, M. *Prog. Polym. Sci.* **2005**, *30*, 1049-1118.

(162) Dobrynin, A. V.; Deshkovski, A.; Rubinstein, M. *Macromolecules* **2001**, *34*, 3421-3436.

(163) Kawaguchi, M.; Kawaguchi, H.; Takahashi, A. *J. Colloid Interface Sci.* **1988**, *124*, 57-62.

(164) Hendrickson, E. R.; Neuman, R. D. *J. Colloid Interface Sci.* **1986**, *110*, 243-51.

(165) Budkowski, A. *Interfaces Crystallization Viscoelasticity* **1999**, *148*, 1-111.

(166) Binder, K. *Adv. Polym. Sci.* **1999**, *138*, 1-89.

(167) Binder, K.; Nielaba, P.; Pereyra, V. *Z. Phys. B: Condens. Matter* **1997**, *104*, 81-98.

(168) Rouault, Y.; Baschnagel, J.; Binder, K. *Journal of Statistical Physics* **1995**, *80*, 1009-1031.

(169) Binder, K. *Acta Polym.* **1995**, *46*, 204-25.

(170) Flebbe, T.; Dunweg, B.; Binder, K. *Journal De Physique Ii* **1996**, *6*, 665-693.

(171) Geoghegan, M.; Jones, R. A. L.; Payne, R. S.; Sakellariou, P.; Clough, A. S.; Penfold, J. *Polymer* **1994**, *35*, 2019-2027.

(172) Geoghegan, M.; Krausch, G. *Progress in Polymer Science* **2003**, *28*, 261-302.

(173) Bernasik, A.; Wlodarczyk-Miskiewicz, J.; Luzny, W.; Kowalski, K.; Raczkowska, J.; Rysz, J.; Budkowski, A. *Synthetic Metals* **2004**, *144*, 253-257.

(174) Arias, A. C.; Corcoran, N.; Banach, M.; Friend, R. H.; MacKenzie, J. D.; Huck, W. T. S. *Applied Physics Letters* **2002**, *80*, 1695-1697.

(175) Ibar, J. P. *Polym. Eng. Sci.* **1998**, *28*, 1-20.

(176) Middleman, S. *Journal of Applied Physics* **1987**, *62*, 2530-2532.

(177) Flack, W. W.; Soong, D. S.; Bell, A. T.; Hess, D. W. *Journal of Applied Physics* **1984**, *56*, 1199-1206.

(178) Kontturi, E.; Thune, P. C.; Niemantsverdriet, J. W. *Langmuir* **2003**, *19*, 5735-5741.

(179) Edgar, C. D.; Gray, D. G. *Cellulose* **2003**, *10*, 299-306.

(180) Ahola, S.; Salmi, J.; Johansson, L. S.; Laine, J.; Oesterberg, M. *Biomacromolecules* **2008**, *9*, 1273-1282.

(181) Kontturi, E.; Thune, P. C.; Niemantsverdriet, J. W. H. *Macromolecules* **2005**, *38*, 10712-10720.

(182) Ulman, A. *Chem. Rev.* **1996**, *96*, 1533-1554.

(183) Love, J. C.; Estroff, L. A.; Kriebel, J. K.; Nuzzo, R. G.; Whitesides, G. M. *Chem. Rev.* **2005**, *105*, 1103-1169.

(184) Schreiber, F. *Prog. Surf. Sci.* **2000**, *65*, 151-256.

(185) Schlotter, N. E.; Porter, M. D.; Bright, T. B.; Allara, D. L. *Chem. Phys. Lett.* **1986**, *132*, 93-8.

(186) Ogawa, H.; Chihara, T.; Taya, K. *J. Am. Chem. Soc.* **1985**, *107*, 1365-9.

(187) Allara, D. L.; Nuzzo, R. G. *Langmuir* **1985**, *1*, 45-52.

(188) Allara, D. L.; Nuzzo, R. G. *Langmuir* **1985**, *1*, 52-66.

(189) Sagiv, J. *J. Am. Chem. Soc.* **1980**, *102*, 92-8.

(190) Nuzzo, R. G.; Allara, D. L. *J. Am. Chem. Soc.* **1983**, *105*, 4481-3.

(191) Poirier, G. E.; Pylant, E. D. *Science* **1996**, *272*, 1145-1148.

(192) Laibinis, P. E.; Whitesides, G. M.; Allara, D. L.; Tao, Y. T.; Parikh, A. N.; Nuzzo, R. G. *J. Am. Chem. Soc.* **1991**, *113*, 7152-67.

(193) Bain, C. D.; Whitesides, G. M. *Science* **1988**, *240*, 62-3.

(194) Thomas, R. C.; Sun, L.; Crooks, R. M.; Ricco, A. J. *Langmuir* **1991**, *7*, 620-2.

(195) Chailapakul, O.; Sun, L.; Xu, C.; Crooks, R. M. *J. Am. Chem. Soc.* **1993**, *115*, 12459-67.

(196) Porter, M. D.; Bright, T. B.; Allara, D. L.; Chidsey, C. E. D. *J. Am. Chem. Soc.* **1987**, *109*, 3559-68.

(197) Ulman, A.; Eilers, J. E.; Tillman, N. *Langmuir* **1989**, *5*, 1147-52.

(198) Young, T. *Phil. Trans. Roy. Soc. London* **1805**, *95*, 65.

(199) Wan, Y. Q.; Yang, J.; Yang, J. L.; Bei, J. Z.; Wang, S. G. *Biomaterials* **2003**, *24*, 3757-3764.

(200) Wu, S. *Polymer Interface and Adhesion*; Marcel Dekker, Inc.: NY, 1982.

(201) Petty, M. C. *Langmuir-Blodgett Films*; Cambridge University Press: Cambridge, UK, 1996.

(202) Langmuir, I. *J. Am. Chem. Soc.* **1917**, *39*, 1848-1906.

(203) Butt, H.-J.; Graf, K.; Kappl, M. *Physics and Chemistry of Interfaces*; Wiley-VCH Verlag & Co. KGaA: Weinheim, 2003.

(204) Dynarowicz-Latka, P.; Dhanabalan, A.; Oliveira, O. N. *Adv. Colloid Interface Sci.* **2001**, *91*, 221-293.

(205) Giessibl, F. J. *Rev. Mod. Phys.* **2003**, *75*, 949-983.

(206) Amato, I. *Science* **1997**, *276*, 1982-1985.

(207) Almeida, A. T.; Gliemann, H.; Schimmel, T.; Petri, D. F. S. *Prog. Colloid Polym. Sci.* **2004**, *128*, 63-67.

(208) Spangenberg, T.; De Mello, N. F.; Creczynski-Pasa, T. B.; Pasa, A. A.; Niehus, H. *Phys. Status Solidi A* **2004**, *201*, 857-860.

(209) Dong, M.; Howard, K. A.; Oupicky, D.; Bisht, H.; Kjems, J.; Besenbacher, F. *Nanotechnology* **2007**, *18*, 185501/1-185501/5.

(210) Earp, R. L.; Dessy, R. E. In *Commercial Biosensors: Applications to Clinical, Bioprocess, and Environmental Samples*; Ramsay, G., Ed.; John Wiley & Sons, Inc.: New York: 1996, p 99-164.

(211) Hecht, E.; Zajac, A. *Optics*; Addison-Wesley Publishing Company, Inc. USA, 1975.

(212) Liedberg, B.; Johansen, K. In *Affinity Biosensors*; Rogers, K. R., Mulchandani, A., Eds.; Humana Press: Totowa, N.J.: 1998.

(213) Green, R. J.; Frazier, R. A.; Shakesheff, K. M.; Davies, M. C.; Roberts, C. J.; Tendler, S. J. B. *Biomaterials* **2000**, *21*, 1823-1835.

(214) Van Krevelen, D. W. *Properties of Polymers: Their Correlation with Chemical Structure; Their Numerical Estimation and Prediction from Additive Group Contributions*; Elsevier: Amsterdam, 1997.

(215) Defeijter, J. A.; Benjamins, J.; Veer, F. A. *Biopolymers* **1978**, *17*, 1759-1772.

(216) Sigal, G. B.; Mrksich, M.; Whitesides, G. M. *Langmuir* **1997**, *13*, 2749-2755.

(217) Brockman, J. M.; Nelson, B. P.; Corn, R. M. *Annu. Rev. Phys. Chem.* **2000**, *51*, 41-63.

(218) Jordan, C. E.; Frutos, A. G.; Thiel, A. J.; Corn, R. M. *Anal. Chem.* **1997**, *69*, 4939-4947.

(219) Karlsson, R.; Michaelsson, A.; Mattsson, L. *J. Immunol. Methods* **1991**, *145*, 229-40.

(220) Fischer, B.; Heyn, S. P.; Egger, M.; Gaub, H. E. *Langmuir* **1993**, *9*, 136-40.

(221) Frutos, A. G.; Corn, R. M. *Anal. Chem.* **1998**, *70*, 449A-455A.

(222) Curie, J.; Curie, P. *Comput. Rend. Acad. Sci. Paris* **1880**, *91*, 294-297.

(223) Sauerbrey, G. *Z. Phys.* **1959**, *155*, 206-22.

(224) Nomura, T.; Okuhara, M. *Anal. Chim. Acta* **1982**, *142*, 281-284.

(225) Kurosawa, K.; Tawara, E.; Kamo, N.; Kobatake, Y. *Anal. Chim. Acta* **1990**, *230*, 41-49.

(226) Rodahl, M.; Hook, F.; Krozer, A.; Brzezinski, P.; Kasemo, B. *Rev. Sci. Instrum.* **1995**, *66*, 3924-30.

(227) Stochbridge, C. D. In *Vacuum Microbalance Techniques*; Plenum Press:: 1966; Vol. 5, p 147.

(228) Voinova, M. V.; Rodahl, M.; Jonson, M.; Kasemo, B. *Phys. Scr.* **1999**, *59*, 191-196.

(229) Dutta, A. K.; Nayak, A.; Belfort, G. *J. Colloid Interface Sci.* **2008**, *324*, 55-60.

(230) Hook, F.; Kasemo, B.; Nylander, T.; Fant, C.; Sott, K.; Elwing, H. *Anal. Chem.* **2001**, *73*, 5796-5804.

(231) Gurdak, E.; Booth, J.; Roberts, C. J.; Rouxhet, P. G.; Dupont-Gillain, C. C. *Journal of Colloid and Interface Science* **2006**, *302*, 475-484.

(232) Hedin, J.; Lofroth, J. E.; Nyden, M. *Langmuir* **2007**, *23*, 6148-6155.

CHAPTER 3

Materials and Experimental Methods

3.1 Synthesis and Characterization of Pullulan Derivatives

3.1.1 Materials for Synthesis

Pullulan (P), from *Aurebasidium pullulans*, 4-chlorocinnamic acid (4CCA, 98+%), 3-methoxycinnamic acid (3MCA, 98+%), cinnamoyl chloride (98+%), 1,1,1,3,3,3-hexamethyl disilazane (HMDS, 99.9%), chlorotrimethylsilane (TMS-Cl, 99+%), methyl *trans*-cinnamate (Me-Cinn, 99%), and N,N dimethylacetamide (DMAc, 99%) were purchased from Sigma-Aldrich. Pyridine (spectrophotometric grade, 99.5+%,) and trifluoroacetic acid (TFA, 99%) were purchased from Alfa Aesar. N,N'-Carbonyl diimidazole (CDI, 98%) and dimethyl sulfoxide, (DMSO, spectrophotometric grade, 99.9+%) were purchased from Alfa Aesar. N,N-Dimethyl formamide (DMF, 99.9%) was purchased from Fisher Scientific and distilled under reduced pressure with anhydrous magnesium sulfate as a drying agent. Sulfuric acid (98 wt. %), ammonium hydroxide (28 wt. % solution), and hydrochloric acid were purchased from Fisher Chemical. Hydrogen peroxide (30 wt. % solution) was purchased from VWR. Tetrahydrofuran (THF, HPLC Grade, Fisher Scientific), hexanes (HPLC Grade, Fisher Scientific), methanol (HPLC Grade, Fisher Scientific), ethanol (Decon Lab Inc.), and toluene (HPLC Grade, EMD) were consistently used as solvents. Ultrapure water was used in all experiments (Millipore, Milli-Q Gradient A-10, 18.2 MΩ•cm, < 5 ppb organic impurities).

3.1.2 Synthesis and Characterization of Pullulan 3-methoxycinnamates (P3MC) and Pullulan 4-chlorocinnamates (P4CC)

Pullulan cinnamates synthesized in Chapter 3.1.2 were used as models for

ligin-carbohydrate materials. Pullulan 3-methoxycinnamates (P3MC) and pullulan 4-chlorocinnamates (P4CC) were synthesized by the reaction of pullulan with 3MCAand 4CCA in the presence of CDI as a coupling agent, respectively (**Figure 3.1**). The carbonyl group in cinnamic acid was activated by CDI. CDI and desired amounts of cinnamic acid were dissolved in 10 mL anhydrous DMF. The mixture was stirred for 24 hours at room temperature. 1.0 g of pullulan [5.6 mmol anhydroglucose units, (AGU)] was dissolved in 20 mL DMAc at 70 ℃ and stirred for ~1 hour. The activated cinnamic acid was added to the reaction flask. The mixture was stirred for 24 hours at 80 ℃. The product was precipitated in absolute ethanol, washed 3 times using 600 mL ethanol, and dried under vacuum at 40 ℃ for 24 hours. The degrees of cinnamate substitution (DS_{Cinn}) of pullulan cinnamate derivatives were determined by ^{1}H NMR and UV-Vis measurements. Degrees of substitution were defined as the number of functional groups per AGU throughout this thesis.

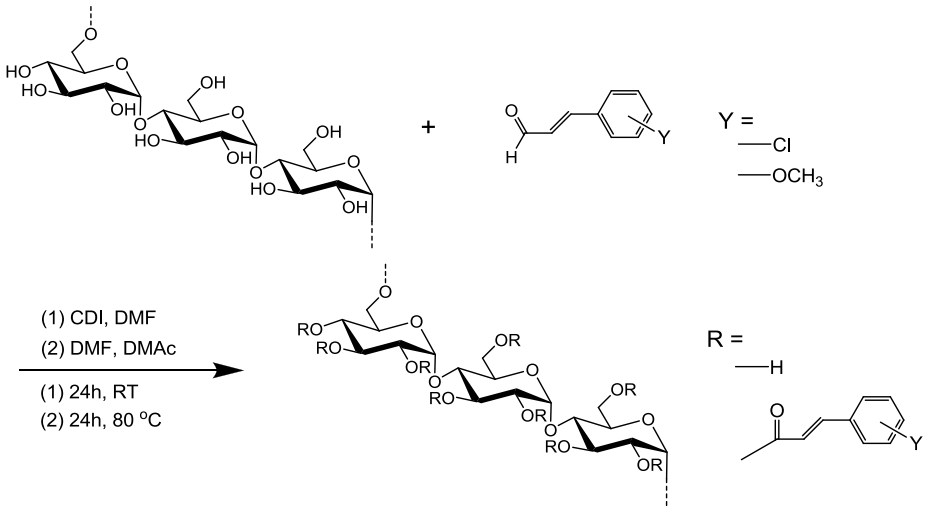

Figure 3.1. Reaction scheme for the synthesis of P3MC and P4CC.

Methyl 3-methoxycinnamate (M3MC) and methyl 4-chlorocinnamate (M4CC) were

also synthesized as reference compounds for determining the DS_{Cinn} of pullulan derivatives. 0.50 g (2.8 mmol) 3MCA was dissolved in 20.0 mL (50.0 mmol) methanol and 1.0 mL concentrated sulfuric acid was added as a catalyst. The reactant mixture was refluxed for 6 hours. The product was extracted by 100 mL hexanes and the hexanes phase was washed with a saturated aqueous sodium bicarbonate solution, water and then dried by anhydrous sodium sulfate. The hexanes was removed by rotary evaporation to yield 0.40 g of white crystalline product (72%). M4CC was synthesized following the same procedure as M3MC. ^{1}H NMR (400 Hz, $CDCl_3$), δ (ppm): **M3MC**: 3.80 (s, 3H), 3.82 (s, 3H), 6.43 (d, J = 16 Hz, 1H), 6.93 (q, J_A = 6.4 Hz, J_B = 3.2 Hz, 1H), 7.04 (t, J = 2 Hz, 1H), 7.12 (d, J = 7.2 Hz, 1H), 7.30 (t, J = 8 Hz, 1H), 7.66 (d, J = 16 Hz, 1H); **M4CC**: 3.01 (s, 3H), 6.41 (d, J = 16 Hz, 1H), 7.35-7.46 (m, 4H), 7.63 (d, J = 16 Hz, 1H).

Table 3.1. Selected properties of synthesized pullulan cinnamates

	Theo. DS_{Cinn}	Obs. DS_{Cinn}		(d*n*/d*c*) (mL•g^{-1})
		^{1}H NMR	UV	
P	0	0	0	0.146 ± 0.002
P4CC03	0.050	0.029	0.034 ± 0.001	0.147 ± 0.001
P4CC06	0.100	0.053	0.054 ± 0.001	0.142 ± 0.001
P3MC03	0.050	0.026	0.027 ± 0.001	0.142 ± 0.001
P3MC06	0.100	0.050	0.057 ± 0.002	0.146 ± 0.001

3.1.2.1 ^{1}H NMR Characterization of P3MCs and P4CCs

^{1}H NMR spectra were recorded on a Varian INOVA-400 spectrometer at 400 MHz, using DMSO-d_6 and tetramethylsilane (TMS) as a solvent and internal standard, respectively. For ^{1}H NMR analysis, 5.0 mg of polymer was dissolved in 1 mL of DMSO-d_6. Pullulan consists of linear chains of AGUs that alternate regularly between one α-(1-6) linkage and two α-(1-4) linkages, or stated another way, maltotriosyl repeating units (MTU) connected by α-(1-6) linkages.[1] Trifluoroacetic acid (TFA) was added to the ^{1}H NMR samples to shift hydroxyl protons on pullulan chains downfield.[2] Then, only

signals from protons connected to the carbon atoms (H-C) were used to calculate the amount of AGUs. A representative ^{1}H NMR spectrum for pullulan in DMSO-d_6 with TFA is provided in **Figure 3.2**. The integrated area between chemical shifts of δ = 2.8 and δ = 5.2 ppm (Area1) corresponded to 21 protons (H-C) of a MTU (3AGUs).

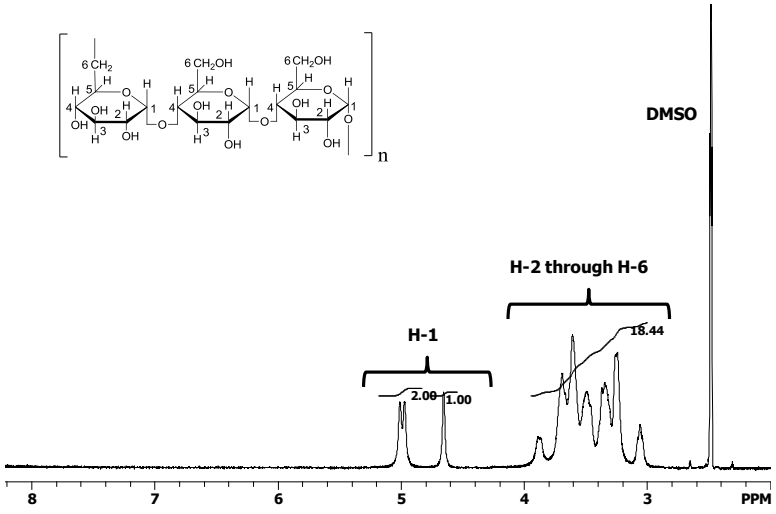

Figure 3.2. ^{1}H NMR spectrum of pullulan (P) in DMSO-d_6 with TFA and TMS.

^{1}H NMR spectra of P3MCs in DMSO-d_6 with TFA are provided in **Figure 3.3**. The integrated area between chemical shifts of δ = 2.8 and δ = 5.2 ppm (*Area*1) corresponded to 21 protons (H-C) of a MTU (3AGUs) and 3 protons from cinnamate groups (methoxyl group). The integrated area between δ = 6.6 and δ = 8.0 ppm (*Area*2) corresponded to 6 protons of the cinnamate group. The DS_{Cinn} was defined as the number of 3-methoxycinnamate groups per AGU and was calculated from Equation 3-1.

$$DS_{Cinn} = \frac{\left(\dfrac{Area2/6}{(Area1 - 0.5 \times Area2)/21} \right)}{3} \qquad (3\text{-}1)$$

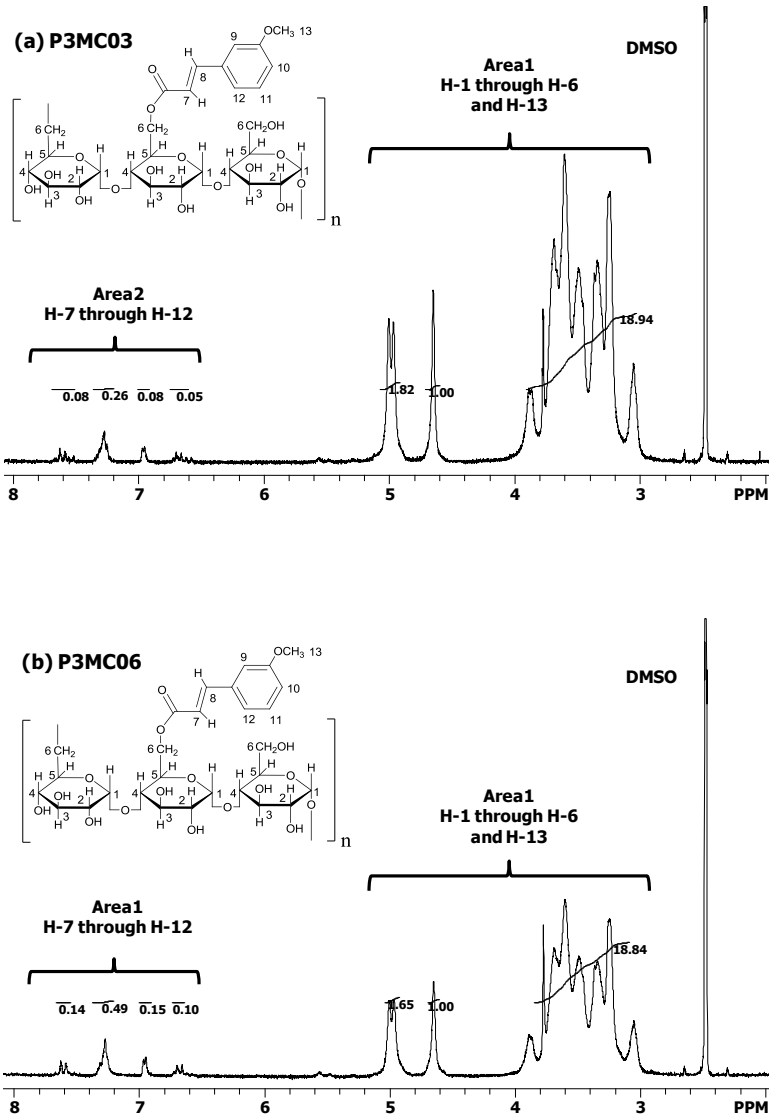

Figure 3.3. ^{1}H NMR spectra of P3MCs in DMSO-d_6 with TFA and TMS.

^{1}H NMR spectra of P4CCs in DMSO-d_6 with TFA are provided in **Figure 3.4**. The integrated area between chemical shifts of δ = 2.8 and δ = 5.2 ppm (*Area*1) corresponded to 21 protons (H-C) of a MTU (3AGUs). The integrated area between δ = 6.6 and δ = 8.0 ppm (*Area*2) corresponded to 6 protons of the cinnamate group. The DS_{Cinn} was defined as the

number of 4-chlorocinnamate groups per AGU and was calculated from Equation 3-2. DS_{Cinn} values deduced from the ^{1}H NMR spectra are summarized in **Table 3.1**.

$$DS_{Cinn} = \frac{\left(\frac{Area2/6}{Area1/21}\right)}{3} \tag{3-2}$$

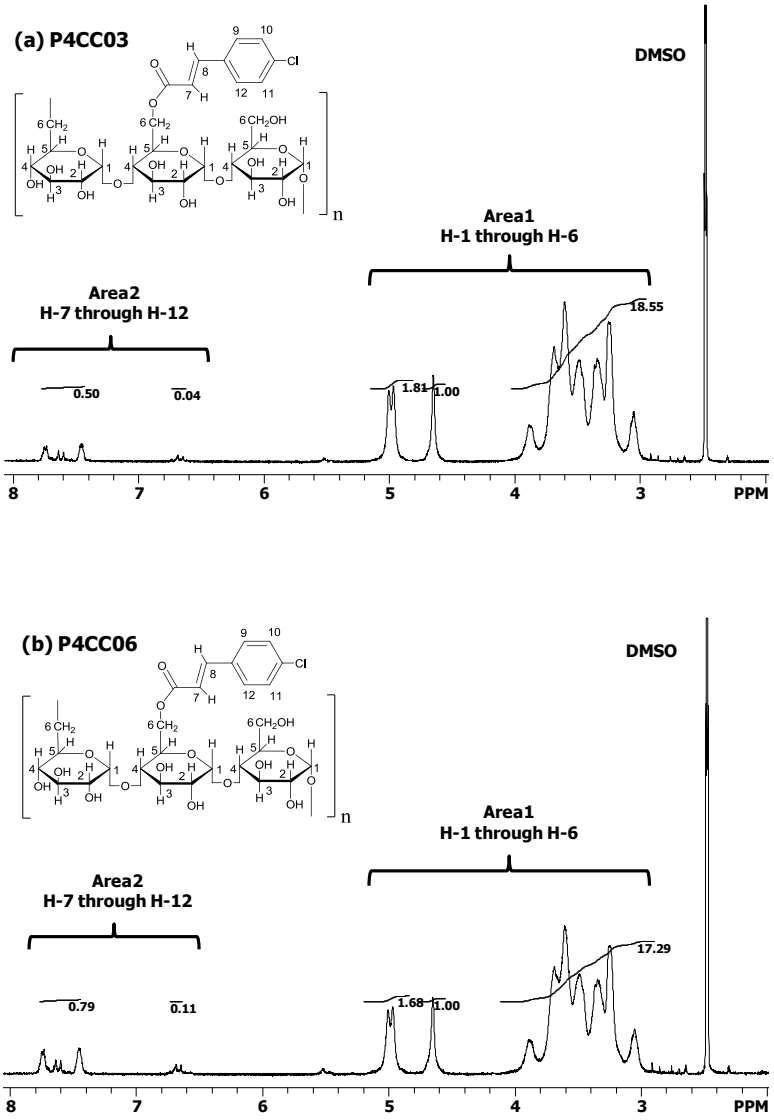

Figure 3.4. ^{1}H NMR spectra of P4CCs in DMSO-d_6 with TFA and TMS.

3.1.2.2 UV Spectroscopic Characterization of P3MCs and P4CCs

UV measurements were obtained on a UV-Vis spectrophotometer (Cary 50 UV-Vis spectrophotometer) with 3 mL quartz cuvettes that had 1 cm path lengths. UV spectra for methyl 3-methoxycinnamate (M3MC) at different concentrations in DMSO are provided in **Figure 3.5**. As seen in **Figure 3.5**, all spectra showed an absorbance maximum at a wavelength of λ_{max} = 281 nm. A calibration curve for M3MC at λ_{max} = 281 nm in DMSO had a slope of $(17.40 \pm 0.60) \times 10^3$ $M^{-1} \cdot cm^{-1}$ and a y-intercept of 0.003 ± 0.01. The curve in **Figure 3.5** is consistent with Beer's Law, $A = \varepsilon \cdot b \cdot c$, where A is absorbance, ε is the molar extinction coefficient, b is the path length, and c is the molar concentration. Hence, a value of $\varepsilon_{max,281nm} = (17.40 \pm 0.60) \times 10^3$ $M^{-1} \cdot cm^{-1}$ was obtained.

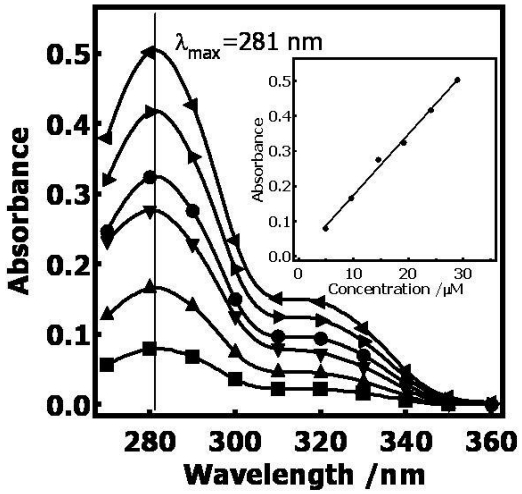

Figure 3.5. UV spectra of M3MC in DMSO. Symbols correspond to (■) 4.83 μM, (▲) 9.51 μM, (▼) 14.5 μM, (●) 19.1 μM, (►) 24.0 μM, and (◄) 28.9 μM. The inset contains an UV absorbance calibration curve for M3MC in DMSO at λ_{max} = 281 nm. The molar extinction coefficient is $\varepsilon_{max,281nm} = (17.40 \pm 0.60) \times 10^3$ $M^{-1} \cdot cm^{-1}$.

UV spectra for pullulan, P3MCs, and M3MC are shown in **Figure 3.6**, and P3MCs and

M3MC had the same shape and λ_{max}. The absorbances of M3MC (46.2 μM), P3MC03 (100.1 mg•L^{-1}), and P3MC06 (76.4 mg•L^{-1}) in DMSO at λ_{max} = 281 nm were 0.931, 0.556, and 0.406, respectively. The absence of strong absorbance for pullulan at a concentration of 100 mg•L^{-1} indicated the absence of strong chromophores in the molecule. However, weak UV absorbance was observed for pullulan at higher concentrations (**Figure 3.7**). Due to weak UV absorbance by pullulan at λ = 281 nm, an UV absorbance calibration curve was also established for pullulan. As seen in **Figure 3.7**, a calibration curve for pullulan at λ = 281 nm in DMSO yielded a slope of 23 ± 2 M^{-1}•cm^{-1} with a y-intercept of -0.0078 ± 0.0089. The curve in **Figure 3.7** is also consistent with Beer's Law. Hence, ε_{281nm} is equal to 23 ± 2 M^{-1}•cm^{-1}.

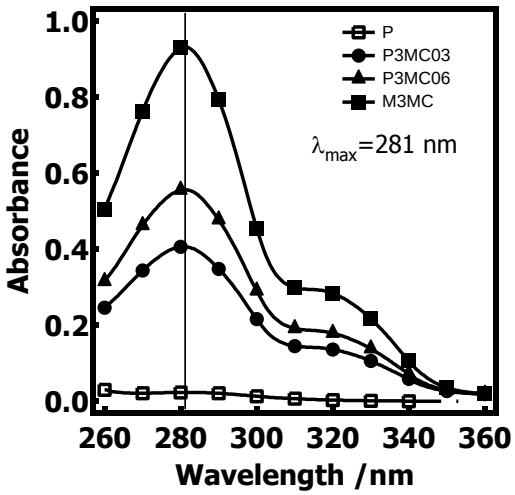

Figure 3.6. UV spectra of Pullulan (P), P3MCs, and M3MC in DMSO. Symbols correspond to (■) 46.2 μM M3MC, (□) 100.0 mg•L^{-1} P, (●) 100.1 mg•L^{-1} P3MC03, and (▲) 74.6 mg•L^{-1} P3MC06.

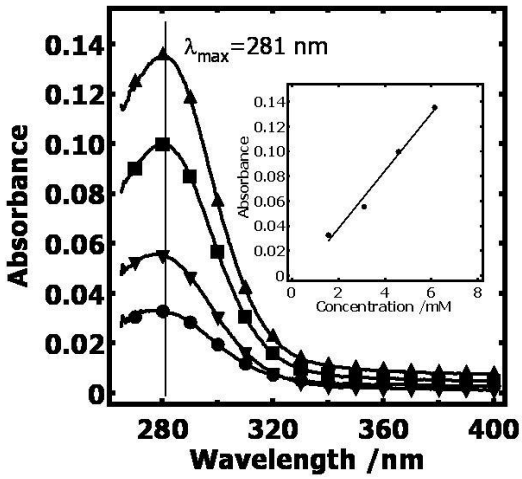

Figure 3.7. UV spectra of pullulan (P) in DMSO. Symbols correspond to pullulan with AGU concentrations of (●) 1.54 mM, (▼) 3.08 mM, (■) 4.57 mM, and (▲) 6.12 mM. The inset contains an UV absorbance calibration curve for pullulan in DMSO at λ = 281 nm. The molar extinction coefficient for pullulan is $\varepsilon_{281nm} = 23 \pm 2\ M^{-1} \bullet cm^{-1}$.

DS_{Cinn} for P3MCs is formulated as

$$DS_{Cinn} = C_{Cinn} / C_{AGU} \qquad (3\text{-}3)$$

where C_{Cinn} is the molar concentration of cinnamate groups and C_{AGU} is the molar concentration of AGUs. DS_{Cinn} for pullulan 3-methoxycinnamate is calculated from Equations. 3-4 and 3-5:

$$m = (C_{Cinn} \times V \times MW_{Cinn}) + (C_{AGU} \times V \times MW_{AGU}) \qquad (3\text{-}4)$$

$$A = (\varepsilon_{Cinn} \times b \times C_{Cinn}) + (\varepsilon_{AGU} \times b \times C_{AGU}) \qquad (3\text{-}5)$$

where m is the mass of the pullulan 3-methoxycinnamate, MW_{Cinn} is the molar mass of a 3-methoxycinnamate group, MW_{AGU} is the molecular weight of an AGU, V is the volume of the polymer solution, and ε_{Cinn} and ε_{AGU} are the molar extinction coefficients for 3-methoxycinnamate and AGUs, respectively. Simultaneous solution of Equations 3-4 and

3-5 yielded C_{Cinn} and C_{AGU}.

DS_{Cinn} values for P4CCs were also obtained using the same method described for P3MC. UV spectra for M4CC at different concentrations in DMSO are provided in **Figure 3.8**. As seen in **Figure 3.8**, all spectra showed an absorbance maximum at a wavelength of λ_{max} = 286 nm. A calibration curve for M4CC at λ_{max} = 286 nm in DMSO had a slope of (25.42 ± 0.34) × 10^3 M^{-1}•cm^{-1} and a y-intercept of 0.001 ± 0.004. Hence, a value of $\varepsilon_{max,286nm}$ = (25.42 ± 0.34) × 10^3 M^{-1}•cm^{-1} was obtained. UV spectra for pullulan, P4CCs, and M4CC are shown in **Figure 3.9**, and P4CCs and M4CC had the same shape and λ_{max}. The absorbances of M4CC (26.4 μM), P4CC03 (50.0 mg•L^{-1}), and P4CC06 (33.6 mg•L^{-1}) in DMSO at λ_{max} = 286 nm were 0.682, 0.308, and 0.325, respectively. DS_{Cinn} results for the P3MCs and P4CCs used are summarized in **Table 3.1**.

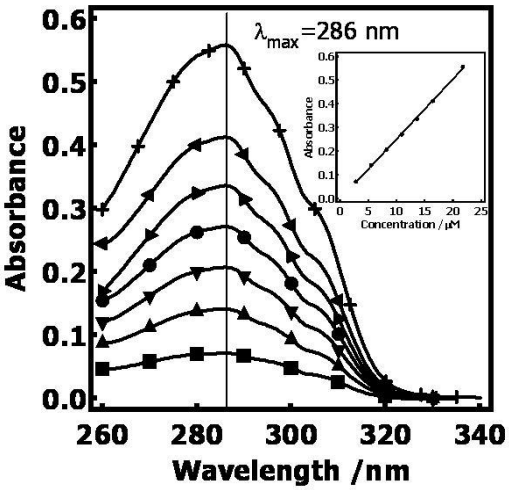

Figure 3.8. UV spectra of methyl 4-chlorocinnamate (M4CC) in DMSO. Symbols correspond to (■) 2.73 μM, (▲) 5.47 μM, (▼) 8.20 μM, (●) 10.9 μM, (►) 13.6 μM, (◄) 16.4 μM, and (+) 21.7 μM. The inset contains an UV absorbance calibration curve for M4CC in DMSO at λ_{max} = 286 nm. The molar extinction coefficient is $\varepsilon_{max,286nm}$ = (25.42 ± 0.34) × 10^3 M^{-1}•cm^{-1}.

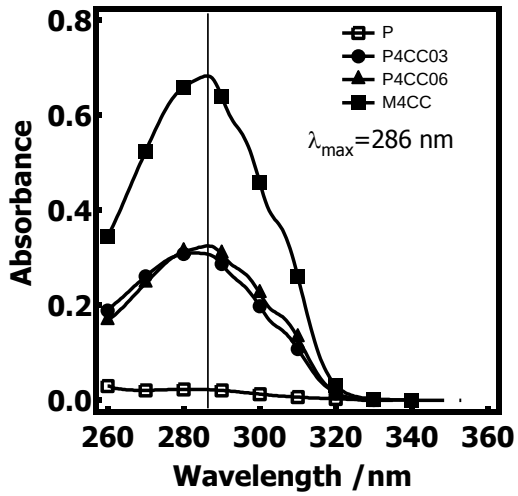

Figure 3.9. UV spectra of Pullulan (P), P4CCs, and M4CC in DMSO. Symbols correspond to (■) 26.4 μM M4CC, (□) 100.0 mg•L^{-1} P, (●) 50.0 mg•L^{-1} P4CC03, and (▲) 33.6 mg•L^{-1} P4CC06.

3.1.2.3 ATR-IR Spectroscopic Characterization of P3MCs and P4CCs

A Midac M series Fourier Transform Infrared (FT-IR) spectrometer equipped with a Durascope attenuated total reflectance (ATR) attachment was used to scan the 4000-750 cm^{-1} region of bulk powders, with 64 scans and a 2 cm^{-1} resolution. IR spectra of the pullulan, P3MCs, and P4CCs with different DS_{Cinn} are shown in **Figure 3.10**. Absorbance at 1710 cm^{-1} *ν*(C=O ester group) from cinnamate groups was observed in P3MC06 and P4CC06 differed from pure pullulan. Significant OH signals at 3400 cm^{-1} were observed for all samples, indicating the DS_{Cinn} values were low. All samples are water soluble.

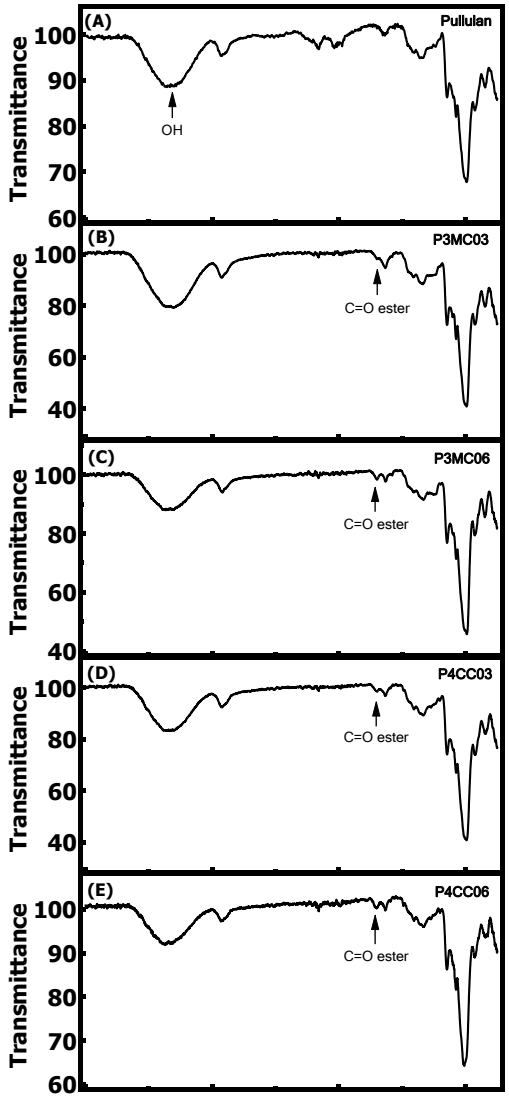

Figure 3.10. ATR-IR spectra of (A) pullulan, (B, C) P3MCs, and (D, E) P4CCs.

3.1.3 Synthesis and Characterization of Pullulan Cinnamates (PC) and Trimethylsilyl Pullulan Cinnamates (TMSPC)

PCs and TMSPCs synthesized in Chapter 3.1.3 were used to prepare substrates as models for lignocellulosic biomass. Pullulan was dried for 12 h in a vacuum oven at 70 ℃ before the reaction. As a representative procedure, 2.00 g pullulan (12.3 mmol AGUs) and

40 mL DMAc were added to a 100 mL two-necked round bottom flask equipped with a reflux condenser and magnetic stirrer under nitrogen. After pullulan was dissolved at 70 ℃, 6.0 g pyridine (75.9 mmol) was added to the solution. Subsequently, 1.03 g cinnamoyl chloride (6.2 mmol) was dissolved in 10 mL DMAc and added dropwise to the pullulan/pyridine solution. This mixture was allowed to react for 24 h at 70 ℃. The product was precipitated into ethanol and the precipitate was collected by filtration and washed three times with ethanol. The precipitate was dried in a vacuum oven at 60 ℃ and yielded 2.0 g PC03. The reaction scheme is shown in **Figure 3.11**. Variation of the feed ratio of cinnamoyl chloride yielded different DS_{Cinn}. The DS_{Cinn} of the products are summarized in **Table 3.2**.

As a representative procedure, 1.5 g PC (DS_{Cinn} = 0.28) was dissolved in 30 mL DMAc at 70 ℃. Next, 0.2 mL TMS-Cl was added as a catalyst, followed by 10.0 mL HMDS (41.7 mmol). This reaction ran for 24 h at 100 ℃, and a precipitate formed at the bottom of the flask. The liquid portion of the mixture was decanted and the precipitate was dissolved in THF. Next, the product in THF was precipitated into methanol and the precipitate was collected by filtration and washed three times with methanol. The precipitate was dried in a vacuum oven at 60 ℃ and yielded 2.4 g TMSPC03. This procedure was used for silylation of all PC samples. The degrees of trimethylsilyl substitution (DS_{TMS}) of the products are summarized in **Table 3.3**.

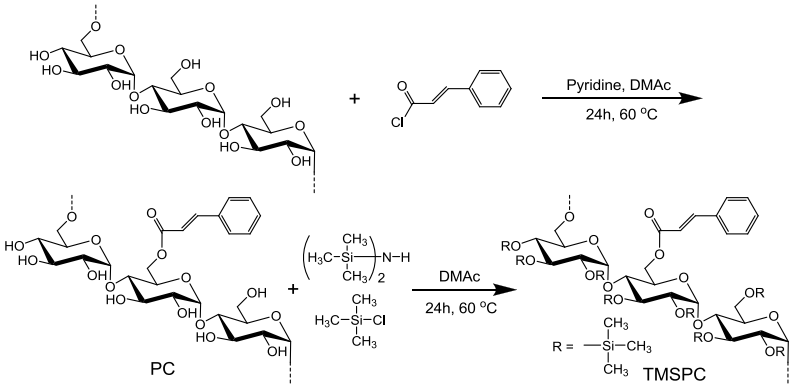

Figure 3.11. Reaction scheme for the synthesis of PC and TMSPC.

Table 3.2. Substitution data for PCs

Sample	Feed Ratio[a]	Theo. DS_{Cinn}	Obs. DS_{Cinn}	
			(NMR)	(UV)
PC02	0.30	0.30	0.19	0.200 ± 0.001
PC03	0.50	0.50	0.27	0.280 ± 0.001
PC07	1.00	1.00	0.70	0.670 ± 0.001
PC12	1.50	1.50	1.12	1.220 ± 0.001
PC23	3.30	3.00	2.17	2.300 ± 0.001

[a]Molar ratio of cinnamoyl chloride to AGUs of pullulan.

Table 3.3. Substitution data for TMSPCs

Sample	Theo. DS_{TMS}[a]	Obs. DS_{TMS} (UV)
TMSPC02	2.800	2.750 ± 0.001[a]
TMSPC03	2.720	2.670 ± 0.001[a]
TMSPC07	2.330	2.260 ± 0.001[a]
TMSPC12	1.780	1.700 ± 0.001[b]
TMSPC23	0.700	0.600 ± 0.001[b]

[a]Calculated using DSCinn from UV (Table 3-2) assuming complete silylation of the remains hydroxyl groups.
[b]DS_{TMS} was measured from TMSPC hexanes solution.
[c]DS_{TMS} was measured from TMSPC tetrahydrofuran solution.

3.1.3.1 ^{1}H NMR Characterization of PCs

^{1}H NMR spectra of PCs in DMSO-d_6 with TFA are provided in **Figure 3.12**. The integrated area between chemical shifts of δ = 2.8 and δ = 5.2 ppm (*Area*1) corresponded to 21 protons (H-C) of a MTU (3AGUs). The integrated area between δ = 6.6 and δ = 8.0 ppm

(*Area*2) corresponded to 7 protons of the cinnamate group. The DS_{Cinn} was calculated from Equation 3-6:

$$DS_{Cinn} = \frac{\left(\frac{Area2/7}{Area1/21}\right)}{3} \qquad (3\text{-}6)$$

DS_{Cinn} values deduced from the ^{1}H NMR spectra are summarized in **Table 3.2**.

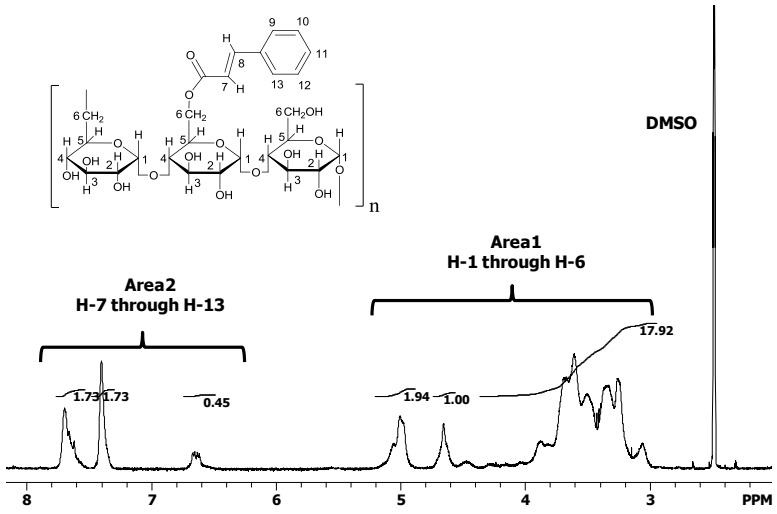

Figure 3.12. ^{1}H NMR spectrum of PC02 in DMSO-d_6 with TFA and TMS.

3.1.3.2 UV Spectroscopic Characterization of PCs and TMSPCs

DS_{Cinn} for PCs were also calculated using the same method used as P3MC. UV spectra for methyl *trans*-cinnamate at different concentrations in DMSO are provided in **Figure 3.13**. As seen in **Figure 3.13**, all spectra showed an absorbance maximum at a wavelength of λ_{max} = 281 nm. A calibration curve for methyl *trans*-cinnamate at λ_{max} = 281 nm in DMSO had a slope of $(19.02 \pm 0.22) \times 10^3$ M^{-1}•cm^{-1} and a y-intercept of 0.015 ± 0.005. Hence, a value of $\varepsilon_{max,281nm} = (19.02 \pm 0.22) \times 10^3$ M^{-1}•cm^{-1} was obtained. UV spectra for pullulan, PCs, and methyl *trans*-cinnamate are shown in **Figure 3.14**. UV spectra of the

PCs and methyl *trans*-cinnamate had the same shape and λ_{max}. The absorbances of PC02 (29.7 mg•L^{-1}), PC03 (16.1 mg•L^{-1}), PC07 (8.1 mg•L^{-1}), PC12 (7.5 mg•L^{-1}), and PC23 (1.8 mg•L^{-1}) in DMSO at λ_{max} = 281 nm were 0.600, 0.428, 0.415, 0.542, and 0.156, respectively. DS_{Cinn} results for the PCs are summarized in **Table 3.2**.

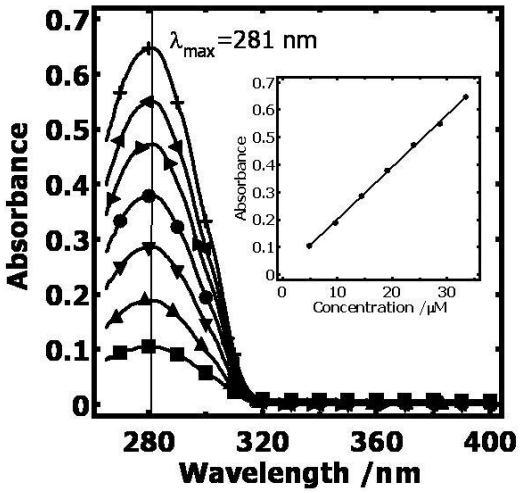

Figure 3.13. UV spectra of methyl *trans*-cinnamate in DMSO. Symbols correspond to (■) 4.76 μM, (▲) 9.52 μM, (▼) 14.3 μM, (●) 19.0 μM, (►) 23.8 μM, (◄) 28.6 μM, and (+) 33.3 μM. The inset contains an UV absorbance calibration curve for methyl *trans*-cinnamate in DMSO at λ_{max} = 281 nm. The molar extinction coefficient was $\varepsilon_{max,281nm} = (19.02 \pm 0.22) \times 10^3$ M^{-1}•cm^{-1}.

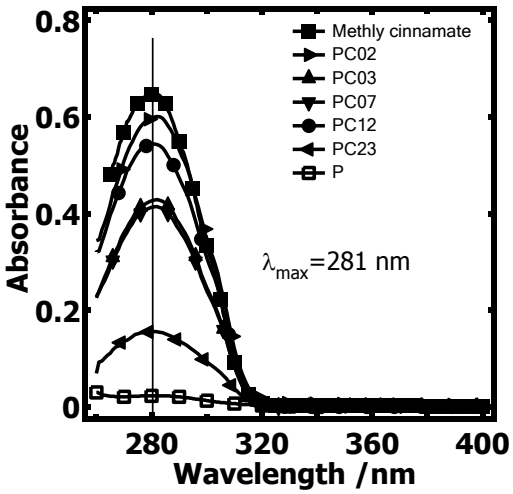

Figure 3.14. UV spectra of methyl *trans*-cinnamate, pullulan (P), and PCs in DMSO. Symbols correspond to (■) 33.3 μM methyl *trans*-cinnamate, (□) 100.0 mg•L^{-1} P, (►) 29.7 mg•L^{-1} PC02, (▲) 16.1 mg•L^{-1} PC03, (▼) 8.1 mg•L^{-1} PC07, (●) 7.5 mg•L^{-1} PC12, and (◄) 1.8 mg•L^{-1} PC23.

UV-Vis measurements were also used to determine the degree of substitution of TMS groups (DS_{TMS}). A methyl *trans*-cinnamate calibration curve in hexanes (**Figure 3.15)** was used to deduce the DS_{TMS} for trimethylsilyl pullulan cinnamates (TMSPC02, TMSPC03, TMSPC07), because TMSPC02, TMSPC03 and TMSPC07 were soluble in hexanes and their UV spectra had the same shape and λ_{max} as methyl *trans*-cinnamate (**Figure 3.16**). A calibration curve for methyl *trans*-cinnamate at λ_{max} = 271 nm in hexanes showed that the slope was (20.29 ±0.03) ×10^3 M^{-1}•cm^{-1} with a y-intercept of 0.001 ±0.001. Hence, a value of $\varepsilon_{max,271nm}$ = (20.29 ±0.02) ×10^3 M^{-1}•cm^{-1} was obtained.

A methyl *trans*-cinnamate calibration curve in tetrahydrofuran (**Figure 3.17)** was used to deduce the DS_{TMS} for TMSPC12 and TMSPC23, because they were soluble in tetrahydrofuran and their spectra had the same shape and λ_{max} as methyl *trans*-cinnamate

(**Figure 3.18)**. A calibration curve for methyl *trans*-cinnamate at λ_{max} = 276 nm in tetrahydrofuran showed that the slope was (20.59 ±0.19) ×10^3 M^{-1}•cm^{-1} with a y-intercept of 0.022 ±0.001. Hence, a value of $\varepsilon_{max,276nm}$ = (20.29 ±0.02) ×10^3 M^{-1}•cm^{-1} was obtained.

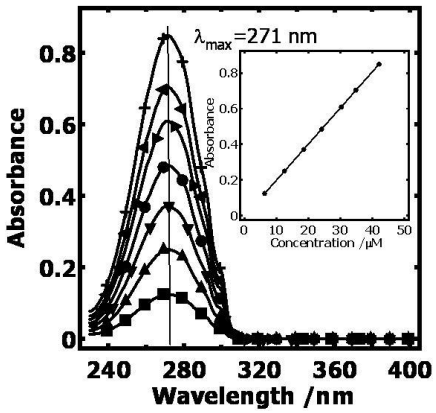

Figure 3.15. UV spectra of methyl *trans*-cinnamate in hexanes. Symbols correspond to (■) 6.17 μM, (▲) 12.4 μM, (▼) 18.4 μM, (●) 24.0 μM, (►) 30.1 μM, (◄) 34.7 μM, and (+) 41.9 μM. The inset contains an UV absorbance calibration curve for methyl *trans*-cinnamate in hexanes at λ_{max} = 271 nm. The molar extinction coefficient is $\varepsilon_{max,\ 271nm}$ = (20.29 ±0.03) ×10^3 M^{-1}•cm^{-1}.

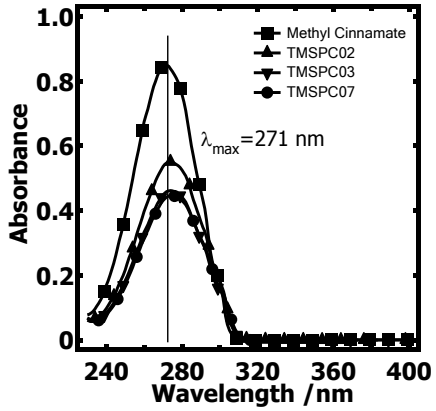

Figure 3.16. UV spectra of methyl *trans*-cinnamate and trimethylsilyl pullulan cinnamates (TMSPCs) in hexanes. Symbols correspond to (■) 41.9 μM methyl *trans*-cinnamate, (▲) 54.9 mg•L^{-1} TMSPC02, (▼) 32.7 mg•L^{-1} TMSPC03, and (●) 13.5 mg•L^{-1} TMSPC07.

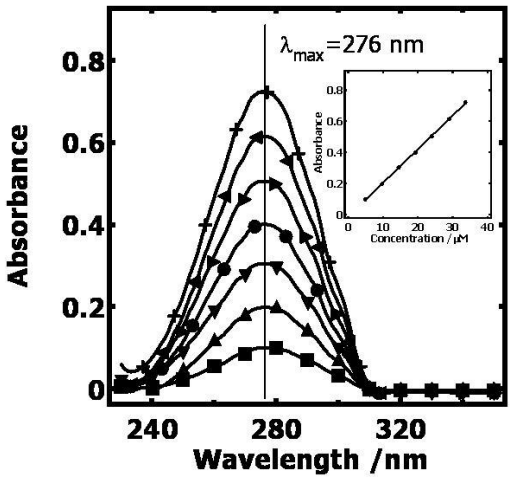

Figure 3.17. UV spectra of methyl *trans*-cinnamate in tetrahydrofuran. Symbols correspond to (■) 4.74 μM, (▲) 9.58 μM, (▼) 14.4 μM, (●) 19.2 μM, (►) 23.9 μM, (◄) 28.8 μM, and (+) 33.5 μM. The inset contains an UV absorbance calibration curve for methyl *trans*-cinnamate in tetrahydrofuran at λ_{max} = 276 nm. The molar extinction coefficient is $\varepsilon_{max,276nm} = (21.59 \pm 0.19) \times 10^3\ M^{-1} \bullet cm^{-1}$.

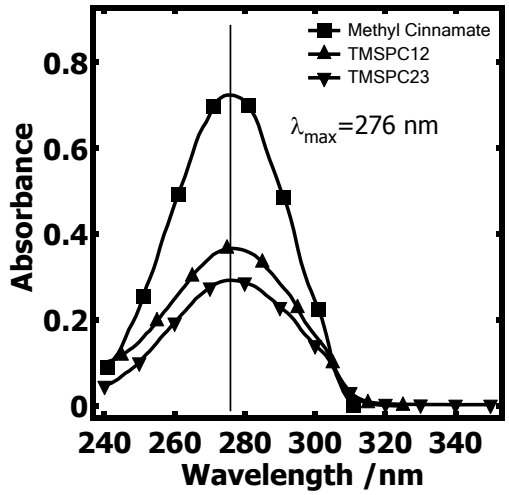

Figure 3.18. UV spectra of methyl *trans*-cinnamate and trimethylsilyl pullulan cinnamates (TMSPCs) in tetrahydrofuran. Symbols correspond to (■) 33.5 μM methyl *trans*-cinnamate, (▲) 7.8 mg•L^{-1} TMSPC12 and (▼) 3.5 mg•L^{-1} TMSPC23.

The absorbances of TMSPC02 (54.9 mg•L^{-1}), TMSPC03 (32.7 mg•L^{-1}), and TMSPC07 (13.5 mg•L^{-1}) in hexanes at λ_{max} = 271 nm were 0.544, 0.454, and 0.437, respectively. The absorbances of TMSPC12 (7.8 mg•L^{-1}) and TMSPC23 (3.5 mg•L^{-1}) in tetrahydrofuran at λ_{max} = 276 nm were 0.369 and 0.295, respectively. DS_{TMS} were formulated as

$$DS_{TMS} = C'_{TMS} / C'_{AGU} \tag{3-7}$$

where C'_{TMS} is the molar concentration of TMS groups and C'_{AGU} is the molar concentration of AGUs in TMSPC. DS_{TMS} was calculated from Equations 3-8 and 3-9:

$$m' = (C'_{Cinn} \times V \times MW_{Cinn}) + (C'_{AGU} \times V \times MW_{AGU}) + (C'_{TMS} \times V \times MW_{TMS}) \tag{3-8}$$

$$A' = (\varepsilon'_{Cinn} \times b \times C'_{Cinn}) \tag{3-9}$$

where m′ is the mass of the TMSPC, MW_{Cinn} is the molecular weight of a cinnamate group, MW_{AGU} is the molar mass of an AGU, MW_{TMS} is the molar mass weight of a TMS group, V is the volume of the polymer solution, and ε'_{Cinn} is the molar extinction coefficient for a cinnamate in hexanes [$(20.29 \pm 0.03) \times 10^3$ M^{-1}•cm^{-1}] or in tetrahydrofuran [$(20.59 \pm 0.19) \times 10^3$ M^{-1}•cm^{-1}]. Simultaneous solution of Equations. 3-8 and 3-9 yielded C'_{TMS} and C'_{AGU}. DS_{TMS} results for the TMSPCs used in this thesis are summarized in **Table 3.3**.

3.1.3.3 ATR-IR Spectroscopic Characterization of PCs and TMSPCs

ATR-IR spectra of the pullulan cinnamates with different DS_{Cinn} (**Figure 3.19A**) showed absorbance at 1710 cm^{-1} *ν*(C=O ester group) from cinnamate groups increased and OH signal at 3400 cm^{-1} decreased with increasing DS_{Cinn}. IR spectra of silylated pullulan cinnamates (**Figure 3.19B**) showed additional absorbance at 1246 cm^{-1} *ν*(Si-C) and 833 cm^{-1} *ν*(Si-C), and insignificant OH signals that were consistent with nearly complete replacement of the hydroxyl groups of the AGU by cinnamate and trimethylsilyl groups.

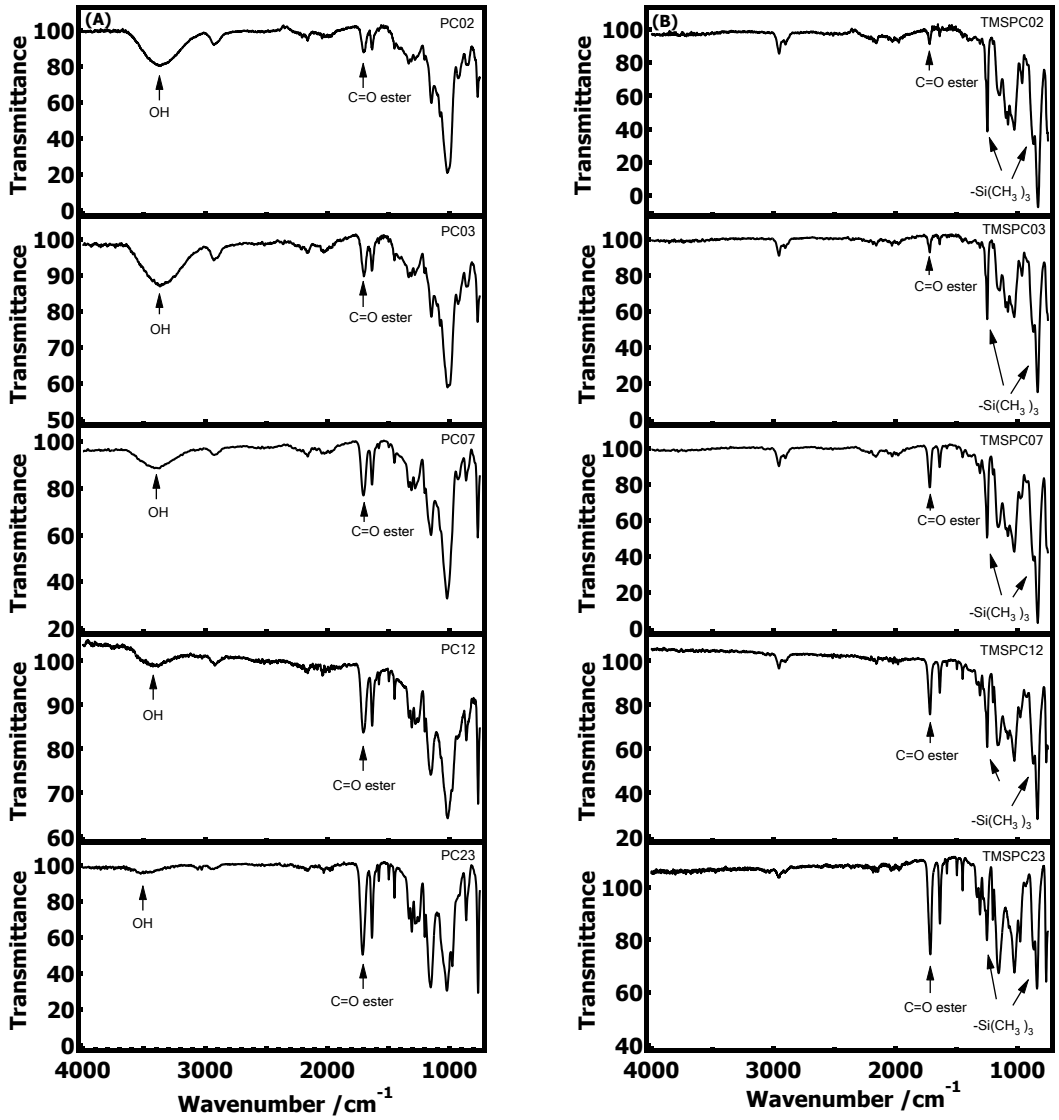

Figure 3.19. ATR-IR spectra of (A) PCs and (B) TMSPCs.

3.2 Film Preparation and Characterization Techniques

3.2.1 Preparation of Model Films

Model films were prepared onto SPR and QCM-D sensors by spincoating and self-assembled monolayers (SAMs). Cellulose, thermoplastic, and SAM surfaces were used for studies of substrate hydrophobicity effects on pullulan cinnamate adsorption at

liquid/solid interfaces. Pullulan cinnamate and cellulose blend films were used for studies of cellulase adsorption and activity on lignocellulosic biomass.

3.2.1.1 Materials for the Preparation of Model Films

Trimethylsilyl cellulose (TMSC DS_{TMS} = 2.71) was synthesized and provided by the Heinze group at the Friedrich Schiller University of Jena in Germany.[3] Cellulose acetate propionate (CAP, M_n ~ 15,000 g/mol, 0.6 wt.% acetyl, and 42.5 wt.% propionyl content) was purchased from Aldrich. Poly(L-lactic acid) (PLLA, M_n ~ 4,700 g/mol, M_w/M_n = 1.09) was purchased from Polymer Source, Inc. 1-Dodecanethiol (SAM-CH_3) was purchased from Sigma-Aldrich. Ethanol was purchased from Decon Lab Inc.

3.2.1.2 Regenerated Cellulose Films

Smooth, uniform films of regenerated cellulose were prepared on quartz crystal microbalance with dissipation monitoring (QCM-D) sensors (diameter = 14 mm and thickness = 0.3 mm) and surface plasmon resonance (SPR) sensor slides (12.0 mm × 12.0 mm × 0.9 mm). QCM-D sensors consisted of a disk-shaped AT-cut quartz crystal covered with 5 nm of chromium and 100 nm of gold. SPR sensor slides consisted of a glass slide covered with 2 nm of chromium and 48 nm of gold. QCM-D sensors were cleaned via an UV/Ozone ProCleaner™ (Bioforce Nanoscience, Inc.) for 10 minutes and boiled in a 1:1:5 by volume solution of ammonium hydroxide:hydrogen peroxide:water for 1 hour. SPR sensor slides were cleaned by immersion in a 7:3 by volume solution of sulfuric acid:hydrogen peroxide (piranha solution) for 1 hour. Both QCM-D and SPR sensors were rinsed exhaustively with ultrapure water prior to spincoating. TMSC was spincoated onto the cleaned sensors with a spinning speed of 2000 revolutions per minute (rpm) from 10 $g \cdot L^{-1}$ TMSC solutions in toluene. Trimethylsilyl groups of TMSC were cleaved by

exposing the coated gold surface to HCl vapor for 3 minutes in a process that yielded regenerated cellulose surfaces.

3.2.1.3 Thermoplastic Films

The sensor slides underwent the same cleaning procedure described for the preparation of cellulose films. CAP and PLLA were spincoated onto cleaned QCM-D and SPR sensors with a spinning speed of 2000 rpm from 5 $g \cdot L^{-1}$ CAP and PLLA solutions in tetrahydrofuran and chloroform, respectively.

3.2.1.4 Self-assembled Monolayers (SAMs)

The sensor slides underwent the same cleaning procedure described for the preparation of cellulose films. Once dried, the sensor slides were placed in a 1 mM solution of the 1-dodecanethiol in ethanol for at least 24 hours. Once the SAM sensor was needed, the slide was removed from the 1-dodecanethiol solution, rinsed with absolute ethanol for the removal of excess 1-dodecanethiol molecules, and dried with nitrogen. Finally, the SAM sensor slide was washed with ultrapure water and dried with nitrogen. Surfaces prepared from 1-dodecanethiol are hydrophobic with a water contact angle of $101 \pm 1°$.

3.2.1.5 Regenerated Pullulan Cinnamate Films and Blend Films

Regenerated PC films were also prepared on QCM-D and SPR sensors. TMSPCs synthesized in Chapter 3.1.3 were spincoated from 10 $g \cdot L^{-1}$ solutions in toluene with a spinning speed of 2000 rpm. Then, the TMS groups were removed by HCl vapor. TMSPC/TMSC blends with desired mass ratios were also spincoated onto QCM-D and SPR sensor from toluene solutions to prepare regenerated cellulose/PC blend thin films using the same procedure described for the preparation of regenerated cellulose and PC films.

3.2.2 X-Ray Photoelectron Spectroscopy (XPS)

XPS measurements provided elemental compositions of the polymer films in this study. A X-ray photo electron spectrometer (PHI 5400, Perkin-Elmer, Mg KR radiation) with a magnesium anode operated at 250 W and a background pressure of 5×10^{-7} Torr was used to perform XPS. The spectra were recorded with an 89.45 eV pass energy, 0.1 eV step, and 25 ms dwelling time. The angle between the X-ray beam and surface normal was 15 °.

3.2.3 Ellipsometry

Thicknesses of the polymer films in this study were determined by ellipsometry. Angle resolved laser (632.8 nm, He-Ne laser) ellipsometry (Picometer Ellipsometer, Beaglehole Instruments, Wellington, New Zealand) was used to determine the thicknesses of model polymer films. The data were collected in 1.0 ° intervals from 65 to 80 °. The angles were chosen around the Brewster angle (~74 °) since the sensitivity for changes in the layer thickness was the greatest. Measurements were made at 3 spots and reported values are the average with one standard deviation error bars.

3.2.4 Contact Angle Measurements

Contact angle measurements provided hydrophobicities of the polymer films in this study. Static contact angle measurements were recorded using a FTA125 Contact Angle Analyzer (First Ten Angstroms). The static contact angles of a drop of ultrapure water on a given surface were measured. All data were collected at room temperature. A minimum of three different measurements for each surface were recorded and averaged.

3.2.5 Surface Tension Measurements

Surface tension measurements provided surface activities of the polysaccharide

derivatives at the air/water interface in this study. The surface tension measurements of aqueous polymer solutions were determined by the Wilhemy plate method using a paper plate attached to a Cahn 2000 electrobalance. In general, polymer solutions were placed in a specially designed glass jar that consisted of an inner cup containing the solution and an outer jacket that contained 20.0 ℃ water flowing from a thermostated circulating bath. The sample cell was inside a Plexiglass^{TM} box to minimize water evaporation and maintain a constant relative humidity (~ 75%). For surface tension measurements of aqueous P, P3MC, and P4CC solutions, a fixed volume of 20 mL of ultrapure water was placed in the specially designed glass jar. Next, P, P3MC, and P4CC stock solutions (~ 1000 mg•L^{-1}) were added to the water incrementally with a digital variable volume pipettor that controlled the solution concentration.

3.2.6 Refractive Index Increment Measurements

The refractive index increments (dn/dc) of polymer solutions were determined with a Wyatt Optilab rEX differential refractometer. The experiments were carried out at a wavelength of λ = 690 nm at 20 ℃. Samples were flowed at 0.25 mL•min^{-1} into the differential refractometer using a syringe pump and a syringe affixed with a 0.80 μm cellulose acetate (CA) syringe filter. The (dn/dc) values were determined using the Wyatt Astra V software package. For aqueous P, P3MC, and P4CC solutions, (dn/dc) values were evaluated over the concentration range of 0 to 1000 mg•L^{-1}, whereas (dn/dc) values for CMC solutions in aqueous $CaCl_2$ and NaCl were evaluated over the concentration range of 0 to 500 mg•L^{-1}.

3.2.7 Atomic Force Microscopy (AFM)

AFM measurements in air provided roughnesses of the polymer films in this study. A

MFP-3D-Bio^{TM} atomic force microscope (Asylum Research, Santa Barbara) was used for tapping mode imaging of polymer surfaces in air. The cantilever was an Olympus AC160TS. The probe of the standard Si cantilever had a nominal radius of <10 nm, a spring constant of 42 N•m^{-1}, and a typical resonant frequency of 300 kHz. All measurements were performed in laboratory air and at room temperature.

3.2.8 In Situ AFM Measurements

In situ AFM measurements provided morphology changes of the substrates at liquid/solid interfaces in this sutdy. A Nanoscope III atomic force microscope (Dimension 3000 scope with a Nanoscope IIIa controller, Digital Instruments) imaged the samples in tapping mode. The probes, standard silicon nitride tips, had a nominal radius of 20 nm and a spring constant of 0.12 N•m^{-1}. Cantilevers were exposed to ultraviolet irradiation for at least 30 minutes for the removal of organic contaminants. After the fluid cell was installed, pure solvent was flowed over the model surface. Images of the reference surface were taken after a flow time of 1 hour. Next, the sample solution used in QCM-D measurements was injected into the liquid cell for the desired time. Prior to the collection of post-adsorption images, a large excess of pure solvent was flowed over the surface for 30 minutes.

3.2.9 Surface Plasmon Resonance (SPR)

Sample adsorption onto model surfaces was investigated by SPR. After a desired film was prepared on the sensor, the sensor was refractive index-matched to the prism of a Reichert SR 7000 SPR refractometer using immersion oil (n_D = 1.5150). This system used a laser diode with an emission wavelength of 780 nm. The flow cell body was equipped with a Viton gasket (Dupont Dow Elastomers, LLC) and was mounted on top of the sensor.

Solutions were pumped into the flow cell at a flow rate of 0.25 mL•min^{-1} via Teflon tubing connected to a cartridge pump (Masterflex) at 20.0 ℃. For SPR experiments, sample stock solutions were degassed before SPR experiments. Prior to data acquisition, the model surfaces were allowed to reach equilibrium swelling as pure solvent was flowed through the system. Once a stable baseline was established, sample solutions were pumped into the flow cell. Each sample solution flowed over the sensor until adsorption ceased and then pure solvent was flowed over the surface. Key parameters extracted from SPR experiments are schematically depicted in **Figure 3.20**. Each SPR experiment was performed three times, and data points on the adsorption isotherms represent the average value with one standard deviation error bars.

3.2.9.1 Analysis of SPR Data

Refractive index changes in the vicinity of the gold surface were detected through changes in the resonance angle (θ_{sp}), the incident angle at which reflected light intensity was at a minimum.[4] θ_{sp} was sensitive to changes that occurred within ~200 nm of the surface, i.e. both adsorbed molecules and bulk changes. This latter effect (bulk effect) produced a displacement in θ_{sp} with respect to increasing analyte concentration. A schematic depiction of how θ_{sp} changed as analyte adsorbed onto the sensor surface and partially desorbed from the sensor surface after analyte-free solvent flowed over the surface is provided as **Figure 3.20**. As shown in **Figure 3.20**, the total increase in the resonance angle ($\Delta\theta_{tot}$) corresponded to the observed change in the resonance angle ($\Delta\theta_{sp}$) caused by reversible adsorption ($\Delta\theta_{rev}$), irreversible adsorption ($\Delta\theta_{irr}$), and the bulk effect ($\Delta\theta_{bulk}$). The decrease in $\Delta\theta_{sp}$ after pure solvent was subsequently flowed over the surface corresponded to $\Delta\theta_{sp}$ caused by the desorption of some analyte molecules and elimination

of the bulk effect. The residual $\Delta\theta_{sp}$ corresponded to $\Delta\theta_{irr}$.[5]

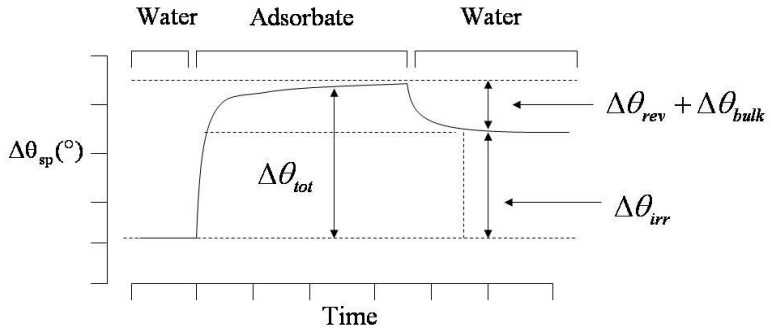

Figure 3.20. A schematic depiction of raw SPR data for the case where water is used to establish a baseline value for $\Delta\theta_{sp}$. A solution containing adsorbate produces a total change in $\Delta\theta_{sp}$ ($\Delta\theta_{tot}$). Switching from adsorbate solution to water eliminates the bulk contribution ($\Delta\theta_{bulk}$), removes reversibly bound adsorbate ($\Delta\theta_{rev}$), and yields irreversibly bound adsorbate ($\Delta\theta_{irr}$).

$\Delta\theta_{tot}$ and $\Delta\theta_{irr}$ values were deduced for each sample as depicted in **Figure 3.20**. Next, the change in the resonant angle associated with adsorption ($\Delta\theta_a = \Delta\theta_{rev} + \Delta\theta_{irr}$) was obtained by subtraction of the contribution of bulk refractive index changes in the dielectric medium from $\Delta\theta_{tot}$:

$$\Delta\theta_a = \Delta\theta_{tot} - c\left(\frac{d\theta_{sp}}{dc}\right) \qquad (3\text{-}10)$$

where c is the bulk solution concentration, and

$$\left(\frac{d\theta_{sp}}{dc}\right) = \left(\frac{d\theta_{sp}}{dn}\right)\left(\frac{dn}{dc}\right) \qquad (3\text{-}11)$$

where (dn/dc) is the refractive index increment of the adsorbate solution and ($d\theta_{sp}/dn$) = 61.5 ° is an instrument specific parameter obtained by calibration of the instrument with ethylene glycol standards. $\Delta\theta_a$ was used to calculate the surface excess (Γ) for each

concentration with the equation of de Feijter et al.:[6]

$$\Gamma = \frac{L(n_f - n)}{(dn/dc)} = \frac{\Delta\theta_a(n_f - n)}{(d\theta/dL)(dn/dc)} \qquad (3\text{-}12)$$

where, n_f is the refractive index of the film (assumed to be 1.45), and n ≈ 1.32813 is the refractive index of the solvent (water or dilute electrolyte solutions).[7] The other constant in Equation 3-12, (dθ/dL), was obtained from Fresnel calculations. Theoretical Fresnel calculations were carried out with a computer simulation program written in Matlab. The values of n and the thickness of the six layers used in the Fresnel calculations are summarized in **Table 3.4**. (dθ/dL) values for model polymer surfaces and SAM surface were $(4.2 \pm 0.2) \times 10^{-3}$ deg•Å^{-1} and $(3.9 \pm 0.2) \times 10^{-3}$ deg•Å^{-1}, respectively. (dθ/dL) values did not change with increasing $CaCl_2$ and NaCl concentration values.

Table 3.4. Layer parameters for the determination of (dθ/dL) in SPR studies

	Layer	Thickness (Å)	Refractive Index n	Adsorption Coefficient *K*
L1	Sapphire prism	5×10^6	1.76074[8]	0
L2	Chromium	20	4.1106[9]	4.3492[9]
L3	Gold	480	0.174[9]	4.86[9]
L4	Cellulose or SAM	195[10]	1.44[12]	0
		16[11]	1.45215[11]	
L5	Adsorbed Layers	Variable	1.45[a]	0
	Water			0
L6	5 and 10 mM $CaCl_2$[b] 15 and 30 mM NaCl[b]	500	1.32813[7]	

[a]Assumed to be 1.45 which is generally a good assumption for organic materials.
[b]The refractive index of water was used for dilute $CaCl_2$ (5 and 10 mM) and NaCl (15 and 30 mM) solutions.

3.2.10 Quartz Crystal Microbalance with Dissipation Monitoring (QCM-D)

Sample adsorption onto model polymer films was also investigated by QCM-D (Q-Sense E4). The QCM-D sensor with a desired polymer film was placed in a flow cell. The polymer film was allowed to equilibrate for 20 minutes in air and 20 minutes in an

appropriate solvent at 20.0 °C at a flow rate of 0.25 mL•min^{-1} using a cartridge pump (ISMATEC-ISM935). Once the system stabilized, a sample solution was flowed over the polymer film until a new constant value was established. Frequency (Δf) and dissipation (ΔD) changes for the fundamental frequency (4.95 MHz for gold coated quartz crystals) and six odd overtones (n = 3 through 13) were monitored simultaneously. After sample adsorption, pure solvent was pumped into the system for the removal of residual sample. Each QCM-D experiment was performed three times and average values with one standard deviation were obtained.

3.2.10.1 Analysis of QCM-D Data

The surface concentration for dry polymer films and rigid adsorbed layers ($\Delta D < 2\times10^{-6}$) were calculated from the QCM-D data through Sauerbrey equation:[13]

$$\Delta m = -\frac{C\Delta f}{n} \qquad (3\text{-}13)$$

where n is the overtone number and C is a constant (0.177 mg•m^{-2}•Hz^{-1})

A Voigt-based viscoelastic model[14] was used to fit the adsorption curves for viscoelastic layers. In this model, the adsorbed layer was treated as a viscoelastic layer between the quartz crystal and a semi-infinite Newtonian liquid layer (**Figure 3.21**). The quartz crystals were assumed to be purely elastic (thickness $h_q = 3\times10^{-4}$ m and density ρ_q = 2650 kg•m^{-3}), and the surrounding solution was assumed to be purely viscous (density ρ_0 = 1000 k•gm^{-3} and viscosity $\eta_0 = 1\times10^{-3}$ N•s•m^{-2}). The model polymer films were treated as an extension of the quartz crystal. The adsorbed polymer layer was represented by four unknown parameters: thickness (h_f), density (ρ_f), viscosity (η_f), and elastic shear modulus (μ_f).

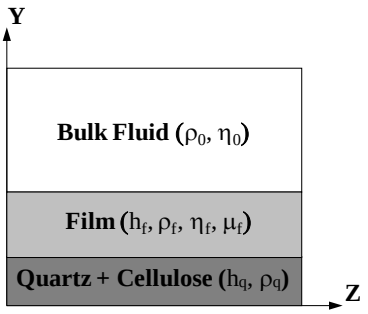

Figure 3.21. Diagram of the system modeled by the Voigt-based viscoelastic model. The QCM-D sensor (quartz crystal plus cellulose surface) was covered by an adsorbed film that can be described by h_f, ρ_f, η_f, and μ_f under no slip boundary conditions. The adsorbed film was covered by a semi-infinite Newtonian fluid with ρ_0 and η_0.

The adsorption curves for multiple overtones were used to estimate the thickness (h_f) and viscoelastic parameters of viscoelastic layers using the instrument software package QTools 3.0.5 (Q-Sense). The fitting parameters were constrained to the following levels: viscosity (1×10^{-4} to 0.1 N•s•m^{-2}), elastic shear modulus (1×10^{5} to 1×10^{8} N•m^{-2}), and thickness (1×10^{-10} to 1×10^{-6} m). h_f and ρ_f were not independent variables, and within this model, ρ_f was initially fixed to obtain effective thicknesses. The surface concentrations (Γ_{QCM}) were calculated from Equation 3-14:

$$\Gamma_{QCM} = h_f \rho_f \qquad (3\text{-}14)$$

3.3 References:

(1) Donabedian, D. H.; McCarthy, S. P. *Macromolecules* **1998**, *31*, 1032-1039.

(2) Samaranayake, G.; Glasser, W. G. *Carbohydrate Polymers* **1993**, *22*, 79-86.

(3) Rivera-Armentaa, J. L.; Heinze, T.; Mendoza-Mart ńez, A. M. *Eur. Polym. J* **2004**, *40*, 2803-2811.

(4) Toyama, S.; Aoki, K.; Kato, S. *Sens. Actuators, B* **2005**, *B108*, 903-909.

(5) Sigal, G. B.; Mrksich, M.; Whitesides, G. M. *Langmuir* **1997**, *13*, 2749-2755.

(6) De Feijter, J. A.; Benjamins, J.; Veer, F. A. *Biopolymers* **1978**, *17*, 1759-72.

(7) Harvey, A. H.; Gallagher, J. S.; Sengers, J. M. H. L. *J. Phys. Chem. Ref. Data* **1998**, *27*, 761-774.

(8) Malitson, I. H. *J. Opt. Soc. Am.* **1962**, *52*, 1377-9.

(9) Palik, E. D. *Handbook of Optical Constants of Solids;Academic Press: Orlando, FL*, **1985**.

(10) Kontturi, E.; Thune, P. C.; Niemantsverdriet, J. W. *Langmuir* **2003**, *19*, 5735-5741.

(11) Peterlinz, K. A.; Georgiadis, R. *Langmuir* **1996**, *12*, 4731-4740.

(12) Holmberg, M.; Berg, J.; Stemme, S.; Oedberg, L.; Rasmusson, J.; Claesson, P. *J. Colloid Interface Sci.* **1997**, *186*, 369-381.

(13) Sauerbrey, G. *Z. Phys.* **1959**, *155*, 206-22.

(14) Voinova, M. V.; Rodahl, M.; Jonson, M.; Kasemo, B. *Phys. Scr.* **1999**, *59*, 191-196.

CHAPTER 4

Quartz Crystal Microbalance with Dissipation Monitoring and Surface Plasmon Resonance Studies of Carboxymethyl Cellulose Adsorption onto Cellulose Surfaces

4.1 Abstract

Adsorption of anionic polyelectrolytes, sodium salts of carboxymethyl celluloses (CMC) with different degrees of substitution (DS = 0.9 and 1.2), from aqueous electrolyte solutions onto regenerated cellulose surfaces was studied through quartz crystal microbalance with dissipation monitoring (QCM-D) and surface plasmon resonance (SPR) experiments. The influence of both calcium chloride ($CaCl_2$) and sodium chloride (NaCl) on CMC adsorption was examined. QCM-D results demonstrated that $CaCl_2$ (divalent cation) caused significantly greater CMC adsorption onto regenerated cellulose surfaces than NaCl (monovalent cation) at the same ionic strength. The CMC layers adsorbed onto regenerated cellulose surfaces from $CaCl_2$ solutions exhibited greater stability upon exposure to flowing water than layers adsorbed from NaCl solutions. Both QCM-D and SPR results showed that CMC adsorption onto regenerated cellulose surfaces from $CaCl_2$ solutions increased with increasing $CaCl_2$ concentration up to the solubility limit (10 mM). Voigt-based viscoelastic modeling of the QCM-D data indicated that the CMC layers adsorbed onto regenerated cellulose surfaces had shear viscosities of $\eta_f \sim 10^{-3}$ N•s•m^{-2} and elastic shear moduli $\mu_f \sim 10^5$ N•m^{-2}. Furthermore, the combination of SPR and QCM-D showed that the CMC layers contained 90 to 95% water. Adsorption isotherms for CMCs in $CaCl_2$ solutions were also obtained from QCM-D and could be fit by Freundlich isotherms. This study demonstrated that CMC adsorption could be used for the

modification of cellulose.

4.2 Introduction

Adsorption of polyelectrolytes onto material surfaces has been identified as a promising method to create materials with tailored surface chemistry and greater hydrophilicity, adsorption capacity, and biocompatibility.[1] Likewise, bacterial cellulose (BC) has exhibited many excellent properties including high mechanical strength, high crystallinity, and strongly bound water, that have prompted studies of possible biomedical applications, such as artificial blood vessels for microsurgery and substrates for tissue engineering of cartilage.[2] However, the fabrication of materials with properties comparable to natural bone from BC requires negatively charged groups on the BC surface to enhance the heterogeneous nucleation of apatite. Carboxymethyl cellulose (CMC), a cheap polysaccharide derivative that has been widely used in paper making, food, and textile industries, can be used to introduce negative charge onto cellulose fiber surfaces.[3,4] While people believe a negatively charged layer could be formed on BC surfaces via self-assembly,[2] heterogeneity of BC surfaces has made it difficult to obtain fundamental information about CMC adsorption. In contrast, model cellulose surfaces have well-defined morphological and chemical characteristics.[5]

Polyelectrolyte adsorption onto solid surfaces has been quantitatively studied by quartz crystal microbalance with dissipation monitoring (QCM-D)[1,6-8] and surface plasmon resonance (SPR).[9] Both QCM-D and SPR are surface-sensitive techniques that have been used to investigate the adsorption of surfactants,[10] polysaccharides,[11] proteins,[12,13] and DNA[14] at liquid/solid interfaces. Adsorption of cationically modified starches onto cellulose surfaces has been studied via QCM-D by Kontturi et al.[1] Modeling of QCM-D

results provided the mass and viscoelastic properties of adsorbed layers.[15] Furthermore, the combination of QCM-D and SPR facilitated the determination of coupled water for hydrated layers.[10]

In this study, the adsorption of anionic polyelectrolytes, sodium salts of CMC, with different degrees of substitution (DS) per anhydroglucose unit (AGU) onto model cellulose surfaces from aqueous electrolyte solutions was studied. The model cellulose surfaces were regenerated by hydrolyzing spincoated trimethylsilylcellulose (TMSC) films. The influence of both calcium chloride ($CaCl_2$) and sodium chloride (NaCl) on CMC adsorption was examined. The coupled water and viscoelastic properties of CMC layers were determined by the combination of QCM-D and SPR studies and Voigt-based viscoelastic modeling of QCM-D data. Understanding how different salts affect CMC adsorption to create stable functional layers on cellulose surfaces was the focus of this work.

4.3 Experimental

Sodium salts of carboxymethyl celluloses (CMC, weight average molar mass of M_w ~ 250,000 g•mol^{-1}, DS = 0.9 and 1.2 carboxymethyl groups per AGU) were purchased from Aldrich and were used without further purification, as was calcium chloride ($CaCl_2$, 99.9%). Sodium chloride (NaCl, 99.9%) was purchased from Mallinckrodt Baker, Inc. Procedures for the preparation of regenerated cellulose films, refractive index increment measurements (dn/dc) for CMC solutions, SPR measurements, and QCM-D measurements were described in Chapter 3.2.1.1, 3.2.6, 3.2.9, and 3.2.10, respectively. The (dn/dc) values of CMC solutions in aqueous $CaCl_2$ and NaCl are summarized in **Table 4.1**.

Table 4.1. (dn/dc) of CMC in $CaCl_2$ and NaCl solutions

Polymer	[$CaCl_2$] (mM)	(dn/dc)[a] (mL•g^{-1})	[NaCl] (mM)	(dn/dc)[a] (mL•g^{-1})
CMC09	5	0.147 ± 0.002	15	0.149 ± 0.007
(DS = 0.9)	10	0.137 ± 0.003	30	0.153 ± 0.003
CMC12	5	0.145 ± 0.003	15	0.147 ± 0.006
(DS = 1.2)	10	0.142 ± 0.006	30	0.145 ± 0.004

[a]Measured with a differential refractometer in water at λ = 690 nm at 20 °C.

4.4 Results and Discussion

4.4.1 Characterization of Cellulose Films

A representative surface morphology for regenerated cellulose films on SPR and QCM-D sensors has been provided as **Figure 4.1**. The root-mean-square (rms) roughness of the regenerated cellulose surfaces was determined from 1 μm × 1 μm atomic force microscopy (AFM) images and was approximately 1.5 nm. The thicknesses of the regenerated cellulose surfaces were determined via QCM-D and ellipsometry. Mass changes per unit area (Δm) for regenerated cellulose films were calculated from the Sauerbrey equation (Equation 3-13).The Δm values in air were converted to thicknesses (*h*), assuming the density of the "dry" regenerated cellulose was 1583 kg•m^{-3}.[16] The thicknesses of regenerated cellulose films were also determined via ellipsometry measurements. These results are consistent and are summarized in **Table 4.2**. If the dissipation change (ΔD) caused by the coated film is less than 2×10^{-6}, the film could be treated as a rigid film.[17] The ΔD of quartz crystals covered by regenerated cellulose films was less than 2×10^{-6} in both air and water, indicating that regenerated cellulose films were rigid enough to be treated as an extension of quartz crystals in both air and water. Comparison of Δm obtained from measurements in air and water indicated that regenerated cellulose films swelled slightly. A percentage swelling ratio of ~19% was calculated from

$$\text{Percentage Swelling Ratio} = [(\Delta m_{water} - \Delta m_{air})/\Delta m_{air}] \times 100 \quad (4\text{-}1)$$

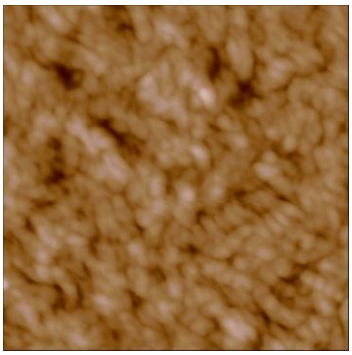

Figure 4.1. A representative AFM height image of a regenerated cellulose surface. The image is 1 μm × 1 μm and has a Z-axis scale of 0 to 10 nm.

Table 4.2. (Δf/n), ΔD, Δm, and h of regenerated cellulose films on QCM-D sensors[a]

	Air	Water
(Δf/n) (Hz)	-185 ± 7	-217 ± 8
$\Delta D \times 10^6$	2.3 ± 0.1	1.9 ± 0.2
Δm (mg•m^{-2})	32 ± 1	38 ± 1
h (nm) [b]	20.2 ± 0.6	-
h_e (nm) [c]	18.1 ± 0.4	-

[a](Δf/n) and ΔD were from the 3rd overtone.
[b]The density of the dry cellulose was assumed to be 1583 kg•m^{-3}.[16]
[c] Thickness determined by ellipsometry assuming n = 1.50.

4.4.2 CMC Adsorption onto Cellulose Surfaces from $CaCl_2$ and NaCl Solutions by QCM-D

Representative raw QCM-D data for the adsorption of CMC09 (CMC with DS = 0.9) from water with different concentrations onto regenerated cellulose surfaces were provided in **Figure 4.2A**. As seen in **Figure 4.2A**, there was no significant scaled frequency change (Δf/n). Changes in the dissipation (ΔD) occurred when CMC solutions flowed over regenerated cellulose surfaces, however, ΔD returned to zero after switching back to water.

This result meant that adsorption, if any, in the presence of CMC solution was reversible and that ΔD likely reflected a change in the viscosity of the solution rather than reversible adsorption. CMC12 (CMC with DS = 1.2) did not adsorb from water onto regenerated cellulose surfaces as seen in **Figure 4.2B**.

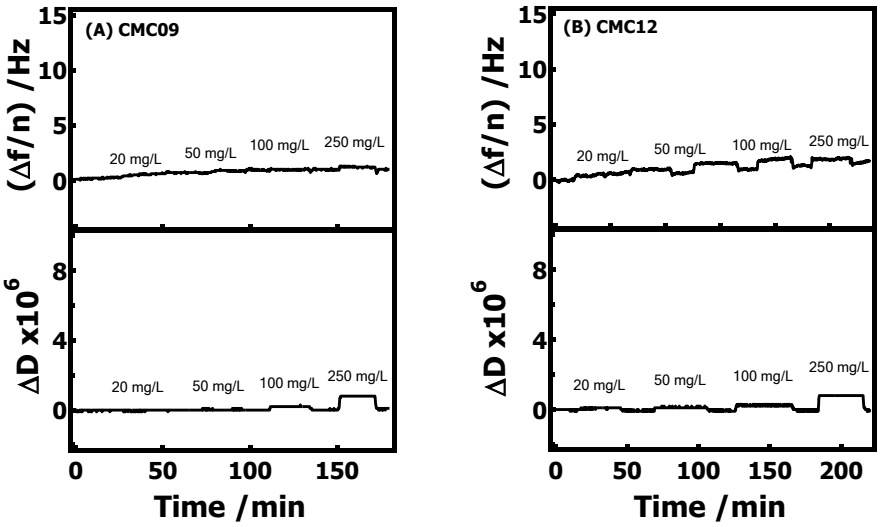

Figure 4.2. (Δf/n) and ΔD from QCM-D for regenerated cellulose surfaces exposed to (A) CMC09 (DS = 0.9) and (B) CMC12 (DS = 1.2) in water. CMC concentrations are indicated on the graphs. Curves correspond to the 3rd overtone.

In contrast, representative raw QCM-D data in **Figure 4.3** show CMC09 adsorption onto regenerated cellulose surfaces from $CaCl_2$ and NaCl solutions, respectively. After the introduction of 250 mg•L^{-1} CMC09 solution with electrolytes ($CaCl_2$ and NaCl) CMC adsorption onto regenerated cellulose equilibrated in ~ 1.5 hours. Then pure electrolyte solutions and water were flowed sequentially over adsorbed CMC layers. (Δf/n) values indicated that both $CaCl_2$ and NaCl promoted adsorption, and the failure of the (Δf/n) values to return to zero after switching back to pure electrolyte solutions indicated that

some irreversible adsorption had occurred. The observation of $\Delta D > \sim 4\times10^{-6}$ meant that CMC09 formed relatively soft layers. Moreover, **Figure 4.3** shows that CMC09 adsorption from $CaCl_2$ solutions was significantly greater than CMC09 adsorption from NaCl solutions at the same ionic strength (I). Another key difference was that CMC09 adsorption from $CaCl_2$ solutions increased as the $[CaCl_2]$ increased from 5 to 10 mM, whereas CMC09 adsorption from NaCl solutions was essentially independent of [NaCl].

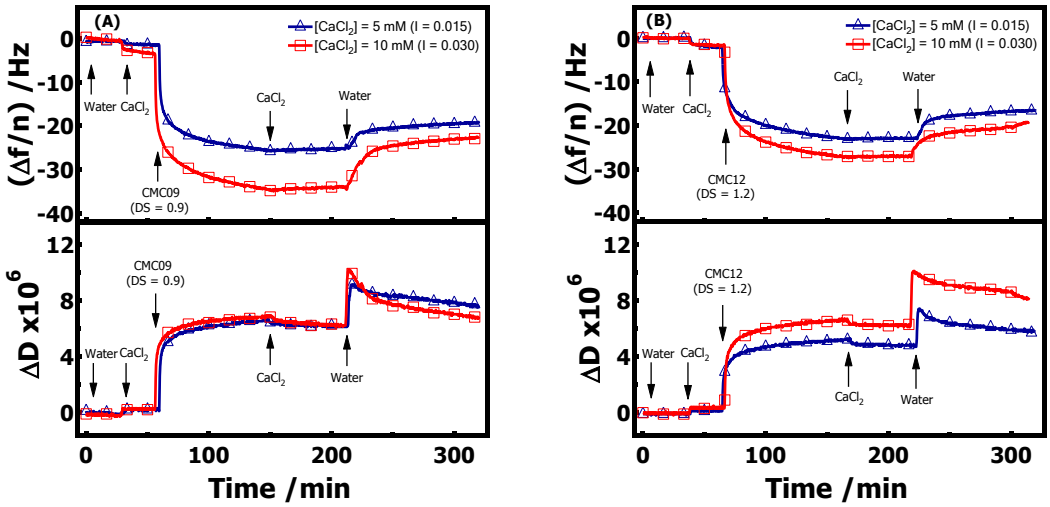

Figure 4.3. Representative (Δf/n) and ΔD versus time plots for QCM-D studies of regenerated cellulose surfaces exposed to 250 mg•L^{-1} (A) CMC09 and (B) CMC12 solutions with added $CaCl_2$. Curves with markers correspond to the 3rd overtone. Arrows indicate where solutions were switched.

There were no significant qualitative differences between CMC adsorption data for the DS = 0.9 and 1.2 samples (**Figure 4.4**). (Δf/n) and ΔD for CMC09 and CMC12 layers after adsorption equilibrium occurred are summarized in **Table 4.3**. (Δf/n) values for CMC layers adsorbed from $CaCl_2$ solutions were approximately twice those for NaCl solutions.

ΔD values for CMC layers adsorbed from $CaCl_2$ solutions were also greater than those observed for NaCl solutions.

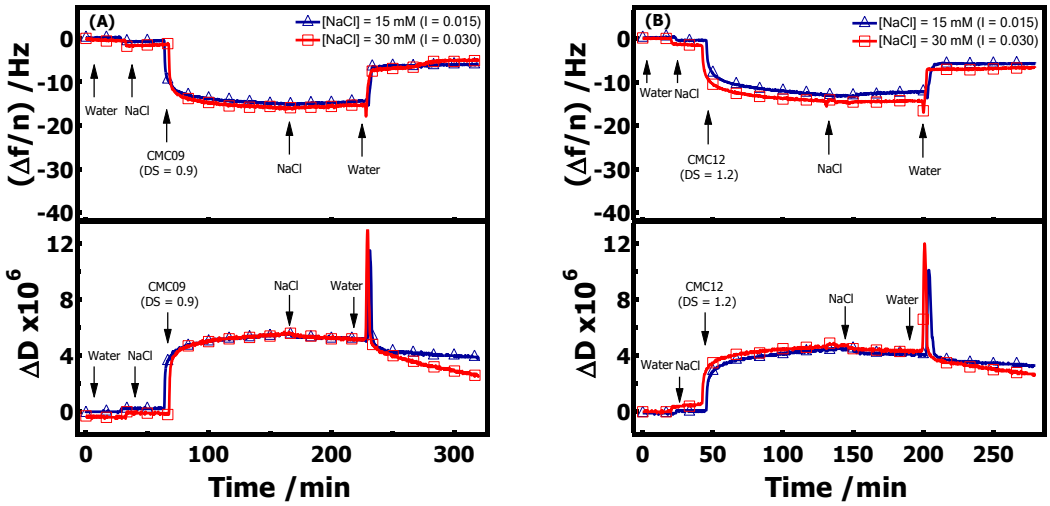

Figure 4.4. Representative (Δf/n) and ΔD versus time plots for QCM-D studies of regenerated cellulose surfaces exposed to 250 mg•L^{-1} (A) CMC09 and (B) CMC12 solutions with added NaCl. Curves with markers correspond to the 3rd overtone. Arrows indicate where solutions were switched.

Table 4.3. (Δf/n) and ΔD for CMC adsorbed from $CaCl_2$ and NaCl solutions[a]

		CMC09 (DS = 0.9)		CMC12 (DS = 1.2)	
[$CaCl_2$] (mM)	I	(Δf/n) (Hz)	ΔD×10^6	(Δf/n) (Hz)	ΔD×10^6
5	0.015	-25.2 ±0.5	6.4 ±0.1	-22.9 ±0.4	5.5 ±0.3
10	0.030	-34.5 ±0.2	7.0 ±0.2	-27.8 ±1.0	6.7 ±0.2
[NaCl] (mM)					
15	0.015	-13.7 ±1.1	5.1 ±0.3	-12.4 ±1.8	4.5 ±0.1
30	0.030	-16.3 ±1.9	5.0 ±0.5	-15.2 ±1.7	4.7 ±0.3

[a]Data for equilibrium adsorption from 250 mg•L^{-1} CMC solutions (n = 3) ± one standard deviation.

CMC adsorbed onto regenerated cellulose surfaces from $CaCl_2$ and NaCl solutions formed stable layers. However, when pure water was flowed over the CMC layers, CMC layers adsorbed from $CaCl_2$ solutions were more stable than those formed from NaCl

solutions. (Δf/n) for CMC layers adsorbed from $CaCl_2$ solutions increased but did not return to zero as water flowed over the surface, while ΔD values increased. These observations indicated that CMC layers adsorbed from $CaCl_2$ solutions became softer, but remained on the regenerated cellulose surfaces. CMC layers formed from NaCl solutions showed different behavior after exposure to flowing water. (Δf/n) for CMC layers formed from NaCl solutions almost returned to zero, while ΔD values decreased. Hence, water removed most of the CMC layers adsorbed from NaCl solutions (**Table 4.4**).

Table 4.4. (Δf/n) and ΔD for adsorbed CMC layers after exposure to water[a]

		CMC09 (DS = 0.9)		CMC12 (DS = 1.2)	
[$CaCl_2$] (mM)	I	(Δf/n) (Hz)	$\Delta D \times 10^6$	(Δf/n) (Hz)	$\Delta D \times 10^6$
5	0.015	-19.2 ± 1.2	8.1 ± 0.1	-17.3 ± 1.0	6.3 ± 0.6
10	0.030	-22.6 ± 0.1	7.1 ± 0.3	-21.7 ± 1.1	8.8 ± 0.3
[NaCl] (mM)					
15	0.015	-4.5 ± 1.1	3.1 ± 0.5	-4.9 ± 0.7	3.2 ± 0.1
30	0.030	-6.1 ± 1.7	1.9 ± 0.9	-6.6 ± 1.7	2.2 ± 0.4

[a]Data for adsorption from 250 mg•L^{-1} CMC solutions (n = 3) ± one standard deviation.

4.4.3 CMC Adsorption onto Cellulose Surfaces from $CaCl_2$ and NaCl Solutions by SPR

CMC adsorption onto regenerated cellulose surfaces was also studied by SPR. Representative raw SPR data for CMC09 and CMC12 adsorption onto regenerated cellulose surfaces from water are provided in **Figure 4.5**. For both CMC09 and CMC12, SPR angles only increased by ~0.004 ° when regenerated cellulose was exposed to an aqueous 250 mg•L^{-1} CMC09 or CMC12 solution, respectively, and returned to the baseline after a water rinse. The SPR angle change probably resulted from the higher refractive index of the CMC solution compared to pure water. SPR angle changes due to CMC09 and CMC12 adsorption onto regenerated cellulose surfaces from $CaCl_2$ solutions are provided

in **Figure 4.6**, respectively. SPR angles increased after CMC09 or CMC12 in a $CaCl_2$ solution was flowed over the sensors and did not return to the baseline after CMC-free $CaCl_2$ solutions were flowed over the sensors. SPR angles also increased due to CMC09 and CMC12 adsorption onto regenerated cellulose surfaces from NaCl solutions (**Figure 4.7**). Hence, salt enhanced CMC adsorption onto the regenerated cellulose surfaces. SPR results also showed that the amount of CMC adsorbed from $CaCl_2$ solution was significantly greater than the amount adsorbed from NaCl solutions at the same ionic strength. Furthermore, CMC adsorption increased when [$CaCl_2$] increased from 5 to 10 mM. However, an increase of the [NaCl] from 15 to 30 mM did not enhance adsorption. SPR angle changes for CMC layers after adsorption equilibrium are summarized in **Table 4.5**.

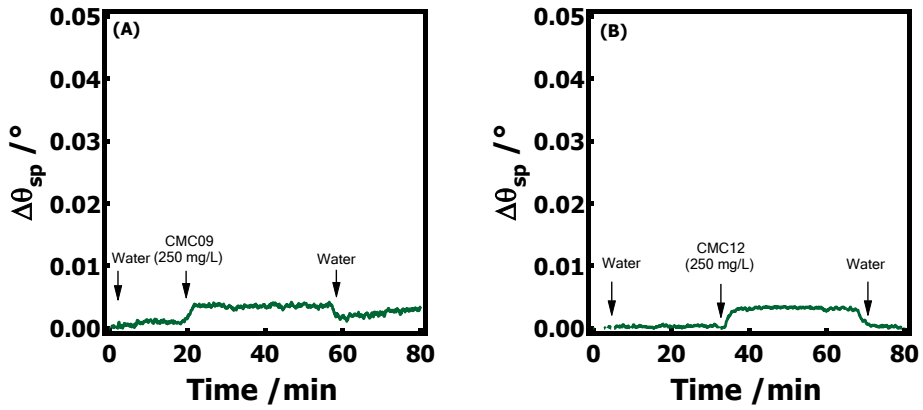

Figure 4.5. $\Delta\theta_{sp}$ versus time for SPR studies of regenerated cellulose surfaces exposed to 250 mg•L^{-1} aqueous (A) CMC09 and (B) CMC12 solutions. Arrows indicate where solutions were switched.

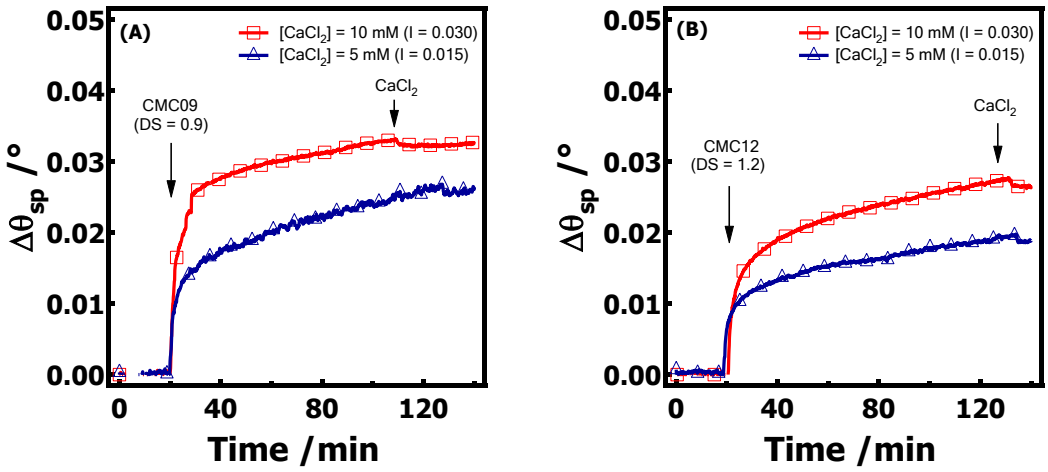

Figure 4.6. $\Delta\theta_{sp}$ versus time for SPR studies of regenerated cellulose surfaces exposed to 250 mg•L^{-1} (A) CMC09 and (B) CMC12 solutions with added $CaCl_2$. Arrows indicate where solutions were switched.

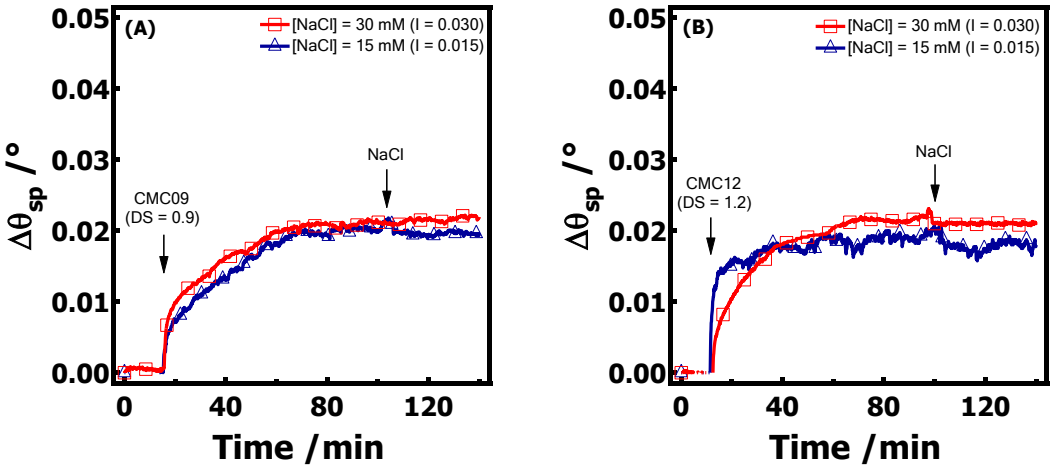

Figure 4.7. $\Delta\theta_{sp}$ versus time for SPR studies of regenerated cellulose surfaces exposed to 250 mg•L^{-1} (A) CMC09 and (B) CMC12 solutions with added NaCl. Arrows indicate where solutions were switched.

Table 4.5. $\Delta\theta_{sp}$ for CMC adsorbed from $CaCl_2$ and NaCl solutions at equilibrium[a]

	CMC09 (DS = 0.9)		CMC12 (DS = 1.2)	
[$CaCl_2$] (mM)	5	10	5	10
I	0.015	0.030	0.015	0.030
$\Delta\theta_{sp}$ (°)	0.035 ± 0.002	0.029 ± 0.002	0.031 ± 0.004	0.023 ± 0.003
[NaCl] (mM)	15	30	15	30
I	0.015	0.030	0.015	0.030
$\Delta\theta_{sp}$ (°)	0.020 ± 0.001	0.021 ± 0.001	0.019 ± 0.001	0.020 ± 0.002

[a]Data for adsorption from 250 mg•L^{-1} CMC solutions ± one standard deviation.

4.4.4 Viscoelastic Modeling of QCM-D Data

For the case of CMC adsorbed from electrolyte solutions onto regenerated cellulose surfaces, the layer was strongly dissipative ($\Delta D > 4\times10^{-6}$). For such layers, the Sauerbrey equation is invalid for the calculation of the mass of the adsorbed layer. Hence, CMC adsorption curves were fit with a Voigt-based viscoelastic model and the masses of the adsorbed layers were obtained. The CMC layers were treated as a homogeneous layer between the QCM-D sensor (quartz plus cellulose) and a semi-infinite Newtonian liquid layer under no-slip boundary conditions. The adsorbed film was represented by four parameters: a thickness (h_f,), density (ρ_f), shear viscosity (η_f), and elastic shear modulus (μ_f). The density and viscosity of water (ρ_0 = 1000 kg•gm^{-3} and η_0 = 1×10^{-3} N•s•m^{-2}, respectively) were used for all of the bulk liquids, because the effects of dissolved electrolytes and CMC on the values of ρ_0 and η_0 were small and could be ignored. Normally, Δf and ΔD from the first overtone were noisy because of insufficient energy trapping.[18] Thus, the adsorption curves from multiple odd overtones (n = 3 through 13) were used for the estimation of h_f, η_f, and μ_f. The experimental data for CMC09 layers adsorbed from a 5 mM $CaCl_2$ solution and the best fits using the Voigt-based viscoelastic model are provided in **Figure 4.8A** (curves with n = 3, 5, and 7) and **Figure 4.8B** (curves

with n = 9, 11, and 13). Time-dependent viscosities (**Figure 4.9A**), shear moduli (**Figure 4.9B**), and effective thicknesses (**Figure 4.9C**) correspond to the best-fit curves in **Figure 4.8**.

The adsorption curves with lower frequency (n = 3, 5, and 7) and higher frequency (n = 9, 11, and 13) were fit by the Voigt-based viscoelastic model, respectively (**Figure 4.8**). These two cases provided an estimate of the frequency dependence of thickness and viscoelastic parameters. The results showed that the thicknesses and the surface concentrations (Γ_{QCM}) from lower frequency data were greater than those values from higher frequency data, whereas the shear moduli from lower frequency data were smaller than values from higher frequency data. This difference was attributed to a decrease of the penetration depth of the acoustic shear wave with increasing frequency.[19,20] The effect of frequency on the viscosity was very small. Hook et al.[12] and Larsson et al.[12] have observed similar frequency effects on the viscoelastic parameters of adsorbed protein layers on solid surfaces. Γ_{QCM} for CMC09 layers from 5 mM $CaCl_2$ solutions remained constant when the ρ_f of the CMC layer for modeling varied between 1000 and 1500 kg•m^{-3} (**Figure 4.10**). The viscoelastic model fit all CMC adsorption curves well and parameters deduced with high and low frequency data showed the same trends (**Figures 4.9** and **4.10**).

As Γ_{QCM} was unaffected by ρ_f, ρ_f = 1100 kg•m^{-3} was initially used for the calculation of the effective thickness. Then the hydrodynamic surface concentrations (Γ_{QCM}) were calculated from Equation 3-14. In this work, results from viscoelastic modeling of adsorption curves obtained from both lower frequency data (n = 3, 5, and 7) and higher frequency data (n = 9, 11, and 13) were used for comparisons with SPR results.

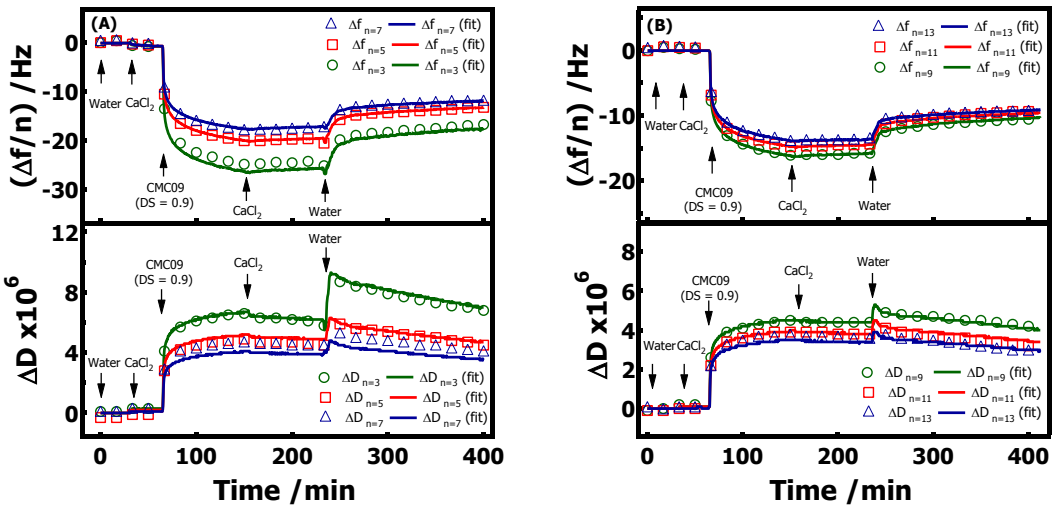

Figure 4.8. QCM-D studies of adsorption of 250 mg•L^{-1} 5 mM $CaCl_2$ CMC09 solutions onto a regenerated cellulose surface: (A) (Δf/n) and ΔD versus time for (○) n = 3, (□) n = 5, and (Δ) n = 7 and the best fits obtained using Voigt-based viscoelastic modeling (solid lines), and (B) (Δf/n) and ΔD versus time for (○) n = 9, (□) n = 11, and (Δ) n = 13 and the best fits obtained using Voigt-based viscoelastic modeling (solid lines).

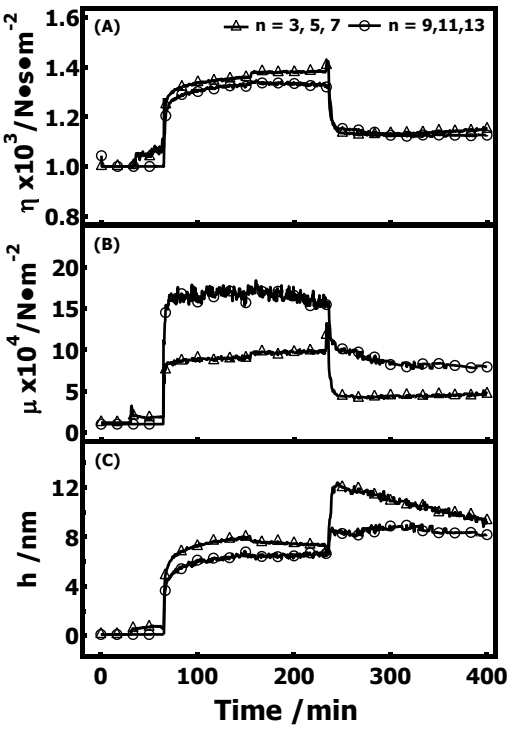

Figure 4.9. Time dependent evolution of changes in parameters associated with the Voigt-based viscoelastic modeling of the data in Figure 4.8 for CMC adsorption from 250 mg•L^{-1} CMC09 aqueous solutions onto a regenerated cellulose surface: (A) viscosity versus time from, (B) elastic shear modulus versus time, and (C) effective thickness versus time.

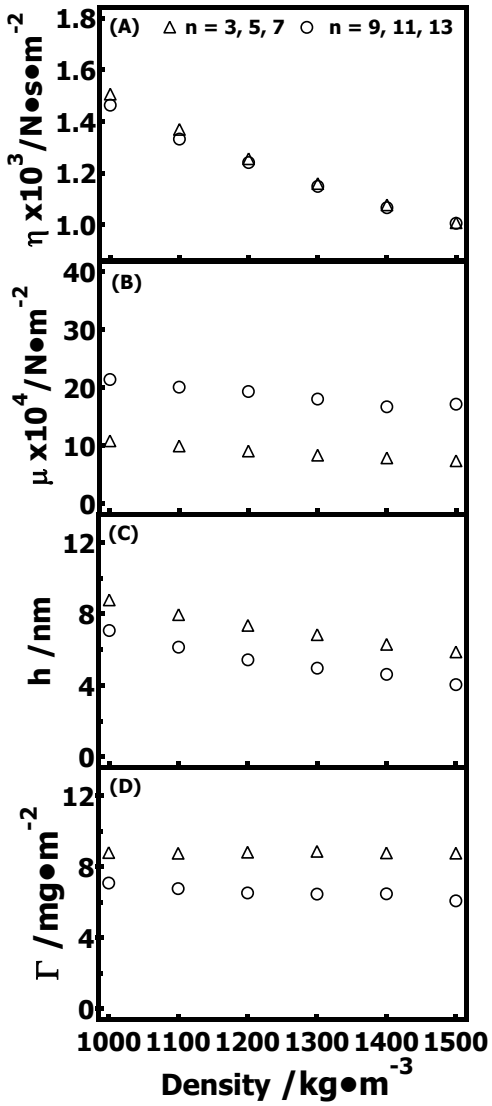

Figure 4.10. (A) Shear viscosity, (B) elastic shear modulus, (C) thickness, and (D) surface concentration versus density used for viscoelastic modeling of a CMC09 layer adsorbed onto a regenerated cellulose surface from a 250 mg•L^{-1} solution with 5 mM $CaCl_2$. Symbols correspond to fitting curves using overtones (Δ) n = 3, 5, and 7 and (○) n = 9, 11, and 13.

4.4.5 Densities of CMC Layers

In this study, SPR was used for the determination of the optical surface concentration (Γ_{SPR}) of CMC layers adsorbed from electrolyte solutions onto regenerated cellulose surfaces (analysis of SPR data was described in Chapter 3.2.9.1). The combination of SPR and QCM-D yielded different surface concentrations for the same adsorption process. Surface concentrations from QCM-D measurements were significantly greater than those from SPR measurements. The surface concentration from QCM-D modeling corresponded to the total mass of the layer, and included both CMC chains and coupled water, while the surface concentration from SPR quantified the dry mass of the layer (CMC chains without water). Hence, the amount of water coupled to the CMC layers could be deduced from the QCM-D and SPR results. In both $CaCl_2$ and NaCl solutions, CMCs (DS = 0.9 and 1.2) formed highly hydrated layers on regenerated cellulose surfaces that were independent of the surface concentrations of the CMC layers. The calculated water percentage from lower frequency data (n = 3, 5, and 7) and SPR results was ~ 94%, while the values from higher frequency data (n = 9, 11, and 13) was ~ 92%. CMC layers showed a similar level of hydration to adsorbed protein layers.[21] Moreover, the density of the CMC layer was calculated from:[14]

$$\rho = \frac{\Gamma_{QCM}}{\frac{\Gamma_{SPR}}{\rho_{CMC}} + \frac{\Gamma_{QCM} - \Gamma_{SPR}}{\rho_{Water}}} \qquad (4\text{-}2)$$

where the density of water ρ_{water} = 1000 kg•m^{-3} and the density of CMC ρ_{CMC} = 1590 kg•m^{-3} were bulk values. The surface concentration values, the percentage amounts of coupled water, and the densities of CMC layers are summarized in **Tables 4.6** and **4.7**.

Table 4.6. Properties of CMC layers adsorbed from $CaCl_2$ solutions onto regenerated cellulose surfaces[a]

		CMC09 (DS = 0.9)		CMC12 (DS = 1.2)	
[$CaCl_2$] (mM)		5	10	5	10
I		0.015	0.030	0.015	0.030
Γ_{SPR} (mg•m^{-2})		0.52 ±0.05	0.68 ±0.03	0.47 ±0.05	0.60 ±0.05
Γ_{QCM} (mg•m^{-2})	n = 3, 5, 7	8.6 ±0.1	10.8 ±0.3	7.6 ±0.1	10.0 ±0.3
	n = 9, 11, 13	6.6 ±0.3	7.7 ±0.2	6.4 ±0.3	7.4 ±0.3
% H_2O in film	n = 3, 5, 7	94 ±1	94 ±1	94 ±1	94 ±1
	n = 9, 11, 13	92 ±1	91 ±1	93 ±1	92 ±1
ρ (kg•m^{-3})	n = 3, 5, 7	1023 ±2	1024 ±1	1023 ±3	1023 ±2
	n = 9, 11, 13	1030 ±3	1034 ±2	1028 ±3	1031 ±3

[a]Averages of three measurements ± one standard deviation.

Table 4.7. Properties of CMC layers adsorbed from NaCl solutions onto regenerated cellulose surfaces[a]

		CMC09 (DS = 0.9)		CMC12 (DS = 1.2)	
[NaCl] (mM)		15	30	15	30
I		0.015	0.030	0.015	0.030
Γ_{SPR} (mg•m^{-2})		0.34 ±0.01	0.35 ±0.02	0.33 ±0.01	0.35 ±0.03
Γ_{QCM} (mg•m^{-2})	n =3, 5, 7	6.6 ±0.4	5.8 ±0.3	6.1 ±0.9	5.8 ±0.4
	n = 9, 11, 13	4.1 ±0.1	4.3 ±0.3	3.3 ±0.3	4.1 ±0.3
% H_2O in film	n =3, 5, 7	95 ±1	94 ±1	95 ±1	94 ±1
	n = 9, 11, 13	92 ±1	92 ±1	90 ±1	91 ±1
ρ (kg•m^{-3})	n =3, 5, 7	1019 ±1	1023 ±2	1020 ±3	1023 ±3
	n = 9, 11, 13	1031 ±1	1031 ±3	1039 ±4	1033 ±4

[a]Averages of three measurements ± one standard deviation.

4.4.6 Viscoelastic Properties of CMC Layers

Film densities in **Tables 4.6** and **4.7** were used for final viscoelastic modeling of QCM-D data and the estimation of the thickness and viscoelastic parameters of the CMC layers. The deduced viscoelastic parameters for CMC layers adsorbed from $CaCl_2$ solutions and NaCl solutions were summarized in **Tables 4.8** and **4.9**, respectively. Surface concentrations of CMC layers adsorbed from $CaCl_2$ solutions were significantly greater than those from NaCl solutions at the same ionic strength and surface concentration increased with $CaCl_2$ concentration. The viscosities of CMC layers adsorbed from $CaCl_2$

and NaCl solutions were in the ranges of 1.3 $\times 10^{-3}$ to 1.5 $\times 10^{-3}$ N•s•m^{-2} and 1.1 $\times 10^{-3}$ to 1.3 $\times 10^{-3}$ N•s•m^{-2}, respectively, and were independent on the frequency. However, the elastic shear moduli of the adsorbed CMC layers were dependent on the frequency. The elastic shear moduli of the CMC layers from $CaCl_2$ solutions were in the ranges of 9.6 $\times 10^4$ to 11.6 $\times 10^4$ N•m^{-2} (n = 3, 5, and 7) and 19.7 $\times 10^4$ to 29.9 $\times 10^4$ N•m^{-2} (n = 9, 11, and 13), respectively, while the elastic shear moduli of CMC layers from NaCl solutions were in the ranges of and 5.6 $\times 10^4$ to 9.8 $\times 10^4$ N•m^{-2} (n = 3, 5, and 7) and 17.3 $\times 10^4$ to 20.7 $\times 10^4$ N•m^{-2} (n = 9, 11, and 13), respectively. The large amounts of water coupled in the layers mean CMC layers showed relatively low viscosities and elastic shear moduli that were much lower than bulk CMC.

Table 4.8. Viscoelastic properties of CMC layers adsorbed from $CaCl_2$ solutions onto regenerated cellulose[a]

		CMC09 (DS = 0.9)		CMC12 (DS = 1.2)	
[$CaCl_2$] (mM)		5	10	5	10
I		0.015	0.030	0.015	0.030
n = 3, 5, 7	$\eta_f \times 10^3$ (N•s•m^{-2})	1.37 ± 0.02	1.54 ± 0.06	1.42 ± 0.03	1.43 ± 0.05
	$\mu_f \times 10^{-4}$ (N•m^{-2})	9.6 ± 0.5	11.6 ± 0.4	9.3 ± 0.5	9.6 ± 0.9
	h_f (nm)	8.4 ± 0.1	10.5 ± 0.3	7.4 ± 0.1	9.9 ± 0.3
	Γ_{QCM}[b] (mg•m^{-2})	8.6 ± 0.1	10.8 ± 0.3	7.6 ± 0.1	10.0 ± 0.3
n = 9, 11, 13	$\eta_f \times 10^3$ (N•s•m^{-2})	1.36 ± 0.04	1.52 ±0.09	1.49 ± 0.02	1.46 ± 0.06
	$\mu_f \times 10^{-4}$ (N•m^{-2})	19.7 ± 4.0	29.9 ± 1.2	26.8 ± 6.3	27.3 ± 3.8
	h_f (nm)	6.4 ± 0.3	7.4 ± 0.4	6.2 ± 0.2	7.1 ± 0.1
	Γ_{QCM} (mg•m^{-2})	6.6 ± 0.3	7.7 ± 0.2	6.4 ± 0.3	7.4 ± 0.1

[a]Averages of three measurements ± one standard deviation.

After CMC adsorption reached a steady state in $CaCl_2$ and NaCl solutions, ultrapure water was flowed over the adsorbed CMC layers. ($\Delta f/n$) values (**Table 4.4**) showed that adsorbed CMC layers formed from $CaCl_2$ solutions were more stable in water than those formed from NaCl solutions. Viscoelastic modeling of QCM-D data, allowed the swelling of CMC/Ca^{2+} complex layers in water to be studied. The viscoelastic parameters for the

CMC/Ca^{2+} layers after water was flowed over the sensor are summarized in **Table 4.10**. The results showed that masses of CMC/Ca^{2+} layers increased 20-40% compared to the original layers, and viscosities and moduli of the CMC/Ca^{2+} layers decreased by ~20% and ~60%, respectively. These values indicated that CMC/Ca^{2+} layers were stable on regenerated cellulose, and became softer as they swelled with water.

Table 4.9. Viscoelastic properties of CMC layers adsorbed from NaCl solutions onto regenerated cellulose[a]

		CMC09 (DS = 0.9)		CMC12 (DS = 1.2)	
[NaCl] (mM)		5	10	5	10
I		0.015	0.030	0.015	0.030
n = 3, 5, 7	$\eta_f \times 10^3$ (N•s•m^{-2})	1.15 ±0.01	1.22 ±0.07	1.16 ±0.02	1.31 ±0.10
	$\mu_f \times 10^{-4}$ (N•m^{-2})	5.6 ±0.5	9.8 ±0.7	6.3 ±1.0	9.6 ±0.4
	h_f (nm)	6.5 ±0.4	5.7 ±0.3	6.0 ±0.8	5.7 ±0.4
	Γ_{QCM}[b] (mg•m^{-2})	6.6 ±0.4	5.8 ±0.3	6.1 ±0.9	5.8 ±0.4
n = 9, 11, 13	$\eta_f \times 10^3$ (N•s•m^{-2})	1.17 ±0.01	1.15 ±0.06	1.15 ±0.06	1.25 ±0.08
	$\mu_f \times 10^{-4}$ (N•m^{-2})	17.4 ±1.1	17.3 ±1.8	20.2 ±2.1	20.7 ±0.9
	h_f (nm)	3.9 ±0.1	4.2 ±0.3	3.2 ±0.3	3.9 ±0.3
	Γ_{QCM}[b] (mg•m^{-2})	4.1 ±0.1	4.3 ±0.3	3.3 ±0.3	4.1 ±0.3

[a]Averages of three measurements ± one standard deviation.

Table 4.10. Viscoelastic properties of CMC layers adsorbed onto regenerated cellulose and swelled by water[a]

	CMC09 (DS = 0.9)		CMC12 (DS = 1.2)	
[$CaCl_2$] (mM)	5	10	5	10
I	0.015	0.030	0.015	0.030
$\eta_f \times 10^3$ (N•s•m^{-2})	1.16 ±0.01	1.22 ±0.07	1.18 ±0.01	1.15 ±0.03
$\mu_f \times 10^{-4}$ (N•m^{-2})	4.8 ±0.3	4.6 ±0.2	4.2 ±0.4	3.8 ±0.4
h_f (nm)	10.2 ±0.3	12.0 ±0.3	10.0 ±0.8	14.4 ±0.7
Γ_{QCM} (mg•m^{-2})[b]	10.5 ±0.3	12.3 ±0.3	10.2 ±0.8	14.7 ±0.7

[a]Averages of three measurements ± one standard deviation.
[b]Results from viscoelastic modeling of adsorption curves with n = 3, 5, and 7. The density of CMC layer used for modeling is 1023 kg•m^{-3}.

4.4.7 CMC Adsorption Isotherms onto Cellulose Surfaces from $CaCl_2$ Solutions by QCM-D

Adsorption isotherms for CMC (DS = 0.9 and 1.2) adsorption onto regenerated cellulose from $CaCl_2$ solutions were obtained from QCM-D experiments. Values of the adsorbed surface excess or surface concentration were deduced from Voigt-based viscoelastic modeling of raw QCM-D data (representative fitting curves are provided in **Figure 4.11**).

Different theoretical models to describe adsorption have been widely reported. In this study, the Langmuir and Freundlich adsorption isotherms as models for the adsorption of CMC onto regenerated cellulose surfaces were tested. The Langmuir adsorption isotherm can be written as:

$$\Gamma = \frac{\Gamma_m K_L C}{1 + K_L C} \Rightarrow \frac{1}{\Gamma} = \frac{1}{\Gamma_m} + \left(\frac{1}{\Gamma_m K_L} \right) \frac{1}{C} \qquad (4\text{-}3)$$

where K_L is the Langmuir constant, C is the bulk concentration of the adsorbate, and Γ_m is the maximum surface concentration at infinite bulk concentration.[22] The empirical Freundlich isotherm was also employed to fit the experimental data and can be expressed as

$$\Gamma = K_F C^{(1/n_F)} \Rightarrow \ln \Gamma = \ln K_F + (1/n_F) \ln C \qquad (4\text{-}4)$$

where K_F is the adsorbent capacity, and $1/n_F$ is the adsorption affinity constant. Fitting parameters for both approaches are summarized in **Table 4.11**. Γ_m increased with increasing [$CaCl_2$] for both CMC09 and CMC12 and failed to plateau. For Freundlich isotherm fitting results, K_F increased as [$CaCl_2$] increased for both CMC09 and CMC12. In contrast, $1/n_F$ was relatively independent of ionic strength and was on the order of 0.2.

Overall, there were no significant differences between CMC09 and CMC12 adsorbed onto the regenerated cellulose surfaces at comparable [CMC] and [$CaCl_2$]. One of the key assumptions of the Langmuir model is that adsorption occurs on a homogeneous surface, while the Freundlich isotherm is empirically used to describe the adsorption on heterogeneous surfaces. As seen in **Figure 4.12**, Freundlich isotherms fit the experimental isotherms better than Langmuir models, which is consistent with the heterogeneity of the regenerated cellulose surface.

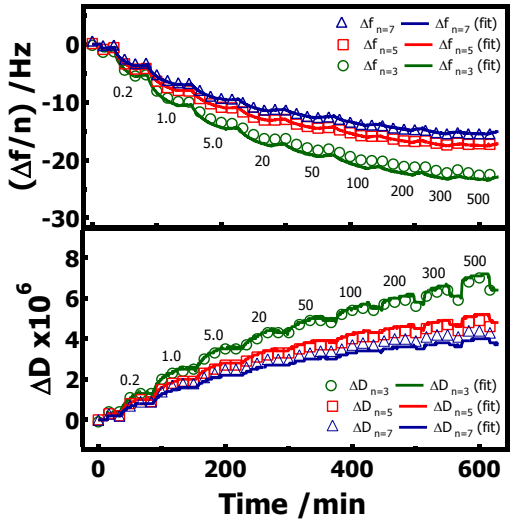

Figure 4.11. Representative Voigt-based viscoelastic modeling of QCM-D data for CMC09 adsorption onto a regenerated cellulose surface from 5 mM $CaCl_2$ solutions at 20.0 ℃. (Δf/n) and ΔD versus time for (○) n = 3, (□) n = 5, and (Δ) n = 7 and the best fits (solid lines). Solution concentrations in units of mg•L^{-1} correspond to the numbers on the graph. Pure $CaCl_2$ solution was flowed over the regenerated cellulose surface before and after each new adsorbate solution.

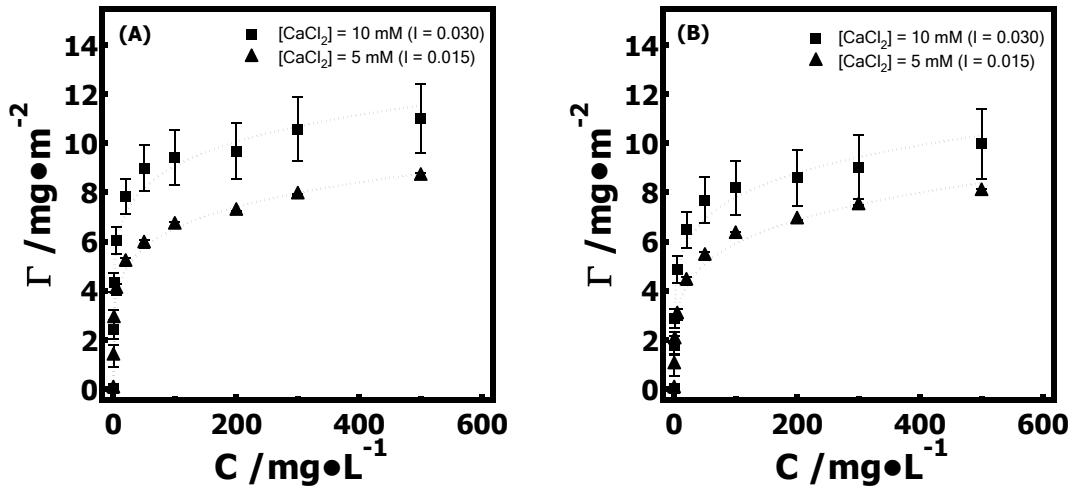

Figure 4.12. Adsorption isotherms for the adsorption of (A) CMC09 and (B) CMC12 onto regenerated cellulose surfaces at 20.0 °C from (▲) 5 mM and (■) 10 mM $CaCl_2$ solutions with one standard deviation error bars. The dashed lines represent fits with Freundlich isotherms.

Table 4.11. Adsorption isotherm parameters for CMC adsorption onto regenerated cellulose from $CaCl_2$ solutions

Polymer	$[CaCl_2]$ (mM)	I	Γ_m[a] (mg•m^{-2})	K_L[a] (L•mg^{-1})	K_F[b]	$1/n_F$[b]
CMC09	5	0.015	6.06 ± 0.58	1.38 ± 0.17	2.45 ± 0.19	0.22 ± 0.02
	10	0.030	9.34 ± 0.76	2.30 ± 0.32	4.74 ± 0.28	0.16 ± 0.01
CMC12	5	0.015	5.14 ± 0.76	1.14 ± 0.20	1.81 ± 0.11	0.26 ± 0.02
	10	0.030	6.97 ± 0.96	1.60 ± 0.30	2.94 ± 0.20	0.21 ± 0.02

[a]Determined by fitting the data to a linearized Langmuir model: Equation 4-3.
[b]Determined by fitting the data to a linearized Freundlich model: Equation 4-4.

4.4.8 Driving Force for CMC Adsorption

CMCs negatively charged did not adsorb onto regenerated cellulose surfaces in water. This result was consistent with the fact there are very few ionic groups on regenerated cellulose surfaces (Osterberg reported that the regenerated cellulose surface was weakly negatively charged with a surface potential = -2 mV[23]). Calcium cations (divalent)

enhanced CMC adsorption onto regenerated cellulose surfaces more than sodium cations (monovalent). First, the presence of Ca^{2+} in solution provided strong bridges between CMC and regenerated cellulose surfaces. Furthermore, the carboxylic acid groups in the CMC could form intramolecular and intermolecular crosslinks through calcium ions (**Figure 4.13**). These interactions are stronger than analogous ones for monovalent ions such as sodium at the same ionic strength.[24] Such results were demonstrated by Parolis et al. who studied the effect of Ca^{2+} on the adsorption of CMC onto talc surface.[25,26] Divalent cations also showed significant effects on the adsorption of xanthan (a polysaccharide macromolecule similar to CMC)[27] and alginate.[24,28]

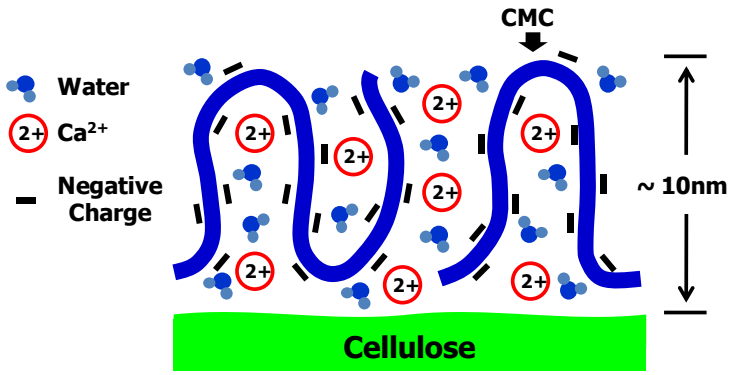

Figure 4.13. Schematic depiction of CMC layers adsorbed onto cellulose surfaces.

4.5 Conclusions

This study demonstrated that electrolytes (NaCl and $CaCl_2$) enhanced CMC adsorption onto regenerated cellulose surfaces. $CaCl_2$ (divalent cation) showed a more significant effect on the CMC adsorption than NaCl (monovalent cation). The adsorption of CMC from $CaCl_2$ solutions increased with increasing $CaCl_2$ concentration (from 5 to 10 mM), whereas the adsorption of CMC from NaCl solutions was independent of the NaCl concentration. Moreover, since Ca^{2+} had a stronger interaction with carboxylic acid

groups, CMC/Ca^{2+} complex layers adsorbed onto regenerated cellulose surfaces exhibited greater stability after flowing water over the surface. QCM-D and SPR showed that CMC formed highly hydrated layers from $CaCl_2$ and NaCl solutions on regenerated cellulose surfaces (90 to 95% water). Voigt-based viscoelastic modeling of the QCM-D data was consistent with the existence of highly hydrated CMC layers on regenerated cellulose surfaces with shear viscosities of ~ 10^{-3} N•s•m^{-2} and elastic shear moduli of ~10^5 N•m^{-2}. As such, CMC adsorption from electrolyte solutions is an effective method for introducing carboxylic acid groups to cellulose surfaces though physisorption.

4.6 References:

(1) Kontturi, K. S.; Tammelin, T.; Johansson, L.-S.; Stenius, P. *Langmuir* **2008**, *24*, 4743-4749.

(2) Nge, T. T.; Sugiyama, J. *Journal of Biomedical Materials Research Part A* **2006**, 124-134.

(3) Fras-Zemljic, L.; Stenius, P.; Laine, J.; Stana-Kleinschek, K. *Cellulose* **2006**, *13*, 655-663.

(4) Zemljic, L. F.; Stenius, P.; Laine, J.; Stana-Kleinschek, K. *Cellulose* **2008**, *15*, 315-321.

(5) Kontturi, E.; Thune, P. C.; Niemantsverdriet, J. W. *Langmuir* **2003**, *19*, 5735-5741.

(6) Tammelin, T.; Merta, J.; Johansson, L.-S.; Stenius, P. *Langmuir* **2004**, *20*, 10900-10909.

(7) Plunkett, M. A.; Claesson, P. M.; Rutland, M. W. *Langmuir* **2002**, *18*, 1274-1280.

(8) Enarsson, L.-E.; Wagberg, L. *Langmuir* **2008**, *24*, 7329-7337.

(9) Gandubert, V. J.; Lennox, R. B. *Langmuir* **2006**, *22*, 4589-4593.

(10) Tehrani-Bagha, A. R.; Holmberg, K. *Langmuir* **2008**, *24*, 6140-6145.

(11) Kaya, A.; Du, X.; Liu, Z.; Lu, J. W.; Morris, J. R.; Glasser, W. G.; Heinze, T.; Esker, A. R. *Biomacromolecules* **2009**, *10*, 2451-2459.

(12) Hook, F.; Kasemo, B.; Nylander, T.; Fant, C.; Sott, K.; Elwing, H. *Anal. Chem.* **2001**, *73*, 5796-5804.

(13) Reimhult, E.; Larsson, C.; Kasemo, B.; Hoeoek, F. *Anal. Chem.* **2004**, *76*, 7211-7220.

(14) Larsson, C.; Rodahl, M.; Hoeoek, F. *Anal. Chem.* **2003**, *75*, 5080-5087.

(15) Stengel, G.; Hook, F.; Knoll, W. *Anal. Chem.* **2005**, *77*, 3709-3714.

(16) Mwaikambo, L. Y.; Ansell, M. P. *J. Mater. Sci. Lett.* **2001**, *20*, 2095-2096.

(17) Vogt, B. D.; Soles, C. L.; Lee, H.-J.; Lin, E. K.; Wu, W.-l. *Langmuir* **2004**, *20*, 1453-1458.

(18) Bottom, V. E. *Introduction to Quartz Crystal Unit Design*; Van Nostrand Reinhold Co.: New York, 1982.

(19) Vogt, B. D.; Lin, E. K.; Wu, W.-L.; White, C. C. *J. Phys. Chem. B* **2004**, *108*, 12685-12690.

(20) Patel, A. R.; Kanazawa, K. K.; Frank, C. W. *Anal. Chem.* **2009**, *81*, 6021-6029.

(21) Malmstrom, J.; Agheli, H.; Kingshott, P.; Sutherland, D. S. *Langmuir* **2007**, *23*, 9760-9768.

(22) Romero-Cano, M. S.; Martin-Rodriguez, A.; de las Nieves, F. J. *J. Colloid Interface Sci.* **2000**, *227*, 322-328.

(23) Osterberg, M. *J. Colloid Interface Sci.* **2000**, *229*, 620-627.

(24) De Kerchove, A. J.; Elimelech, M. *Macromolecules* **2006**, *39*, 6558-6564.

(25) Khraisheh, M.; Holland, C.; Creany, C.; Harris, P.; Parolis, L. *Int. J. Miner. Process.* **2005**, *75*, 197-206.

(26) Parolis, L. A. S.; van der Merwe, R.; Groenmeyer, G. V.; Harris, P. J. *Colloids Surf., A* **2008**, *317*, 109-115.

(27) Mohammed, Z. H.; Haque, A.; Richardson, R. K.; Morris, E. R. *Carbohydr. Polym.* **2007**, *70*, 38-45.

(28) de Kerchove, A. J.; Elimelech, M. *Biomacromolecules* **2007**, *8*, 113-121.

CHAPTER 5

Quartz Crystal Microbalance with Dissipation Monitoring and Surface Plasmon Resonance Studies of Pullulan and Pullulan Cinnamate Adsorption onto Cellulose and Thermoplastics

5.1 Abstract

A biomimetic approach to improve adhesion between wood-fibers and thermoplastics is explored by investigating the interaction between pullulan derivatives and polymer surfaces. Pullulan cinnamates (PCs) used as models for the lignin carbohydrate complex were synthesized by modifying pullulan with 4-chlorocinnamic acid and 3-methoxycinnamic acid to obtain different degrees of cinnamate substitution (DS_{Cinn}) per anhydroglucose unit (DS_{Cinn} = 0.034 and 0.054 for pullulan 4-chlorocinnamates, and DS_{Cinn} = 0.027 and 0.057 for pullulan 3-methoxycinnamates). Self-assembly of pullulan and pullulan derivatives onto regenerated cellulose, cellulose acetate propionate (CAP), poly(L-lactic acid) (PLLA), and methyl terminated SAM (SAM-CH_3) surfaces was investigated via surface plasmon resonance (SPR) and quartz crystal microbalance with dissipation monitoring (QCM-D). The SPR and QCM-D results showed that hydrophobic cinnamate groups enhanced the adsorption of pullulan cinnamates onto cellulose, CAP, PLLA, and SAM-CH_3 surfaces and highly hydrated PC layers formed at the liquid/solid interfaces. Voigt-based viscoelastic modeling of the QCM-D data indicated that PCs formed relatively "soft layers" with low shear viscosities of ~ 10^{-3} N•s•m^{-2} and elastic shear moduli between 1×10^5 and 3×10^5 N•m^{-2}.

5.2 Introduction

Wood-plastic composites exhibit promising physical properties, such as high stiffness and resistance to the propagation of cracks.[1] However, the natural fiber-polymer interface presents a formidable challenge. The presence of hydroxyl groups and other polar substances in various natural fibers promotes moisture absorption leading to poor interfacial bonding between polyhydroxyl fiber surfaces and the hydrophobic matrix.[2] Bonding between components can often be increased by derivatization of cellulosic fibers with hydrophobic ester moieties. However, derivatization of cellulose leads to the degradation of the cellulose structure by disrupting the extensive hydrogen bonding network and cleavage of the glucan chain, two important contributions to the strength of native cellulose materials.[3] Surface modification with self-assembling polysaccharides and polysaccharide derivatives is a gentler method to improve adhesion between wood-fibers and thermoplastics compared to chemical modification. In our group, previous studies already showed that hydrophobic moieties enhance the adsorption of pullulan, a water soluble polysaccharide, onto model cellulose surfaces.[4,5]

In this chapter, a biomimetic approach to improve adhesion between wood-fibers and thermoplastics is explored through studies of the self-assembly of pullulan and pullulan derivatives onto cellulose, thermoplastics, and methyl-terminated self-assembled monolayers (SAM-CH_3). Pullulan, a water soluble polysaccharide composed of anhydroglucose units (AGU), was hydrophobically modified by the incorporation of 3-methoxycinnamate and 4-chlorocinnamate groups. The model cellulose surface was prepared through regeneration of spincoated trimethylsilyl cellulose (TMSC) thin films, while the model thermoplastic surfaces were prepared via spincoating cellulose acetate

propionate (CAP) and poly(L-lactic acid) (PLLA). In order to study the self-assembly of pullulan and pullulan derivatives onto model surfaces, surface plasmon resonance (SPR) and quartz crystal microbalance with dissipation monitoring (QCM-D) used in Chapter 4 were also employed in this study. Modeling of QCM-D results provided viscoelastic properties of adsorbed polymer layers.[6] Furthermore, the combination of SPR and QCM-D facilitated the determination of wt% of coupled water for hydrated layers.[7]

5.3 Experimental

Cellulose acetate propionate (CAP, number average molar mass, M_n ~ 15,000 g•mol^{-1}, 0.6 wt.% acetyl and 42.5 wt.% propionyl content) and 1-dodecanethiol (SAM-CH_3) were purchased from Sigma-Aldrich. Poly(L-lactic acid) (PLLA, M_n ~ 4,700 g•mol^{-1}, polydispersity index, M_w/M_n = 1.09) was purchased from Polymer Source, Inc. Synthesis and characterization of the pullulan cinnamates (PCs) used in this study, pullulan 3-methoxycinnamates (P3MC) and pullulan 4-chlorocinnamates (P4CC), were described in Chapter 3.1.2. In this chapter, P3MC03, P3MC06, P4CC03, and P4CC06 indicate sample with degrees of cinnamate substitution per AGU of DS_{Cinn} = 0.034, 0.054, 0.027, and 0.057, respectively. Ultrapure water was used in all experiments (Millipore, Milli-Q Gradient A-10, 18.2 MΩ•cm, < 5 ppb organic impurities). Procedures for the preparation of cellulose, CAP, PLLA, and SAM-CH_3 surfaces are provided in Chapter 3.2.1.1, 3.2.1.2, and 3.2.1.3, respectively. Finally, surface tension measurements, atomic force microscopy (AFM) measurements, SPR measurements, and QCM-D measurements were described in Chapter 3.2.5, 3.2.7, 3.2.9, and 3.2.10, respectively.

5.4 Results and Discussion

5.4.1 Characterization of Model Polymer Films

Representative surface morphologies for cellulose, CAP, PLLA, and SAM-CH_3 surfaces on SPR and QCM-D sensors are provided in **Figure 5.1**. The root-mean-square (rms) roughnesses of the model surfaces were determined from 2 μm × 2 μm images and are summarized in **Table 5.1**. The rms roughness values for CAP and SAM-CH_3 surfaces were ~ 1.5 nm and were similar to that of the cellulose surface. The PLLA surface was smoother than the cellulose surface with a rms roughness of ~ 0.6 nm. The thicknesses of the cellulose and thermoplastic surfaces were determined via ellipsometry and are summarized in **Table 5.1**. Furthermore, hydrophobicity of model surfaces was evaluated by static contact angle measurements. The contact angle of ultrapure water on regenerated cellulose films is ~ 20 °, an indication of a hydrophilic surface, whereas the contact angle of water on a SAM-CH_3 surface is ~ 100 °, an indication of a hydrophobic surface. The contact angles of water on CAP and PLLA surfaces were ~ 70 °, indicating that CAP and PLLA were more hydrophobic than the cellulose surface and more hydrophilic than the SAM-CH_3 surface.

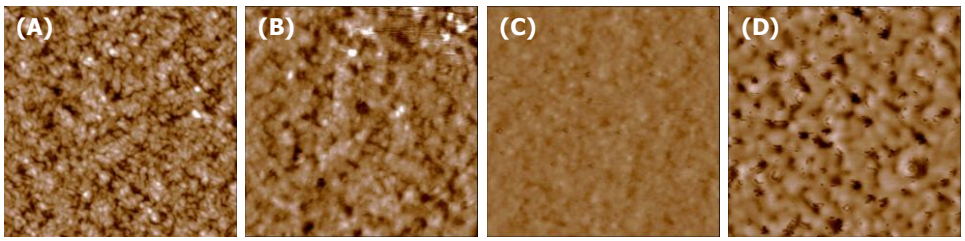

Figure 5.1. Representative AFM height images of (A) regenerated cellulose, (B) CAP, (C) PLLA, and (D) SAM-CH_3 surfaces. The images are 2 μm × 2 μm and have Z-axis scales of 0 to 10 nm.

Table 5.1. Roughnesses, thicknesses, and static contact angles of water on cellulose, CAP, PLLA, and SAM-CH_3 surfaces

Surface	RMS Roughness (nm)	Thickness (nm)[a]	Contact angle (ϑ)[a]
Cellulose	1.5	18 ±1	19 ±1
CAP	1.4	22 ±2	71 ±1
PLLA	0.6	12 ±1	73 ±3
SAM-CH_3	1.5	1.8[b]	101 ±1

[a]Average of three measurements with one standard deviation error bars.
[b]Reference value[8]

5.4.2 Surface Tension Measurements

Surface tension measurements probed surface activity of pullulan derivatives at the air/water interface. Plots of surface tension (γ) versus concentration for pullulan, P3MCs and P4CCs are provided in **Figure 5.2**. The surface tension values of P and the low DS_{Cinn} PC (P3MC03 and P4CC03) solutions were the same as the surface tension of water (γ_{water}). Pullulan exhibited no surface activity at the air/water interface up to 400 mg•L^{-1} as previously reported.[9,10] However, high DS_{Cinn} PCs (P3MC06 and P4CC06) caused a slight depression of the surface tension, $\Delta\gamma = \gamma_{water} - \gamma_{PC(aq)}$, where $\gamma_{PC(aq)}$ is the surface tension of the pullulan cinnamate solution. The changes in surface tension ($\Delta\gamma$) were ~ 1.0 mN•m^{-1} and ~ 2.7 mN•m^{-1} for 300 mg•L^{-1} P3MC06 and P4CC06 solutions, respectively. The cinnamate groups connected to pullulan chains made pullulan more hydrophobic, however, the cinnamate groups are too short for the formation of ordered structures at the air/water interface.

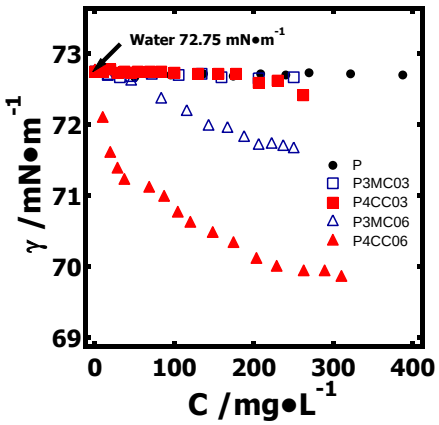

Figure 5.2. γ versus concentration for P, P3MC03, P3MC06, P4CC03, and P4CC06 at the air/water interface at 20.0 ℃. Symbols correspond to (●) P, (□) P3MC03, (Δ) P3MC06, (■) P4CC03, and (▲) P4CC06.

5.4.3 P3MC and P4CC Adsorption onto Cellulose, Thermoplastic, and SAM-CH_3 Surfaces by SPR

Representative raw SPR data for the adsorption of P, P3MCs and P4CCs from aqueous solutions onto cellulose, CAP, PLLA, and SAM-CH_3 surfaces are provided in **Figures 5.3** and **5.4**. Each individual experiment was carried out three times. Surface plasmon resonance angle changes ($\Delta\theta_a$) due to PC adsorption were extracted from the SPR raw data as depicted in **Figure 3.20** and are summarized in **Table 5.2**. There was no significant adsorption of P onto cellulose, CAP, and PLLA surfaces. Whereas, there was a slight adsorption for pullulan onto SAM-CH_3 surfaces. Adsorption of P3MCs onto all four surfaces from aqueous solutions was greater than pullulan and increased with increasing the DS_{Cinn} value. The amounts of P3MC06 adsorbed onto the four model surfaces were 2-3 times greater than those of P3MC03. For both P3MC03 and P3MC06, the adsorption onto hydrophobic surfaces was greater than onto hydrophilic surfaces

(SAM-CH_3 > CAP, PLLA > cellulose). P4CC adsorption showed the same trend as P3MC (**Figure 5.4**). Furthermore, P4CC adsorption onto all four model surfaces was greater than that of P3MC at the same DS_{Cinn}. These results suggested that PC adsorption onto all model surfaces was facilitated by cinnamate groups of the PCs in a hydrophobically driven process. The hydrophobicity of the substrates also affected the adsorption of PCs. Hydrophobic surfaces provided stronger interaction with PCs than hydrophilic surfaces. As seen in **Figures 5.3** and **5.4**, most of the adsorbed polymer was irreversibly bound.

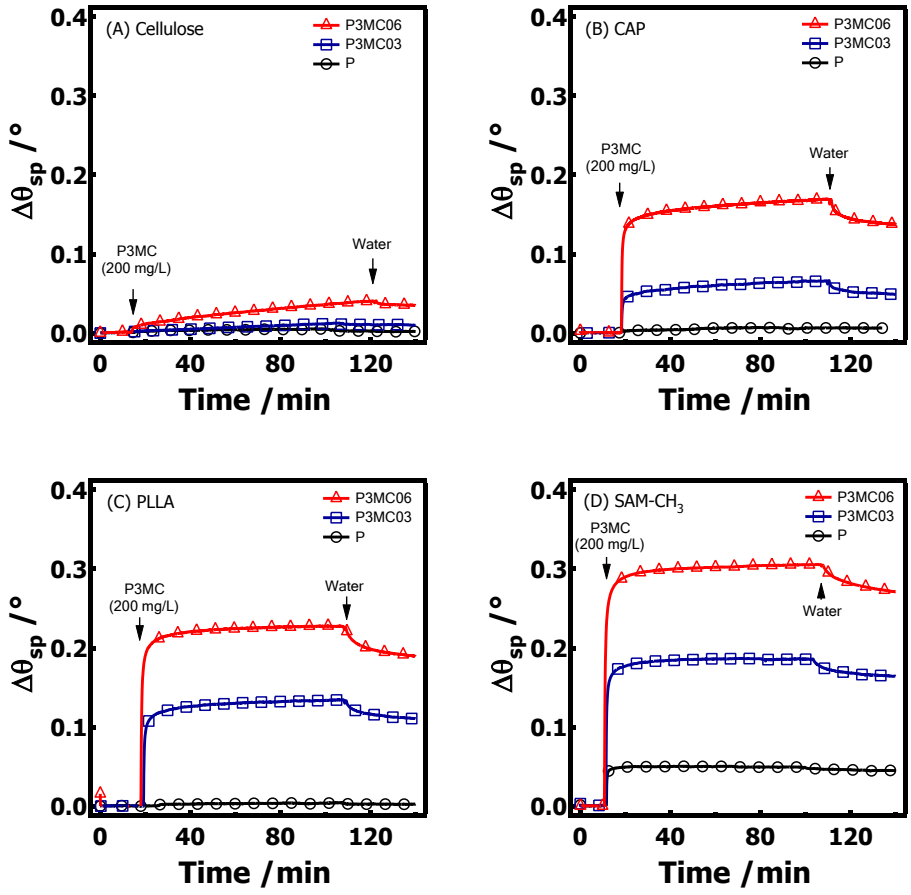

Figure 5.3. Representative SPR data for (○) P, (□) P3MC03, and (Δ) P3MC06 adsorbed from 200 mg•L^{-1} aqueous solutions onto (A) cellulose, (B) CAP, (C) PLLA, and (D) SAM-CH_3 surfaces at 20.0 ℃.

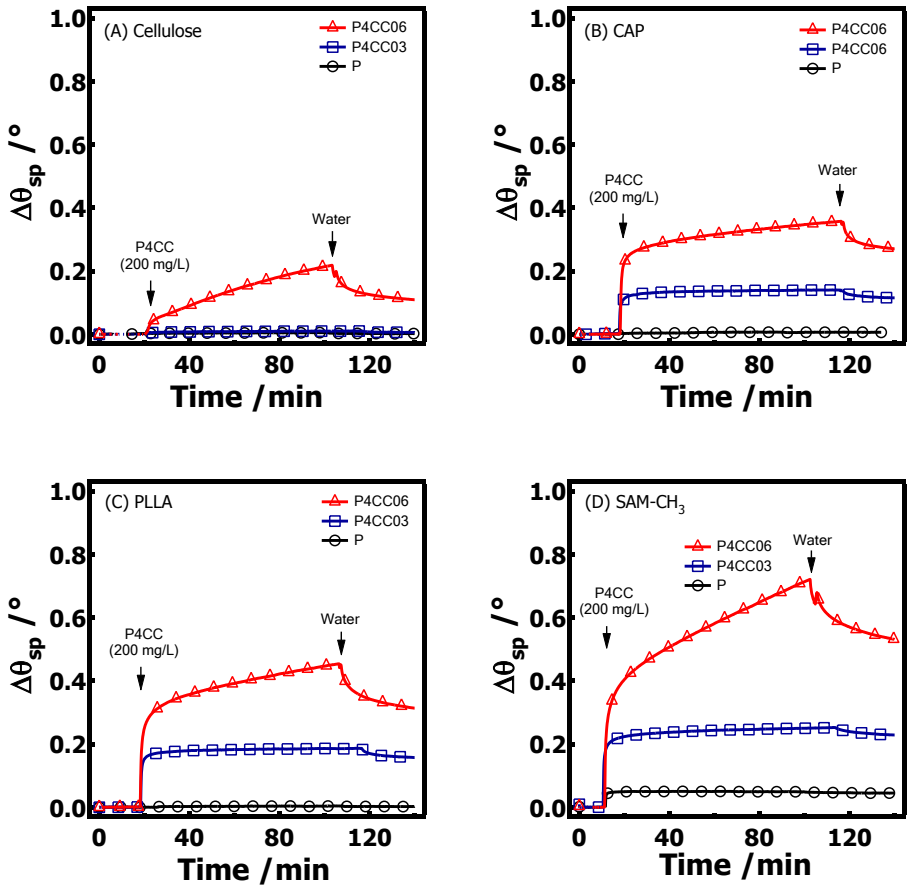

Figure 5.4. Representative SPR data for (○) P, (□) P4CC03, and (Δ) P4CC06 adsorbed from 200 mg•L^{-1} aqueous solutions onto (A) cellulose, (B) CAP, (C) PLLA, and (D) SAM-CH_3 surfaces at 20.0 ℃.

Table 5.2. $\Delta\theta_a$ for P3MC and P4CC layers adsorbed from aqueous solutions[a]

Surface	P	P3MC03	P3MC06	P4CC03	P4CC06
Cellulose	0.003 ± 0.001	0.009 ± 0.002	0.031 ± 0.010	0.009 ± 0.001	0.246 ± 0.047
CAP	0.006 ± 0.001	0.064 ± 0.001	0.170 ± 0.002	0.136 ± 0.003	0.363 ± 0.011
PLLA	0.001 ± 0.001	0.124 ± 0.013	0.219 ± 0.011	0.188 ± 0.004	0.500 ± 0.069
SAM-CH_3	0.045 ± 0.004	0.174 ± 0.014	0.287 ± 0.025	0.247 ± 0.005	0.683 ± 0.047

[a]Average of three measurements ± one standard deviation for adsorption from 200 mg•L^{-1} aqueous solutions.

5.4.4 P3MC and P4CC Adsorption onto Cellulose, Thermoplastic, and SAM-CH_3 Surfaces by QCM-D

QCM-D was also used to study PC adsorption. Representative raw QCM-D data for the adsorption of P, P3MCs and P4CCs from aqueous solutions onto cellulose, CAP, PLLA, and SAM-CH_3 surfaces are provided in **Figures 5.5** and **5.6**. As seen in **Figure 5.5**, there was no significant scaled frequency change ($\Delta f/n$) when pullulan solutions flowed over the cellulose, CAP, and PLLA surfaces. Changes in the dissipation when pullulan solutions flowed over these surfaces were also insignificant. In contrast, the frequency decreased when pullulan solutions flowed over the SAM-CH_3 surfaces and the frequency did not return to the base line after water was flowed over the sensor, indicating irreversible adsorption had occurred. In contrast, ($\Delta f/n$) values for P3MC adsorption onto the four model surfaces were greater than that of pullulan and increased with increasing DS_{Cinn}. The ($\Delta f/n$) and ΔD values from the third overtone (n = 3) for PC adsorption are summarized in **Table 5.3**. ($\Delta f/n$) values for PC adsorption on hydrophobic surfaces were greater than those on hydrophilic surfaces. ΔD values for most PC adsorbed layers were greater than 4×10^{-6}, indicating that soft layers formed on the model surfaces. As seen in **Figure 5.6**, P4CC adsorption showed the same trend as P3MC. However, the amount of adsorption for P4CCs was greater than P3MCs at the same

DS_{Cinn} value. Most PC adsorption was irreversible. In this respect, QCM-D results qualitatively matched the SPR results.

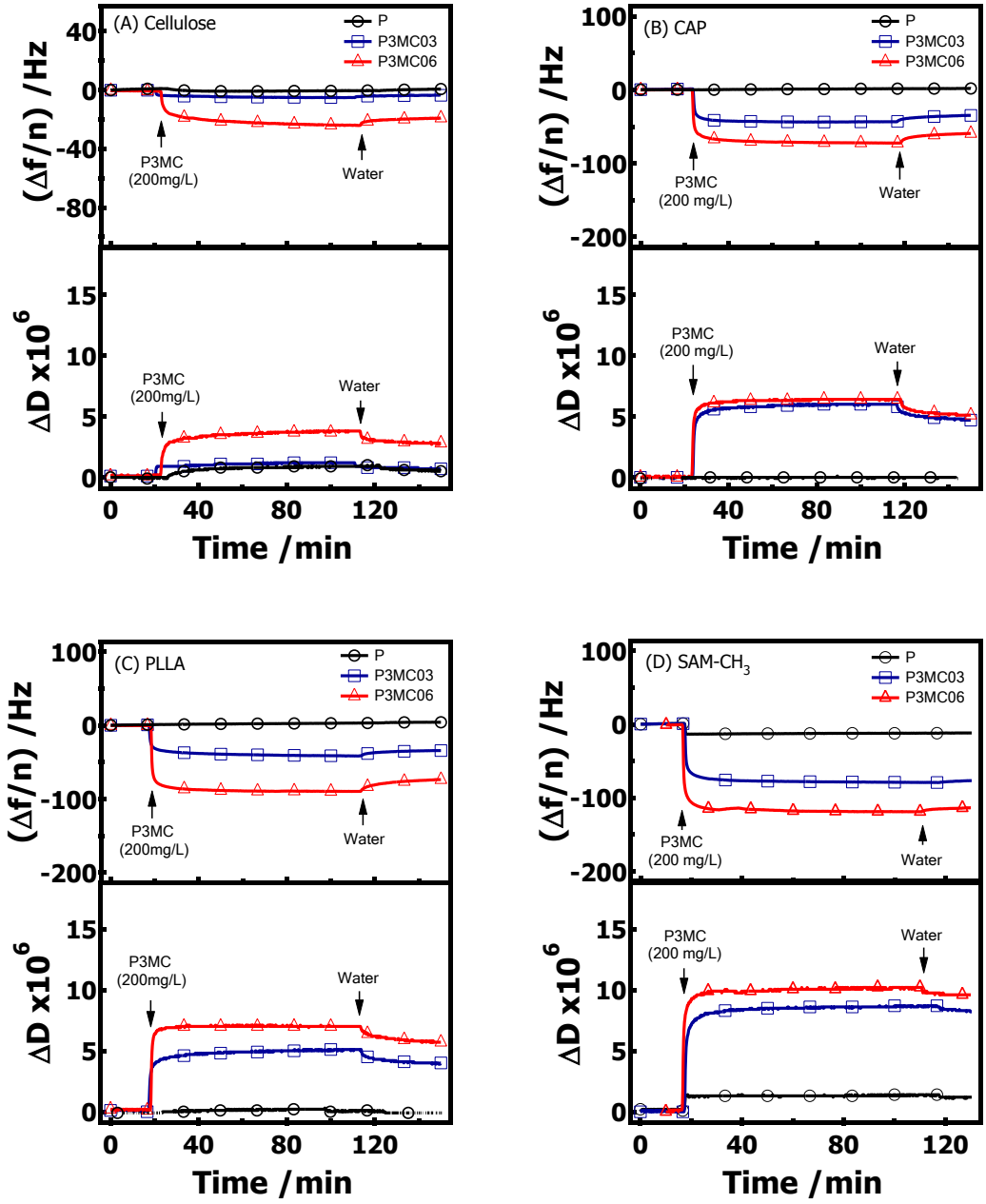

Figure 5.5. Representative QCM-D data for P, P3MC03, and P3MC06 adsorbed from 200 mg•L^{-1} aqueous solutions onto (A) cellulose, (B) CAP, (C) PLLA, and (D) SAM-CH_3 surfaces at 20.0 ℃ (n = 3).

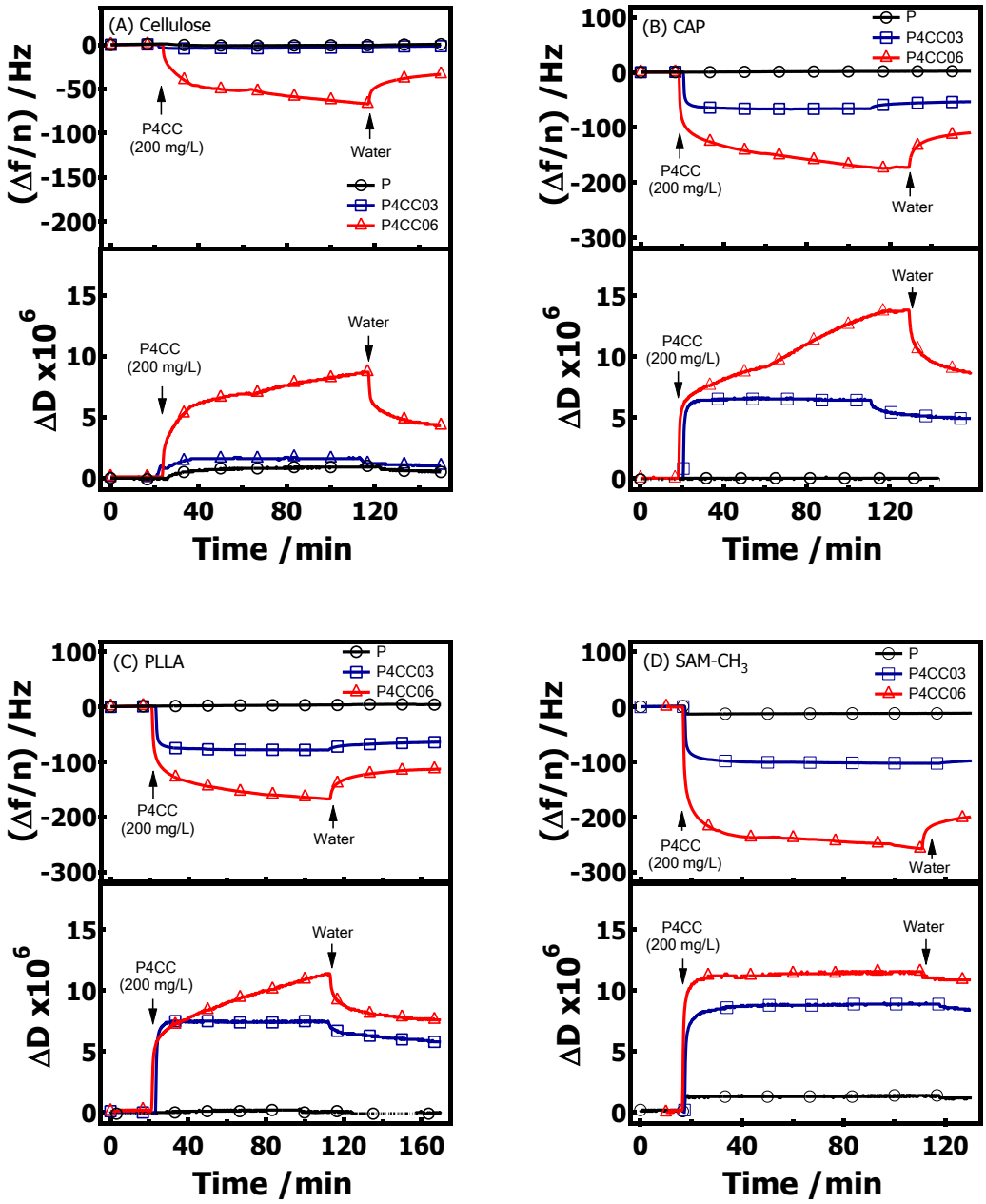

Figure 5.6. Representative QCM-D data for P, P4CC03, and P4CC06 adsorbed from 200 mg•L^{-1} aqueous solutions onto (A) cellulose, (B) CAP, (C) PLLA, and (D) SAM-CH_3 surfaces at 20.0 ℃ (n = 3).

Table 5.3. (Δf/n) and ΔD for P3MC and P4CC layers adsorbed from aqueous solutions[a]

Surface		P	P3MC03	P3MC06	P4CC03	P4CC06
Cellulose	(Δf/n) (Hz)	0.0 ±0.5	-2.7 ±2.2	-20.2 ±3.6	-3.8 ±0.7	-68.6 ±24.3
	$\Delta D \times 10^6$	1.1 ±0.2	0.8 ±0.3	3.5 ±0.5	1.4 ±0.2	8.5 ±2.2
CAP	(Δf/n) (Hz)	-0.4 ±0.7	-41.4 ±2.0	-71.7 ±0.3	-66.1 ±0.9	-177.6 ±5.2
	$\Delta D \times 10^6$	0.1 ±0.1	5.7 ±0.3	6.4 ±0.1	6.6 ±0.2	14.0 ±0.6
PLLA	(Δf/n) (Hz)	0.0 ±0.1	-55.2 ±11.8	-88.8 ±0.7	-74.8 ±3.8	-164.2 ±2.4
	$\Delta D \times 10^6$	0.0 ±0.5	6.3 ±1.1	7.0 ±0.1	7.4 ±0.1	10.7 ±0.5
SAM-CH_3	(Δf/n) (Hz)	-19.4 ±4.3	-79.1 ±8.7	-119.0 ±5.0	-102.7 ±6.4	-257.0 ±10.0
	$\Delta D \times 10^6$	1.9 ±0.8	7.8 ±1.1	10.2 ±2.0	7.9 ±1.4	14.6 ±1.0

[a]Average of three measurements ± one standard deviation for adsorption from 200 mg•L^{-1} aqueous solutions (n = 3).

5.4.5 Viscoelastic Properties of P3MC and P4CC Layers

In this study, SPR was used for the determination of the optical surface concentration (Γ_{SPR}) of PC layers adsorbed from aqueous solutions onto four model surfaces (analysis of SPR data was described in Chapter 3.2.9.1). The Γ_{SPR} values are summarized in **Table 5.4**.

The surface concentrations (Γ_{QCM}) for adsorbed PC layers could also be obtained from QCM-D results. For the case of PC layers adsorbed onto four model surfaces, most layers were strongly dissipative ($\Delta D > 5 \times 10^{-6}$). For such layers, the Sauerbrey equation is invalid for the calculation of the mass of the adsorbed layer. Hence, PC adsorption curves were fit with the Voigt-based viscoelastic model and Γ_{QCM} of the adsorbed layers were obtained. The PC layers were modeled as a homogeneous layer with four parameters: a thickness (h_f), density (ρ_f), shear viscosity (η_f), and elastic shear modulus (μ_f). This layer was sandwiched between the QCM-D sensor (quartz plus the model surface) and a semi-infinite Newtonian liquid layer under no-slip boundary conditions. The density and viscosity of water (ρ_0 = 1000 kg•gm^{-3} and $\eta_0 = 1 \times 10^{-3}$ N•s•m^{-2}, respectively) were used for all of the bulk liquids, because the effects of dissolved PCs on the values of ρ_0 and η_0

were small and could be ignored. Thus, the adsorption curves from multiple odd overtones (n = 3, 5, and 7) were used for the estimation of h_f, η_f, and μ_f. A density of 1100 kg•m^{-3} was initially used for the calculation of an effective h_f. Then, the hydrodynamic surface concentrations (Γ_{QCM}) were calculated from Equation 3-14.

The representative Voigt-based viscoelastic modeling of QCM-D data for P3MC06 layers adsorbed onto four model surfaces are provided in **Figures 5.7** through **5.10**. Time-dependent η_f, μ_f, and h_f corresponding to the best-fit curves are also shown on **Figures 5.7** through **5.10**. The same modeling method was also used to analyze P4CC QCM-D data. The Γ_{QCM} were significantly greater than Γ_{SPR} and are summarized in **Table 5.4**. The Γ_{QCM} corresponded to the total mass of the layer and included both PC chains and coupled water, while the Γ_{SPR} from SPR quantified the dry mass of the layer (without water). Hence, the amount of water coupled to the PC layers could be deduced from the QCM-D and SPR results. Both P3MCs and P4CCs formed highly hydrated layers on the four model surfaces and the calculated water values were in the range of 70 to 90% by mass. Moreover, the density of the PC layer was calculated from

$$\rho = \frac{\Gamma_{QCM}}{\frac{\Gamma_{SPR}}{\rho_{PC}} + \frac{\Gamma_{QCM} - \Gamma_{SPR}}{\rho_{Water}}} \qquad (5\text{-}1)$$

where the density of water is ρ_{water} = 1000 kg•m^{-3} and the density of PC is ρ_{PC} = 1250 kg•m^{-3}. The percentage amounts of coupled water and the densities of the PC layers are summarized in **Table 5.4**.

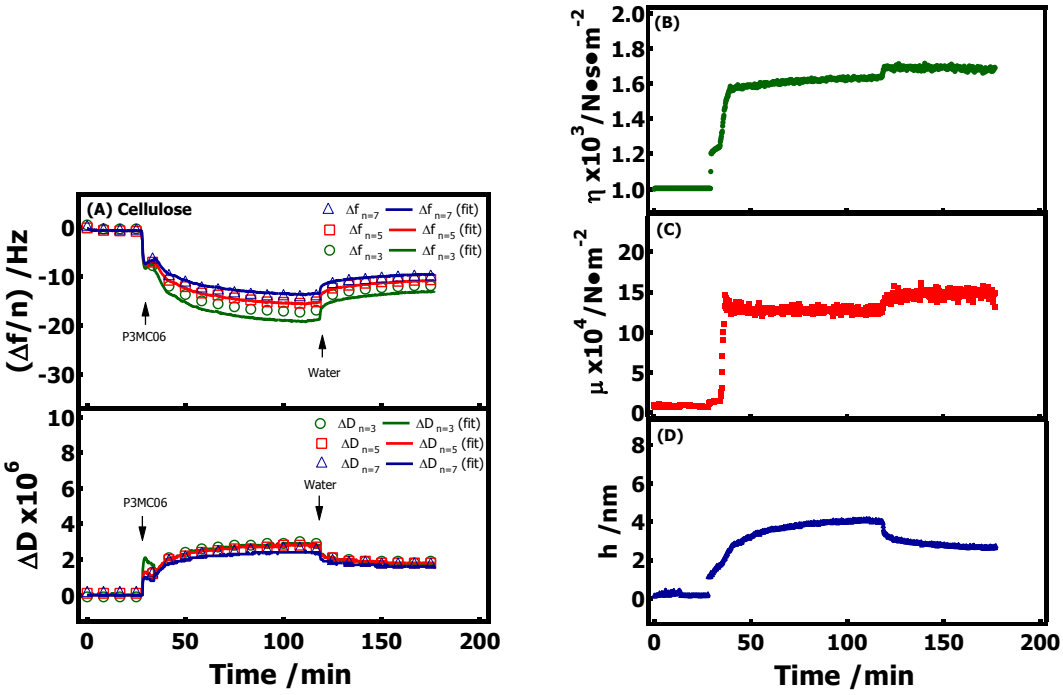

Figure 5.7. Adsorption of P3MC06 onto a cellulose surface from a 200 mg•L^{-1} aqueous solution: (A) (Δf/n) and ΔD versus time for (○) n = 3, (□) n = 5, and (Δ) n = 7 and the best fits obtained using Voigt-based viscoelastic modeling (solid lines). Time dependent evolution of changes in parameters associated with the Voigt-based viscoelastic modeling of the data in (A): (B) viscosity versus time, (C) elastic shear modulus versus time, and (D) effective thickness versus time assuming ρ_f = 1100 kg•m^{-3}.

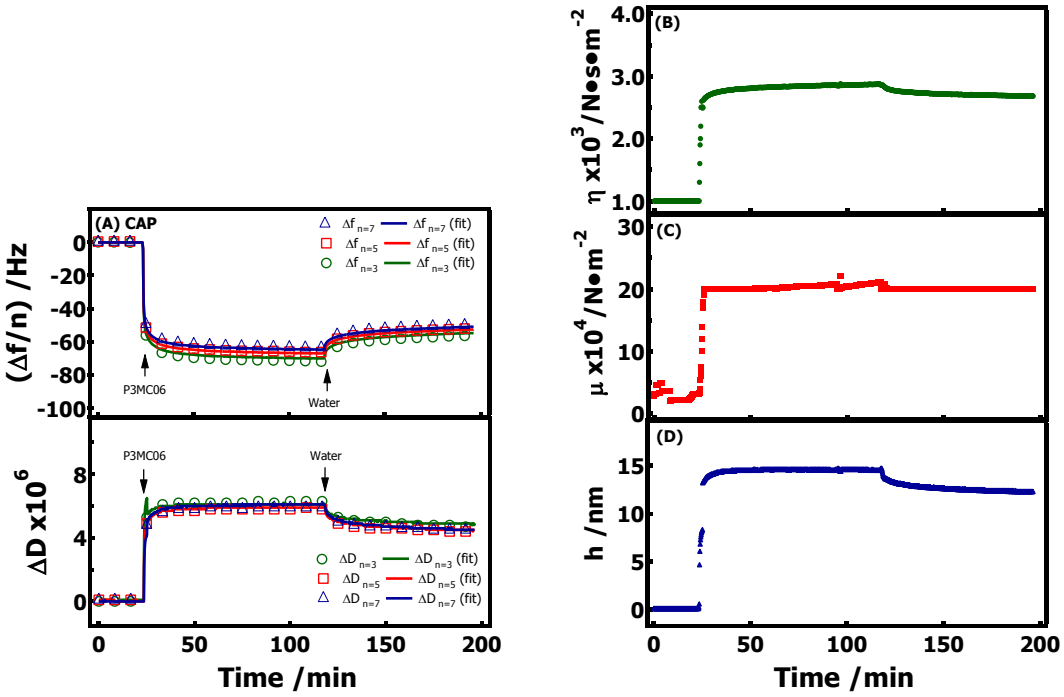

Figure 5.8. Adsorption of P3MC06 onto a CAP surface from a 200 mg•L^{-1} aqueous solution: (A) (Δf/n) and ΔD versus time for (○) n = 3, (□) n = 5, and (Δ) n = 7 and the best fits obtained using Voigt-based viscoelastic modeling (solid lines). Time dependent evolution of changes in parameters associated with the Voigt-based viscoelastic modeling of the data in (A): (B) viscosity versus time, (C) elastic shear modulus versus time, and (D) effective thickness versus time assuming ρ_f = 1100 kg•m^{-3}.

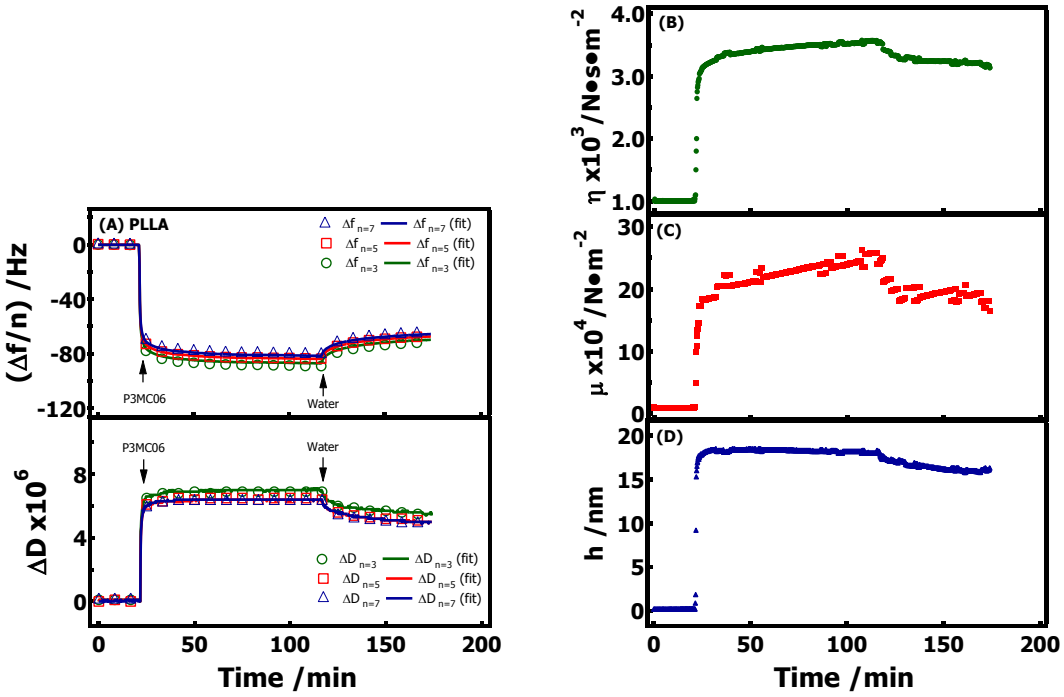

Figure 5.9. Adsorption of P3MC06 onto a PLLA surface from a 200 mg•L^{-1} aqueous solution: (A) (Δf/n) and ΔD versus time for (○) n = 3, (□) n = 5, and (Δ) n = 7 and the best fits obtained using Voigt-based viscoelastic modeling (solid lines). Time dependent evolution of changes in parameters associated with the Voigt-based viscoelastic modeling of the data in (A): (B) viscosity versus time, (C) elastic shear modulus versus time, and (D) effective thickness versus time assuming ρ_f = 1100 kg•m^{-3}.

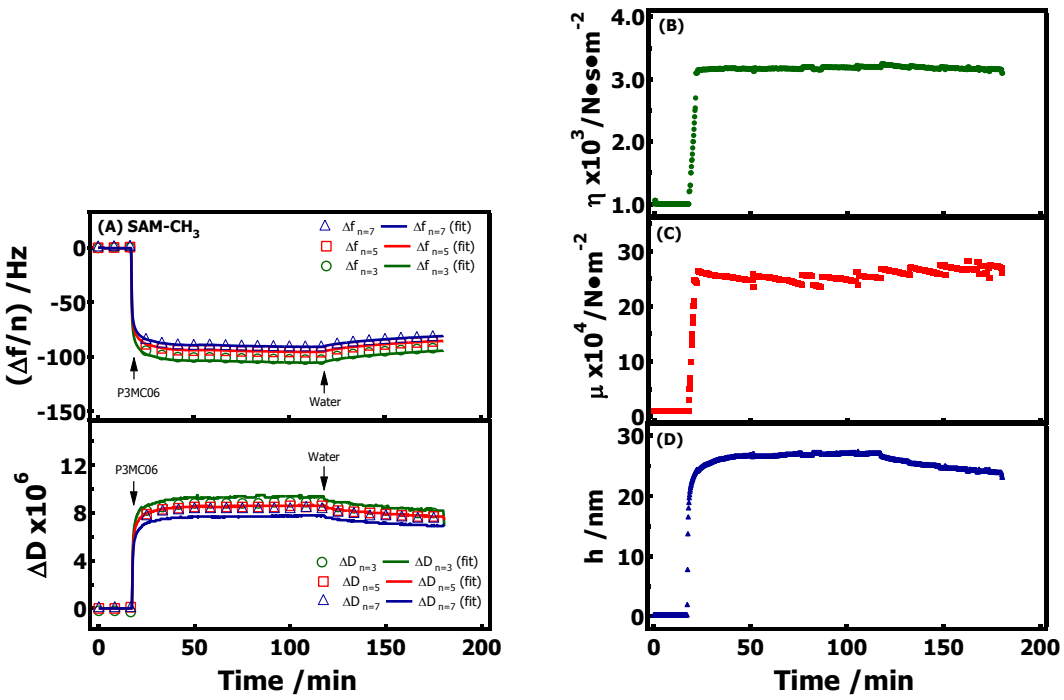

Figure 5.10. Adsorption of P3MC06 onto a SAM-CH_3 surface from a 200 mg•L^{-1} aqueous solution: (A) (Δf/n) and ΔD versus time for (○) n = 3, (□) n = 5, and (Δ) n = 7 and the best fits obtained using Voigt-based viscoelastic modeling (solid lines). Time dependent evolution of changes in parameters associated with the Voigt-based viscoelastic modeling of the data in (A): (B) viscosity versus time, (C) elastic shear modulus versus time, and (D) effective thickness versus time assuming ρ_f = 1100 kg•m^{-3}.

Table 5.4. Water contents and densities of adsorbed layers[a]

Surface	Adsorbate	Γ_{SPR} (mg•m^{-2})	Γ_{QCM} (mg•m^{-2})	% H_2O in film	ρ_f (kg•m^{-3})
Cellulose	P	-	-	-	-
	P3MC03	0.2 ±0.1	0.5 ±0.4[b]	-	-
	P3MC06	0.6 ±0.2	5.3 ±1.2	88 ±5	1023 ±10
	P4CC03	0.2 ±0.1	0.7 ±0.1[b]	-	-
	P4CC06	5.0 ±0.9	15.5 ±1.1	68 ±6	1069 ±14
CAP	P	-	-	-	-
	P3MC03	1.3 ±0.1	10.2 ±0.8	87 ±2	1026 ±3
	P3MC06	3.3 ±0.1	16.2 ±1.1	80 ±2	1042 ±3
	P4CC03	2.7 ±0.1	14.9 ±1.1	82 ±1	1038 ±3
	P4CC06	7.3 ±0.2	46.7 ±0.7	84 ±1	1032 ±1
PLLA	P	-	-	-	-
	P3MC03	2.5 ±0.3	9.9 ±0.8	75 ±4	1053 ±8
	P3MC06	4.3 ±0.2	19.0 ±0.5	77 ±1	1047 ±3
	P4CC03	3.7 ±0.1	17.1 ±0.8	78 ±1	1045 ±3
	P4CC06	10.1 ±1.4	41.0 ±1.7	75 ±4	1052 ±8
SAM-CH_3	P	0.9 ±0.1	3.5 ±0.7	74 ±6	1054 ±13
	P3MC03	3.9 ±0.3	18.2 ±1.2	79 ±2	1045 ±5
	P3MC06	6.2 ±0.5	28.1 ±1.5	78 ±2	1046 ±5
	P4CC03	5.3 ±0.1	20.1 ±1.0	74 ±1	1056 ±3
	P4CC06	15.2 ±1.0	55.2 ±4.1	72 ±3	1058 ±6

[a]Average of three measurements ±one standard deviation.
[b]The surface concentration was calculated by Sauerbrey equation.

Layer densities in **Table 5.4** were used for final viscoelastic modeling of QCM-D data and estimation of the viscoelastic parameters for PC layers. The deduced viscoelastic parameters for PC layers adsorbed from aqueous solutions are summarized in **Table 5.5**. The viscosities and elastic shear moduli of PC layers were in the ranges of 1.5 $\times 10^{-3}$ to

3.5 $\times 10^{-3}$ N•s•m^{-2} and 15.0 $\times 10^{4}$ to 30.0 $\times 10^{4}$ N•m^{-2}, respectively. The large amounts of water coupled in the layers meant PC layers showed relatively low viscosities and elastic shear moduli that were much lower than those of the bulk materials.

Table 5.5. Film properties of adsorbed PC layers[a]

Surface	Adsorbate	$\eta_f \times 10^3$ (N•s•m^{-2})	$\mu_f \times 10^{-4}$ (N•m^{-2})	% H_2O in film	ρ_f (kg•m^{-3})	h_f (nm)[b]
Cellulose	P	-	-	-	-	-
	P3MC03	-	-	-	-	-
	P3MC06	1.61 ±0.04	14.6 ±3.1	88 ±5	1023 ±10	5.0 ±1.1
	P4CC03	-	-	-	-	-
	P4CC06	2.11 ±0.35	26.2 ±3.1	68 ±6	1069 ±14	14.8 ±1.0
CAP	P	-	-	-	-	-
	P3MC03	2.03 ±0.09	18.6 ±2.6	87 ±2	1026 ±3	9.7 ±0.8
	P3MC06	2.88 ±0.04	22.3 ±0.1	80 ±2	1042 ±3	15.4 ±1.0
	P4CC03	2.72 ±0.10	26.1 ±2.0	82 ±1	1038 ±3	14.2 ±1.0
	P4CC06	3.10 ±0.03	15.7 ±0.1	84 ±1	1032 ±1	44.5 ±0.7
PLLA	P	-	-	-	-	-
	P3MC03	2.22 ±0.09	18.4 ±0.8	75 ±4	1053 ±8	9.4 ±0.8
	P3MC06	3.42 ±0.04	29.0 ±1.0	77 ±1	1047 ±3	18.1 ±0.5
	P4CC03	2.77 ±0.13	22.7 ±1.4	78 ±1	1045 ±3	16.3 ±0.8
	P4CC06	3.38 ±0.08	15.8 ±0.8	75 ±4	1052 ±8	39.0 ±1.6
SAM-CH_3	P	2.50 ±0.13	20.7 ±2.3	74 ±6	1054 ±13	3.3 ±0.7
	P3MC03	2.52 ±0.15	19.5 ±2.1	79 ±2	1045 ±5	17.3 ±1.1
	P3MC06	2.95 ±0.08	25.6 ±2.5	78 ±2	1046 ±5	26.8 ±1.4
	P4CC03	3.19 ±0.13	22.5 ±1.7	74 ±1	1056 ±3	19.1 ±1.0
	P4CC06	3.10 ±0.10	23.4 ±1.5	72 ±3	1058 ±6	52.6 ±3.9

[a]Average of three measurements ±one standard deviation.

[b]The thickness values were obtained from the QCM-D measurements.

5.4.6 Discussion

5.4.6.1 Possible Molecular Dimensions of PC Layers

For a flat polysaccharide monolayer, the surface concentration (Γ) is ~ 0.45 mg•m^{-2} assuming a cross-sectional area per AGU of ~ 60 Å^2•AGU^{-1}.[11] The molecular dimensions of PC layers could be deduced, when Γ_{SPR} values for PC layers in **Table 5.4** were compared to the value of a polysaccharide monolayer adsorbed flat on a surface. Γ_{SPR} values in **Table 5.4** showed that pullulan did not adsorb onto regenerated cellulose or thermoplastic surfaces at even the monolayer level (i.e. submonolayer coverage), whereas thicker films (> monolayer coverage) were observed for P adsorption onto SAM-CH_3 surfaces that were consistent with values reported in a previous study.[5] For lower DS_{Cinn} samples, P3MC03 and P4CC03, layers adsorbed onto cellulose surfaces were also less than a full monolayer. For the higher DS_{Cinn} samples, adsorbed amounts of P3MC06 and P4CC06 on the cellulose surfaces were in excess of a monolayer (~ 1.5 and ~ 10 "monolayers," respectively). Adsorption of P3MCs and P4CCs onto CAP, PLLA, and SAM-CH_3 all yielded films several "monolayers" thick. **Figure 5.11** schematically depicts P3MC06 (6 cinnamate groups per 100 AGUs) films on cellulose and CAP surfaces, respectively. P3MC06 adsorption onto cellulose was consistent with a predominantly train-like structure, whereas P3MC06 adsorption onto CAP surfaces was consistent with a looped structure due to strong hydrophobic interaction between cinnamate groups and alkyl groups on the substrates. On the basis of these observations, it could be concluded that the hydrophobic interaction between cinnamate groups and substrates is the most important factor for PC adsorption. The substituent on cinnamate groups also affected the PC adsorption. As the adsorption of the methoxyl substituted

cinnamates were comparable to previously reported data for pullulan cinnamates,[12] it would appear that the introduction of halogenated substituents is a promising approach to enhance PC adsorption. P4CC03 and P4CC06 adsorption onto cellulose and SAM-CH_3 surfaces were significantly greater than P3MC03 and P3MC06 and PC03 and PC06 adsorption[12] onto cellulose and SAM-CH_3 surfaces.

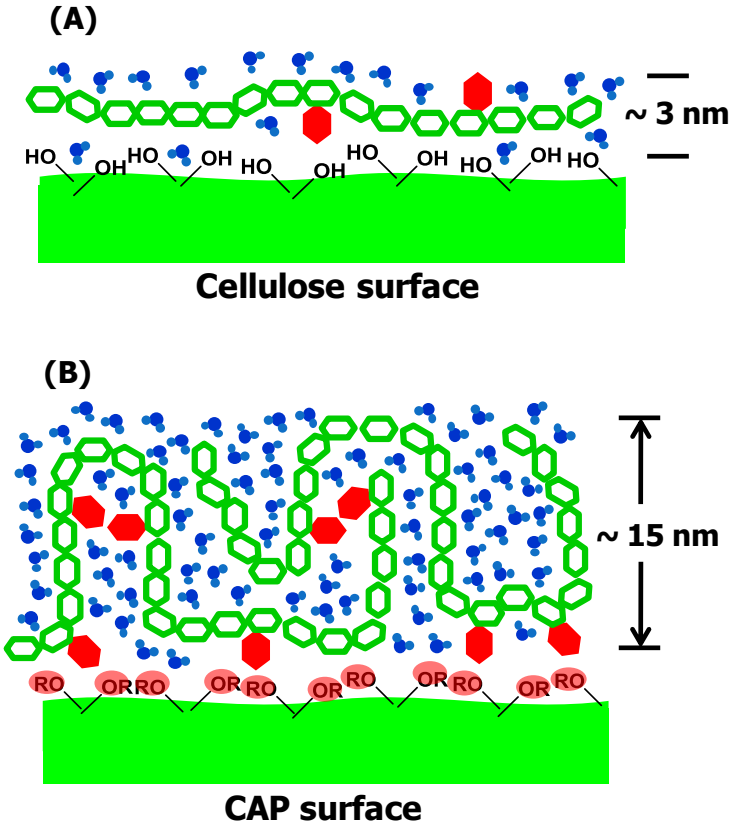

Figure 5.11. Schematic depiction of adsorbed pullulan 3-methoxycinnamate layers on cellulose and CAP surfaces.

5.4.6.2 Comparisons Between Adsorbed Carboxymethyl Cellulose and Pullulan Cinnamate Films

Carboxymethyl cellulose (CMC) adsorption (Chapter 4) and PC adsorption (Chapter 5) were studied via SPR and QCM-D. The combination of these two techniques provided

hydration and viscoelastic properties of adsorbed layers that are summarized in **Table 5.6**. CMC formed layers through electrostatic interactions, whereas PC formed layers through hydrophobic interactions. CMC layers contained more water than PC layers and consequently had relatively lower viscosities and elastic shear moduli.

Table 5.6. Comparison of selected properties between adsorbed CMC and PC layers

Layers	CMC	PC
Predominant Interaction	Electrostatic	Hydrophobic
% H_2O in Film by Mass	~ 95	70 to 90
ρ ($kg \cdot m^{-3}$)	~ 1023	~ 1050
$\eta_f \times 10^3$ ($N \cdot s \cdot m^{-2}$)	1.3 to 1.5	1.5 to 3.5
$\mu_f \times 10^{-4}$ ($N \cdot m^{-2}$)	9.6 to 11.6	15.0 to 30.0

5.5 Conclusions

This study demonstrated that hydrophobic cinnamate substituents strongly promoted pullulan adsorption onto cellulose, CAP, PLLA, and SAM-CH_3 surfaces. The adsorption of PCs increased with increasing DS_{Cinn} of cinnamate groups and PCs adsorbed onto thermoplastic surfaces more strongly than cellulose surfaces. QCM-D and SPR showed that PCs formed highly hydrated layers from aqueous solutions on model surfaces (70 to 90% water by mass). Voigt-based viscoelastic modeling of the QCM-D data was consistent with the existence of highly hydrated PC layers on regenerated cellulose surfaces with lower shear viscosities and moduli relative to bulk materials. These results suggest that hydrophobically modified polysaccharides may be able to serve as surface modifying agents to improve adhesion between wood-fibers and thermoplastics.

5.6 References:

(1) Jeronimidis, G. *Proc. R. Soc. Lond. B.* **1980**, *208*, 447-460.

(2) Mohanty, A. K.; Misra, M.; Drzal, L. T. *Compos. Interfaces* **2001**, *8*, 313-343.

(3) Gustavsson, M. T.; Persson, P. V.; Iversen, T.; Martinelle, M.; Hult, K.; Teeri, T. T.; Brumer, H., III *Biomacromolecules* **2005**, *6*, 196-203.

(4) Gradwell, S. E.; Renneckar, S.; Esker, A. R.; Heinze, T.; Gatenholm, P.; Vaca-Garcia, C.; Glasser, W. *C. R. Biol.* **2004**, *327*, 945-953.

(5) Kaya, A.; Glasser, W. G.; Esker, A. R. *Polym. Prepr. (Am. Chem. Soc., Div. Polym. Chem.)* **2007**, *48*, 758-759.

(6) Hoeoek, F.; Kasemo, B.; Nylander, T.; Fant, C.; Sott, K.; Elwing, H. *Anal. Chem.* **2001**, *73*, 5796-5804.

(7) Tehrani-Bagha, A. R.; Holmberg, K. *Langmuir* **2008**, *24*, 6140-6145.

(8) Kondo, T.; Yanagida, M.; Shimazu, K.; Uosaki, K. *Langmuir* **1998**, *14*, 5656-5658.

(9) Duval-Terrie, C.; Huguet, J.; Muller, G. *Colloids Surf., A* **2003**, *220*, 105-115.

(10) Deme, B.; Lee, L. T. *Journal of Physical Chemistry B* **1997**, *101*, 8250-8258.

(11) Kawaguchi, T.; Nakahara, H.; Fukuda, K. *Thin Solid Films* **1985**, *133*, 29-38.

(12) Kaya, A.; Du, X.; Liu, Z.; Lu, J. W.; Morris, J. R.; Glasser, W. G.; Heinze, T.; Esker, A. R. *Biomacromolecules* **2009**, *10*, 2451-2459.

CHAPTER 6

Cellulase Adsorption onto Pullulan Cinnamate Surfaces

6.1 Abstract

Pullulan-based lignin-carbohydrate model surfaces were made via spincoating of trimethylsilyl pullulan cinnamates (TMSPCs) from toluene onto gold substrates followed by the removal of trimethylsilyl groups in the presence of HCl vapor. The lowest degree of substitution for cinnamate groups (DS_{Cinn}) that afforded aqueous stable regenerated pullulan cinnamate (PC) films was DS_{Cinn} ~ 0.28. The regenerated pullulan cinnamate surfaces were smooth with root-mean-square surface roughnesses determined by atomic force microscopy of ~ 1 nm. The adsorption of a cellulase mixture onto regenerated cellulose, TMSPC, and PC surfaces was studied by quartz crystal microbalance with dissipation monitoring and in situ atomic force microscopy measurements. It was found that cellulase showed weak adsorption onto DS_{Cinn} ~ 0.28 PC surfaces, whereas cellulase adsorbed strongly onto TMSPC and higher DS_{Cinn} surfaces. This study provided further understanding of how surface hydrophobicity affected protein adsorption.

6.2 Introduction

Lignocellulosic biomass, as a renewable resource for the production of fuel and composite materials, has recently attracted considerable attention.[1,2] The lignocellulosic materials could be converted into glucose either by thermochemical or enzymatic processes. Compared to thermochemical technologies, enzymatic processes were cleaner and more efficient. However, enzymatic conversion of raw lignocellulosic biomasses comprised of cellulose, hemicelluloses, and lignin is complicated by the heterogeneous nature of the composite feedstocks. In these complex systems, both covalent and non-

covalent interactions led to network structures that were difficult to degrade.[3] To fundamentally study the interactions between enzymes and lignocellulosic materials, model surface systems have been employed. During the past decade, model cellulose surfaces have been prepared by Langmuir-Blodgett deposition of cellulose derivatives and spincoating of cellulose and cellulose derivative solutions and suspensions.[4-7] The well-defined model surfaces enabled fundamental studies using surface sensitive techniques such as surface plasmon resonance spectroscopy (SPR),[8,9] quartz crystal microbalance with dissipation monitoring (QCM-D),[10,11] atomic force microscopy (AFM),[9,12] and ellipsometry.[13,14] However, the model surfaces for lignin-carbohydrate complexes have received little attention.

The inherent heterogeneity of hemicelluloses has sparked interest in pullulan as a model for a hemicellulose. Pullulan is attractive, because it is a linear, water-soluble polysaccharide with a uniform structure[15,16] that consists of α-(1-6)-linked maltotriose residues, units of three glucose molecules connected by two α-(1-4)-linkages.[17] However, pullulan is difficult to process by conventional melt processing techniques, because it begins to degrade thermally at approximately 250 ℃ and is insoluble in regular organic solvents such as ethanol, chloroform, and tetrahydrofuran. Hydrophobic modification improves the solubility of pullulan in regular organic solvents such as chloroform, tetrahydrofuran, and toluene.[18,19]

In this work, water-insoluble pullulan cinnamates (PCs) were prepared by modifying pullulan with cinnamoyl chloride. Then, PCs were silylated with 1,1,1,3,3,3-hexamethyl disilazane (HMDS) in a process that yielded trimethylsilyl pullulan cinnamates (TMSPC) that were soluble in toluene. Regenerated PC surfaces were made via spincoating of

TMSPC solutions in toluene onto gold substrates followed by the removal of trimethylsilyl groups in the presence of HCl vapor. Regenerated PC surfaces served as models for lignin-carbohydrate complexes because the cinnamate groups were structurally similar to monolignols. Surface hydrophobicity was controlled by tuning the degree of cinnamate substitution (DS_{Cinn}, the number of cinnamate groups per anhydroglucose unit (AGU)). Surface hydrophobicity and morphology were studied by contact angle measurements and AFM, respectively. Adsorption of cellulase produced by fermentation of *Trichoderma reesei* onto regenerated PC surfaces was investigated by QCM-D and in situ AFM which provided further understanding of how surface hydrophobicity affected protein adsorption.

6.3 Experimental

Synthesis and characterization of trimethylsilyl pullulan cinnamates (TMSCP) were described in Chapter 3.1.3. Specific characteristics for DS_{Cinn} and the degree of trimethylsilyl substitution (DS_{TMS}) per AGU are summarized in **Tables 3.2** and **3.3**. Procedures for the preparation and characterization (X-ray photoelectron spectroscopy (XPS), ellipsometry, contact angle, and AFM) of cellulose and pullulan cinnamate (PC) films were described in Chapter 3.2.1, 3.2.2, 3.2.3, 3.2.4, and 3.2.7. The “cellulase” was a commercial cellulase cocktail Celluclast1.5L (a mixture of endo- and exo-glucanases, Novozymes A/S, Bagsvaerd, Denmark) produced by fermentation of *Trichoderma reesei*. Citric acid monohydrate was purchased from Fisher Chemical. Cellulase solutions for QCM-D measurements were prepared by dilution of 0.50 g commercial cellulase solution to 100 mL in citrate buffer solution (pH = 4.8, ionic strength of 0.05). In situ AFM measurements and QCM-D measurements were described in Chapter 3.2.8 and 3.2.10

respectively.

6.4 Results and Discussion

6.4.1 Characterization of Pullulan Cinnamate Films

Regenerated PC films on gold were prepared from TMSPCs with different DS_{Cinn} values via spincoating. XPS was performed to determine the surface chemical composition of the films. Wide scan XPS spectra from all TMSPC films before and after desilylation are provided as **Figures 6.1** through **6.5**. The experimental and theoretical atomic percentages of TMSPC and regenerated PC films are compared in **Table 6.1** and were consistent with the DS_{Cinn} and DS_{TMS} values obtained from ^{1}H NMR and UV measurements (**Tables 3.2** and **3.3**). For low DS_{Cinn} TMSPC films (TMSCP02, TMSPC03, and TMSPC07), silicon peaks completely disappeared after desilylation, an indication that trimethylsilyl groups were removed by the HCl vapor. Weak silicon peaks were observed for TMSPC12 and TMSPC23 films after desilylation, especially for TMSPC23 films. Apparently the high hydrophobic group density inhibited the removal of all TMS groups by HCl vapor. However, the amount of remaining TMS groups in PC12 and PC23 was small relative to the amount of cinnamate groups in the initial TMSPC12 and TMSPC23 films. Furthermore, gold could be seen for the regenerated PC02 film (**Figure 6.1**). In contrast, gold peaks were not observed for PC films regenerated from higher DS_{Cinn} TMSPCs (**Figures 6.2** through **6.5**). These observations were correlated with film stability in water. Regenerated PC02 films were unstable in water, whereas the PC films regenerated from higher DS_{Cinn} TMSPCs were stable in water. As such, the regenerated PC03 films suggested that $DS_{Cinn} \sim 0.28$ must be very close to the minimum DS_{Cinn} for the formation of aqueous stable regenerated PC films.

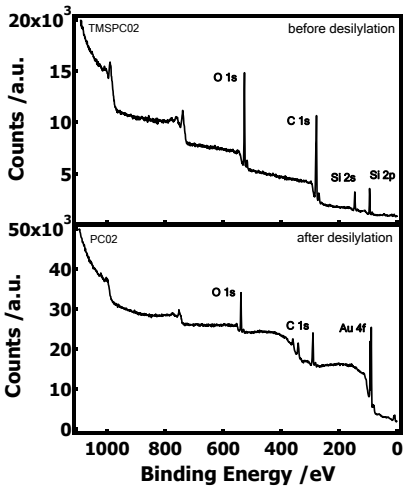

Figure 6.1. XPS wide scans from TMSPC02 films before and after desilylation with HCl vapor for 3 minutes. TMSPC02 was spincoated onto a QCM-D sensor with a gold surface from a 10 g•L^{-1} toluene solution at 2000 rpm.

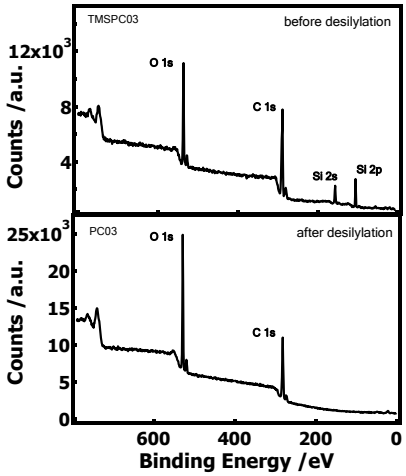

Figure 6.2. XPS wide scans from TMSPC03 films before and after desilylation with HCl vapor for 3 minutes. TMSPC03 was spincoated onto a QCM-D sensor with a gold surface from a 10 g•L^{-1} toluene solution at 2000 rpm.

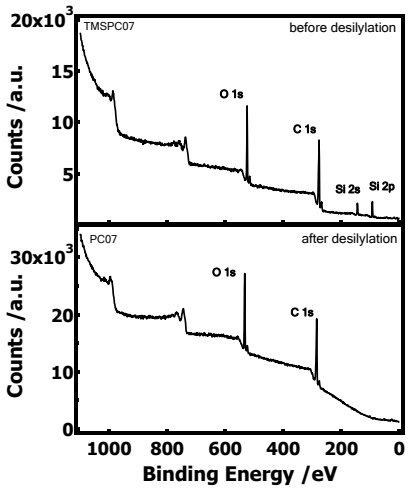

Figure 6.3. XPS wide scans from TMSPC07 films before and after desilylation with HCl vapor for 3 minutes. TMSPC07 was spincoated onto a QCM-D sensor with a gold surface from a 10 g•L^{-1} toluene solution at 2000 rpm.

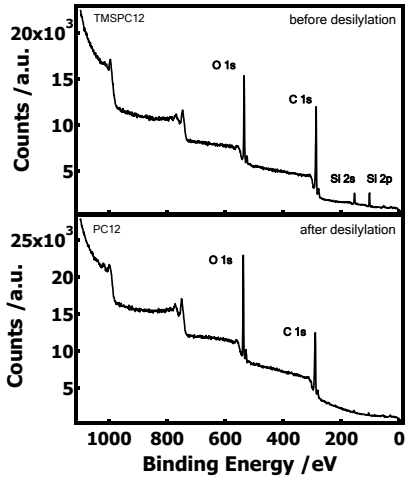

Figure 6.4. XPS wide scans from TMSPC12 films before and after desilylation with HCl vapor for 3 minutes. TMSPC12 was spincoated onto a QCM-D sensor with a gold surface from a 10 g•L^{-1} toluene solution at 2000 rpm.

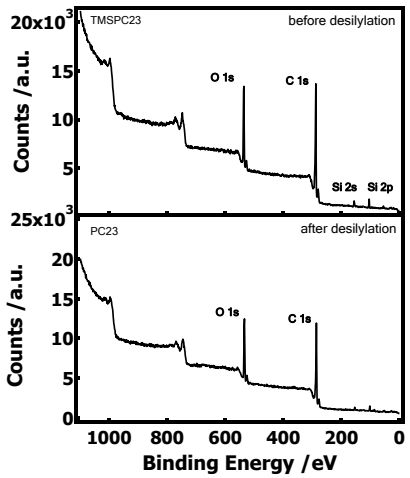

Figure 6.5. XPS wide scans from TMSPC23 films before and after desilylation with HCl vapor for 3 minutes. TMSPC23 was spincoated onto a QCM-D sensor with a gold surface from a 10 g•L^{-1} toluene solution at 2000 rpm.

The morphologies of TMSPC films were studied by AFM. Roughness values for the TMSPC films before and after desilyaltion are summarized in **Table 6.2**. TMSPCs formed uniform and smooth films on gold surfaces with root-mean-square (RMS) roughness less than 1.0 nm (**Figure 6.6A, C, E, G,** and **I**). After desilylation, the obtained regenerated PC films were rougher than TMSPC films (**Figure 6.6B, D, F, H,** and **J**). The regenerated PC02 films were rougher than other PC surfaces (~1.6 nm versus ~1.0 nm RMS). This observation was consistent with the observation of Au by XPS and the instability of the resulting films in water.

Table 6.1. Elemental compositions for spincoated TMSPC films before and after desilylation

Sample			C 1s[a]	O 1s[a]	Si 2p[a]	Au 4f[a]
TMSPC02	Before	Expt.[b]	65.2	23.9	10.9	0
(DS_{Cinn} = 0.2)		Theo.[c]	66.9	21.7	11.5	0
	After[d]	Expt.[b]	64.5	35.5	0	0
		Theo.[c]	60.0	40.0	0	0
TMSPC03	Before	Expt.[b]	67.4	21.7	10.9	0
(DS_{Cinn} = 0.28)		Theo.[c]	67.5	21.6	10.9	0
	After	Expt.[b]	62.1	37.9	0	0
		Theo.[c]	61.7	38.3	0	0
TMSPC07	Before	Expt.[b]	68.6	21.8	9.6	0
(DS_{Cinn} = 0.67)		Theo.[c]	70.3	21.1	8.5	0
	After	Expt.[b]	69.8	30.2	0	0
		Theo.[c]	68.0	32.0	0	0
TMSPC12	Before	Expt.[b]	71.0	22.9	6.1	0
(DS_{Cinn} = 1.22)		Theo.[c]	73.6	20.7	5.7	0
	After	Expt.[b]	70.3	29.6	0.1	0
		Theo.[c]	73.2	26.8	0	0
TMSPC23	Before	Expt.[b]	75.4	22.1	2.5	0
(DS_{Cinn} = 2.30)		Theo.[c]	78.3	20.1	1.6	0
	After	Expt.[b]	75.8	23.3	0.9	0
		Theo.[c]	78.5	21.5	0	0

[a]Atomic percentages excluding hydrogen
[b]Experimental results from XPS measurements
[c]Theoretical percentages on the basis of the molecular structure for DS_{Cinn} and DS_{TMS} from UV measurements summarized in Tables 3.2 and 3.3
[d]Recalculated excluding Au

Table 6.2. RMS surface roughness of TMSPC films before and after desilylation

Surface	RMS Roughness (nm)	
	Before Desilylation	After Desilylation
TMSPC02	0.8	1.6
TMSPC03	0.4	1.0
TMSPC07	0.6	1.1
TMSPC12	0.6	0.9
TMSPC23	0.5	1.0

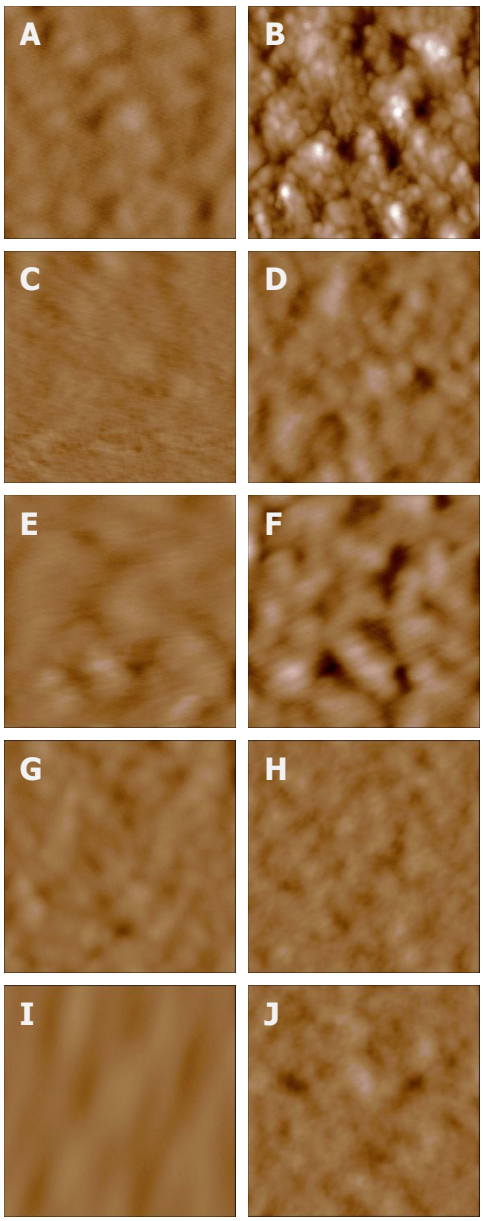

Figure 6.6. AFM height images of a TMSPC02 film (A) before and (B) after, TMSPC03 film (C) before and (D) after, TMSPC07 (E) before and (F) after, TMSPC12 (G) before and (H) after, and TMSPC23 (I) before and (J) after desilylation on gold surfaces of QCM-D sensors. The images are 1μm × 1 μm and have *Z*-axis scales of 0 to 10 nm.

Static contact angle measurements for ultrapure water drops on TMSPC and regenerated PC films are summarized in **Table 6.3**. TMSPC surfaces were hydrophobic with contact angles around 100 °, while regenerated PC surfaces were much more hydrophilic following the removal of the TMS groups. However, regenerated PC surfaces were still more hydrophobic than regenerated cellulose surfaces which exhibited a water contact angle around 20 ° (**Table 5.1**).

Table 6.3. Static contact angles for water on TMSPC films before and after desilylation

Surface	Contact Angle (°)[a]	
	Before Desilylation	After Desilylation
TMSPC02	102 ± 2	-[b]
TMSPC03	100 ± 1	43 ± 4
TMSPC07	99 ± 3	44 ± 5
TMSPC12	103 ± 2	55 ± 3
TMSPC23	94 ± 4	75 ± 5

[a]Average of three measurements ± one standard deviation
[b]TMSPC02 films were unstable on gold surfaces in aqueous media after desilylation in aqueous media.

QCM-D was employed to track mass losses of films during the desilylation process and their swelling behavior in aqueous solutions. Scaled frequency (Δf/n) and dissipation (ΔD) changes from TMSPC film coated QCM-D sensors before and after desilylation in air and water were provided in **Table 6.4**. Relative to the bare gold sensor, TMSPC and regenerated PC film coated sensors showed small ΔD in both air and water, hence both TMSPC and PC films could be treated as rigid layers and masses of the films were calculated through the Sauerbrey equation (Equation 3-13). Surface concentrations (Γ) from a Sauerbrey analysis are provided in **Table 6.5**. Moreover, the %mass losses due to the film regeneration were calculated though Equation 6-1:

$$\%mass\ loss = (\Gamma_b - \Gamma_a)/\Gamma_b \times 100 \qquad (6\text{-}1)$$

where Γ_b and Γ_a are the surface concentration values of TMSPC films before and after desilylation. The measured %mass loss values in both air and water matched the theoretical values, an indication that the regenerated PC films formed on the QCM-D sensors. The large error associated with removing and reseating the crystal in the sample cell meant differences in %mass loss between measurements in air and measurements in water where hydrophilic PC could swell were not statistically significant. The QCM-D results did show significant swelling for regenerated PC films.

Table 6.4. (Δf/n) and ΔD for spincoated TMSPC films before and after desilylation in air and water[a]

Surface		In Air		In Water	
		Before Desilylation	After Desilylation	Before Desilylation	After Desilylation
TMSPC03	(Δf/n) (Hz)	258 ±29	138 ±13	251 ±26	164 ±14
	$\Delta D \times 10^6$	0.2 ±0.1	0.2 ±0.2	0.2 ±0.4	0.1 ±0.2
TMSPC07	(Δf/n) (Hz)	282 ±14	158 ±12	255 ±14	163 ±17
	$\Delta D \times 10^6$	0.1 ±0.1	0.1 ±0.2	0.1 ±0.2	0.4 ±0.1
TMSPC12	(Δf/n) (Hz)	271 ±18	189 ±16	266 ±20	185 ±17
	$\Delta D \times 10^6$	0.1 ±0.3	0.2 ±0.2	0.2 ±0.2	0.2 ±0.2
TMSPC23	(Δf/n) (Hz)	278 ±14	264 ±24	275 ±15	261 ±12
	$\Delta D \times 10^6$	0.2 ±0.4	0.2 ±0.4	0.1 ±0.2	0.1 ±0.2

[a]Data was an average from 6 overtones (n = 3, 5, 7, 9, 11, and 13) of three measurements ± one standard deviation.

Table 6.5. Γ and %mass loss of TMSPC films after desilylation in air and water[a]

Surface	Theo. %mass loss[b]	Γ In Air ($mg•m^{-2}$)			Γ In Water ($mg•m^{-2}$)		
		Γ_b Before Desilylation	Γ_a After Desilylation	%Mass Loss	Γ_b Before Desilylation	Γ_a After Desilylation	%Mass Loss
TMSPC03	49.2	45.7 ±5.1	24.4 ±2.3	46.5 ±7.8	44.4 ±4.6	29.0 ±2.5	34.7 ±8.8
TMSPC07	45.2	49.9 ±2.5	28.0 ±2.1	44.0 ±5.1	45.1 ±5.1	28.9 ±3.0	36.1 ±9.8
TMSPC12	27.6	48.0 ±3.2	33.5 ±2.8	30.1 ±7.5	47.1 ±3.5	32.7 ±3.0	30.5 ±8.2
TMSPC23	8.6	49.2 ±5.1	45.7 ±2.5	5.0 ±10.9	48.7 ±2.7	46.2 ±2.1	5.1 ±6.8

[a]Γ was calculated from (Δf/n) in Table 6.
[b]Theoretical %mass loss on the basis of the molecular structure (DS_{Cinn} and DS_{TMS} were determined from UV measurements in Tables 3.2 and 3.3).

6.4.2 Cellulase Adsorption onto TMSPC and Regenerated PC Films by QCM-D

Representative QCM-D data (n = 3) for cellulase adsorption from a citrate buffer solution onto regenerated cellulose and subsequent hydrolysis of the film was used as a control and is shown in **Figure 6.7**. As seen in **Figure 6.7**, (Δf/n) went negative quickly before a nearly linear increase. At late times (t > ~ 150 minutes), (Δf/n) plateaued around (Δf/n) ~ 180 Hz. The profile observed in **Figure 6.7** was consistent with rapid enzyme adsorption onto the surface and subsequent, complete degradation of the cellulose film. Throughout the process, the dissipation remained low ($\Delta D < 2.5\times10^{6}$ for all t). These observations were consistent with a previously published study.[20]

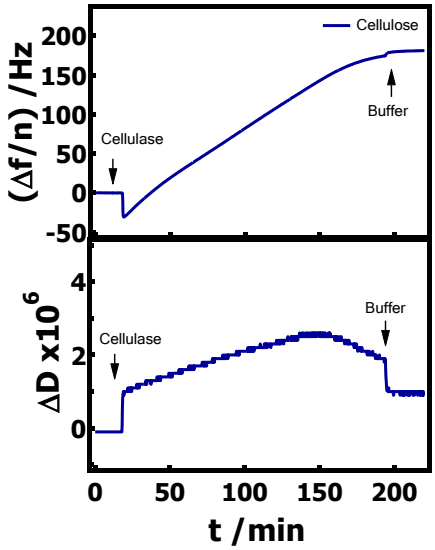

Figure 6.7. (Δf/n) and ΔD versus time from QCM-D for a regenerated cellulose film exposed to a citrate buffer solution of cellulase at 20 ℃. Curves correspond to the 3rd overtone. Arrows indicate where solutions were switched.

Representative QCM-D data (n = 3) for cellulase adsorption from a citrate buffer solution onto TMSPC and regenerated PC surfaces are shown in **Figure 6.8**. Comparable cellulase adsorption occurred on all TMSPC surfaces ((Δf/n) ~ 40 Hz) and was independent of the DS_{Cinn}. After desilylation, cellulase adsorption onto the regenerated PC surfaces differed for each PC surface. Cellulase adsorption onto regenerated PC surfaces increased with increasing DS_{Cinn}. Cellulase adsorption onto PC03 surfaces was rapid with (Δf/n) ~ 8 Hz and remained essentially constant over ~ 3 hours, while cellulase adsorption onto PC07 and PC12 surfaces was a slower process with (Δf/n) ~ 25 Hz and ~ 27 Hz, respectively, occurring over ~ 3 hours. Cellulase adsorption onto PC23 surfaces was similar to the TMSPC surfaces with (Δf/n) ~ 36 Hz. Degradation of TMSPC and regenerated PC surfaces did not occur. As seen in **Figure 6.8** there were no significant

differences in dissipation ($\Delta D < \sim 2.5\times10^{6}$) for any of the systems. ($\Delta f/n$), ΔD, and surface concentration (Γ) for cellulase adsorption onto TMSPC and regenerated PC surfaces are summarized in **Table 6.6**.

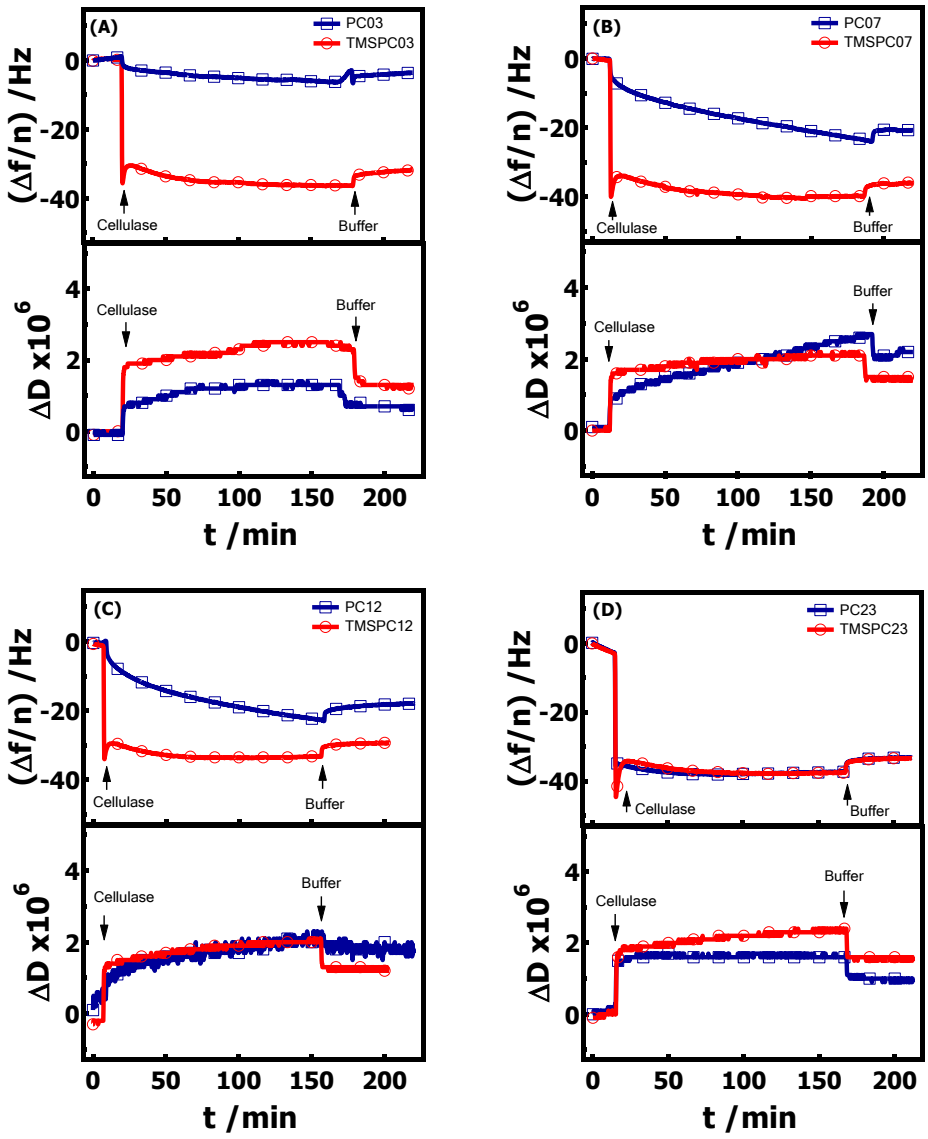

Figure 6.8. ($\Delta f/n$) and ΔD versus time from QCM-D for cellulase adsorption from a citrate buffer onto (A) TMSPC03 and regenerated PC03, (B) TMSPC07 and regenerated PC07, (C) TMSPC12 and regenerated PC12, and (D) TMSPC23 and regenerated PC23 films. Curves correspond to the 3rd overtone. Arrows indicate where solutions were switched.

Table 6.6. (Δf/n), ΔD, and Γ for cellulase adsorption onto different surfaces[a]

Surface	(Δf/n) (Hz)	$\Delta D \times 10^6$	Γ (mg•m^{-2})
TMSPC03	-37.2 ± 1.1	2.4 ± 0.1	6.6 ± 0.2
PC03	-7.8 ± 1.6	1.7 ± 0.3	1.4 ± 0.3
TMSPC07	-36.5 ± 4.9	2.1 ± 0.5	6.5 ± 0.9
PC07	-24.8 ± 1.1	2.4 ± 0.1	4.4 ± 0.2
TMSPC12	-36.9 ± 4.3	2.1 ± 0.1	6.5 ± 0.8
PC12	-27.2 ± 4.9	2.5 ± 0.5	4.8 ± 0.9
TMSPC23	-39.5 ± 0.7	2.5 ± 0.1	7.0 ± 0.2
PC23	-36.0 ± 2.8	1.9 ± 0.2	6.4 ± 0.5

[a]Averages of three measurements ± one standard deviation for n = 3

6.4.3 Cellulase Adsorption onto TMSPC and Regenerated PC Films by In Situ AFM

Representative in situ AFM images of the solid/liquid interface for regenerated PC and TMSPC surfaces on gold prior to and after cellulase adsorption from citrate buffer solutions are provided in **Figures 6.9** and **6.10**, respectively. PC surfaces were exposed to cellulase for 1 h or 3 h and were rinsed with citrate buffer for 0.5 h before the images were taken (**Figure 6.9**). Comparable images for TMSPC surfaces are provided in **Figure 6.10**. Cellulase aggregates were observed on all TMSPC surfaces after exposure to cellulase solutions and could not be removed by the 0.5 h rinse with citrate buffer. This observation indicated that irreversible adsorption occurred on the hydrophobic TMSPC surfaces. In contrast, no significant morphological changes were observed after the regenerated PC03 surface was exposed to cellulase (**Figure 6.9A** through **C**). With increasing DS_{Cinn}, more and larger cellulase aggregates were observed on regenerated PC07, PC12, and PC23 surfaces (**Figure 6.9D** through **L**). As seen in **Figure 6.9**, cellulase adsorption onto a regenerated PC23 surface was similar to morphological changes observed for the TMSPC films. RMS roughnesses obtained from the images in

Figures 6.9 and **6.10** are summarized in **Table 6.7**. As expected from the images, the roughness changes for TMSPC surfaces after cellulase adsorption were obvious, while roughness changes for the regenerated PC surfaces were smaller than TMSPC surfaces. The roughness of regenerated PC03 surfaces was unaffected by the weak cellulase adsorption.

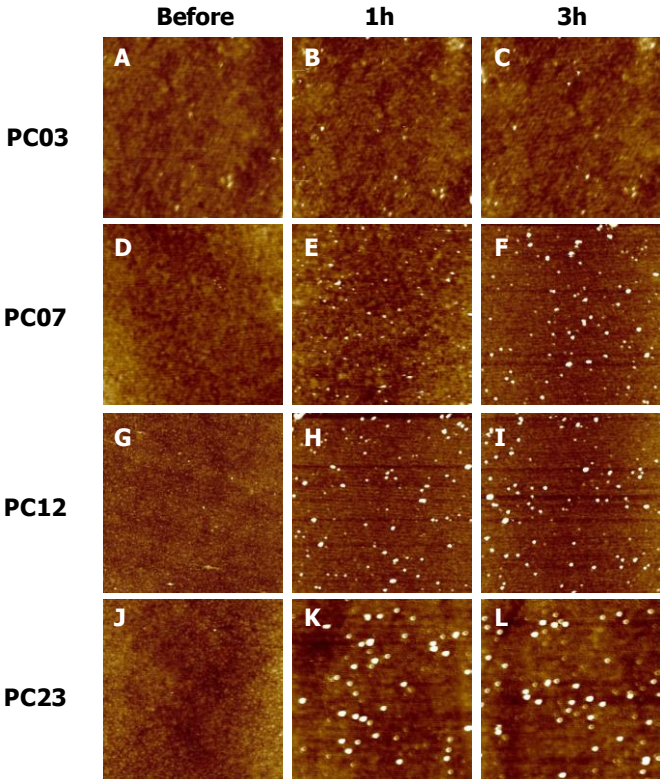

Figure 6.9. Representative AFM height images of the solid/liquid interfaces for PC films before and after exposure to a citrate buffer solution of cellulase followed by a citrate buffer rinse. Images correspond to: PC03 (A) before exposure to enzyme and after (B) 1 h and (C) 3 h of exposure to enzyme; PC07 (D) before exposure to enzyme and after (E) 1 h and (F) 3 h of exposure to enzyme; PC12 (G) before exposure to enzyme and after (H) 1 h and (I) 3 h of exposure to enzyme; PC23 (J) before exposure to enzyme and after (K) 1 h and (L) 3 h of exposure to enzyme. All AFM images are 5 μm × 5 μm and have

Z-axis scales of 0 to 20 nm.

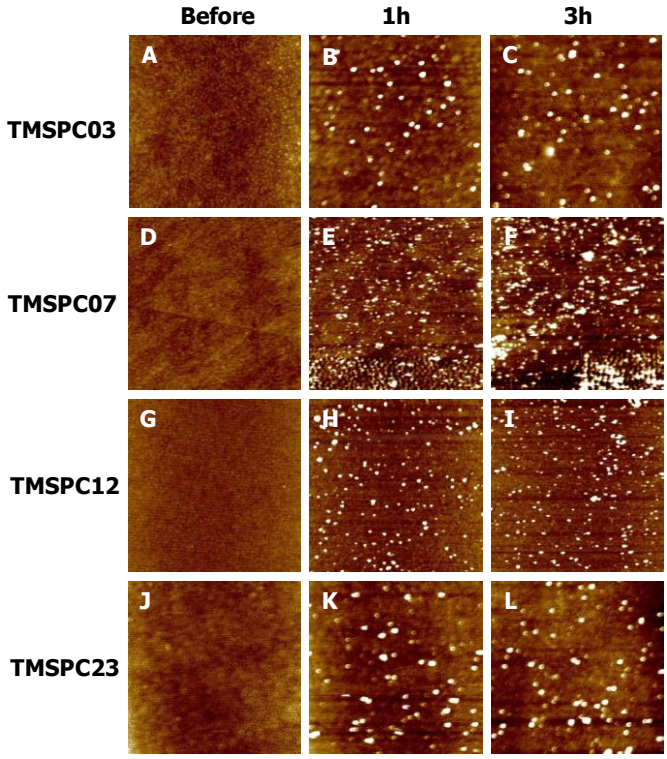

Figure 6.10. Representative AFM height images of the solid/liquid interfaces for TMSPC films before and after exposure to a citrate buffer solution of cellulase followed by a citrate buffer rinse. Images correspond to: TMSPC03 (A) before exposure to enzyme and after (B) 1 h and (C) 3 h of exposure to enzyme; TMSPC07 (D) before exposure to enzyme and after (E) 1 h and (F) 3 h of exposure to enzyme; TMSPC12 (G) before exposure to enzyme and after (H) 1 h and (I) 3 h of exposure to enzyme; TMSPC23 (J) before exposure to enzyme and after (K) 1 h and (L) 3 h of exposure to enzyme. All AFM images are 5 μm × 5 μm and have *Z*-axis scales of 0 to 20 nm.

Table 6.7. RMS surface roughnesses of TMSPC and regenerated PC surfaces before and after cellulase adsorption

Surface	RMS Roughness (nm)		
	Before Adsorption	After Adsorption (1h)	After Adsorption (3h)
TMSPC03	0.9	2.0	2.1
PC03	0.8	0.9	0.9
TMSPC07	0.7	2.1	2.9
PC07	0.9	1.3	1.6
TMSPC12	0.7	2.1	2.3
PC12	0.9	1.8	1.9
TMSPC23	1.0	2.5	2.6
PC23	1.0	2.4	2.5

6.4.4 Discussion

A plausible molecular level explanation for why cellulase adsorbed onto hydrophobic surfaces (TMSPC surfaces) more significantly than onto hydrophilic surfaces (PC surfaces) lies within the structure of cellulase. Cellulase used in this work was produced by *Trichoderma reesei*. It was comprised of two exo-glucanases (CBH I and CBH II) (80 - 90%) and several endo-glucanases (EG I, EG II, EG III, and EG V).[21,22] One common feature of these enzymes is that they each have a catalytic domain (CD), a carbohydrate binding module (CBM), and a highly glycosylated linker.[23] The larger catalytic domain constitutes the major part of the enzyme and contains the reactive site for substrate hydrolysis.[24] The smaller CBM includes aromatic side chains that are responsible for specific binding to substrates.[25] For example, one face of the CBM from CBH I from *Trichoderma reesei* contains a row of three tyrosines (**Figure 6.11**).[26] The hydrophobic effect has been identified as a major contributor to protein-substrate interactions.[27] Computational molecular dynamics studies from Zhong and his co-worker also indicated that the CBM from *Trichoderma reesei* CBH I binds to cellulose surfaces via strong

hydrophobic interactions and tyrosine groups play an important role in the binding process.[28,29] Our results are consistent with those previous studies. As seen in **Figure 6.9**, cellulase had a strong hydrophobic interaction with TMSPC surfaces, whereas the limited number of hydrophobic groups along regenerated PC03 chains led to weak hydrophobic interactions between cellulase and regenerated PC03.

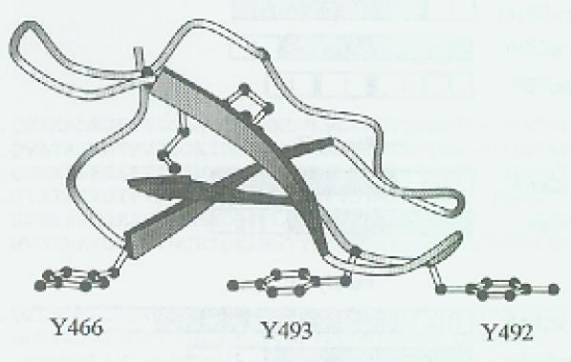

Figure. 6.11. The backbone structures of the CBM from the CBHI from *T. reesei*.[25] "Reprinted from Journal of Colloid and Interface Science, 285, Eriksson, J.; Malmsten, M.; Tiberg, F.; Callisen, T. H.; Damhus, T.; Johansen, K. S. Model cellulose films exposed to H. insolens glucoside hydrolase family 45 endo-cellulase - the effect of the carbohydrate-binding module, 94 - 99, Copyright (2005), with permission from Elsevier."

6.5 Conclusions

Smooth regenerated pullulan cinnamate surfaces were made via spincoating of trimethylsilyl pullulan cinnamates (TMSPC) from toluene solutions onto gold substrates followed by the removal of trimethylsilyl groups in the presence of HCl vapor. The lowest degree of cinnamate substitution (DS) that afforded aqueous stable regenerated PC films was DS_{Cinn} ~ 0.28. The hydrophobicity of the regenerated PC surface could be

controlled through the DS_{Cinn} and it was demonstrated that DS_{Cinn} also controlled cellulase adsorption to the surfaces. These studies reveal how mimics to lignin-carbohydrate complexes can be used to create protein resistant surfaces for possible applications as biomaterials.

6.6 References:

(1) Himmel, M. E.; Ruth, M. F.; Wyman, C. E. *Curr. Opin. Biotechnol.* **1999**, *10*, 358-364.

(2) Lin, Y.; Tanaka, S. *Appl. Microbiol. Biotechnol.* **2006**, *69*, 627-642.

(3) Bjorkman, A. *Sven. Papperstidn.* **1957**, *60*, 243-51.

(4) Schaub, M.; Wenz, G.; Wegner, G.; Stein, A.; Klemm, D. *Adv. Mater.* **1993**, *5*, 919-22.

(5) Kontturi, E.; Thune, P. C.; Niemantsverdriet, J. W. *Langmuir* **2003**, *19*, 5735-5741.

(6) Kontturi, E.; Tammelin, T.; Osterberg, M. *Chemical Society Reviews* **2006**, *35*, 1287-1304.

(7) Aulin, C.; Ahola, S.; Josefsson, P.; Nishino, T.; Hirose, Y.; Osterberg, M.; Wagberg, L. *Langmuir* **2009**, *25*, 7675-7685.

(8) Gradwell, S. E.; Renneckar, S.; Esker, A. R.; Heinze, T.; Gatenholm, P.; Vaca-Garcia, C.; Glasser, W. *C. R. Biologies* **2004**, *327*, 945-953.

(9) Kaya, A.; Du, X.; Liu, Z.; Lu, J. W.; Morris, J. R.; Glasser, W. G.; Heinze, T.; Esker, A. R. *Biomacromolecules* **2009**, *10*, 2451-2459.

(10) Faelt, S.; Waagberg, L.; Vesterlind, E.-L. *Langmuir* **2003**, *19*, 7895-7903.

(11) Kontturi, K. S.; Tammelin, T.; Johansson, L.-S.; Stenius, P. *Langmuir* **2008**, *24*, 4743-4749.

(12) Kontturi, E.; Johansson, L.-S.; Kontturi, K. S.; Ahonen, P.; Thuene, P. C.; Laine, J. *Langmuir* **2007**, *23*, 9674-9680.

(13) Bergstrom, L.; Stemme, S.; Dahlfors, T.; Arwin, H.; Odberg, L. *Cellulose* **1999**, *6*, 1-13.

(14) Eriksson, J.; Malmsten, M.; Tiberg, F.; Callisen, T. H.; Damhus, T.; Johansen, K. S. *J. Colloid Interface Sci.* **2005**, *284*, 99-106.

(15) Shingel, K. I. *Carbohydr. Res.* **2004**, *339*, 447-460.

(16) Rekha, M. R.; Sharma, C. P. *Trends Biomater. Artif. Organs* **2007**, *20*, 116-121.

(17) Singh, R. S.; Saini, G. K.; Kennedy, J. F. *Carbohydr. Polym.* **2008**, *73*, 515-531.

(18) Shibata, M.; Asahina, M.; Teramoto, N.; Yosomiya, R. *Polymer* **2000**, *42*, 59-64.

(19) Akiyoshi, K.; Deguchi, S.; Tajima, H.; Nishikawa, T.; Sunamoto, J. *Macromolecules* **1997**, *30*, 857-861.

(20) Turon, X.; Rojas, O. J.; Deinhammer, R. S. *Langmuir* **2008**, *24*, 3880-3887.

(21) Zandona, A.; Siika-Aho, M.; Ramos, P. *World Journal of Microbiology & Biotechnology* **2006**, *22*, 821-825.

(22) Pinto, R.; Carvalho, J.; Mota, M.; Gama, M. *Cellulose* **2006**, *13*, 557-569.

(23) Gerber, P. J.; Joyce, T. W.; Heitmann, J. A.; Siika-Aho, M.; Buchert, J. *Cellulose* **1997**, *4*, 255-268.

(24) Divne, C.; Stahlberg, J.; Reinikainen, T.; Ruohonen, L.; Pettersson, G.; Knowles, J. K. C.; Teeri, T. T.; Jones, T. A. *Science* **1994**, *265*, 524-528.

(25) Eriksson, J.; Malmsten, M.; Tiberg, F.; Callisen, T. H.; Damhus, T.; Johansen, K. S. *J. Colloid Interface Sci.* **2005**, *285*, 94-99.

(26) Linder, M.; Teeri, T. T. *Journal of Biotechnology* **1997**, *57*, 15-28.

(27) Elbert, D. L.; Hubbell, J. A. *Annu. Rev. Mater. Sci.* **1996**, *26*, 365-394.

(28) Nimlos Mark, R.; Matthews James, F.; Crowley Michael, F.; Walker Ross, C.; Chukkapalli, G.; Brady John, W.; Adney William, S.; Cleary Joseph, M.; Zhong, L.; Himmel Michael, E. *Protein Eng Des Sel* **2007**, *20*, 179-87.

(29) Zhong, L.; Matthews, J. F.; Crowley, M. F.; Rignall, T.; Talon, C.; Cleary, J. M.; Walker, R. C.; Chukkapalli, G.; McCabe, C.; Nimlos, M. R.; Brooks, C. L.; Himmel, M. E.; Brady, J. W. *Cellulose* **2008**, *15*, 261-273.

CHAPTER 7

Cellulase Hydrolytic Activity on Blend Surfaces

7.1 Abstract

Enzyme catalyzed hydrolysis of cellulose in regenerated cellulose:pullulan cinnamate (PC) and regenerated cellulose:polystyrene (PS) blends was studied by quartz crystal microbalance with dissipation monitoring (QCM-D) and in situ atomic force microscopy (AFM). The cellulose:PC and cellulose:PS blend surfaces were prepared via spincoating trimethylsilyl cellulose (TMSC):trimethylsilyl pullulan cinnamate (TMSPC) and TMSC:PS blends from toluene solutions onto gold substrates followed by the removal of trimethylsilyl groups in the presence of HCl vapor. The composition of cellulose:PC blend surfaces was controlled by tuning the degree of cinnamate substitution (DS_{Cinn}) per anhydroglucose unit and TMSC:PC mass ratio, while the composition of cellulose:PS blend surfaces was controlled by tuning the TMSC:PS mass ratio. The QCM-D results showed that the cellulase catalyzed hydrolysis rates for cellulose in cellulose:PC blend surfaces with low DS_{Cinn} (DS_{Cinn} = 0.3) were faster than those on regenerated cellulose surfaces, whereas the cellulase catalyzed hydrolysis rates for cellulose in cellulose:PC blend surfaces with high DS_{Cinn} ($DS_{Cinn} \geq 0.7$) were slower than those on regenerated cellulose surfaces. AFM images revealed smooth surfaces for cellulose:PC (DS_{Cinn} = 0.3) blend surfaces and lateral phase separated morphologies for cellulose:PC ($DS_{Cinn} \geq 0.7$) blend surfaces. A combination of QCM-D and AFM measurements indicated that the cellulase catalyzed hydrolytic activity was strongly dependent on surface morphology. PC (DS_{Cinn} = 0.3) that was miscible with cellulose, could disperse cellulose chains and enhance the accessibility of cellulose. The cellulose:PS blend surfaces showed similar

lateral phase separated morphologies to cellulose:PC ($DS_{Cinn} \geq 0.7$) blend surfaces, which also led to slower cellulase catalyzed hydrolysis rates.

7.2 Introduction

Lignocellulosic biomass has long been recognized as a renewable resource for the production of fuels, especially as fossil fuel reserves decrease.[1-3] Recently, people have paid greater attention to the bioconversion of lignocellulosic materials into ethanol. The bioconversion of lignocellulosic biomass involves three steps: a pretreatment process to reduce substrate recalcitrance, enzymatic hydrolysis of the cellulose and hemicellulose components to simple sugars, and fermentation of sugars to ethanol.[4] The enzymes used in the second step play an important role in the whole process and normally include three different cellulases: exoglucanases (CBHs) that degrade cellulose by splitting off molecules from both ends of the cellulose chain producing cellobiose, endoglucanases (EGs) that target cellulose chains in random locations, and glucosidases (BGLs) that hydrolyze the cellobiose units into glucose.[5-8] As raw lignocellulosic biomasses are indeed composite materials composed of cellulose, hemicelluloses, and lignin and these components are connected through both covalent and non-covalent interactions, the resulting network is highly inaccessible to enzymatic attack.[9] During the past decade, people have studied enzymatic activity on different cellulose model surfaces[10-13] and native cellulose nanofibril surface[14] and found that the enzymatic hydrolysis rate was strongly affected by physicochemical properties of the cellulose substrate including its morphology, composition, accessibility, degree of polymerization, and crystallinity. However, the enzymatic activity on model surfaces for heterogeneous systems has received little attention. To fundamentally understand effects of chemical composition

and morphology of lignocellulosic materials, novel model surface systems were prepared by spincoating blends of a cellulose derivative and pullulan derivatives.

In this chapter, trimethylsilyl cellulose (TMSC) was mixed with trimethylsilyl pullulan cinnamates (TMSPCs) to create polymer blends. Regenerated cellulose:pullulan cinnamate (PC) blend surfaces were prepared via spincoating TMSC:TMSPC blends from toluene solutions onto gold substrates followed by the removal of trimethylsilyl groups in the presence of HCl vapor. The model surfaces contained three components: cellulose, pullulan that represented hemicelluloses, and hydrophobic cinnamate groups that represented lignin. As the cinnamate groups were covalently linked to pullulan, PCs better represent a lignin-carbohydrate complex. By varying the degree of cinnamate substitution (DS_{Cinn}) per anhydroglucose unit (AGU) and TMSC:TMSPC mass ratio, the composition of model surfaces was controlled. Enzymatic activity of a mixture of cellulases produced by fermentation of *Trichoderma reesei* on cellulose:PC blend surfaces was investigated by quartz crystal microbalance with dissipation monitoring (QCM-D) and in situ atomic force microscopy (AFM) experiments. QCM-D is widely used to monitor in situ and real-time adsorption and hydrolysis activities of enzymes on model cellulose surfaces,[11,13,14] while AFM provided the morphological changes of the surfaces before and after exposure to the enzyme.[15] The relationship between the hydrolysis kinetics and the morphology of the surfaces was investigated by combining QCM-D and AFM measurements. Moreover, the enzymatic activity on regenerated cellulose:polystyrene (PS) blend surfaces was also studied for comparison with the cellulose:PC system.

7.3 Experimental

Synthesis and characterization of trimethylsilyl pullulan cinnamates (TMSPC) were described in Chapter 3.1.3. Polystyrene (PS, number average molar mass, M_n = 62600 g•mol^{-1} and polydispersity index, M_w/M_n = 1.03) was purchased from Polymer Source, Inc. Procedures for the preparation and characterization (ellipsometry) of cellulose:pullulan cinnamate (PC) and cellulose:PS blend films were described in Chapter 3.2.1 and 3.2.3. The DS_{Cinn} value and the mass ratio of cellulose:PC and cellulose:PS varied. The "cellulase" was a commercial cellulase cocktail Celluclast1.5L (a mixture of endo- and exo-glucanases, Novozymes A/S, Bagsvaerd, Denmark) produced by fermentation of *Trichoderma reesei*. Citric acid monohydrate was purchased from Fisher Chemical. Cellulase solutions for QCM-D measurements were prepared by dilution of 0.50 g commercial cellulase solution to 100 mL in citrate buffer solution (pH = 4.8, ionic strength of 0.05). In situ atomic force microscopy (AFM) and QCM-D measurements were described in Chapter 3.2.8 and 3.2.10, respectively.

7.4 Results and Discussion

7.4.1 Characterization of Blend Films

Regenerated cellulose:PC blend films were prepared by spincoating TMSC:TMSPC blends from toluene solutions onto gold substrates followed by the removal of trimethylsilyl (TMS) groups in the presence of HCl vapor. First, TMSC and TMSPCs with different DS_{Cinn} were mixed with a 1:1 mass ratio to prepare regenerated cellulose:PC blend films. Ellipsometry results showed that thicknesses of blend films were ~30 nm and were similar to the single-component regenerated cellulose film. After removing TMS groups, thicknesses of cellulose:PC blend films were approximately one-

half the thicknesses of the original TMSC:TMSPC blend films. Cellulose:PC blend films with higher DS_{Cinn} were thicker than those with lower DS_{Cinn}, because the degree of TMS substitution (DS_{TMS}) per AGU was smaller for TMSPC with higher DS_{Cinn}. Second, regenerated cellulose:PC03 blend films with different mass ratio were also prepared by spincoating TMSC:TMSPC03 blends with different mass ratios. The thicknesses of TMSC:TMSPC03 and regenerated cellulose:PC03 films were weakly dependent on the mass ratio and are summarized in **Table 7.1**.

Table 7.1. Thicknesses of blend films from ellipsometry

Surface	TMSC:TMSPC Mass Ratio	Thickness (nm)[a]	Cellulose:PC Mass Ratio[b]	Thickness (nm)[a]
Cellulose	1:0	31.5 ± 0.4	1:0	17.0 ± 0.3
Cellulose:PC03	1:20	29.1 ± 0.3	1:22.4	14.8 ± 0.3
	1:10	29.4 ± 0.3	1:11.2	13.4 ± 0.3
	1:6	29.5 ± 0.2	1:6.7	14.3 ± 0.2
	1:3	29.6 ± 0.4	1:3.3	13.9 ± 0.4
	1:1	29.4 ± 0.5	1:1.1	15.4 ± 0.2
	3:1	29.1 ± 0.6	3:1.1	16.8 ± 1.0
Cellulose:PC07	1:1	29.0 ± 0.3	1:1.3	16.8 ± 0.2
Cellulose:PC12	1:1	29.6 ± 0.5	1:1.6	21.2 ± 0.1
Cellulose:PC23[c]	1:1	-	1:2.0	-

[a]Data was an average of three measurements ± one standard deviation.
[b]Values were calculated on the basis of DS_{TMS} determined by UV measurements (Table 3.3).
[c]TMSC:TMSPC23 blend films were not smooth enough for ellipsometry measurements.

7.4.2 Cellulase Catalyzed Hydrolysis of Cellulose in Cellulose/PC Blend Films by QCM-D and In Situ AFM

Representative scaled frequency (Δf/n) and dissipation (ΔD) change profiles obtained from QCM-D for the regenerated cellulose surface exposed to a citrate buffer solution of cellulase at 20 ℃ are shown in **Figure 7.1**. The citrate buffer was flowed over the regenerated cellulose surface for 30 minutes to obtain a flat baseline. Then, the cellulase solution (pH = 4.8, ionic strength of I = 0.05) was flowed over the cellulose surface. A

rapid decrease of (Δf/n) = -35 Hz, indicated that cellulase rapidly adsorbed onto the cellulose surface. Normally, the cellulase adsorption reached dynamic equilibrium in 1-2 minutes.[11] The dissipation value change (ΔD) was positive, as adsorbed cellulase at the liquid/solid interface formed a floppy film that enhanced energy dissipation. Thereafter, a turning point in the (Δf/n) versus time plot was observed as enzyme catalyzed hydrolysis of cellulose chains began. Then, (Δf/n) increased due to the mass loss of cellulose from the surface. Hydrolysis of the cellulose film was accompanied by a slow increase in the dissipation. During this process, the initial slope during hydrolysis provided an initial hydrolysis rate. Finally, the frequency was stable and a plateau was observed. At this point, the entire cellulose surface had been hydrolyzed.

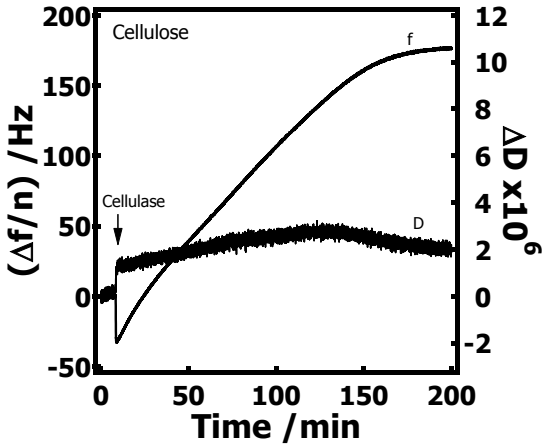

Figure 7.1. (Δf/n) and ΔD versus time from QCM-D for a regenerated cellulose surface exposed to a citrate buffer solution of a cellulase mixture at 20 ℃. Curves correspond to the 3rd overtone. Arrows indicate where solutions were switched.

Cellulase activity on cellulose:PC blend surfaces was also studied by QCM-D. **Figure 7.2** shows (Δf/n) and ΔD profiles for cellulose:PC blend surfaces with different DS_{Cinn}

prepared from 1:1 mass ratio blends of TMSC:TMSPC exposed to citrate buffer solutions of cellulase at 20 ℃. At the beginning, (Δf/n) rapidly decreased due to cellulase adsorption for all cellulose:PC blend surfaces. Then, (Δf/n) increased as degradation of the cellulose chains in the blends began. The ellipsometry results (**Table 7.1**) showed that thicknesses of TMSC:TMSPC blend surfaces were similar to those of TMSC surfaces, however, the total (Δf/n) increase observed for the regenerated cellulose:PC surfaces were smaller than the single-component cellulose surfaces. This difference is attributed to the inability of the cellulases to degrade the PC chains.

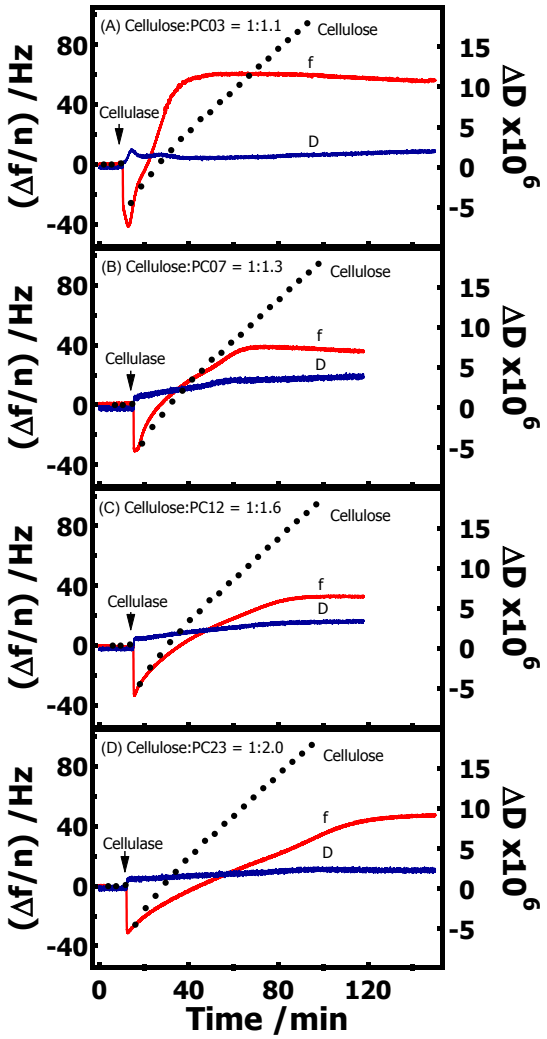

Figure 7.2. (Δf/n) (red curves labeled with f) and ΔD (blue curves labeled with D) versus time from QCM-D for cellulose:PC blend surfaces exposed to citrate buffer solutions of cellulase at 20 ℃: (A) Cellulose:PC03 = 1:1.1, (B) Cellulose:PC07 = 1:1.3, (C) Cellulose:PC12 = 1:1.6, and (D) Cellulose:PC23 = 1:2.0. All cellulose:PC blend surfaces were prepared via spincoating 1:1 mass ratio TMSC:TMSPC blends. Ratios expressed on the graphs are also mass ratios. The dashed black lines represent (Δf/n) for a single-component regenerated cellulose surface. Curves correspond to the 3rd overtone. Arrows indicate where solutions were switched.

As seen in **Figure 7.2**, the most important observation was that the initial cellulase hydrolysis rate on cellulose chains in cellulose:PC blend surfaces varied with DS_{Cinn} and the cellulose:PC mass ratio. The initial hydrolysis rates were obtained from the initial slope in the linear part of ($\Delta f/n$) versus time plots ($d\Delta f/dt$) (**Figure 7.3**). ($d\Delta f/dt$) was converted into an initial hydrolysis rate using the Sauerbrey equation (Equation 3-13), as the films were regarded as rigid, because the ΔD values were relatively small ($\Delta D < 4\times10^{-6}$) during the hydrolysis process. The initial hydrolysis rate values for cellulose:PC blend surfaces with different DS_{Cinn} and cellulose:PC mass ratio are summarized in **Table 7.2**. The initial hydrolysis rate of cellulase catalyzed hydrolysis of cellulose chains in cellulose:PC blend surfaces decreased with the increasing DS_{Cinn} and cellulose:PC mass ratio. The initial hydrolysis rate of cellulase on the cellulose:PC03 surface was 3 times greater than that on the single-component cellulose surface, while the initial hydrolysis rate on the cellulose:PC23 surface was lower than that on the single-component cellulose surface. The initial hydrolysis rates on cellulose:PC07 and cellulose:PC12 blend surfaces were similar to the rate on the single-component cellulose surface, however, the initial hydrolysis rates on these two cellulose:PC blend surfaces decreased over the course of the hydrolysis process, unlike the single-component cellulose surface where the hydrolysis rate remained nearly constant over the entire hydrolysis process.

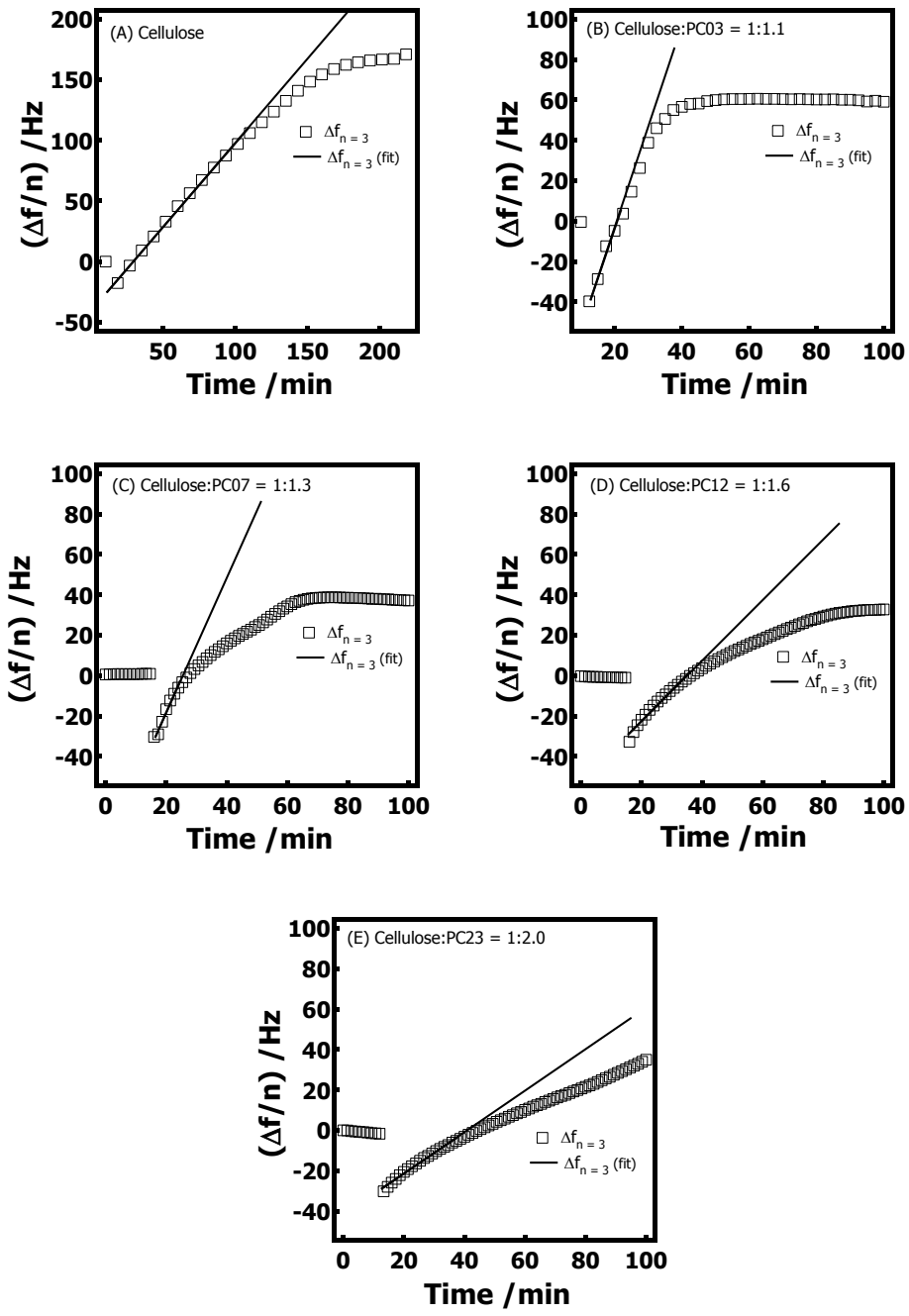

Figure 7.3. Experimental (Δf/n) versus time from QCM-D (□) and best fit (line) for the initial hydrolysis rates for cellulase catalyzed hydrolysis of (A) cellulose and blends of (B) cellulose:PC03, (C) cellulose:PC07, (D) cellulose:PC12, and (E) cellulose:PC23 derived from 1:1 mass ratio blends of TMSC:TMSPC. Ratios expressed on the graphs are also mass ratios. Data correspond to the 3rd overtone.

Table 7.2. Initial hydrolysis rate of cellulase catalyzed hydrolysis of cellulose in cellulose:PC blends[a]

Surface	Cellulose:PC Mass Ratio	Initial ($d\Delta f/dt$) ($Hz \cdot min^{-1}$)	Initial Hydrolysis Rate ($mg \cdot m^{-2} \cdot min^{-1}$)
Cellulose	1:0	1.3 ± 0.1	0.25 ± 0.02
Cellulose:PC03	1:1.1	5.0 ± 0.2	0.89 ± 0.04
Cellulose:PC07	1:1.3	2.7 ± 0.6	0.49 ± 0.10
Cellulose:PC12	1:1.6	1.3 ± 0.2	0.23 ± 0.04
Cellulose:PC23	1:2.0	1.1 ± 0.1	0.19 ± 0.02

[a]Data were an average of three measurements with ± one standard deviation. ($\Delta f/n$) were from the 3rd overtone.

Figure 7.4 shows surface morphologies of regenerated cellulose:PC blend surfaces with different DS_{Cinn} before and after cellulase hydrolysis. As seen in **Figure 7.4A**, cellulose:PC03 blend surfaces were smooth before cellulase hydrolysis. After cellulase was flowed over the surface, the surface became rougher, because cellulase degraded cellulose chains and only pullulan cinnamate domains remained on the substrate (**Figure 7.4B**). Some cellulase aggregates were also observed on the surface. Lateral phase separation occurred for cellulose:PC07, cellulose:PC12, and cellulose:PC23 blends (**Figure 7.4C** through **H**). Cinnamate groups made TMSPC immiscible with TMSC, which led to the phase separated morphologies of cellulose:PC blends with high DS_{Cinn}. As seen in **Figure 7.4D**, **F**, and **H**, after exposure of the surfaces to cellulases, the higher regions in **Figure 7.4C**, **E**, and **G** respectively were actually the PC-rich domains that were revealed after the TMS groups were removed. After cellulase hydrolysis, the PC-rich domains remained and the cellulose domains were degraded and removed (**Figure 7.4D**, **F**, and **H**). The relative heights of the PC-rich domains increased with increasing DS_{Cinn} and the phase separation was also more obvious. It is also interesting to note that cellulose:PC23 blend surfaces showed sharp phase boundaries that are consistent with coexisting phases with greater relative amounts of the major component. Furthermore, all

cellulose:PC blend surfaces were derived from 1:1 mass ratio TMSC:TMSPC blends, so the cellulose occupied areas were similar for all cellulose:PC blend surfaces with different cellulose:PC mass ratios after removal of TMS groups. The cellulose:PC mass ratios did not significantly affect the hydrolysis rates.

A combination of QCM-D results and AFM images indicated that physicochemical properties of the substrates strongly affected enzymatic activity. The cellulase catalyzed hydrolysis rates on cellulose:PC surfaces with different DS_{Cinn} were dependent upon the morphology of the blends. Cellulose and PC with low DS_{Cinn} appeared to be miscible. Although cellulase did not degrade pullulan cinnamate, pullulan cinnamate could disrupt the hydrogen bonding between cellulose chains and increased cellulose accessibility. This effect has been recognized as an important factor for improving cellulase catalyzed hydrolysis processes for biomass conversion.[8,16] The major component of the cellulase mixture used in this work was exo-glucanase (CBH I and CBH II, 80 to 90%), that degraded cellulose only by splitting off molecules from the ends of cellulose chains. Cellulase activity was enhanced on cellulose:PC blend surfaces with higher accessibility. In contrast, pullulan cinnamates with higher DS_{Cinn} were immiscible with cellulose and had a very limited ability to disrupt the hydrogen bonding between cellulose chains. Cellulose domains were only exposed in some areas of the surface of the blends. As a consequence of the phase separated morphology, the hydrolysis rates were slower than those for the single-component cellulose surfaces. Moreover, pullulan cinnamate with higher DS_{Cinn} offered more hydrophobic domains on cellulose:PC blend surfaces which allowed more cellulase molecules to adsorb to the surface via hydrophobic interactions. **Figure 7.4B** and **5F** showed that more cellulase aggregates formed on the cellulose:PC12

blend surface than on the cellulose:PC03 blend surface.

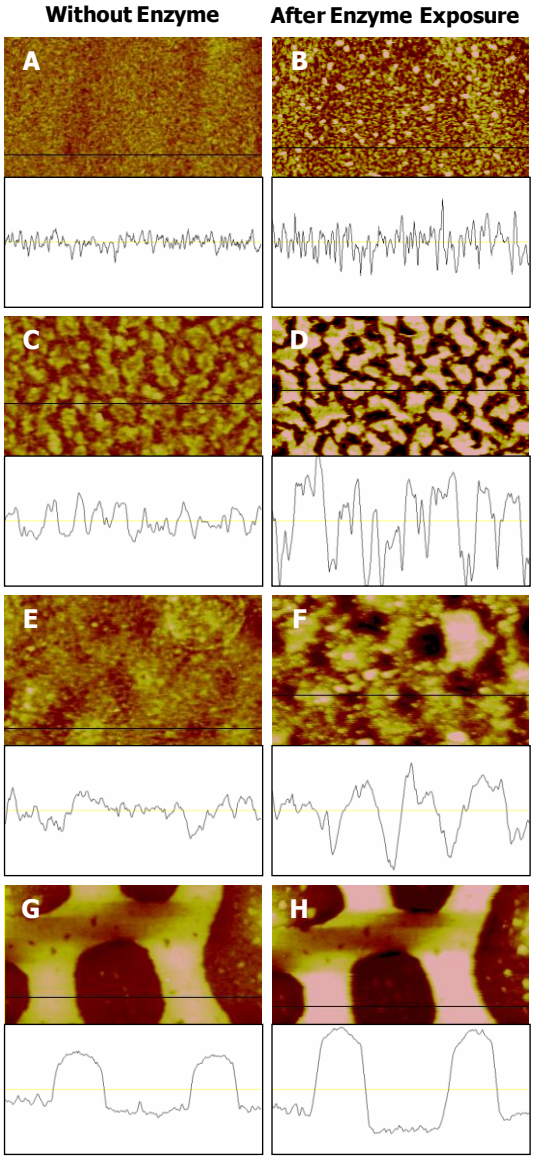

Figure 7.4. In situ AFM height images of (A and B) cellulose:PC03 (1:1.1), (C and D) cellulose:PC07 (1:1.3), (E and F) cellulose:PC12 (1:1.6), and (G and H) cellulose:PC23 (1:2.0) blend surfaces before (A, C, E, and G) and after (B, D, F, and H) cellulase catalyzed hydrolysis. All cellulose:PC blends surfaces were prepared by spincoating 1:1 mass ratio TMSC:TMSCP blends. The images are 5 μm × 5 μm and have Z-axis scales of 0 to 30 nm.

7.4.3 Cellulase Catalyzed Hydrolysis of Cellulose in Cellulose/PC03 Blend Films by QCM-D and In Situ AFM

The pullulan cinnamate with low DS_{Cinn} (PC03) enhanced cellulase catalyzed hydrolysis rates for cellulose in cellulose:PC blend surfaces. In this chapter, cellulase activity on cellulose:PC03 blend surfaces with different mass ratios was studied via QCM-D. **Figure 7.5** shows (Δf/n) and ΔD profiles for cellulose:PC03 blend surfaces exposed to citrate buffer solutions of cellulase at 20 ℃. The mass losses of cellulose:PC03 blend surfaces with different mass ratios, expressed as $(\Delta f/n)_{max}$ the difference between (Δf/n) after the completion of hydrolysis and (Δf/n) after enzyme adsorption, and initial hydrolysis rates are summarized in **Table 7.3**. The mass losses were proportional to the wt% cellulose in the blends and cellulase aggregates were observed in in situ AFM images (**Figure 7.6**) of all cellulose:PC03 blend surfaces after hydrolysis. As such, the mass losses were mainly due to the degradation of the cellulose chains. The cellulase catalyzed hydrolysis rates for cellulose in all blend surfaces were larger than those on single-component cellulose surfaces. As seen in **Figure 7.7**, the hydrolysis rate increased dramatically as the amount of cellulose in the blends decreased. This observation indicated that cellulose chains were readily dispersed in the PC03 matrix and PC03 had to increase enzyme accessibility to compensate for less substrate in the films as the amount of PC03 increased.

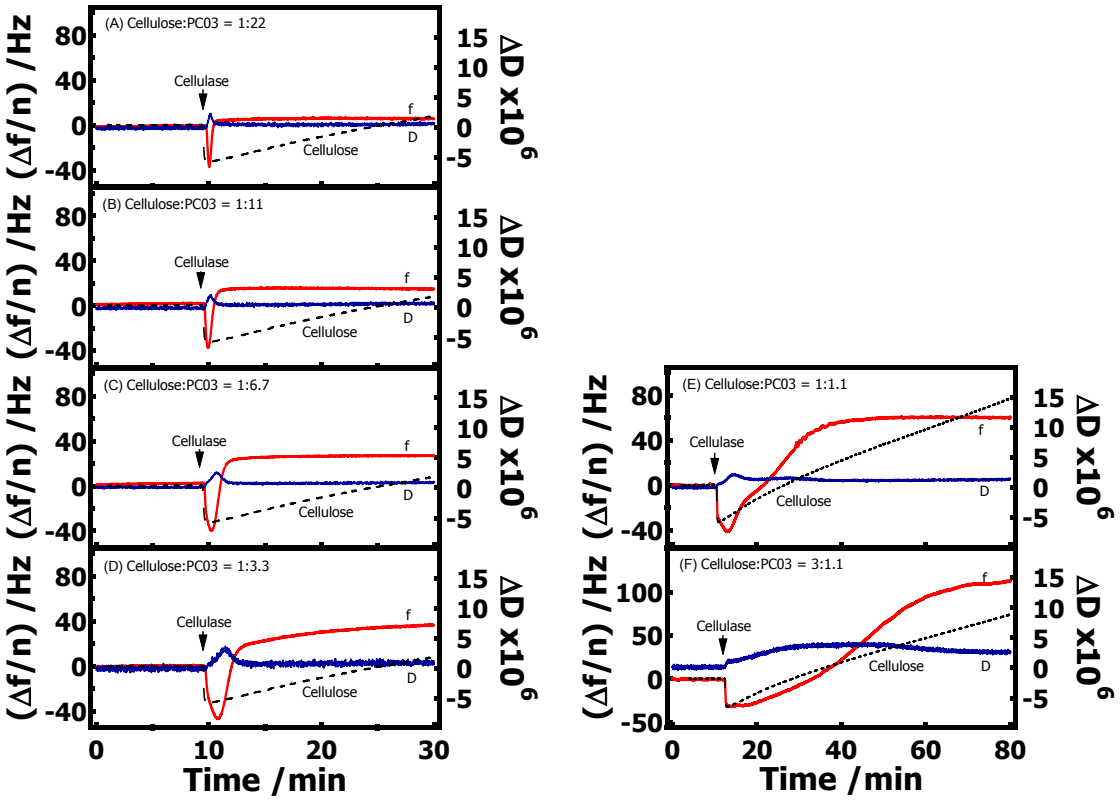

Figure 7.5. (Δf/n) (red curves labeled with f) and ΔD (blue curves labeled with D) versus time from QCM-D for cellulose:PC03 blend surfaces exposed to citrate buffer solutions of cellulase at 20 ℃. Cellulose:PC03 mass ratios are varied: (A) 1:22, (B) 1:11, (C) 1:6.7, (D) 1:3.3, (E) 1:1.1, and (F) 3:1.1. Cellulose:PC03 blend surfaces were prepared via regeneration of spincoated TMSC:TMSPC03 blends. The dashed black lines represent (Δf/n) for regenerated cellulose surfaces. Curves correspond to the 3rd overtone. Arrows indicate where solutions were switched.

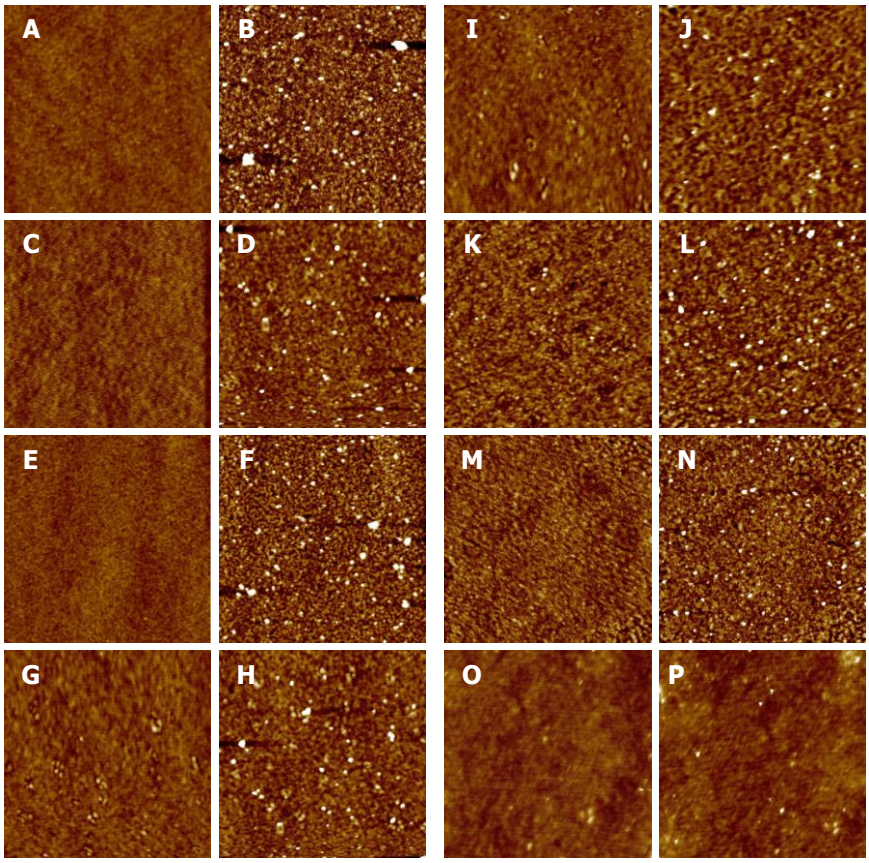

Figure 7.6. In situ AFM height images of cellulose:PC03 blend surfaces before (A, C, E, G, I, K, M, and O) and after (B, D, F, H, J, L, N, and P) cellulase catalyzed hydrolysis. Cellulose:PC03 mass ratios are varied: (A and B) 1:0 (single-component cellulose), (C and D) 3:1.1, (E and F) 1:1.1, (G and H) 1:3.3, (I and J) 1:6.7, (K and L) 1:11, (M and N) 1:22, and (O and P) 0:1 (single-component PC03). The cellulose:PC03 blend surfaces were prepared via regeneration of spincoated TMSC:TMSCP blends. The images are 5 μm × 5 μm and have Z-axis scales of 0 to 30 nm.

Table 7.3. Initial hydrolysis rates for cellulase catalyzed hydrolysis of cellulose in cellulose:PC03 blends[a]

Surface	Cellulose:PC Mass Ratio	$(\Delta f/n)_{max}$[b] (Hz)	Δm[c] ($mg \bullet m^{-2}$)	Initial ($d\Delta f/dt$) ($Hz \bullet min^{-1}$)	Initial Hydrolysis Rate ($mg \bullet m^{-2} \bullet min^{-1}$)
Cellulose	1:0	199.8 ± 7.7	35.4 ± 1.4	1.3 ± 0.1	0.25 ± 0.02
Cellulose:PC03	3:1.1	147.0 ± 7.8	26.0 ± 1.4	3.1 ± 1.0	0.55 ± 0.17
Cellulose:PC03	1:1.1	120.0 ± 11.9	21.2 ± 2.1	5.0 ± 0.2	0.89 ± 0.04
Cellulose:PC03	1:3.3	82.7 ± 5.7	14.6 ± 1.0	20.2 ± 6.7	3.59 ± 1.19
Cellulose:PC03	1:6.7	65.0 ± 1.0	11.5 ± 0.2	59.9 ± 5.5	10.7 ± 1.0
Cellulose:PC03	1:11.2	53.3 ± 2.7	9.4 ± 0.5	87.5 ± 8.3	15.6 ± 1.5
Cellulose:PC03	1:22.4	42.5 ± 2.0	7.5 ± 0.4	118.4 ± 10.6	21.1 ± 1.9

[a]Data was an average of three measurements ± one standard deviation. ($\Delta f/n$) values were from the 3rd overtone.
[b]$(\Delta f/n)_{max}$ was the maximum frequency change between the maximum and minimum frequency in the QCM-D files.
[c]Δm was calculated from $(\Delta f/n)_{max}$ by the Sauerbrey equation (Equation 3-13).

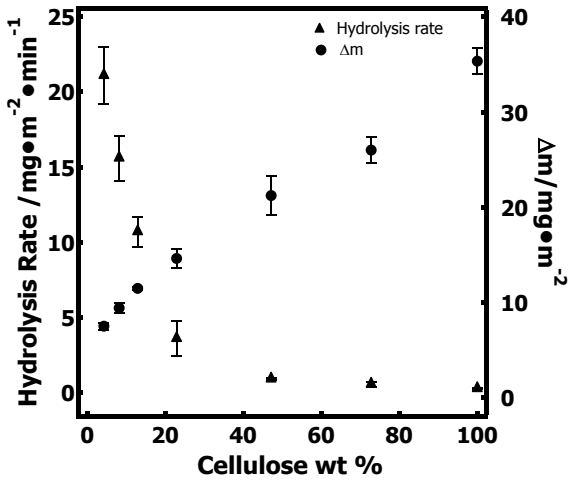

Figure 7.7. (▲) Initial hydrolysis rates and (●) mass changes of cellulose:PC03 blend surfaces with different cellulose wt% in the presence of cellulase. Data are an average of three measurements ± one standard deviation.

7.4.4 Cellulase Catalyzed Hydrolysis of Cellulose in Cellulose/PS Blend Films by QCM-D and In Situ AFM

Cinnamate groups, as hydrophobic aromatic molecules, changed the miscibility of TMSC:TMSPC blends to generate different morphologies upon spincoating and regeneration to form cellulose:PC blends. As seen in **Figures 7.4** and **7.5**, these morphologies affected cellulase catalyzed hydrolysis rates on cellulose domains. Polystyrene (PS), a linear polymer with aromatic substituents, was mixed with TMSC with different mass ratios to prepare regenerated cellulose:PS blend surfaces. **Figure 7.8** shows representative blend morphologies of the cellulose:PS surfaces before and after cellulase catalyzed hydrolysis. Lateral phase separation occurred for cellulose:PS blend surfaces due to consecutive phase separation and dewetting.[17-19] When TMSC:PS blends were spincoated onto the substrate, PS and TMSC initially formed a vertically phase separated structure. TMSC had greater affinity for gold substrates, and thus the PS layer was above the TMSC layer. At the end of the spincoating process, the upper PS layer was broken and holes that formed were filled by TMSC from the lower layer. This process is depicted in **Figure 2.15**. For cellulose:PS blend surfaces made from TMSC:PS blends with a mass ratio of 1:2, a PS-rich phase formed a continuous domain surrounding cellulose-rich domains (**Figure 7.8A**). When the TMSC:PS mass ratio reached 2:1, the island-like PS-rich domains protruded from the cellulose-rich domains (**Figure 7.8C**). Cellulose:PC23 blend surfaces (prepared from a 1:1 mass ratio TMSC:TMSCP23 blend) showed similar laterally phase separated morphologies as cellulose:PS blend surfaces (prepared from a 1:2 mass ratio TMSC:PC blend) (**Figure 7.8A** and **E**). After citrate buffer solutions of cellulase were flowed over the cellulose:PS surfaces, cellulose-rich

domains were hydrolyzed (low areas of the AFM images) and PS-rich domains remained on the substrates (**Figure 7.8B** and **D**).

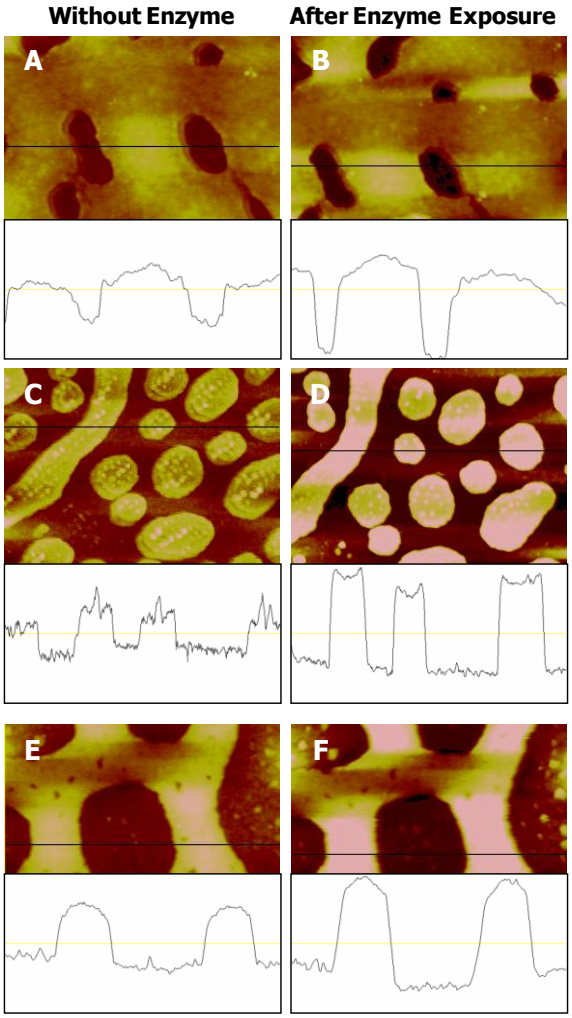

Figure 7.8. In situ AFM height images of cellulose:PS and cellulose:PC23 blend surfaces before (A, C, and E) and after (B, D, and F) cellulase catalyzed hydrolysis. (A and B) Cellulose:PS = 1:4.4, (C and D) cellulose:PS = 1:1.1, and (E and F) cellulose:PC23 = 1:2.0. The images are 5 μm × 5 μm and have Z-axis scales of 0 to 30 nm.

Figure 7.9 shows (Δf/n) and ΔD profiles for cellulose:PS blend surfaces exposed to citrate buffer solutions of cellulase at 20 ℃. The initial hydrolysis rates for cellulase

catalyzed hydrolysis of cellulose:PS blend surfaces were lower than those of the single-component cellulose surfaces (**Table 7.4**). The (Δf/n) versus time curve for the cellulose:PS blend surface (prepared from a 2:1 mass ratio TMSC:PS blend) was similar to the curve for the cellulose:PC23 blend surface (prepared from a 1:1 mass ratio TMSC:TMSCP23 blends) (**Figure 7.9B and C**). The phase separated morphologies of blend surfaces led to lower hydrolysis rates, These results are consistent with the cellulose:PC blends, even with the structural differences between PS and PC.

Table 7.4. Initial hydrolysis rates for cellulase catalyzed hydrolysis of cellulose in cellulose:PS blends[a]

Surface	TMSC:PS Mass Ratio	Cellulose:PS Mass Ratio	Initial (dΔf/dt) ($Hz \bullet min^{-1}$)	Initial Hydrolysis Rate ($mg \bullet m^{-2} \bullet min^{-1}$)
Cellulose	1:0	1:0	1.3 ± 0.1	0.25 ± 0.02
Cellulose:PS	2:1	1:1.1	1.3 ± 0.5	0.23 ± 0.08
Cellulose:PS	1:2	1:4.4	1.0 ± 0.1	0.17 ± 0.01

[a]Data was an average of three measurements with one standard deviation error bars. (Δf/n) were from the 3rd overtone

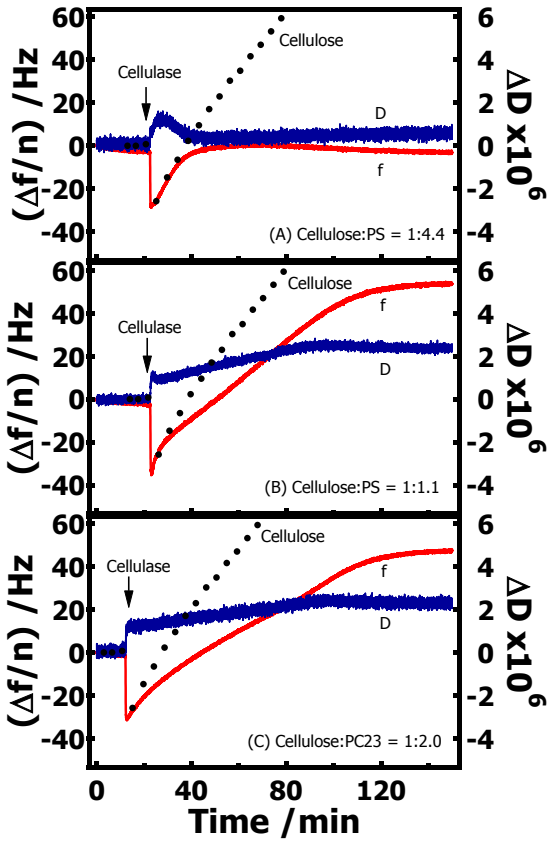

Figure 7.9. (Δf/n) (red curves labeled with f) and ΔD (blue curves labeled with D) versus time from QCM-D for (A) cellulose:PS (1:4.4), (B) cellulose:PS (1:1.1), and cellulose:PC23 (1:2.0) blend surfaces exposed to cellulase citrate buffer solutions at 20 ℃. Cellulose:PS and cellulose:PC blend surfaces were regenerated from blends of TMSC:PS and TMSC:TMSPC23, respectively. The dashed black lines represent (Δf/n) for regenerated cellulose surfaces. Curves correspond to the 3rd overtone. Arrows indicate where solutions were switched.

7.4.5 Advantages of Pullulan Cinnamate Surfaces

Various model cellulose substrates have been used for studying the effects of substrate properties, such as degree of polymerization and crystallinity, on the rate and

efficiency of cellulase catalyzed hydrolysis. These included Avicel,[11] filter paper,[20] cotton, phosphoric acid swollen cellulose,[21] bacterial cellulose,[22] and soluble cellulose derivatives.[23] While studies based on these cellulose substrates have provided an understanding of the role that these substrate characteristics played in hydrolysis, they have also produced additional questions. Do these cellulases act in a similar manner on heterogeneous lignocellulosic substrates? Does the presence of other components such as lignin in biomass influence the cellulase catalyzed hydrolysis? In this chapter, pullulan cinnamate and blend thin films were used for studying the cellulase catalyzed hydrolysis of cellulose. Compared to other cellulose substrates, they showed several advantages:

(1) The model surfaces contain both hydrophilic domains and hydrophobic domains that are similar to heterogeneous lignocellulosic materials in nature.

(2) The hydrophobicity and morphology of the model surfaces can be controlled.

(3) Uniform model surfaces are easily prepared on the sensors for SPR and QCM-D measurements that can provide molecular level insights into the underlying biochemistry.

7.5 Conclusions

Cellulase activity on regenerated cellulose:PC and cellulose:PS blend surfaces was investigated by QCM-D and in situ AFM. AFM images showed that the morphology of the cellulose:PC blend surfaces changed from smooth surfaces to laterally phase separated surfaces as the DS_{Cinn} increased from 0.3 to 2.3. Cellulase catalyzed hydrolysis rates of cellulose in cellulose:PC blend surfaces with low DS_{Cinn} were faster than the rates on cellulose surfaces and cellulose:PC blend surfaces with high DS_{Cinn}. Likewise, cellulose:PS blend surfaces also showed lateral phase separation feature and the cellulase

catalyzed hydrolysis rates on these surfaces were smaller than the rates on the single-component cellulose surfaces. The cellulase activity was strongly affected by the morphology of surfaces. Polymers such as PC03 were miscible with cellulose chains and presumably helped increase enzyme access to the cellulose. This study on cellulose:PC model surfaces may provide further insight into the complex mechanism of cellulase hydrolysis to improve enzyme efficiency for biomass conversion.

7.6 References:

(1) Nonhebel, S. *Renew. Sustain. Energy Rev.* **2005**, *9*, 191-201.

(2) Tilman, D.; Hill, J.; Lehman, C. *Science* **2006**, *314*, 1598-600.

(3) Himmel, M. E.; Ding, S. Y.; Johnson, D. K.; Adney, W. S.; Nimlos, M. R.; Brady, J. W.; Foust, T. D. *Science* **2007**, *315*, 804-807.

(4) Berlin, A.; Balakshin, M.; Gilkes, N.; Kadla, J.; Maximenko, V.; Kubo, S.; Saddler, J. *J. Biotechnol.* **2006**, *125*, 198-209.

(5) Lynd, L. R.; Weimer, P. J.; van Zyl, W. H.; Pretorius, I. S. *Microbiol. Mol. Biol. Rev.* **2002**, *66*, 506-577.

(6) Zandona, A.; Siika-Aho, M.; Ramos, P. *World J. Microbiol. Biotechnol.* **2006**, *22*, 821-825.

(7) Bezerra, R. M. F.; Dias, A. A. *Appl. Biochem. Biotechnol.* **2005**, *126*, 49-59.

(8) Zhang, Y.-H. P.; Lynd, L. R. *Biotechnol. Bioeng.* **2004**, *88*, 797-824.

(9) Bjorkman, A. *Sven. Papperstidn.* **1957**, *60*, 243-51.

(10) Eriksson, J.; Malmsten, M.; Tiberg, F.; Callisen, T. H.; Damhus, T.; Johansen, K. S. *J. Colloid Interface Sci.* **2005**, *284*, 99-106.

(11) Turon, X.; Rojas, O. J.; Deinhammer, R. S. *Langmuir* **2008**, *24*, 3880-3887.

(12) Josefsson, P.; Henriksson, G.; Wagberg, L. *Biomacromolecules* **2008**, *9*, 249-254.

(13) Hu, G.; Heitmann John, A., Jr.; Rojas Orlando, J. *J. Phys. Chem. B* **2009**, *113*, 14761-8.

(14) Ahola, S.; Turon, X.; Osterberg, M.; Laine, J.; Rojas, O. J. *Langmuir* **2008**, *24*, 11592-11599.

(15) Tebeka, I. R. M.; Silva, A. G. L.; Petri, D. F. S. *Langmuir* **2009**, *25*, 1582-1587.

(16) Hong, J.; Ye, X.; Zhang, Y. H. P. *Langmuir* **2007**, *23*, 12535-12540.

(17) Heriot, S. Y.; Jones, R. A. L. *Nat. Mater.* **2005**, *4*, 782-786.

(18) Kontturi, E.; Thuene, P. C.; Niemantsverdriet, J. W. *Macromolecules* **2005**, *38*, 10712-10720.

(19) Nyfors, L.; Suchy, M.; Laine, J.; Kontturi, E. *Biomacromolecules* **2009**, *10*, 1276-1281.

(20) Nidetzky, B.; Steiner, W.; Claeyssens, M. *Biochem. J.* **1994**, *303*, 817-23.

(21) Zhang, Y. H. P.; Cui, J.; Lynd, L. R.; Kuang, L. R. *Biomacromolecules* **2006**, *7*, 644-648.

(22) Samejima, M.; Sugiyama, J.; Igarashi, K.; Eriksson, K.-E. L. *Carbohydr. Res.* **1998**, *305*, 281-288.

(23) Arantes, V.; Saddler Jack, N. *Biotechnol Biofuels* **2010**, *3*, 4.

CHAPTER 8

Overall Conclusions and Suggestions for Future Work

8.1 Overall Conclusions

This study demonstrated that self-assembly of polysaccharides and polysaccharide derivatives could be a useful strategy to modify material surfaces and offer new functionalities. Carboxymethyl celluloses (CMCs) formed aqueous stable layers on cellulose surfaces from electrolyte solutions. $CaCl_2$ (divalent cation) provided a more significant enhancement of CMC adsorption than NaCl (monovalent cation). Surface plasmon resonance (SPR) and quartz crystal microbalance with dissipation monitoring (QCM-D) results showed that CMC formed highly hydrated layers from $CaCl_2$ and NaCl solutions on cellulose surfaces (90 to 95% water). Voigt-based viscoelastic modeling of the QCM-D data was consistent with the existence of highly hydrated CMC layers on cellulose surfaces with shear viscosities of ~ 10^{-3} N•s•m^{-2} and elastic shear moduli of ~10^5 N•m^{-2} for the adsorbed layers. Electrostatic interactions between the ionic groups played an important role on CMC adsorption.

Pullulan cinnamates (PCs), pullulan 3-methoxycinnamates (P3MCs), and pullulan 4-chlorocinnamates (P4CCs) adsorbed onto cellulose, cellulose acetate propionate (CAP), poly(L-lactic acid) (PLLA), and methyl terminated self-assembled alkane thiol monolayers (SAM-CH_3) more strongly than pullulan. The SPR and QCM-D results showed that PCs also formed highly hydrated layers (70 to 90% water) on both hydrophilic and hydrophobic surfaces with shear viscosities of ~ 10^{-3} N•s•m^{-2} and elastic shear moduli between 1×10^5 and 3×10^5 N•m^{-2} for the adsorbed layers. PCs had structures in some ways similar to those of natural lignin-carbohydrate materials, so a biomimetic

approach to improve adhesion between wood-fibers and thermoplastics could be explored by investigating the interaction between hydrophobically modified polysaccharides and polymer surfaces.

Enzyme adsorption onto and activity on PC and cellulose blend films were also studied via QCM-D and in situ atomic force microscopy (AFM). The hydrophobicity of the PC surfaces was controlled by adjusting the degree of cinnamate substitution (DS_{Cinn}) per anhydroglucose unit. It was found that a mixture of cellulases showed weak adsorption onto low DS_{Cinn} PC surfaces, whereas cellulase adsorbed strongly onto high DS_{Cinn} PC surfaces, a clear indication of the role surface hydrophobicity played on enzyme adsorption. Moreover, cellulase catalyzed hydrolysis of cellulose in cellulose/PC and cellulose/polystyrene (PS) blend surfaces was studied by QCM-D and in situ AFM. The composition of cellulose/PC blend surfaces was controlled by tuning the DS_{Cinn} and TMSC:TMSPC mass ratio, while the composition of cellulose:PS blend surfaces was controlled by tuning the TMSC:PS mass ratio. The QCM-D results showed that the cellulase catalyzed hydrolysis rates of cellulose in cellulose:PC blend surfaces with low DS_{Cinn} (DS_{Cinn} = 0.28) were faster than the single-component cellulose surfaces, whereas the cellulase catalyzed hydrolysis rates of cellulose in cellulose:PC blend surfaces with high DS_{Cinn} ($DS_{Cinn} \geq 0.7$) were slower than the single-component cellulose surfaces. AFM images revealed smooth surfaces for cellulose:PC (DS_{Cinn} = 0.3) blend surfaces and laterally phase separated morphologies for cellulose:PC ($DS_{Cinn} \geq 0.7$) blend surfaces. A combination of QCM-D and AFM measurements indicated that the cellulase activity was strongly dependent upon the blend morphology. The cellulose:PS blend surfaces showed similar laterally phase separated morphologies to cellulose:PC ($DS_{Cinn} \geq 0.7$) blends,

where cellulase catalyzed hydrolysis rates of cellulose were also lower. This study provided insight into how substrate accessibility affected enzyme efficiencies in lignocellulosic materials.

8.2 Suggested Future Work

8.2.1 Adsorption of PC onto Model Surfaces by In Situ AFM Measurements

In Chapter 5, adsorption of P3MCs and P4CCs onto cellulose and thermoplastic surfaces was studied by SPR. SPR results (**Figure 8.1**) showed that cinnamate groups enhanced the adsorption of pullulan onto cellulose surfaces. In situ AFM was used to study morphology changes of cellulose surfaces before and after polymer adsorption.[1] Representative in situ AFM images of the liquid/solid interface for regenerated cellulose surfaces before and after adsorption of P3MC and P4CC with DS_{Cinn} ~ 0.06 are provided in **Figure 8.2** and **Figure 8.3**, respectively. Roughness values of cellulose surfaces decreased and cellulose surfaces became smoother due to the adsorption of P3MC06 and P4CC06. SPR and QCM-D results in Chapter 5 indicated that PCs formed highly hydrated layers that contained ~ 80% water. As seen in **Figures 8.2** and **8.3**, the hydrated soft layers might fill the holes in bare cellulose surfaces and change the surface morphology. In situ AFM provided a direct view of the liquid/solid interface involving polymer adsorption. In the future, in situ AFM could be used to study PC adsorption onto thermoplastic surfaces to understand the relationship between the adsorbed mass and the surface roughness.

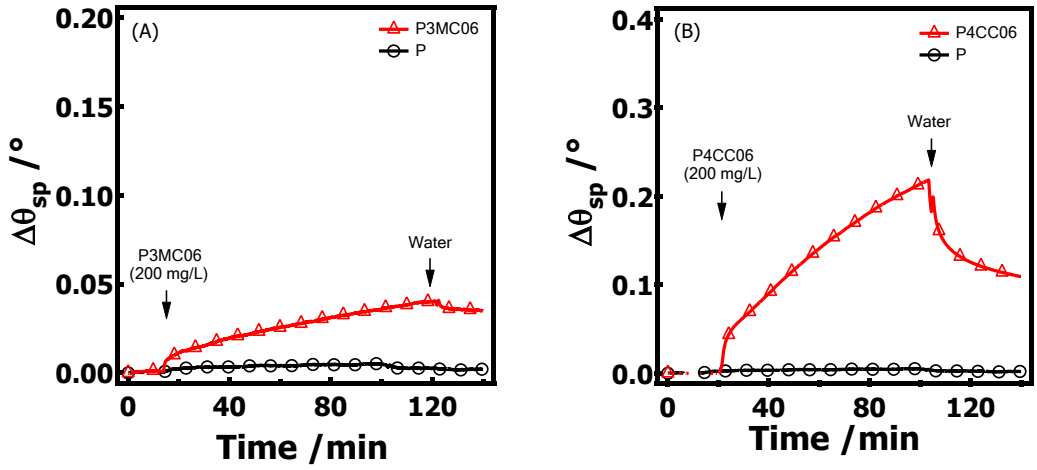

Figure 8.1. Representative SPR data for (A) (○) P and (Δ) P3MC06 and (B) (○) P and (Δ) P4CC06 adsorbed from 200 mg•L^{-1} aqueous solutions onto cellulose surfaces at 20.0 ℃.

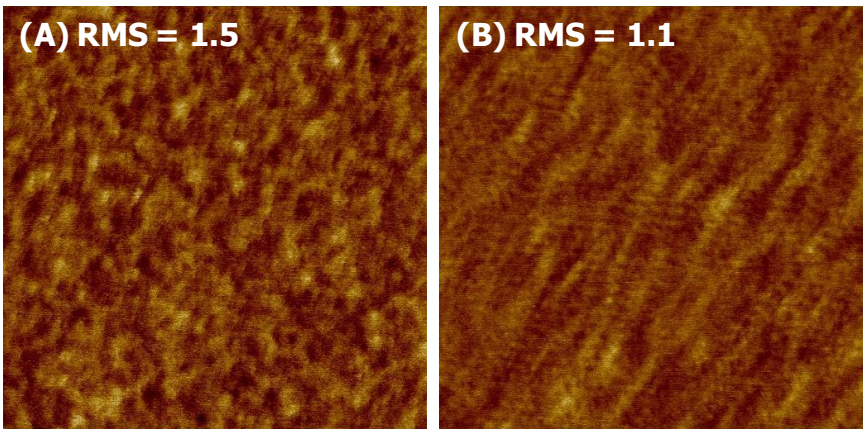

Figure 8.2. Representative AFM height images of the liquid/solid interface for a cellulose surface (A) before and (B) after P3MC06 adsorption from a 200 mg•L^{-1} aqueous solution. AFM images are 2 μm × 2 μm and have *Z*-axis scales of 0 to 20 nm.

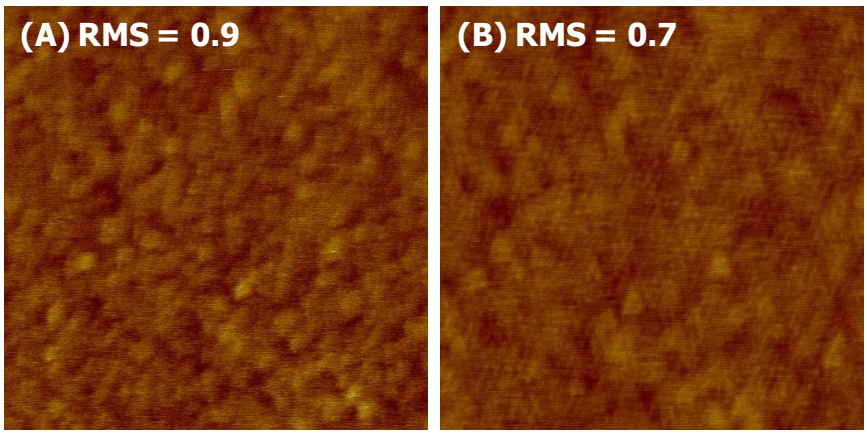

Figure 8.3. Representative AFM height images of the liquid/solid interface for a cellulose surface (A) before and (B) after P4CC06 adsorption from a 200 mg•L^{-1} aqueous solution. AFM images are 2 μm × 2 μm and have *Z*-axis scales of 0 to 20 nm.

8.2.2 Synthesis of New Hydrophobically Modified Pullulan Derivatives

Chapter 5 describes self-assembly of P3MCs and P4CCs onto cellulose, thermoplastic, and SAM-CH_3 surfaces. For the same DS_{Cinn} value sample, P4CC adsorbed onto all model surfaces more strongly than P3MC, indicating that the substituent on the cinnamate groups affected the adsorption of the pullulan derivatives. Hence, pullulan 4-fluorocinnamate (P4FC) and pullulan 4-bromocinnamate (P4BC) derivatives were synthesized through the same procedure used for P4CC (**Figure 8.4**). ^{1}H NMR spectra of P4FC and P4BC are shown in **Figures 8.5** and **8.6**. Water soluble P4FCs and P4BCs with different DS values can be synthesized. Effects of different halogen substituents on the adsorption of pullulan onto cellulose and thermoplastic surfaces could be studied by SPR and QCM-D to understand how different functional groups contribute to the adsorption process.

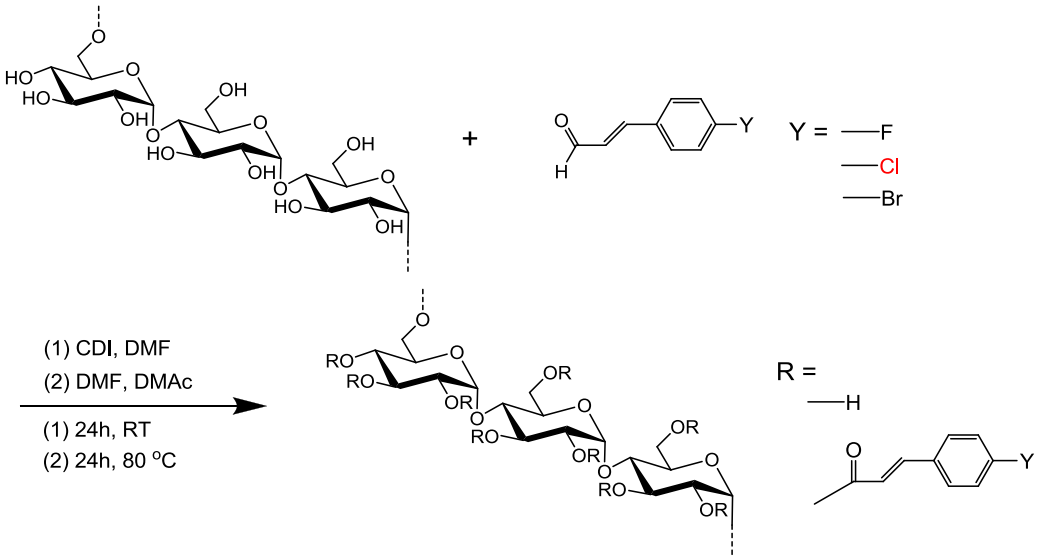

Figure 8.4. Reaction scheme for the synthesis of pullulan 4-fluorocinnamate and pullulan 4-bromocinnamate.

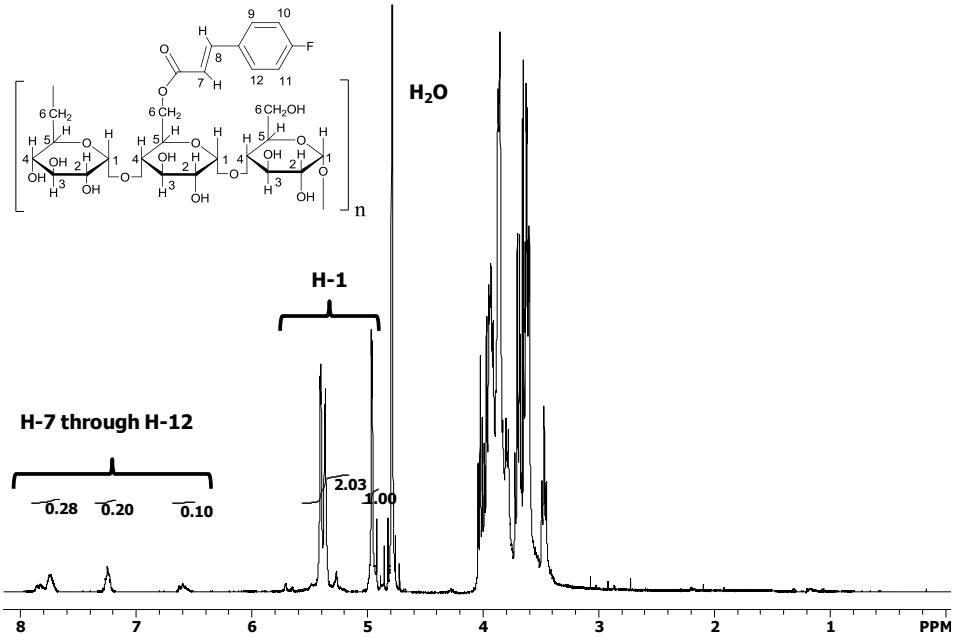

Figure 8.5. ^{1}H NMR spectrum of a pullulan 4-fluorocinnamate (DS_{Cinn} ~ 0.03) in D_2O.

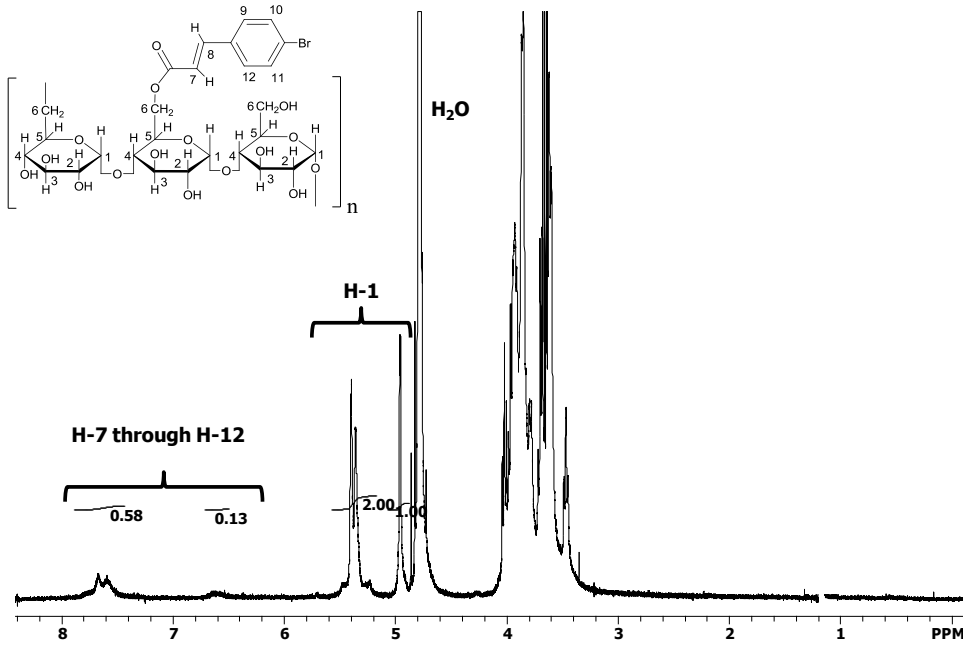

Figure 8.6. ^{1}H NMR spectrum of a pullulan 4-bromocinnamate (DS_{Cinn} ~ 0.04) in D_2O.

8.2.3 Synthesis of Pullulan-Based Polyelectrolytes

Adsorption of polysaccharide-based polyelectrolytes onto solid surfaces is important for both industrial applications and theoretical research.[2] In Chapter 4, carboxymethyl cellulose adsorption onto cellulose surfaces from different electrolyte solutions was studied. Carboxymethyl cellulose adsorbed from calcium chloride solutions onto cellulose surfaces and formed stable layers. These layers introduced ionic groups to the cellulose surface, illustrating a mechanism for potentially modifying biocompatibility between materials.

Polysaccharide-based polyelectrolytes were synthesized from pullulan via incorporation of isocyanate trihead molecules (**Figure 8.7**). Pullulan was dried for 12 h in a vacuum oven at 70 ℃ before the reaction. As a representative procedure, 0.3 g pullulan

(1.9 mmol unhydroglucose units) and 10 mL DMSO were added to a 50 mL two-necked round bottom flask equipped with a reflux condenser and magnetic stirrer under nitrogen. After pullulan was dissolved at 70 ℃, 2.0 g triethyl amine (TEA, 20 mmol) was added to the solution. Subsequently 1.8 g isocyanate trihead (4.1 mmol) was dissolved in 5 mL DMSO and added dropwise to the pullulan/TEA solution. This mixture was allowed to react for 48 h at 70 ℃. The product was dialyzed in ethanol for 3 days. Then, ethanol was removed by rotary evaporation and 0.2 g solid product was obtained. A ^{1}H NMR spectrum of pullulan trihead in DMSO-d_6 is shown in **Figure 8.8**. The peaks between 1.2 – 2.2 ppm were from trihead molecules containing tert-butyl ester protecting groups.

The three tert-butyl groups could be easily removed by acid hydrolysis. 0.1 g Pullulan trihead was dissolved in 10 mL trifluoroacetic acid (TFA) and the mixture was stirred for 24 hours at room temperature. Then, the product was purified by dialysis in water for 3 days. Finally, 0.05 g pullulan triacid product was obtained by freeze drying. A ^{1}H NMR spectrum of pullulan triacid in D_2O is shown in **Figure 8.9**. The peaks from the tert-butyl groups were absent, indicating that tert-butyl groups were removed by TFA.

Pullulan triacid derivatives are interesting polyelectrolytes, because triacid groups introduce not only ionic groups, but also bulky organic groups to pullulan chains. The solubility of pullulan triacid derivatives depends on solution pH value. It offers a possibility to create pH sensitive colloidal agents with potential applications in drug delivery.[3,4] The adsorption of pullulan triacid derivatives at liquid/solid interfaces as a surface modification method can also be studied.

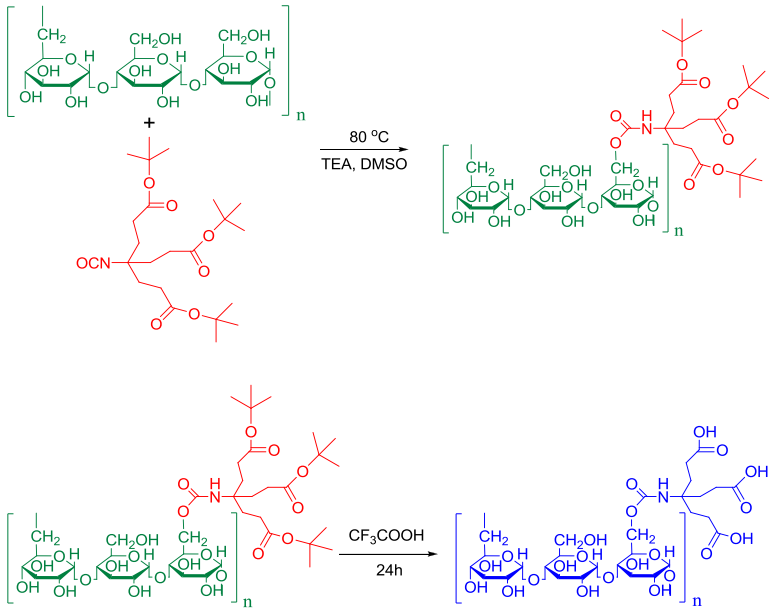

Figure 8.7. Reaction scheme for the synthesis of pullulan trihead and pullulan triacid derivatives.

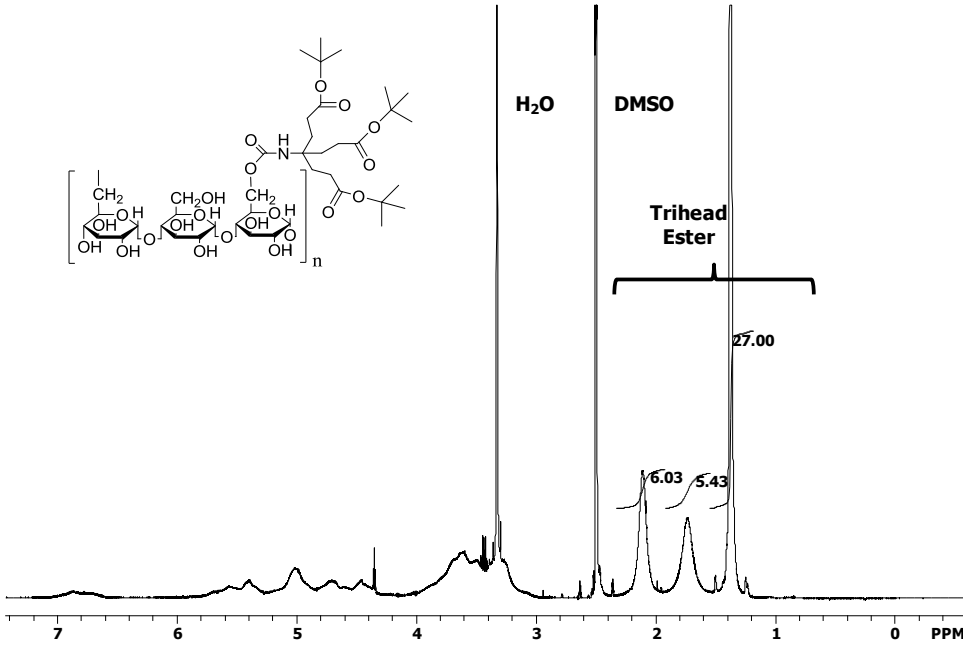

Figure 8.8. ^{1}H NMR spectrum of a pullulan trihead derivative in DMSO-d_6. The degree of substitution is ~ 0.5 per AGU.

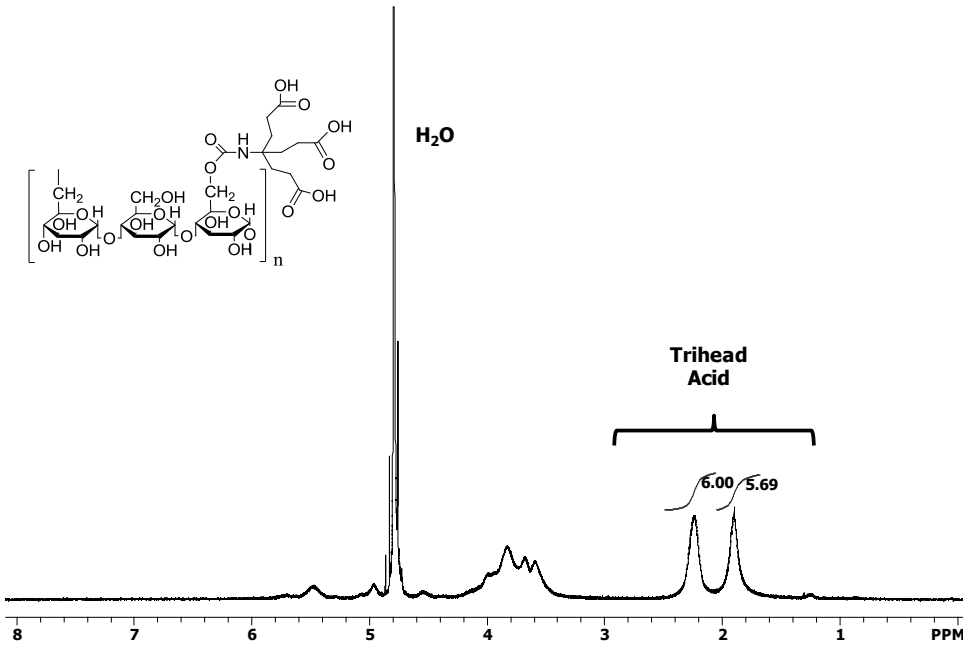

Figure 8.9. ^{1}H NMR spectrum of a pullulan triacid derivative in D_2O. The degree of substitution is ~ 0.5 per AGU.

8.3 References:

(1) Kaya, A.; Du, X.; Liu, Z.; Lu, J. W.; Morris, J. R.; Glasser, W. G.; Heinze, T.; Esker, A. R. *Biomacromolecules* **2009**, *10*, 2451-2459.

(2) Crouzier, T.; Boudou, T.; Picart, C. *Current Opinion in Colloid & Interface Science* **2010**.

(3) Schatz, C.; Domard, A.; Viton, C.; Pichot, C.; Delair, T. *Biomacromolecules* **2004**, *5*, 1882-1892.

(4) Drogoz, A.; David, L.; Rochas, C.; Domard, A.; Delair, T. *Langmuir* **2007**, *23*, 10950-10958.